UNIVERSIDAD COMPLUTENSE DE MADRID

FACULTAD DE CIENCIAS QUÍMICAS

TESIS DOCTORAL

STRUCTURE AND FUNCTION INVESTIGATION ON MEMBRANE-BINDING PROTEINS

INVESTIGACIÓN DE LA ESTRUCTURA Y FUNCIÓN DE PROTEÍNAS DE ASOCIACIÓN A MEMBRANAS

Memoria para optar al grado de doctor presentada por

Andreas Santamaria

Directores

Eduardo Guzmán Solís
Armando Maestro
Nathan Richard Zaccai

Madrid, 2022

UNIVERSIDAD COMPLUTENSE DE MADRID
FACULTAD DE CIENCIAS QUÍMICAS

TESIS DOCTORAL

Structure and function investigation on membrane-binding proteins

Investigación de la estructura y función de proteínas de asociación a membranas

MEMORIA PARA OPTAR AL GRADO DE DOCTOR

PRESENTADA POR

Andreas Santamaria

Directores

Eduardo Guzmán Solís
Armando Maestro
Nathan Richard Zaccai

Madrid

UNIVERSIDAD COMPLUTENSE DE MADRID

FACULTAD DE CIENCIAS QUÍMICAS

TESIS DOCTORAL

STRUCTURE AND FUNCTION INVESTIGATION ON MEMBRANE-BINDING PROTEINS

Memoria para optar al grado de doctor presentada por
Andreas Santamaria

PhD Supervisors

Eduardo Guzmán Solís
Armando Maestro
Nathan Richard Zaccai

Madrid, 2022

UNIVERSIDAD COMPLUTENSE DE MADRID

FACULTAD DE CIENCIAS QUÍMICAS

TESIS DOCTORAL

INVESTIGACIÓN DE LA ESTRUCTURA Y FUNCIÓN DE PROTEÍNAS DE ASOCIACIÓN A MEMBRANAS

Memoria para optar al grado de doctor presentada por
Andreas Santamaria

Directores

Eduardo Guzmán Solís
Armando Maestro
Nathan Richard Zaccai

Madrid, 2022

A Zia Giulia

INDEX

List of abbreviations

NR	neutron reflectometry
SANS	small-angle neutron scattering
QCM-D	Quartz crystal microbalance with dissipation monitoring
BAM	Brewster angle microscopy
HKM	buffer: 25 mM HEPES pH 7.2, 125 mM potassium acetate, 5 mM magnesium acetate, 1 mM DTT
HEPES	N-(2-Hydroxyethyl)piperazine-N′-(2-ethanesulfonic acid), 4-(2-hydroxyethyl)piperazine-1-ethanesulfonic acid
MES	4-Morpholineethanesulfonic acid, 2-(N-Morpholino)ethanesulfonic acid
DTT	*threo*-1,4-Dimercapto-2,3-butanediol
PC	phosphatidylcholine
PE	phosphatidylethanolamine
PS	phosphatidylserine
PI	phosphatidylinositol
PIP	phosphatidylinositol-phosphate (phosphoinositide)
PIP_2 or $PI(4,5)P_2$	phosphatidylinositol-4,5-bisphosphate
SM	sphingomyelin
DPPC	1,2-dipalmitoyl-sn-glycero-3-phosphocholine
POPC	1-palmitoyl-2-oleoyl-sn-glycero-3-phosphocholine
DOPC	1,2-dioleoyl-sn-glycero-3-phosphocholine
POPS	1-palmitoyl-2-oleoyl-sn-glycero-3-phosphoserine
DPPE	1,2-dipalmitoyl-sn-glycero-3- phosphoethanolamine

List of abbreviations

DOPE	1,2-dioleoyl-sn-glycero-3- phosphoethanolamine
PM	plasma membrane
ERGIC	endoplasmic-reticulum-Golgi intermediate compartment
SUV	small unilamellar vesicles
CME	clathrin-mediated endocytosis
CALM	clathrin assembly lymphoid myeloid leukemia protein
AP2	Adaptor Protein (complex) 2
FCHo2	N-terminal Fes-CIP4 homology domain only protein 2
BAR	Bin-Amphiphysin-Rvs167
Eps15	epidermal growth factor pathway substrate 15
FP	Fusion Peptide
CD	circular dichroism
PDB	protein data bank

Resumen

La presente Tesis Doctoral se centra en el estudio de proteínas de asociación a biomembranas, recurriendo para ella a modelos lipídicos *in vitro*. En particular, los modelos utilizados han sido monocapas lipídicas, bicapas soportadas sobre substratos sólidos y vesículas, permitiendo imitar diferentes características de las membranas biológicas de interés, mediante el ajuste de la composición lipídica. Entre las técnicas utilizadas en esta tesis doctoral, la reflectometría de neutrones (NR) ha demostrado ser muy útil para la caracterización de las membranas modelo planas, así como para investigar la asociación lípido-proteína. La organización de las proteínas en las membranas y su interacción con los lípidos presenta gran importancia en multitud de procesos biológicos fundamentales, como el tráfico, la señalización, y los procesos de endocitosis e infección viral. Las proteínas específicas son capaces de unirse a las membranas celulares, normalmente mediante una interacción electrostática o hidrofóbica. En el **Capítulo 1** se ofrece una introducción a los sistemas investigados en la presente tesis. El **Capítulo 2** describe brevemente las membranas modelo utilizadas y las técnicas empleadas para investigar la estructura fuera del plano de dichas membranas (ortogonal con respecto al plano de la membrana), así como la organización lipídica en el plano. Los **Capítulos 3** y **4** se centran en la caracterización de las membranas modelo lipídicas *in vitro*, cuya interacción con diversas proteínas será posteriormente discutida en los **Capítulos 5**, **6** y **7**. Cada capítulo de la presente tesis aborda una actividad de investigación única, que puede englobarse dentro de dos campos principales: (1) la interacción de proteínas de la vía de endocitosis mediada por clatrina (CME) con membranas que contienen fosfatidilinositol 4,5-bisfosfato (PIP2), y (2) la interacción de péptidos de la proteína Spike del SARS-CoV-2 con modelos de membranas plasmáticas.

La CME es el principal mecanismo por el que las células eucariotas internalizan y reciclan la mayoría de las proteínas de membrana (denominadas cargas). Está dirigida por diferentes proteínas adaptadoras (CALM, AP2) y moduladoras (FCHo2, Eps15), que sólo interactúan con la capa interior de la membrana celular cargada negativamente. Esta última presenta lípidos cargados negativamente, como el PIP2, que pueden interactuar con los parches positivos de las proteínas participantes en la endocitosis. El grupo polar del PIP2 contiene un anillo de inositol poliol cuyos grupos hidroxilos en la posición 4 y 5 están fosforilados, proporcionando así las cargas negativas necesarias para la unión de las proteínas. Aunque la interacción del anillo de inositol con las

proteínas implicadas en la CME se ha evaluado a nivel molecular, nunca se ha determinado su orientación antes de la unión a proteínas. El **Capítulo 3** se centra en la caracterización de la estructura fuera del plano de membranas modelo planas, en forma de monocapas lipídicas, que contienen PIP2. El uso de NR permitió determinar la orientación del anillo de inositol. Además, la caracterización en el plano interfacial de dichas monocapas lipídicas permitió la visualización de dominios de PIP2, cuya formación se correlacionó con la orientación del anillo de inositol. Los **Capítulos 5** y **6** se centran en el estudio de la asociación de las proteínas adaptadoras CALM y AP2, y las proteínas moduladoras FCHo2 y Eps15, con sistemas modelo lipídicos *in vitro* enriquecidos en PIP2, así como de la caracterización de las estructuras resultantes de dicha asociación. De hecho, aunque la interacción de dichas proteínas con membranas modelo que contienen PIP2 ha sido ampliamente estudiada desde el punto de vista bioquímico, todavía falta información importante. Por ejemplo, la proteína adaptadora CALM contiene una hélice anfifílica que se cree que se inserta en la membrana, pero su posición al unirse a los lípidos, junto con la orientación de la proteína, no han sido determinadas aún. El **Capítulo 5** trata de dar respuesta a dichos aspectos, mediante la combinación de técnicas interfaciales y de volumen, que permitieron investigar la unión de CALM tanto a membranas planas (monocapas y bicapas), así como a vesículas. En cuanto a la interacción con AP2, se ha resuelto su estructura formando complejos con una molécula que imita a la cabeza polar PIP2, y se ha investigado la interacción con membranas modelo. Sin embargo, falta información detallada sobre la unión de AP2 con sistemas modelo lipídicos complejos *in vitro,* que contengan tanto PIP2 como una molécula que pueda imitar la carga reconocida por AP2. El **Capítulo 6** se centra en la caracterización de una membrana modelo compleja de este tipo, y en el estudio de la asociación de AP2 con NR. Por último, el FCHo2, que desempeña un papel clave en el reclutamiento local de AP2, es una proteína moduladora que está compuesta por diferentes dominios, cuya posición durante su asociación a la membrana aún no se ha determinado. Para ello, el **Capítulo 6** explota NR para obtener información sobre la posición de los diferentes dominios de FCHo2, también cuando se une a Eps15.

El SARS-CoV-2 es un virus encapsulado responsable de una enfermedad respiratoria letal desde su aparición a finales de 2019. Se caracteriza por tener una envoltura lipídica con proteínas de membrana, como las proteínas de envoltura, de membrana y de espiga. Esta última es responsable del reconocimiento de los receptores y contiene un dominio de fusión que desencadena la fusión entre las membranas del virus y del huésped, iniciando la infección. Sin embargo, los mecanismos

moleculares que regulan la fusión de las membranas no se conocen en profundidad. En primer lugar, en el **Capítulo 4** se ha abordado la identificación y caracterización de una membrana modelo adecuada que pueda replicar la membrana plasmática. Para ello, se emplearon monocapas lipídicas compuestas por fosfolípidos naturales extraídos de levadura, y caracterizadas por diferentes contenidos de colesterol. El estudio de estos sistemas tiene como objetivo determinar la estructura fuera del plano de las membranas modelo, así como su organización dentro del plano, evaluando la influencia del contenido de colesterol. Además, se utilizaron modelos de membranas plasmáticas, en forma de monocapa, bicapa y vesículas, para investigar la interacción de los péptidos del dominio de Fusión de Spike (denominados, por tanto, péptidos de fusión, PF). El **Capítulo 7** muestra como los diferentes péptido de fusión presentan diferentes funciones de los péptidos. En particular, NR permitió identificar un modelo molecular detallado para el mecanismo de fusión de las membranas.

Abstract

The present PhD thesis reports the investigation on membrane-interacting proteins with several different *in vitro* lipid model systems. The model membranes used here, in the form of lipid monolayers, solid supported bilayers and vesicles, offer the possibility to mimic biological membranes of interest, by tuning the lipid composition. Among the techniques used in this PhD thesis, neutron reflectometry (NR) has been proven to be very useful to characterize planar model membranes prior to protein addition, as well as to investigate lipid-protein binding. The protein organization in membranes and their interaction with lipids are of paramount importance for a plethora of fundamental biological processes to occur, such as trafficking, signalling, endocytosis pathways as well as viral infection. Specific proteins are able to bind cellular membranes, usually through electrostatic or hydrophobic interaction. **Chapter 1** of this thesis gives an introduction regarding the systems investigated. **Chapter 2** briefly describes the model membranes used and the techniques employed to investigate the out-of-plane structure of such membranes (orthogonal with respect to the plane of the membrane), as well as the lipid organization in the plane of the membrane. **Chapters 3** and **4** report the characterization of *in vitro* lipid model membranes, whose interaction with membrane-binding proteins was subsequently investigated in **Chapters 5**, **6** and **7**. Each chapter of this manuscript addresses a unique research activity, which can be enclosed within two main field: (1) the interaction of proteins from the clathrin-mediated endocytosis (CME) pathway with membranes containing phosphatidylinositol 4,5-bisphosphate (PIP_2); (2) the interaction of peptides from the SARS-CoV-2 Spike protein with plasma membrane models.

CME is the main mechanism by which eukaryotic cells internalize and recycle most membrane proteins (named cargoes). It is driven by different adaptor (CALM, AP2) and modulator (FCHo2, Eps15) proteins, which solely interact with the negatively charged inner leaflet of the cell membrane. Indeed, the latter presents negatively charged lipids, such as PIP_2, that can interact with positive patches of endocytic proteins. PIP_2 polar headgroup contains a polyol inositol ring whose hydroxyl groups in position 4 and 5 are phosphorylated, thus providing the required negative charges for protein binding. Although the interaction of the inositol ring with CME involved proteins has been shown in molecular details, its orientation prior to protein binding has never been determined. **Chapter 3** reports the characterization of PIP_2-containing planar model membranes, in the form of lipid monolayer, whose out-of-plane structural characterization with

NR allowed the determination of the inositol ring orientation. Moreover, the in-plane investigation of such lipid monolayers permitted the visualization of PIP_2 domain, whose formation was correlated with the orientation of the inositol ring. **Chapter 5** and **6** focus on the investigation of the binding and resultant structures formed by adaptor proteins CALM and AP2, and modulator proteins FCHo2 and Eps15, on association with *in vitro* lipid model systems enriched in PIP_2. In fact, although their interaction with PIP_2-containing model membranes has been extensively studied from a biochemical point of view, important information is still missing. For example, the adaptor protein CALM contains an amphipathic helix that is thought to insert in the membrane, but its position upon lipid binding, alongside with the protein orientation, has not been determined yet. **Chapter 5** unravels these important pieces of information, by combining interfacial and bulk techniques, which allowed the investigation of CALM binding to planar membranes (mono- and bilayer) as well as vesicles. Regarding AP2, its structure in complex with a PIP_2-headgroup mimicking molecule has been solved and the interaction with model membranes investigated. However, detailed information on AP2 binding with complex *in vitro* lipid model systems, containing both PIP_2 and a molecule that could mimic the cargo recognized by AP2, is missing. **Chapter 6** reports the characterization of such a complex model membrane, and the investigation of AP2 binding with NR. Finally, FCHo2, which plays a key role in local AP2 recruiting, is composed by different domains, whose position upon membrane binding has not been shown yet. To this end, **Chapter 6** shows how the exploitation of NR allows getting information about the position of the different FCHo2 domains, also when it binds to its partner Eps15.

SARS-CoV-2 is an encapsulated virus responsible for a lethal respiratory illness since its outbreak at the end of 2019. It is characterized by a lipid envelope with membrane proteins, such as Envelope, Membrane and Spike proteins. The latter is responsible for receptor recognition and contains a fusion domain that triggers the fusion between viral and host membranes, initializing the infection. However, the molecular mechanisms regulating membrane fusion are not deeply understood. Firstly, the identification and characterization of an appropriate model membrane that could replicate the plasma membrane have been addressed, in **Chapter 4**. To this end, lipid monolayers composed of natural phospholipid extracted from yeast cells, and characterized by different cholesterol contents, were employed. The study of these systems aimed at determining the lipid out-of-plane structure as well as in-plane organization, and evaluating the influence of cholesterol. Furthermore, plasma membrane models, in the form of monolayer, bilayer and

vesicles, were used to investigate the interaction of peptides from the Spike Fusion domain (thus named fusion peptides, FPs). **Chapter 7** reports the results obtained, which unravelled different roles for the peptides. In particular, NR allowed identifying a detailed molecular model for the membrane fusion mechanism.

Chapter 1

Introduction

Biological membranes provide a platform for fundamental biological reactions to occur, including metabolic pathways, trafficking, signalling, host-pathogen interactions, endocytic pathways and transmembrane transport messengers[1–8], at the basis of which the interactions between lipids and proteins are of paramount importance. Specific phospholipids, commonly negatively charged ones, or phase-separated lipid rafts, are directly involved in these interactions[9]. Different proteins include motifs for the binding of specific lipids, such as phosphatidylinositol phosphates (PIPs) that present a central role in cellular functions[10], just like the attachment of the cytoskeleton to the plasma membrane, membrane trafficking, and ion channel and enzyme activation[3–7]. Thus, a deep understanding of protein-membrane interactions is fundamental to gain insights into several cellular processes.

This thesis aims to investigate the interaction between proteins and *in vitro* lipid model systems, especially unravelling protein orientation and insertion upon binding with negatively charged membranes. After a chapter, which describes the biophysical techniques used, the next chapters focus on the preparation and characterization of *in vitro* lipid model systems that can mimic important features of biological membranes (**Chapters 3** and **4**). For this purpose, synthetic lipids, such as phosphatidylinositol 4,5-bisphosphate and cholesterol were used, appropriately combined with natural phospholipids. **Chapter 3** focuses on the investigation of the out-of-plane structure and in-plane organization of lipid monolayers containing phosphatidylinositol 4,5-bisphosphate, and **Chapter 4** reports, for the first time, the deposition and structural characterization of monolayers made of natural phospholipids, extracted from yeast cells. Finally, the interaction between the studied model membranes and membrane-binding proteins was subsequently investigated with both in solution and interfacial techniques (**Chapters 5** to **7**). The proteins investigated were taken from two distinct processes that happen at the cellular membrane: (1) the clathrin-mediated endocytosis (CME) pathway and (2) the fusion between host and viral membranes, which is the key step of the SARS-CoV-2 infection. Regarding the CME, **Chapters 5** and **6** report the results concerning the binding, insertion and three-dimensional orientation of endocytic proteins with respect to several membrane models, in the form of mono- and bilayer of lipids. **Chapter 7** provides a better comprehension of the SARS-CoV-2 infection mechanism.

Indeed, the interaction of multiple peptides derived from SARS-CoV-2 Spike protein with plasma membrane model systems was investigated, to gain deep knowledge about viral membrane-host membrane fusion mechanism, which is the key step of the viral infection.

1. Lipids

Lipids are the main constituents of cellular membranes that can be considered as bilayers made of lipid molecules, containing embedded membrane proteins. The most abundant structural lipids in eukaryotic cell membranes are glycerophospholipids (usually referred to as phospholipids)[11]. Phospholipids are characterized by a hydrophobic moiety bound to a glycerol backbone, which consists of either saturated or *cis*-unsaturated fatty acyl chains of variable extent length (number of carbon atoms) and unsaturation degree, and a hydrophilic group resulting from the esterification of a phosphatidic acid moiety, whose characteristics influence the general chemical behaviour of the lipid molecule. Thus, phospholipids can be classified in families depending on the nature of the group participating in the esterification of the phosphatidic acid moiety, such as zwitterionic phosphatidylcholines (PC) and phosphatidylethanolamines (PE), negatively charged phosphatidylserines (PS), phosphatidylglycerols (PG) and phosphatidylinositols (PI), together with its phosphorylated variants (PIPs). Each phospholipid family presents a shared structure, including a broad range of molecular species characterized by acyl chains[12] with different lengths and saturation degrees. Moreover, the most abundant phospholipids in eukaryotic cell membranes[13,14], thus the most commonly used for research purposes, are the one containing 16 or 18 carbon atoms acyl chains. Examples of such phospholipids are 1,2-dipalmitoyl-sn-glycero-3-phosphocholine (DPPC)[15–21], 1-palmitoyl-2-oleoyl-glycero-3-phosphocholine (POPC)[22,23], 1,2-dioleoyl-sn-glycero-3-phosphocholine (DOPC)[24], 1,2-dioleoyl-sn-glycero-3-phosphoethanolamine (DOPE)[24], 1-palmitoyl-2-oleoyl-sn-glycero-3-phospho-L-serine (POPS)[25] and 1,2-dipalmitoyl-sn-glycero-3-phospho-(1'-rac-glycerol) (DPPG)[20,26] (**Figure 1.1**). In particular, in mammalian membranes it is possible to find several phospholipid types, including zwitterionic PC and PE, and negatively charged PS and PI, together with its phosphorylated variants (PIPs)[27].

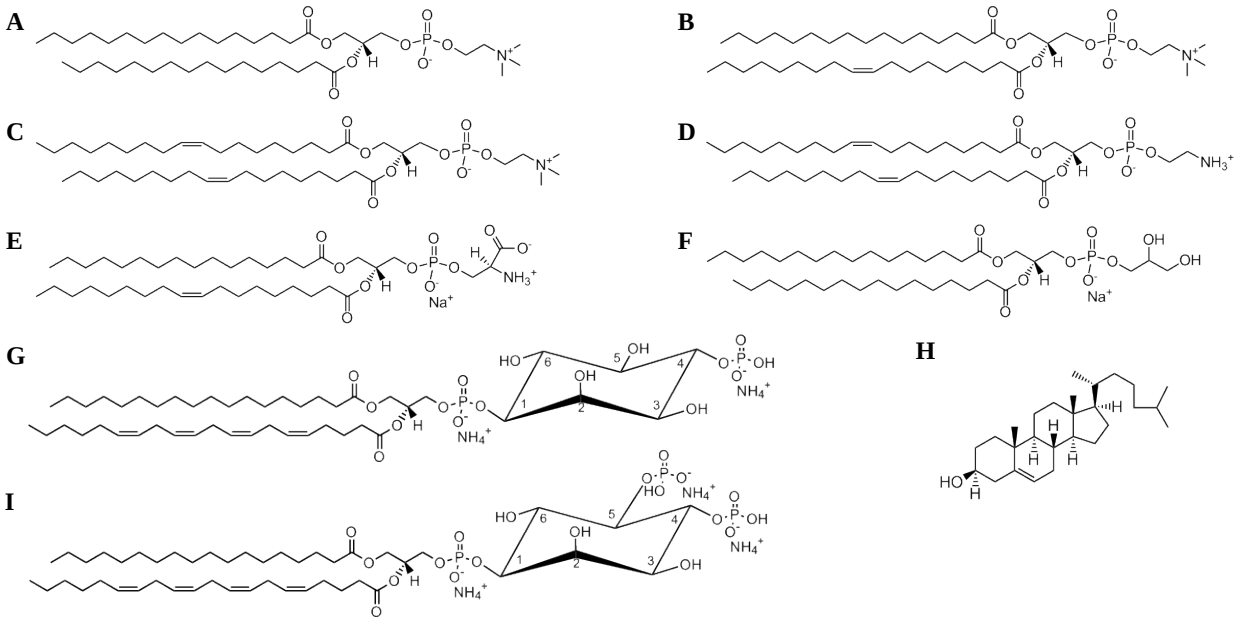

Figure 1.1 Few representative lipids, also used for research purposes. Zwitterionic phosphatidylcholines (**A**) DPPC, (**B**) POPC, (**C**) DOPC, and phosphatidylethanolamines (**D**) DOPE; negatively charged phosphatidylserine (**E**) POPS, phosphatidylglycerol (**F**) DPPG, phosphatidylinositol monophosphate (**G**) PI(4)P and biphosphate (**I**) PI(4,5)P_2; (**H**) cholesterol.

Cholesterol (**Figure 1.1 H**), which is a very important molecule in mammalian cell membranes, consists of four fused rings (steroid backbone) showing a hydroxyl group and a small branched hydrophobic tail. Its content depends on three main mechanisms: *de novo* synthesis, uptake and esterification[28].

The sphingolipids (SL) constitute another important class of structural lipids. They contain a hydrophobic backbone made of ceramide (Cer) and a phosphate headgroup. The major sphingolipids in mammalian cells are sphingomyelin (SM) and the glycosphingolipids (GSLs), which contain mono-, di- or oligosaccharides based on glucosylceramide (GlcCer) and sometimes galactosylceramide (GalCer)[29,30]. In the case of SM, the Cer backbone, consisting of a sphingoid base (such as sphingosine, *i.e.*, an 18-carbon amino alcohol with an unsaturated hydrocarbon chain), is amide-linked to a fatty acid[30] and the headgroup is constituted by a phosphocoline.

The distribution of lipids in biological membranes is highly heterogeneous, and it is possible to define different organization levels. In fact, subcellular organelles are characterized by a broad range of lipid arrangements, whereas plasma membrane is characterized by the existence of very specific lipid domains. Anyway, the lipid distribution is commonly characterized by a high degree

of lateral and transversal asymmetry[31]. **Figure 1.2** displays the average phospho- and sphingolipid compositions of different biomembranes existing in mammalian cell.

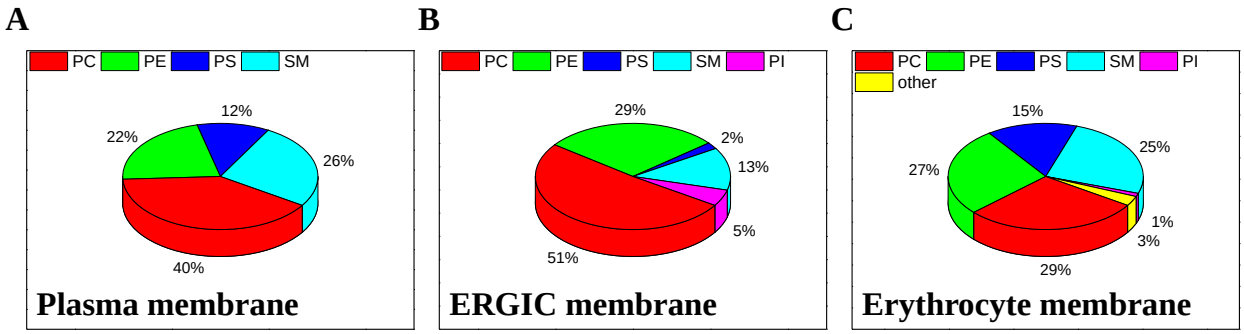

Figure 1.2 Average phospholipid and sphingolipid composition of different biomembranes existing in mammalian cells: (**A**) plasma membrane[32], (**B**) endoplasmic-reticulum-Golgi intermediate compartment (ERGIC) membrane[33,34], (**C**) erythrocyte membrane[35]. The label other indicates polyglycerol phosphatide and lysolecithin. PC, PE, PS, PI and SM stand for phosphatidylcholines, phosphatidylethanolamines, phosphatidylserines, phosphatidylinositols and sphingomyelin, respectively.

Membrane lipids, due to their unique chemistry, can self-organise themselves to form different hierarchical structures depending of the environment (lipid polymorphism)[36]. In particular they spontaneously self-assemble as bilayers with the hydrophobic acyl chains facing each other and the polar headgroups interacting with the external aqueous phase in biomembranes. This can be understood considering the hydrophilic-hydrophobic dual character of lipid molecules. In fact, while the hydrophilic headgroups present a favourable interaction with water molecules, the aliphatic, non-polar groups forming the hydrocarbon tails try to minimize their exposure to water, which results in a bilayer rearrangement of the molecules, with the lipid of the two leaflets oriented in opposite directions, in such a way to obtain an effective shielding of the tails groups from the surrounding aqueous environment (see **Figure 1.3** and **Figure 1.4**). However, it should be stressed that lipid bilayers are an oversimplified representation of the true structure of biological membranes, which are much more complex systems, governed by an intricate interplay of lipid-lipid and lipid-protein interactions.

1.1. Biological membranes

Biological membranes surround cells, as well as organelles, playing extremely important roles: on one side, they are necessary for compartmentalization, establishing a biological barrier against the external environment (*i.e.*, the cytoplasm in the case of organelle membranes and the extracellular medium in the case of cell membrane), and allowing a selective exchange of nutrients and wastes; on the other side, biomembranes provide a platform for the occurrence of fundamental

biochemical reactions, within the cell[37]. The first description of biological membranes was proposed by Singer and Nicolson in 1972[38], as is known as the "fluid mosaic model". It describes the membrane as fluid lipid bilayer in which membrane protein are embedded (**Figure 1.3**). Thus resulting in a random distribution of the components within the membrane, where molecules have a significant rotational and translational freedom.

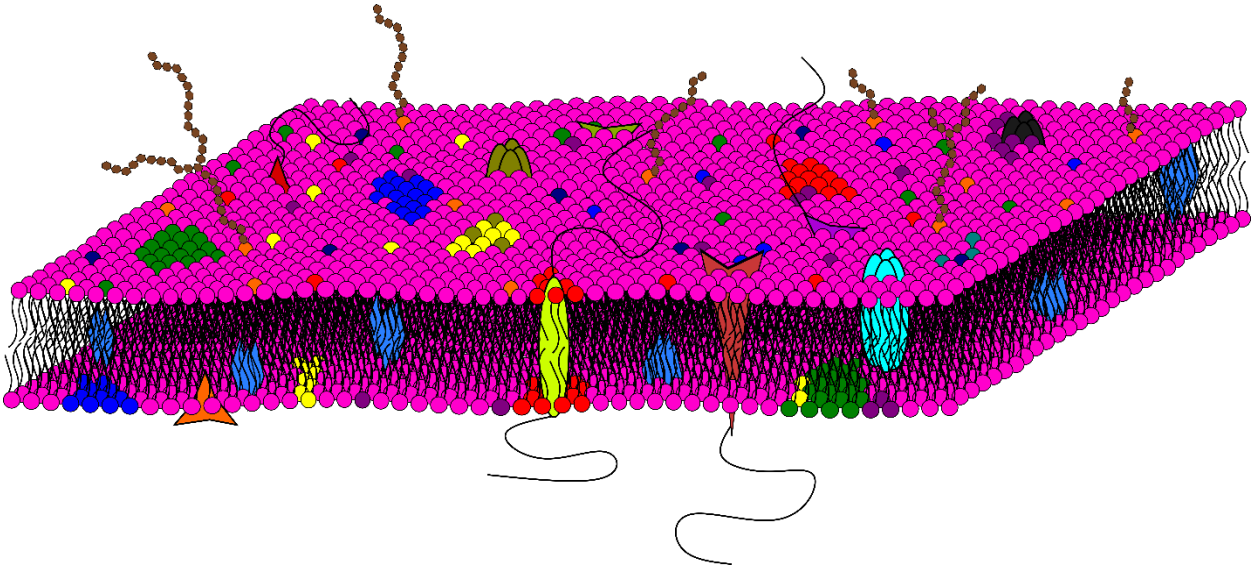

Figure 1.3 Fluid mosaic model sketch. Lipid headgroups are shown in magenta and tails are shown in black. Sketches of integral membrane proteins, with flexible extended soluble domains, are shown. Oligosaccharide moieties are also present.

Many different lipids form biological membranes, such as phospholipids, sphingolipids and sterols. In particular, PC is well known to provide a stable, fluid environment due to its liquid crystalline arrangement, while PE, due to its relatively small polar headgroup, creates defects in the membrane bilayer that facilitate fusion as well as the interaction with peripheral membrane proteins[39]; PS, PI and PIP, even at low concentrations, provide the negative charge of the membranes, which is a key factor in the interaction with positively charged patches of proteins[39–41]. Finally, the high melting temperature sphingolipids, such as sphingomyelin (SM), and sterols, such as cholesterol, whose content varies from a few % up to 50% in mol[32,42,43] in cellular membranes, are needed to form tightly packed structures occurring thanks to hydrophobic interactions[30,44]. Thus, the presence of a broad range of unsaturated and saturated phospholipids leads to the coexistence of condensed and fluid phases in the membrane leaflets. The interaction between these phases gives rise to lipid-lipid interplays that were not considered in the original fluid mosaic model. In 1977, Israelachvili[45] modified the model to implement lipid-lipid and lipid-

membrane protein interactions, and finally in 2014, Nicolson[46] incorporated the intermolecular interactions between the different components. Despite some general features of the fluid mosaic model remain valid, nowadays it is accepted that the lateral mobility of some proteins is very limited[47]. Anyway, the existence of these interactions between fluid and more rigid lipids leads to the formation of the so called "raft-like" membrane domains, which were proposed to be highly dynamic and fluctuating assemblies[48]. Lipid rafts are membrane patches with size in the 50-70 nm range enriched mainly in sphingolipids and cholesterol. The nature of the fatty acid side chains of the sphingolipids constituting the rafts results in thicker structures where certain proteins tend to accumulate[49]. Although the lipid rafts are thought to play pivotal roles in cellular processes such as signal transduction and membrane protein trafficking, their composition, size, lifetime, biological function, and even their existence remain controversial[11,50,51]. Different hypotheses have been postulated regarding the interaction between phospholipids and cholesterol[52–55], aiming to demonstrate and explain the raft formation. For example the existence of phospholipid-cholesterol complexes[52,53], whose stoichiometry would depend on the phospholipid nature, while it has also been suggested that phospholipid headgroups act as "umbrellas", protecting cholesterol from water[54,55]. Nevertheless, none of these hypotheses is fully able to justify the lipid rafts formation, nor explain the related role of cholesterol. A molecular explanation of the formation of such domains can come from the ability of cholesterol to preferentially associate with saturated acyl chains phospholipids, as well as segregate away from unsaturated ones. The balance of both forces is determined by the number of hydrocarbon contacts and attractive van der Waals interactions formed between cholesterol molecules and the other lipids, as was reported by molecular dynamics simulations[56,57]. The use of single-particle tracking techniques pointed out that even lipids can be subjected to transient confinement in lipid rafts[55]. In parallel, experimental[58] and simulation[56,57] works with synthetic lipids show that certain lipid mixtures can be used to induce raft formation in model membranes. Moreover, lateral de-mixing of lipids containing high and low melting acyl chains, which is consistent with the raft hypothesis, was already deduced through small-angle neutron scattering experiments on bacterial membranes[51]. One of the aims of this thesis, developed in **Chapter 4**, has been to study the effect of cholesterol on biologically relevant mimics of planar membranes, investigating its structural role as well as its influence on raft formation and membrane physico-chemical properties.

Particularly important is the family of phosphatidylinositols (PIs), which are minority

phospholipids of all eukaryotic cellular membranes. Like other phospholipids, PIs are composed of a glycerol backbone that is esterified to two fatty acid chains, with various unsaturation degree, and a phosphate. The latter is attached to a cyclic polyol myo-inositol $(CHOH)_6$ ring[59], which has free hydroxyl groups that could be phosphorylated by cytoplasmic lipid kinases, leading to the synthesis of negatively charged phosphatidylinositols phosphate (PIPs), also called phosphoinositides. Interestingly, the PIPs function strictly depends on their phosphorylation pattern. Despite its very low concentration (about 1-2% in mol in the inner leaflet of the plasma membrane)[3–6], phosphatidylinositol 4,5-bisphosphate ($PI(4,5)P_2$ or PIP_2) is the major PIP in mammalian cells. Moreover, it is worth mentioning that PIP_2 is only present on the inner leaflet of the plasma membrane, while other PIPs may be found on different but specific membranes. PIP_2 is involved in a plethora of biological pathways, such as the attachment of the cytoskeleton to the plasma membrane, clathrin-mediated endocytosis, membrane trafficking, ion channel, enzyme activation and generation of second messengers[3–8]. Importantly, PIP_2 is able to form clusters thanks to the electrostatic interaction with intracellular divalent cations, whose function is the local increase of phosphoinositide to provide docking sites crucial for the recruitment of specific proteins from the cytosol[5,59,60]. Recent experimental[61,62] and numerical[63] studies focused on PIP_2 have demonstrated that a purely electrostatic, multivalent ion-mediated mechanism is enough to induce PIP_2 clustering in biomimetic model membranes. In detail, the effects of divalent cations on the in-plane organization of PIP_2 containing membranes have been studied by imaging, spectroscopy[62,64] and atomistic molecular dynamics simulations[63]. The existence of PIP_2 domains was attributed to the capacity of divalent cations, most predominantly Ca^{2+} and Mg^{2+}, to interact with PIP_2 headgroups and act as a bridge between PIP_2 molecules, yielding well-defined clusters. However, the relationship between the PIP_2 cluster formation and the orientation of its inositol ring has never been addressed. Although, molecular dynamics (MD) simulations already investigated the orientation of the inositol ring, no experimental evidence was given so far to determine the tilt angle of PIP_2 inositol biphosphate ring in membranes. Finally, since the key feature of all molecular processes in which PIP_2 is involved is the interaction with the inositol biphosphate, unravelling the ring orientation in biological membranes prior to the presence of protein is essential. Indeed one of the aim of this PhD thesis, reported in **Chapter 3**, has been to determine the tilt angle of the inositol ring in model membranes in presence of divalent cations and correlate it with the membrane in-plane organization.

1.2. Model membranes

As already stated in 1995 by Caffrey and Wang[65], "Understanding membrane structure and how this relates to the biological function of membrane components represents one of the grand challenges in structural biology research. By knowing the impact of structure on function we can hope to manipulate structure to our advantage". However, real biological membranes are complicated systems, characterized by complex structures and lipid compositions. This makes the seeking of biomimetic model membranes, which allow an appropriate and simplified representation of biomembranes under laboratory conditions, a great challenge for the biophysical field. Indeed, model membranes are simpler and controllable systems that can be optimized, up to the use of natural extracted lipids, to mimic the biological membranes of interest. In fact, many model systems have been developed for studying membrane properties and structure, as well as different processes that can occur within biomembranes. Moreover, different types of model membranes can be built and adapted to the use of specific techniques for characterization. The most commonly models used as biomimetic model membranes are planar membranes, such as lipid monolayers, solid supported bilayers, and suspended lipid bilayers, as well as liposomes. These systems allow mimicking the lipid arrangement of natural biomembranes[27,66].

The use of simplified biomimetic models of membranes plays an essential role in the biophysical research, also concerning the investigation of specific interactions of proteins with biomembranes, at the molecular level.

1.2.1. Examples of the most commonly used model membranes

Planar membranes, in the form of both mono- and bilayer of lipids, are extensively used to replicate biological membranes. Although lipid monolayers at the air/water interface (**Figure 1.4 A**) can mimic only one leaflet of the cell membrane and are considered the simplest *in vitro* lipid model systems, they are a versatile tool to study physico-chemical properties of membranes, providing valuable information regarding membrane compressibility as well as stability and orientational assembly of lipids. Moreover, they are extensively exploited to investigate lipid interactions with biologically relevant molecules[19], such as drugs[21], nanoparticles[15,16] as well as viral[67] and eukaryotic[18,20] proteins. Lipid bilayers (**Figure 1.4 B**) are more complicated *in vitro* model systems, made of two lipid leaflets directly deposited onto a surface (hence, supported lipid bilayer) or linked to a solid support usually by polymer branches (tethered lipid bilayer). They are

often exploited to investigate viscoelastic and structural properties of membranes[68,69] as well as to investigate the interaction of integral membrane proteins with lipids[70–73]. Other than planar model systems, liposomes (**Figure 1.4 C**) are used to replicate biological membranes. They are vesicles composed of one or multiple bilayers, whose size could be easily tuned. Thus, they provide an useful tool to investigate the binding of curvature sensing protein, which could interact with liposomes depending on their size[24].

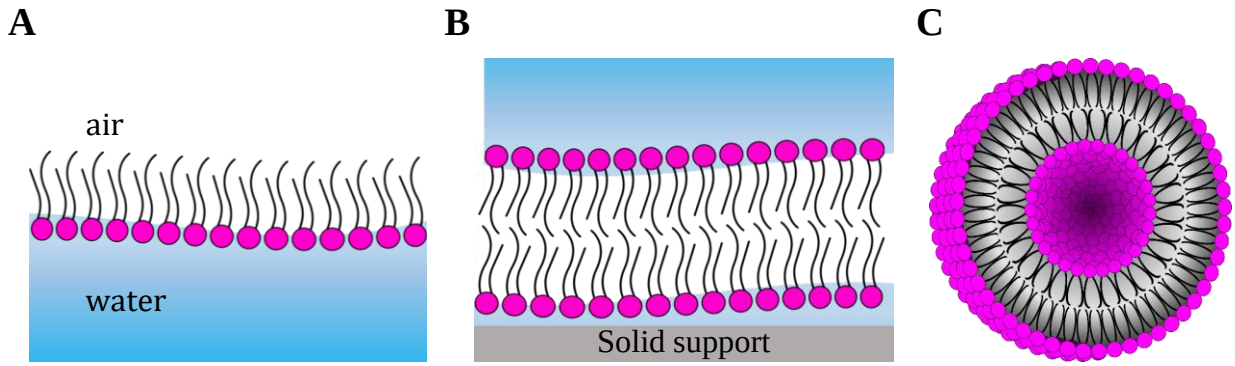

Figure 1.4 Sketches of the most commonly used model membranes, in the form of **A** lipid monolayer, **B** solid supported lipid bilayer and **C** liposome.

1.2.2. Neutron reflectometry as key technique to study planar model membranes

Specular neutron reflectometry (SNR or, more simply, NR) probes the structure of planar membranes in the direction perpendicular to its plane (out-of-plane structure). A neutron beam is directed onto the interface, from which it is reflected (**Figure 1.5**), and the specular reflection is recorded. A detailed explanation of the technique is reported in **Chapter 2**. From the analysis of the reflectivity data, information regarding the composition as well as the thickness of the film present at the interface can be obtained (**Figure 1.5**). Recently, NR has been a key technique to evaluate model membrane structure as well as investigate protein-lipid interaction. For instance, it has been exploited to understand the interaction between viral proteins and mammalian cell mimicking membranes[73], or antimicrobial peptides interacting with bacterial mimicking membranes[74], as well as to gain more information regarding integral membrane protein organization inside the hydrophobic core of a lipid bilayer[71]. Moreover, NR is allows gaining insight about membrane degradation, thus it presents a powerful tool to study the effect of antimicrobial peptides with bacterial cell mimicking membranes[74]. In the context of this PhD thesis, NR was fundamental to reach the designated aims regarding planar membrane

characterization as well as the unravelling of protein insertion and orientation in model membranes (**Figure 1.5**).

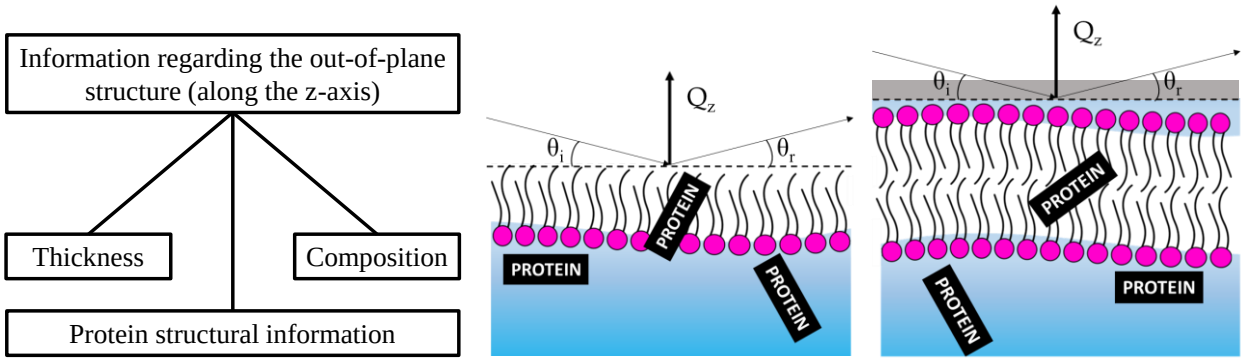

Figure 1.5 Schematic representation of a neutron reflectometry experiment on lipid mono- and bilayer, upon protein binding. The left panel reports the information that NR can provide.

2. Lipid-protein interaction

Proteins can either freely diffuse in membranes or be constrained by their association to lipid rafts, cytoskeleton or large protein-protein complexes. The protein organization in membranes and their interaction with lipids are essential for a plethora of fundamental biological reactions to occur, such as trafficking, signalling and endocytic pathways[1,2,6]. In fact, there is a strong synergy between lipid and protein components of biological membranes that allows membrane proteins to function embedded in the environment provided by the lipid bilayer, without compromising their chemical and/or structural integrity[9].

From a molecular perspective, the interaction between specific lipids and proteins, which are strongly dependent on the lateral packing[75], is essential for controlling the membrane organization[76]. For instance, specific proteins are able to bind cellular membranes, usually through electrostatic interaction between positive patches on their surface and negatively charged lipids present in the membrane[77,78], such as PIPs that have central roles in cellular functions[10]. Moreover, these PIPs-proteins interaction may lead to membrane curvature[79]. Furthermore, lipid-protein interactions play an essential role in a broad range of pathologic processes, including among others the mechanisms of penetration of different virus into the cell cytoplasm[67,80,81].

The understanding of lipid-protein interactions in different biological systems, and their functional and structural role has evolved, in recent years, taking advantage of experimental and computational advances[71,73,82]. These have allowed the elucidation of the complex composition of

different membranes, to probe time and length-scales of lipid-protein interactions, or to link such interactions to specific biological functions. As a result, different aspects of lipid-protein interactions have become particularly interesting to study, such as the modulation of the physico-chemical properties of lipid bilayers upon protein binding, the detailed chemistry of the lipid-protein complexes, and the central role of the specific binding between specialized lipid domains and well-defined protein sites[1].

2.1. Clathrin-mediated endocytosis (CME) pathway

Endocytosis describes the internalization of molecules (termed cargoes) into cells from their external environment. There are different types of endocytic pathways, which can be distinguished depending on the nature of the cargo. In the case in which the cargo is represented by a membrane protein or, sometimes, a virus, the so called receptor-mediated endocytosis, also known as clathrin-mediated endocytosis (CME), is the pathway involved[83,84]. Briefly, cargoes are internalized by being engulfed by the cell plasma membrane, which then buds off inside the cell to form a vesicle. The large number of proteins involved in these different steps makes CME a very complex biological pathway (**Figure 1.6**) which has been studied for years. It requires the cross-interaction between proteins as well as the binding of proteins to the inner leaflet of the plasma membrane. The proteins involved can be divided into adaptor proteins, such as CALM and AP2, and modulator proteins such as FCHo2 and Eps15. The first are able to specifically recognize the cargoes to internalize as well as bind the membrane. Besides, the adaptor proteins can bind clathrin molecules through flexible appendages, creating self-associated polygonal lattices that coat the membrane. Acting as a mechanical scaffold, the clathrin coat deforms the surface membrane forming clathrin-coated pits (CCPs). Thus, the coupling between cargo recognition and clathrin coat assembly, which is tightly regulated by the adaptor proteins, is a key step in the CME pathway[85]. After growth, the CCPs undergo a maturation process until deep invagination is achieved. However, the process of birth and growth of CCP involves many other modulator proteins (such as FCHo2 and Eps15), which, although not able to bind the cargoes, can bind the plasma membrane as well as adaptor proteins. This intricate network of cross-interactions aims to form stable protein-cargo complexes located at the inner leaflet of the plasma membrane which could then results in maturated CCP. Finally, the GTPase dynamin assembles into collar-like structures at the necks of CCPs, where it catalyses membrane fission and vesicle release. Thus, in

the end of this complex pathway, clathrin-coated vesicles (CCVs) are formed, which contain the internalized cargo[86].

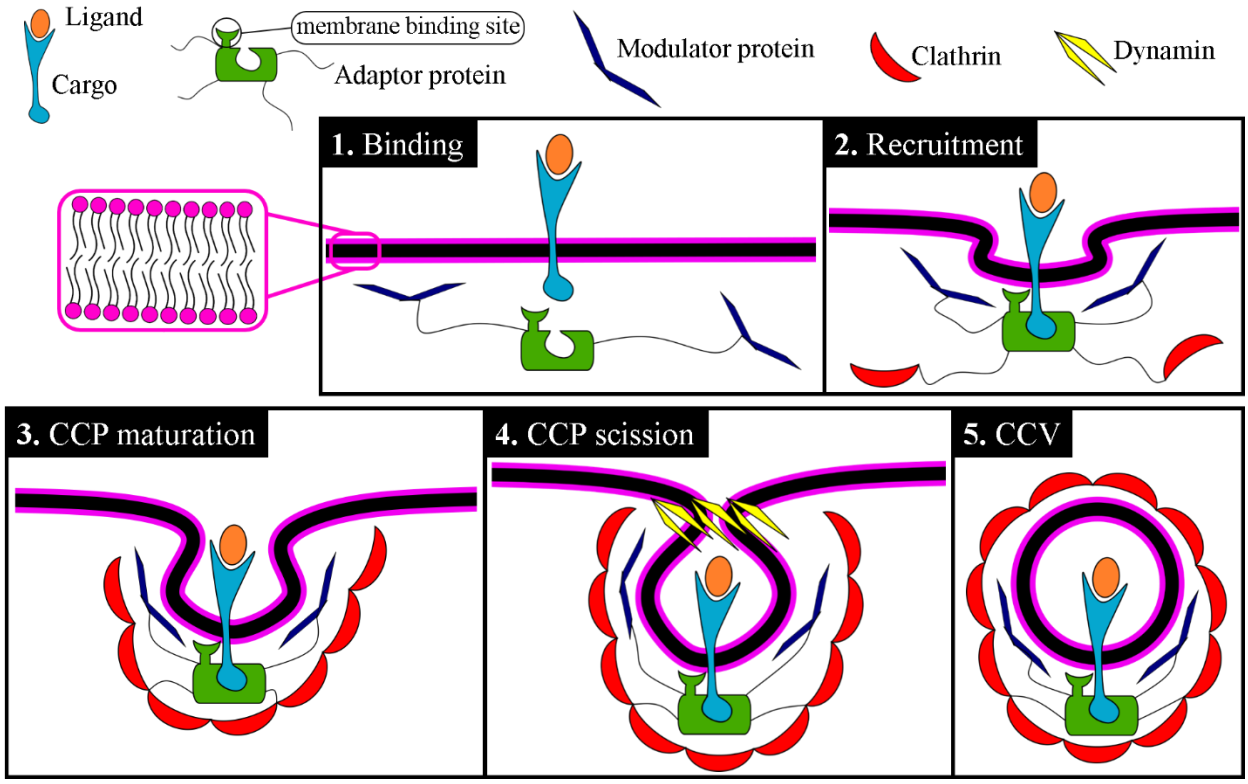

Figure 1.6 CME schematic representation. The figure is based on a figure from Ref[87].

Malfunctioning during any step of this complex biological machinery can result in diseases such as Alzheimer[88] and Stiff man diseases[89]. Molecular biology and proteomic approaches have been essential to fully understand the CME pathway and the crystal structure of many of the proteins involved, such as CALM, AP2, and also domains of FCHo2, has been solved and analyzed. However many questions remain unanswered concerning the interaction between proteins and lipids, which represents the very first steps of the CME. For example, although it is clear that the main interaction driving CALM, AP2 and FCHo2 towards the inner leaflet of the plasma membrane is electrostatic, due to the presence of lipids such as PIP_2 and phosphoserine, and that the adaptor proteins have specific binding sites for PIP_2, the protein-membrane interaction has never been studied from a biophysical point of view, *i.e.*, investigating their structure, viscoelastic properties and influence on the lipid membrane upon binding. In fact, information is missing, regarding the orientation of these proteins with respect to the lipid interface, as well as their eventual insertion in the membrane itself. As a consequence, surface-sensitive techniques

have been exploited to answer these questions. In particular, NR was essential to determine the degree of insertion of these protein in plasma membrane models. Exploiting both monolayers and bilayers model membranes, the experiments performed and reported in **Chapters 5** and **6**, allowed the characterization of CALM, AP2, FCHo2 and Eps15 upon binding.

2.1.1. The adaptor protein CALM

CALM (clathrin assembly lymphoid myeloid leukemia protein) is one of the most abundant clathrin adaptors in endocytic CCVs isolated from tissue culture cells (30%-35% of the adaptors in a CCV[90,91], and it binds to and sorts the small proteins R-SNAREs VAMPs 2, 3, and 8[88,92]. Compared to other adaptor proteins, such as AP2, it possesses a relatively small, compact, stacked-helical domain, called AP180 N-terminal homology (ANTH) domain and defined as residues 19-289[93] (**Figure 1.7**), with large, natively unstructured, C-terminal tails containing clathrin and AP2 binding sites[93–95]. Both PIP_2 and the cargo binding sites are located in the ANTH domain, Lysines 28, 38 and 40[93] and Methionine 244[88] respectively[24]. Moreover, CALM is characterized by a membrane-inserting amphipathic helix at the N-terminus (thus called amphipathic helix 0, AH0), whose 3D orientation is thought to change upon membrane binding. The absence of AH0 leads to the formation of only flat clathrin lattices on lipid monolayers and not invaginated CCPs[93,96]. Other experiments also showed that AH0 is able to drive pearlized liposomes tubulation[24]. Given this, a model for CALM binding and function was proposed, in which the protein is seen as curvature sensitive[97] but also actively driving further membrane curvature. This model, based on biomolecular and biochemical experiments, was supported by cryoEM images showing the tubules formation[24], as well as by the crystallographic structure of CALM in complex with its cargo VAMP8 and inositol-triphosphate[88]. However, the insertion of the helix was not experimentally proved, but only hypothesized on the basis of the obtained results. In **Chapter 5** of this thesis, it is reported how NR demonstrated CALM insertion in the membrane and allowed determining its orientation. Besides, the wild type protein ($CALM_{wt}$) and a mutant missing the AH0 ($CALM_{\Delta AH0}$) were exploited to identify the position of AH0. NR also allowed the determination of the orientation of the protein with respect to the model membrane

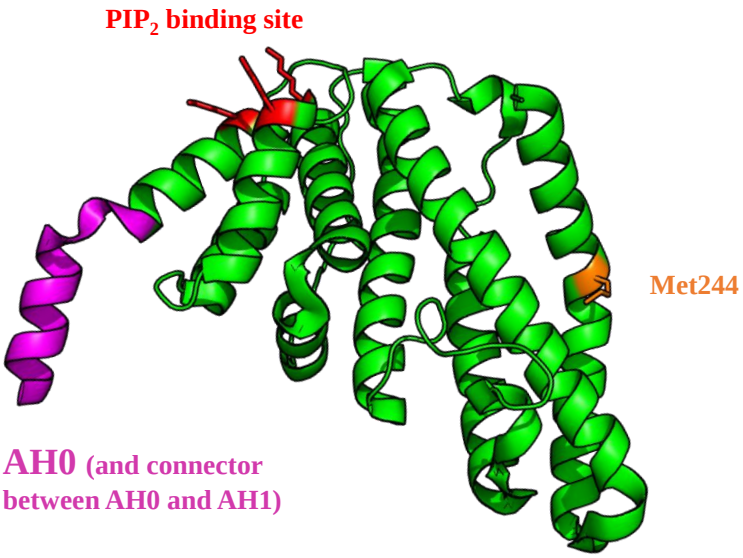

Figure 1.7 Crystallographic structure (cartoon representation) of CALM from PDB ID: 3ZYK[88].

2.1.2. The adaptor protein AP2

The heterotetrameric Adaptor Protein complexes AP1, AP2, AP3 and AP4[10] are composed by four different subunits (α, β, μ, and σ) with different functions. The most detailed structural analyses have been carried out on AP2 (**Figure 1.8**), which is located at the plasma membrane. It is characterized by a protein core made up of the trunk domains of the subunits[98], and flexible appendages, coming from subunits α and β that can bind clathrin[10,99,100] (see cartoon bottom-right panel in **Figure 1.8**). Besides, AP2 is provided with multiple PIP_2 binding sites, localized at the N-terminus of the α subunit[101–103], and on the surface of μ subunits[98,104]. Finally, the C-terminus of the μ subunit contains the YxxF binding site for cargo recognition and the σ subunit contains the dileucine binding box[105,106]. The latter can bind to the so called CD4 sorting signal peptide. Interestingly, the PIP_2 and cargo binding sites are on mutually perpendicular faces, meaning that the cargo binding site is occulted by the β subunit. In fact, after mediation by modulator proteins (such as FCHo2) that recognize AP2 and promote its binding toward PIP_2 phosphate groups, the protein undergoes a conformational change that leads to cargo binding[82]. Specifically, PIP_2 compete with the modulator protein, and once AP2 interacts with the lipids, the modulator protein is released and the AP2 conformational change occurs, which finally frees the cargo binding site[82]. The structure of the AP2 core was determined in complex with inositol(1,2,3,4,5,6) hexakisophosphate (PDB ID: 1GW5[98]) that mimics PIP_2 headgroup, showing the molecular detail of the binding, and the influence of AP2 on PIP_2-containing membranes was investigated with EM

tomography[82,107] and fluorescence microscopy[82]. Recently, the interaction of AP2 with lipid monolayers was studied by NR and AFM[108], unravelling important pieces of information regarding protein-membrane interactions. However a detailed investigation of the binding of AP2 with PIP_2-and cargo-containing membranes in the form of bilayers is still missing. **Chapter 6** reports NR results regarding this topic, using CD4 peptide as AP2 cargo.

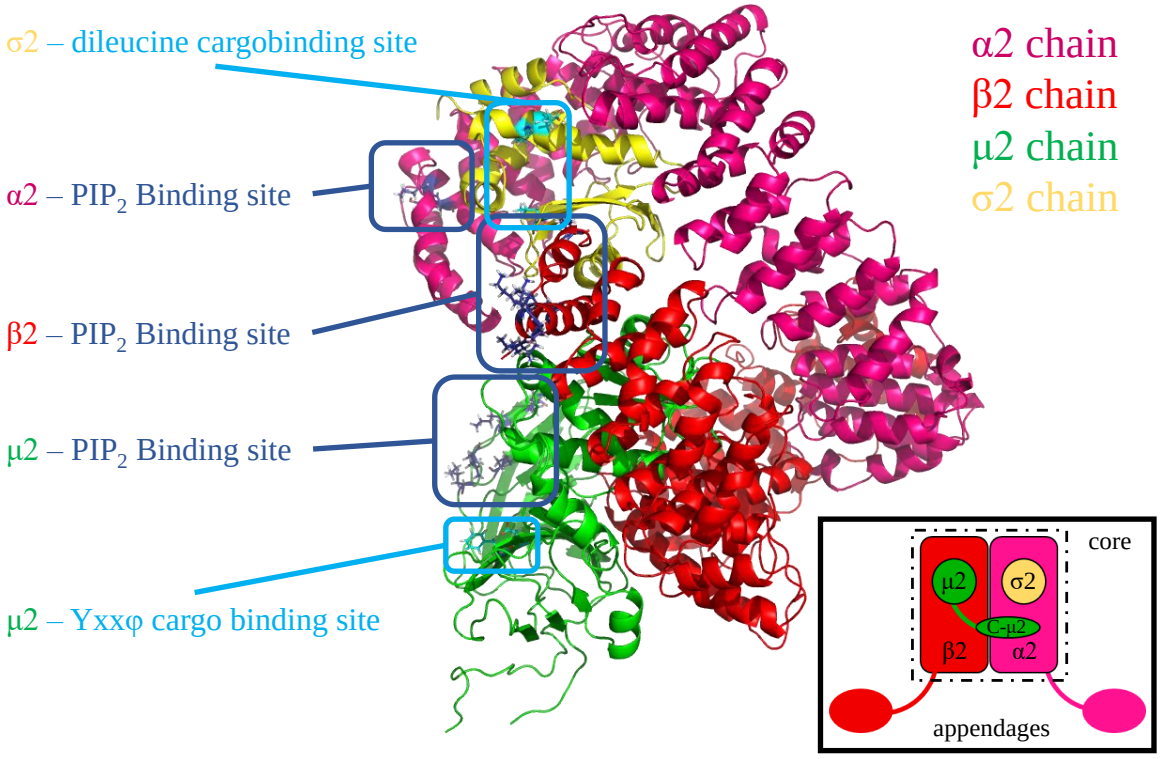

Figure 1.8 Crystallographic structure (cartoon representation) of AP2 from PDB ID: 2XA7[106]. The cartoon on the bottom right is based on a figure from Ref[107].

2.1.3. The modulator proteins FCHo2 and Eps15

An essential requisite for CCV formation and maturation is the gradual increase of membrane curvature. Indeed, membrane regions of distinct curvature are created and maintained by proteins, located at the inner leaflet of the plasma membrane. These curvature sensing and inducing proteins can directly sculpt the lipid bilayer usually by lipid binding via electrostatic interaction or by insertion in the membrane[109]. An increasing number of membrane-interacting proteins have been shown to have domains that influence membrane curvature[109–112]. An example of this kind of proteins is Amphiphysin. This protein induces curvature due to the presence of a Bin-Amphiphysin-Rvs167 (BAR) domain. Indeed, when a dimeric state is formed, BAR domains expose a patch of positive charges on their surface, which is characterized by a defined intrinsic

curvature. Thus, upon binding to the slightly negatively charged inner leaflet of the cell membrane, the BAR can either induce or stabilize membrane curvature[109,113]. An example of BAR domain containing protein is FCHo1/2, *i.e.*, N-terminal Fes-CIP4 homology domain (hence FCH) only protein 1 or 2[112,114–118]. Other than the BAR domain (F-BAR), FCHo1/2 contains intrinsically disordered segment of ~200 amino acid residues, referred to as flexible linkers, that associates with the AP2 adaptor protein[119–121], and a C-terminal µ-homology domain (HD) that binds to the pioneer protein Eps15 (epidermal growth factor pathway substrate 15)[120,122–124], which in return can bind AP2 appendages[125–127]. Thus, the cross-interactions between FCHo1/2, Eps15 and AP2 allow the stabilization of modulator and adaptor proteins complexes localized at the plasma membrane, and induce the initiation of the CME pathway. Indeed, FCHo1/2 play a key role in local AP2 recruiting and restructuring, as they are among the earliest proteins to mark a nascent CCP[118,122] and affect AP2 conformation directly[82,119,121]. Although the atomic structure of the F-BAR domain and the FCHo1-µHD domain in complex with Eps15 have been solved (PDB ID: 2V0O[109] and 5JP2[125], respectively, shown in **Figure 1.9**), and biochemical tools together with microscopy have been employed, both *in vivo* and *in vitro*[82,125], to investigate their binding with AP2 appendages, the resultant structure of FCHo2 and FCHo2-Eps15 complex upon membrane binding has yet to be investigated. **Chapter 6** of this PhD thesis focuses on this aspect of CME pathway.

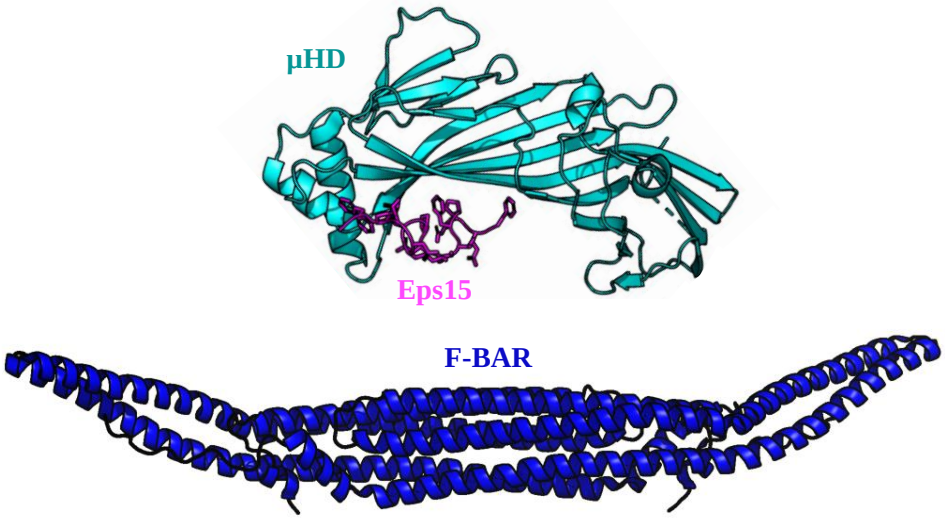

Figure 1.9 Crystallographic structures (cartoon representations) of F-BAR domain (bottom), from PDB ID: 2V0O[109], and µHD in complex with Eps15 (top), from PDB ID: 5JP2[125].

2.2. SARS-CoV-2

β-Coronaviruses (CoVs) are single-stranded positive sense RNA viruses[128] that can infect cells both via direct membrane fusion mechanism[81,129] (**Figure 1.10 2a**) or endocytic pathways[129,130] (**Figure 1.10 2b**). Upon viral entry, copies of the genome are made in the cytoplasm, followed by expression of viral proteins and final assembly of functional viral particles, which are then released from the cell. In the case of β-Coronaviruses, as well as other RNA viruses like the HIV and the influenza virus, which belong to the class I viral fusion viruses, the membrane fusion pathway (**Figure 1.10 2a**) is the most exploited[131]. Indeed, such viruses are able to directly promote fusion between viral and cellular membranes. The main structural components of β-coronaviruses include a lipid envelope, the Spike (S), Membrane (M), and Envelope (E) proteins, as well as the Nucleoprotein (N), which forms complexes with the viral RNA (**Figure 1.10**).

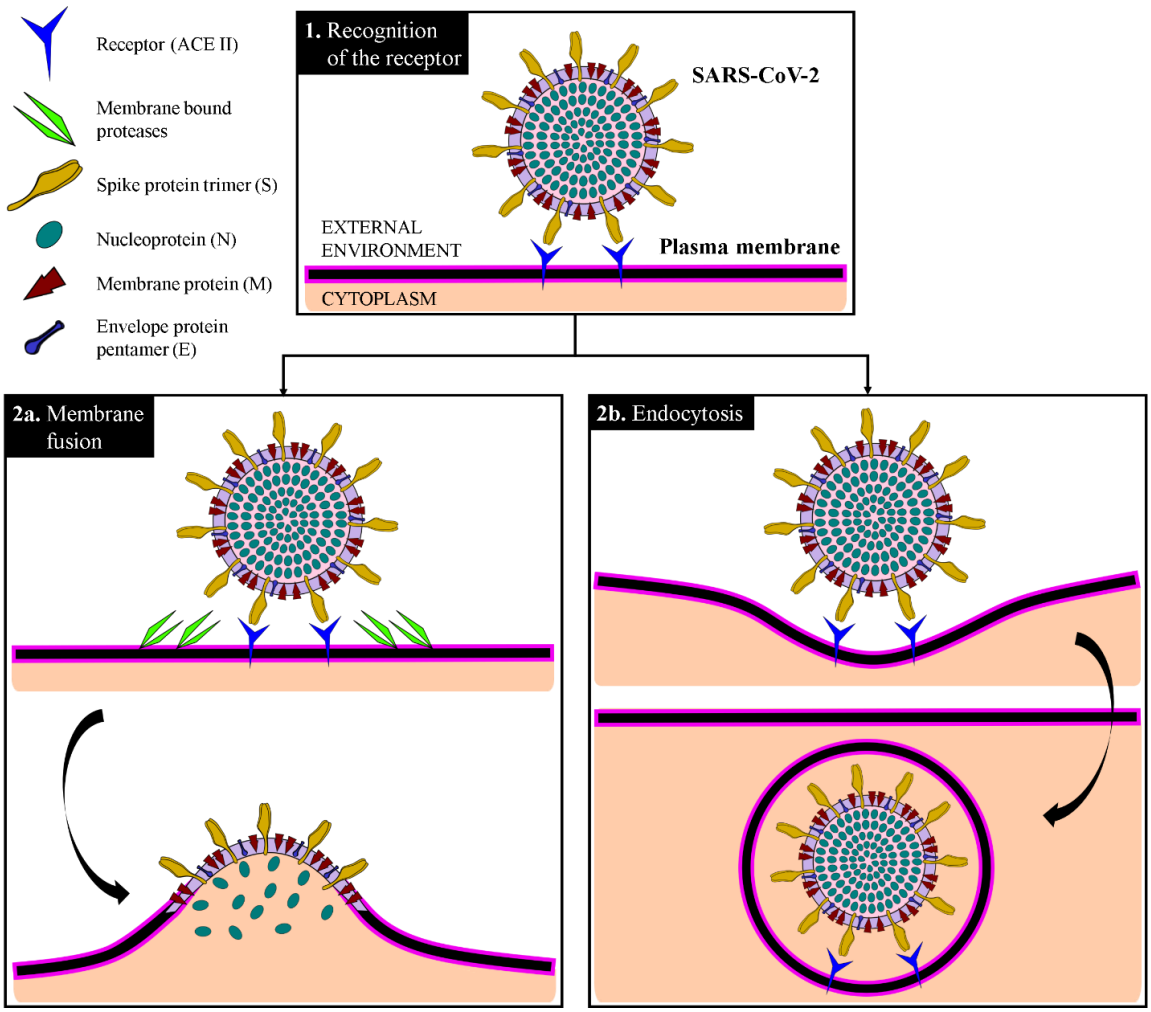

Figure 1.10 Sketch based on a figure from Ref[129]. Model of coronavirus dual entry pathway. This model depicts the two methods of viral entry that may occur as the virus recognises and binds its receptor (**1**): membrane fusion (**2a**)

and endocytosis (**2b**). The presence of exogenous and membrane bound proteases is essential to trigger the fusion between the membranes (**2a**).

β-coronavirus are named after their peculiar crown-shaped outer layer, observed though electron microscopy[132,133], which is a result of the protrusion of Spike protein trimers in the outside environment. The outbreak of a life-threatening respiratory tract infection caused by the SARS-CoV-2 β-coronavirus in 2019, which was then declared a global pandemic, led scientific researchers worldwide to focus their energies in deeply studying this viral infection. Although it is already well-know that the S1 spike protein domain contains the receptor binding site for the angiotensin-converting enzyme 2, ACE-II (**Figure 1.10**)[130,134,135], it has to be underlined that the S2 spike subunit contains a fusion domain (**Figure 1.11**) that is responsible for triggering the fusion between lipid bilayers. After S1-ACE-II binding, a proteolysis-triggered conformational change in the C-terminal S2 subunit occurs[130,136,137]: S2 continues to be embedded in the viral membrane, but its heptad repeat (HR) 1 and 2 domains associate to form a six-helix bundle fusion core[138]. Proteolysis at the S2' site (at residue 816) subsequently frees the Spike protein fusion domain, which associates with the host cell and initiates membrane fusion. However, the molecular mechanisms driving this fusion process are not deeply understood. Thus, part of this PhD thesis (**Chapter 7**) aims to unravel the fusion mechanism, by simplifying the systems down to its core elements. Indeed, small peptides (22 to 25 amino acids) derived from the fusion domain of the Spike, thus called fusion peptides (FP) (**Figure 1.11**) were exploited and their interaction with model membranes was investigated.

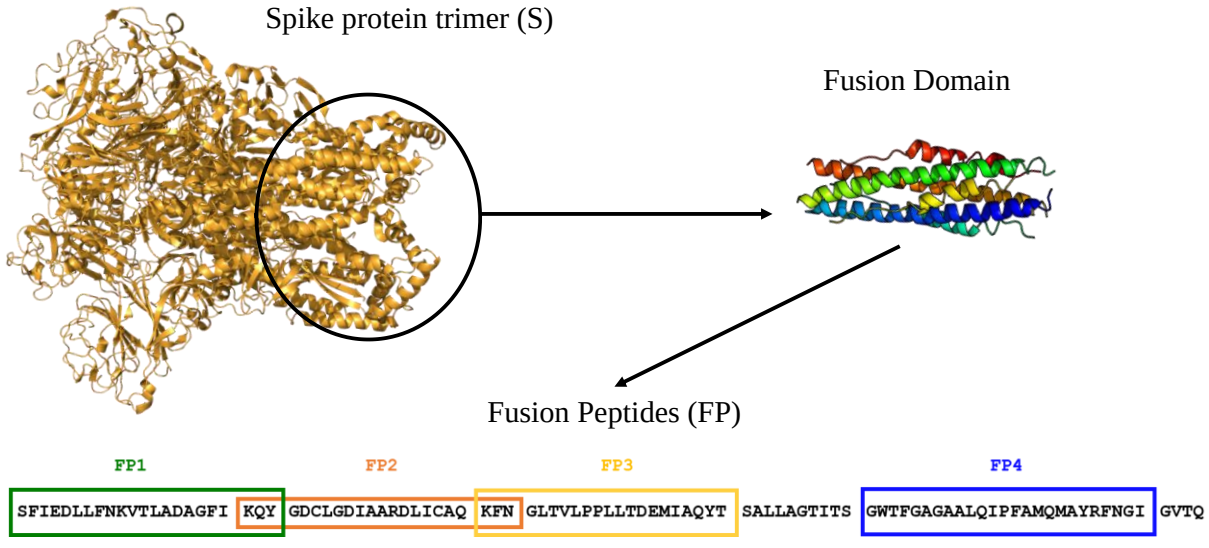

Figure 1.11 Schematic representation of SARS-CoV-2, Spike protein (PDB ID: 3JCL[139]), fusion core domain (PDB ID: 1WNC[140]) and Fusion Peptides.

3. Novelty of the work

This PhD thesis has focused on a rigorous and systematic characterization of different model lipid membranes, investigating both the structure orthogonal to the membrane plane and the in-plane lipid organization. By exploiting both synthetic and natural lipids, the interaction of CME and viral proteins with model membranes, in the form of Langmuir monolayers, solid supported bilayers and small unilamellar vesicles, have been investigated. The thesis approach combines neutron as well as bench techniques, thus providing information regarding the biological function and the structure of lipid-interacting proteins, upon membrane binding. In particular, by describing in molecular details the interaction between proteins and planar model membranes, down to the sub-nanometer scale, NR has been used to determine protein orientation and position with respect to the bound membrane.

References

1. Corradi V, Sejdiu BI, Mesa-Galloso H, et al. Emerging Diversity in Lipid-Protein Interactions. *Chem Rev*. 2019;119(9):5775-5848. doi:10.1021/ACS.CHEMREV.8B00451/ASSET/IMAGES/ACS.CHEMREV.8B00451.SOCIAL.JPEG_V03

2. Sych T, Levental KR, Sezgin E. Lipid-Protein Interactions in Plasma Membrane Organization and Function. *Annu Rev Biophys*. 2022;51(1). doi:10.1146/ANNUREV-BIOPHYS-090721-072718

3. McLaughlin S, Murray D. Plasma membrane phosphoinositide organization by protein electrostatic. *Nature*. 2005;438. doi:10.1038/nature04398.

4. Graber ZT, Jiang Z, Gericke A, Kooijman EE. Phosphatidylinositol-4,5-bisphosphate ionization and domain formation in the presence of lipids with hydrogen bond donor capabilities. *Chem Phys Lipids*. 2012;165(6):696-704. doi:10.1016/j.chemphyslip.2012.07.003

5. Lupyan D, Mezei M, Logothetis DE, Osman R. A molecular dynamics investigation of lipid bilayer perturbation by PIP2. *Biophys J*. 2010;98(2):240-247. doi:10.1016/j.bpj.2009.09.063

6. McLaughlin S, Wang J, Gambhir A, Murray D. PIP2 and proteins: Interactions, organization, and information flow. *Annu Rev Biophys Biomol Struct*. 2002;31:151-175. doi:10.1146/annurev.biophys.31.082901.134259

7. Golebiewska U, Kay JG, Masters T, et al. Evidence for a fence that impedes the diffusion of phosphatidylinositol 4,5-bisphosphate out of the forming phagosomes of macrophages. *Mol Biol Cell*. 2011;22(18):3498-3507. doi:10.1091/mbc.E11-02-0114

8. Lassing I, Lindberg U. Polyphosphoinositide synthesis in platelets stimulated with low concentrations of thrombin is enhanced before the activation of phospholipase C. *FEBS Lett*. 1990;262(2):231-233. doi:10.1016/0014-5793(90)80197-Q

9. Lee AG. Lipid–protein interactions in biological membranes: a structural perspective. *Biochim Biophys Acta - Biomembr*. 2003;1612(1):1-40. doi:10.1016/S0005-2736(03)00056-7

10. Owen DJ, Collins BM, Evans PR. ADAPTORS FOR CLATHRIN COATS: Structure and Function. *Annu Rev Cell Dev Biol*. 2004;20(1):153-191. doi:10.1146/annurev.cellbio.20.010403.104543

11. Fragneto G, Delhom R, Joly L, Scoppola E. Neutrons and model membranes: Moving towards complexity. *Curr Opin Colloid Interface Sci*. 2018;38:108-121. doi:10.1016/j.cocis.2018.10.003

12. De Kroon AIPM, Rijken PJ, De Smet CH. Checks and balances in membrane phospholipid class and acyl chain homeostasis, the yeast perspective. *Prog Lipid Res*. 2013;52(4):374-394. doi:10.1016/J.PLIPRES.2013.04.006

13. Lodish H, Berk A, Zipursky LS. “Biomembranes: Structural Organization and Basic Functions.” In: *Molecular Cell Biology*. 4th ed. New York: Scientific American Books.; 2000.

14. G. M. Cooper. Structure of the Plasma Membrane. In: *The Cell: A Molecular Approach*. 2nd ed. Washington, D.C.: Sunderland, Mass. : Sinauer Associates; 2000.

15. Ravera F, Miller R, Zuo YY, et al. Methods and models to investigate the physicochemical functionality of pulmonary surfactant. *Curr Opin Colloid Interface Sci*. 2021;55:101467. doi:10.1016/j.cocis.2021.101467

16. Guzmán E, Santini E. Lung surfactant-particles at fluid interfaces for toxicity assessments. *Curr Opin Colloid Interface Sci*. 2019;39:24-39. doi:10.1016/j.cocis.2019.01.003

17. Guzmán E, Liggieri L, Santini E, Ferrari M, Ravera F. Mixed DPPC-cholesterol Langmuir monolayers in presence of hydrophilic silica nanoparticles. *Colloids Surfaces B Biointerfaces*. 2013;105:284-293. doi:10.1016/j.colsurfb.2013.01.020

18. Bartkowiak A, Rojewska M, Prochaska K. Study of mucin interaction with model phospholipid membrane at the air–water interface. *Colloids Surfaces A Physicochem Eng Asp*. 2019;578(March):123587. doi:10.1016/j.colsurfa.2019.123587

19. Bertsch P, Bergfreund J, Windhab EJ, Fischer P. Physiological fluid interfaces: Functional microenvironments, drug delivery targets, and first line of defense. *Acta Biomater*. 2021;130:32-53. doi:10.1016/j.actbio.2021.05.051

20. Ege C, Lee KYC. Insertion of Alzheimer's Aβ40 peptide into lipid monolayers. *Biophys J*. 2004;87(3):1732-1740. doi:10.1529/biophysj.104.043265

21. Ortiz-Collazos S, Picciani PHS, Oliveira ON, Pimentel AS, Edler KJ. Influence of levofloxacin and clarithromycin on the structure of DPPC monolayers. *Biochim Biophys Acta - Biomembr*. 2019;1861(10):182994. doi:10.1016/j.bbamem.2019.05.016

22. Videv P, Mladenov N, Andreeva T, et al. Condensing effect of cholesterol on hBest1/POPC and hBest1/SM langmuir monolayers. *Membranes (Basel)*. 2021;11(1):1-8. doi:10.3390/membranes11010052

23. Zhang Z, Hao C, Qu H, Sun R. Studied on the dynamic adsorption process of Lycium barbarum polysaccharide in the POPC/DPPC monolayers. *Colloids Surfaces B Biointerfaces*. 2019;178(February):38-43. doi:10.1016/j.colsurfb.2019.02.046

24. Miller SE, Mathiasen S, Bright NA, et al. CALM Regulates Clathrin-Coated Vesicle Size and Maturation by Directly Sensing and Driving Membrane Curvature. *Dev Cell*. 2015;33(2):163-175. doi:10.1016/j.devcel.2015.03.002

25. Lai AL, Millet JK, Daniel S, Freed JH, Whittaker GR. The SARS-CoV Fusion Peptide Forms an Extended Bipartite Fusion Platform that Perturbs Membrane Order in a Calcium-Dependent Manner. *J Mol Biol*. 2017;429(24):3875-3892. doi:10.1016/j.jmb.2017.10.017

26. Ciumac D, Campbell RA, Xu H, et al. Implications of lipid monolayer charge characteristics on their selective interactions with a short antimicrobial peptide. *Colloids Surfaces B Biointerfaces*. 2017;150:308-316. doi:10.1016/j.colsurfb.2016.10.043

27. Clifton LA, Campbell RA, Sebastiani F, et al. Design and use of model membranes to study biomolecular interactions using complementary surface-sensitive techniques. *Adv Colloid Interface Sci*. 2020;277. doi:10.1016/j.cis.2020.102118

28. Ikonen E. Cellular cholesterol trafficking and compartmentalization. *Nat Rev Mol Cell Biol 2008 92*. 2008;9(2):125-138. doi:10.1038/nrm2336

29. Van Meer G, Lisman Q. Sphingolipid transport: Rafts and translocators. *J Biol Chem*. 2002;277(29):25855-25858. doi:10.1074/jbc.R200010200

30. Van Meer G, Voelker DR, Feigenson GW. Membrane lipids: Where they are and how they behave. *Nat Rev Mol Cell Biol*. 2008;9(2):112-124. doi:10.1038/nrm2330

31. Hullin-Matsuda F, Taguchi T, Greimel P, Kobayashi T. Lipid compartmentalization in the

endosome system. *Semin Cell Dev Biol*. 2014;31:48-56. doi:10.1016/J.SEMCDB.2014.04.010

32. Raghava S, Giorda KM, Romano FB, Heuck AP, Hebert DN. The SV40 late protein VP4 is a viroporin that forms pores to disrupt membranes for viral release. *PLoS Pathog*. 2011;7(6). doi:10.1371/journal.ppat.1002116

33. Sarkar M, Saha S. Structural insight into the role of novel SARSCoV-2 E protein: A potential target for vaccine development and other therapeutic strategies. *PLoS One*. 2020;15(8 August):1-25. doi:10.1371/journal.pone.0237300

34. Kapoor K, Chen T, Tajkhorshid E. Post-Translational Modifications Optimize the Ability of SARS-CoV-2 Spike for Effective Interaction with Host Cell Receptors. *bioRxiv*. 2021. doi:10.1101/2021.12.02.470852

35. Dodge JT, Phillips1 GB. Composition of phospholipids and of phospholipid fatty acids and aldehydes in human red cells. 1967;8. www.jlr.org.

36. Kruijff B de. Lipid polymorphism and biomembrane function. *Curr Opin Chem Biol*. 1997;1(4):564-569. doi:10.1016/S1367-5931(97)80053-1

37. Collawn JF, Bebök Z. Structure and Functions of Biomembranes. *Curr Top Membr*. 2008;61:1-21. doi:10.1016/S1063-5823(08)00201-9

38. Singer SJ, Nicolson GL. The Fluid Mosaic Model of the Structure of Cell Membranes. *Science*. 1972;175(4023):720-731. doi:10.1126/science.175.4023.720

39. Holthuis JCM, Menon AK. Lipid landscapes and pipelines in membrane homeostasis. *Nature*. 2014;510(7503):48-57. doi:10.1038/nature13474

40. Grinstein S. Imaging signal transduction during phagocytosis: Phospholipids, surface charge, and electrostatic interactions. *Am J Physiol - Cell Physiol*. 2010;299(5):876-881. doi:10.1152/AJPCELL.00342.2010

41. Magalhaes MAO, Glogauer M. Pivotal Advance: Phospholipids determine net membrane surface charge resulting in differential localization of active Rac1 and Rac2. *J Leukoc Biol*. 2010;87(4):545-555. doi:10.1189/JLB.0609390

42. Rastogi BK, Nordøy A. Lipid composition of cultured human endothelial cells. *Thromb Res*. 1980;18(5):629-641. doi:10.1016/0049-3848(80)90218-2

43. Nordøy A, Bjørge JM, Strøm E. COMPARISON OF THE MAIN LIPIDS IN PLATELETS AND PLASMA IN MAN. *Acta Med Scand*. 1973;193(1-6):59-64. doi:10.1111/J.0954-6820.1973.TB10539.X

44. Slotte JP. Sphingomyelin - Cholesterol interactions in biological and model membranes. *Chem Phys Lipids*. 1999;102(1-2):13-27. doi:10.1016/S0009-3084(99)00071-7

45. Israelachvili JN. Refinement of the fluid-mosaic model of membrane structure. *Biochim Biophys Acta - Biomembr*. 1977;469(2):221-225. doi:10.1016/0005-2736(77)90185-7

46. Nicolson GL. The Fluid—Mosaic Model of Membrane Structure: Still relevant to understanding the structure, function and dynamics of biological membranes after more than 40 years. *Biochim Biophys Acta - Biomembr*. 2014;1838(6):1451-1466. doi:10.1016/J.BBAMEM.2013.10.019

47. Vereb G, Szöllosi J, Matkó J, et al. Dynamic, yet structured: The cell membrane three decades after the Singer-Nicolson model. *Proc Natl Acad Sci U S A*. 2003;100(14):8053-8058. doi:10.1073/PNAS.1332550100

48. Simons K, Ikonen E. Functional rafts in cell membranes. *Nat 1997 3876633*. 1997;387(6633):569-572. doi:10.1038/42408

49. Simons K, Toomre D. Lipid rafts and signal transduction. *Nat Rev Mol Cell Biol 2000 11*. 2000;1(1):31-39. doi:10.1038/35036052

50. Levental I, Veatch SL. The Continuing Mystery of Lipid Rafts. *J Mol Biol*. 2016;428(24):4749-4764. doi:10.1016/J.JMB.2016.08.022

51. Nickels JD, Chatterjee S, Stanley CB, et al. The in vivo structure of biological membranes and evidence for lipid domains. *PLOS Biol*. 2017;15(5):e2002214. doi:10.1371/JOURNAL.PBIO.2002214

52. Dynarowicz-ŁĄtka P, Hąc-Wydro K. Interactions between phosphatidylcholines and cholesterol in monolayers at the air/water interface. *Colloids Surfaces B Biointerfaces*. 2004;37(1-2):21-25. doi:10.1016/j.colsurfb.2004.06.007

53. Rubio RG, Guzmán E, Ortega F, Liggieri L. Monolayers of Cholesterol and Cholesteryl Stearate at the Water/Vapor Interface: A Physico-Chemical Study of Components of the Meibum Layer. *Colloids and Interfaces*. 2021;5(2):30. doi:10.3390/COLLOIDS5020030

54. Huang J, Feigenson GW. A microscopic interaction model of maximum solubility of cholesterol in lipid bilayers. *Biophys J*. 1999;76(4):2142-2157. doi:10.1016/S0006-3495(99)77369-8

55. Simons K, Vaz WLC. Model systems, lipid rafts, and cell membranes. *Annu Rev Biophys Biomol Struct*. 2004;33:269-295. doi:10.1146/annurev.biophys.32.110601.141803

56. Regen SL. The Origin of Lipid Rafts. *Biochemistry*. 2020;59(49):4617-4621. doi:10.1021/acs.biochem.0c00851

57. Krause MR, Regen SL. The structural role of cholesterol in cell membranes: From condensed bilayers to lipid rafts. *Acc Chem Res*. 2014;47(12):3512-3521. doi:10.1021/ar500260t

58. Wydro P. Sphingomyelin/phosphatidylcholine/cholesterol monolayers - analysis of the interactions in model membranes and Brewster Angle Microscopy experiments. *Colloids Surfaces B Biointerfaces*. 2012;93:174-179. doi:10.1016/j.colsurfb.2011.12.035

59. Falkenburger BH, Jensen JB, Dickson EJ, Suh BC, Hille B. Phosphoinositides: Lipid regulators of membrane proteins. *J Physiol*. 2010;588(17):3179-3185. doi:10.1113/jphysiol.2010.192153

60. Czech MP. PIP2 and PIP3: Complex roles at the cell surface. *Cell*. 2000;100(6):603-606. doi:10.1016/S0092-8674(00)80696-0

61. Ellenbroek WG, Wang YH, Christian DA, Discher DE, Janmey PA, Liu AJ. Divalent cation-dependent formation of electrostatic PIP2 clusters in lipid monolayers. *Biophys J*. 2011;101(9):2178-2184. doi:10.1016/j.bpj.2011.09.039

62. Wang YH, Collins A, Guo L, et al. Divalent cation-induced cluster formation by polyphosphoinositides in model membranes. *J Am Chem Soc*. 2012;134(7):3387-3395. doi:10.1021/ja208640t

63. Bilkova E, Pleskot R, Rissanen S, et al. Calcium Directly Regulates Phosphatidylinositol 4,5-Bisphosphate Headgroup Conformation and Recognition. *J Am Chem Soc*. 2017;139(11):4019-4024. doi:10.1021/jacs.6b11760

64. Levental I, Christian DA, Wang YH, Madara JJ, Discher DE, Janmey PA. Calcium-dependent lateral organization in phosphatidylinositol 4,5-bisphosphate (PIP2)- and cholesterol-containing

monolayers. *Biochemistry*. 2009;48(34):8241-8248. doi:10.1021/bi9007879

65. Caffrey M, Wang J. Membrane-Structure Studies Using X-Ray Standing Waves. *http://dx.doi.org/101146/annurev.bb24060195002031*. 2003;24:351-378. doi:10.1146/ANNUREV.BB.24.060195.002031

66. Rojewska M, Smułek W, Kaczorek E, Prochaska K. Langmuir Monolayer Techniques for the Investigation of Model Bacterial Membranes and Antibiotic Biodegradation Mechanisms. *Membr 2021, Vol 11, Page 707*. 2021;11(9):707. doi:10.3390/MEMBRANES11090707

67. Santamaria A, Batchu KC, Matsarskaia O, et al. Strikingly Different Roles of SARS-CoV-2 Fusion Peptides Uncovered by Neutron Scattering. *J Am Chem Soc*. 2022. doi:10.1021/jacs.1c09856

68. Almeida PFF. Thermodynamics of lipid interactions in complex bilayers. *Biochim Biophys Acta - Biomembr*. 2009;1788(1):72-85. doi:10.1016/j.bbamem.2008.08.007

69. Luchini A, Nzulumike ANO, Lind TK, et al. Towards biomimics of cell membranes: Structural effect of phosphatidylinositol triphosphate (PIP 3) on a lipid bilayer. *Colloids Surfaces B Biointerfaces*. 2019;173(March 2018):202-209. doi:10.1016/j.colsurfb.2018.09.031

70. Wagner ML, Tamm LK. Tethered Polymer-Supported Planar Lipid Bilayers for Reconstitution of Integral Membrane Proteins: Silane-Polyethyleneglycol-Lipid as a Cushion and Covalent Linker. *Biophys J*. 2000;79(3):1400-1414. doi:10.1016/S0006-3495(00)76392-2

71. Heinrich F, Lösche M. Zooming in on disordered systems: Neutron reflection studies of proteins associated with fluid membranes. *Biochim Biophys Acta - Biomembr*. 2014;1838(9):2341-2349. doi:10.1016/j.bbamem.2014.03.007

72. Luchini A, Tidemand FG, Johansen NT, et al. Peptide Disc Mediated Control of Membrane Protein Orientation in Supported Lipid Bilayers for Surface-Sensitive Investigations. *Anal Chem*. 2020;92(1):1081-1088. doi:10.1021/acs.analchem.9b04125

73. Luchini A, Micciulla S, Corucci G, et al. Lipid bilayer degradation induced by SARS-CoV-2 spike protein as revealed by neutron reflectometry. *Sci Rep*. 2021;11(1). doi:10.1038/s41598-021-93996-x

74. Ciumac D, Gong H, Campbell RA, Campana M, Xu H, Lu JR. Structural elucidation upon binding of antimicrobial peptides into binary mixed lipid monolayers mimicking bacterial membranes. *J Colloid Interface Sci*. 2021;598:193-205. doi:10.1016/j.jcis.2021.04.037

75. Chiou PC, Hsu WW, Chang Y, Chen YF. Molecular packing of lipid membranes and action mechanisms of membrane-active peptides. *Colloids Surfaces B Biointerfaces*. 2022;213:112384. doi:10.1016/J.COLSURFB.2022.112384

76. Smith AW. Lipid–protein interactions in biological membranes: A dynamic perspective. *Biochim Biophys Acta - Biomembr*. 2012;1818(2):172-177. doi:10.1016/J.BBAMEM.2011.06.015

77. Liu A, Wenzel N, Qi X. Role of lysine residues in membrane anchoring of saposin C. *Arch Biochem Biophys*. 2005;443(1-2):101-112. doi:10.1016/J.ABB.2005.09.007

78. Li L, Vorobyov I, Allen TW. The different interactions of lysine and arginine side chains with lipid membranes. *J Phys Chem B*. 2013;117(40):11906-11920. doi:10.1021/JP405418Y/SUPPL_FILE/JP405418Y_SI_001

79. Graber Z, Kwarteng DO, Lange SM, et al. The Electrostatic Basis of Diacylglycerol

Pyrophosphate—Protein Interaction. *Cells 2022, Vol 11, Page 290*. 2022;11(2):290. doi:10.3390/CELLS11020290

80. Soñora M, Barrera EE, Pantano S. The stressed life of a lipid in the Zika virus membrane. *Biochim Biophys acta Biomembr*. 2022;1864(1). doi:10.1016/J.BBAMEM.2021.183804

81. Peacock TP, Goldhill DH, Zhou J, et al. The furin cleavage site in the SARS-CoV-2 spike protein is required for transmission in ferrets. *Nat Microbiol*. 2021;6(7):899-909. doi:10.1038/s41564-021-00908-w

82. Zaccai NR, Kadlecova Z, Dickson VK, et al. FCHO controls AP2's initiating role in endocytosis through a PtdIns(4,5)P2-dependent switch. *Sci Adv*. 2022;8(17):2018. doi:10.1126/SCIADV.ABN2018

83. Schmid SL, Conner SD. Regulated portals of entry into the cell. *Nature*. 2003;422(March):37-44. www.nature.com/nature.

84. McMahon HT, Boucrot E. Molecular mechanism and physiological functions of clathrin-mediated endocytosis. *Nat Rev Mol Cell Biol 2011 128*. 2011;12(8):517-533. doi:10.1038/nrm3151

85. Traub LM. Sorting it out: AP-2 and alternate clathrin adaptors in endocytic cargo selection. *J Cell Biol*. 2003;163(2):203-208. doi:10.1083/jcb.200309175

86. Kadlecova Z, Spielman SJ, Loerke D, Mohanakrishnan A, Reed DK, Schmid SL. Regulation of clathrin-mediated endocytosis by hierarchical allosteric activation of AP2. *J Cell Biol*. 2017;216(1):167-179. doi:10.1083/jcb.201608071

87. Chen X, Irani NG, Friml J. Clathrin-mediated endocytosis: the gateway into plant cells. *Curr Opin Plant Biol*. 2011;14(6):674-682. doi:10.1016/J.PBI.2011.08.006

88. Miller SE, Sahlender DA, Graham SC, et al. The molecular basis for the endocytosis of small R-SNAREs by the clathrin adaptor CALM. *Cell*. 2011;147(5):1118-1131. doi:10.1016/j.cell.2011.10.038

89. David C, McPherson PS, Mundigl O, De Camilli P. A role of amphiphysin in synaptic vesicle endocytosis suggested by its binding to dynamin in nerve terminals. *Proc Natl Acad Sci U S A*. 1996;93(1):331-335. doi:10.1073/pnas.93.1.331

90. Blondeau F, Ritter B, Allaire PD, et al. Tandem MS analysis of brain clathrin-coated vesicles reveals their critical involvement in synaptic vesicle recycling. *Proc Natl Acad Sci U S A*. 2004;101(11):3833-3838. doi:10.1073/PNAS.0308186101

91. Borner GHH, Antrobus R, Hirst J, et al. Multivariate proteomic profiling identifies novel accessory proteins of coated vesicles. *J Cell Biol*. 2012;197(1):141-160. doi:10.1083/JCB.201111049/VIDEO-1

92. Koo SJ, Markovic S, Puchkov D, et al. SNARE motif-mediated sorting of synaptobrevin by the endocytic adaptors clathrin assembly lymphoid myeloid leukemia (CALM) and AP180 at synapses. *Proc Natl Acad Sci U S A*. 2011;108(33):13540-13545. doi:10.1073/pnas.1107067108

93. Ford MGJ, Pearse BMF, Higgins MK, et al. Simultaneous binding of PtdIns (4,5) P2 and clathrin by AP180 in the nucleation of clathrin lattices on membranes. *Science*. 2001;291(5506):1051-1055. doi:10.1126/science.291.5506.1051

94. Tebar F, Bohlander SK, Sorkin A. Clathrin assembly lymphoid myeloid leukemia (CALM) protein: Localization in endocytic-coated pits, interactions with clathrin, and the impact of

overexpression on clathrin-mediated traffic. *Mol Biol Cell*. 1999;10(8):2687-2702. doi:10.1091/MBC.10.8.2687/ASSET/IMAGES/LARGE/MK0890936010.JPEG

95. Traub LM. Regarding the Amazing Choreography of Clathrin Coats. *PLOS Biol*. 2011;9(3):e1001037. doi:10.1371/JOURNAL.PBIO.1001037

96. Ford MGJ, Mills IG, Peter BJ, et al. Curvature of clathrin-coated pits driven by epsin. *Nature*. 2002;419(6905):361-366. doi:10.1038/nature01020

97. Baumgart T, Capraro BR, Zhu C, Das SL. Thermodynamics and Mechanics of Membrane Curvature Generation and Sensing by Proteins and Lipids. *http://dx.doi.org/101146/annurev.physchem012809103450*. 2011;62:483-506. doi:10.1146/ANNUREV.PHYSCHEM.012809.103450

98. Collins BM, McCoy AJ, Kent HM, Evans PR, Owen DJ. Molecular Architecture and Functional Model of the Endocytic AP2 Complex. *Cell*. 2002;109(4):523-535. doi:10.1016/S0092-8674(02)00735-3

99. Brett TJ, Traub LM, Fremont DH. Accessory Protein Recruitment Motifs in Clathrin-Mediated Endocytosis. *Structure*. 2002;10(6):797-809. doi:10.1016/S0969-2126(02)00784-0

100. DJ O, Y V, BM P, HT M, PR E. The structure and function of the beta 2-adaptin appendage domain. *EMBO J*. 2000;19(16):4216-4227. doi:10.1093/EMBOJ/19.16.4216

101. Gaidarov I, Keen JH. Phosphoinositide–Ap-2 Interactions Required for Targeting to Plasma Membrane Clathrin-Coated Pits. *J Cell Biol*. 1999;146(4):755-764. doi:10.1083/JCB.146.4.755

102. Padrón D, Wang YJ, Yamamoto M, Yin H, Roth MG. Phosphatidylinositol phosphate 5-kinase Iβ recruits AP-2 to the plasma membrane and regulates rates of constitutive endocytosis. *J Cell Biol*. 2003;162(4):693-701. doi:10.1083/JCB.200302051

103. Page LJ, Robinson MS. Targeting signals and subunit interactions in coated vesicle adaptor complexes. *J Cell Biol*. 1995;131(3):619-630. doi:10.1083/JCB.131.3.619

104. Rohde G, Wenzel D, Haucke V. A phosphatidylinositol (4,5)-bisphosphate binding site within μ2-adaptin regulates clathrin-mediated endocytosis. *J Cell Biol*. 2002;158(2):209-214. doi:10.1083/JCB.200203103

105. Owen DJ, Evans PR. A structural explanation for the recognition of tyrosine-based endocytotic signals. *Science*. 1998;282(5392):1327-1332. doi:10.1126/science.282.5392.1327

106. Jackson LP, Kelly BT, McCoy AJ, et al. A large-scale conformational change couples membrane recruitment to cargo binding in the AP2 clathrin adaptor complex. *Cell*. 2010;141(7):1220-1229. doi:10.1016/j.cell.2010.05.006

107. Kelly BT, Graham SC, Liska N, et al. AP2 controls clathrin polymerization with a membrane-activated switch. *Science*. 2014;345(6195):459-463. doi:10.1126/science.1254836

108. Maestro A, Zaccai NR. Unpublished results.

109. Henne WM, Kent HM, Ford MGJ, et al. Structure and Analysis of FCHo2 F-BAR Domain: A Dimerizing and Membrane Recruitment Module that Effects Membrane Curvature. *Structure*. 2007;15(7):839-852. doi:10.1016/j.str.2007.05.002

110. Chitu V, Stanley ER. Pombe Cdc15 homology (PCH) proteins: coordinators of membrane–cytoskeletal interactions. *Trends Cell Biol*. 2007;17(3):145-156. doi:10.1016/J.TCB.2007.01.003

111. Itoh T, De Camilli P. BAR, F-BAR (EFC) and ENTH/ANTH domains in the regulation of membrane–cytosol interfaces and membrane curvature. *Biochim Biophys Acta - Mol Cell Biol Lipids*. 2006;1761(8):897-912. doi:10.1016/J.BBALIP.2006.06.015

112. McMahon HT, Gallop JL. Membrane curvature and mechanisms of dynamic cell membrane remodelling. *Nature*. 2005;438(7068):590-596. doi:10.1038/nature04396

113. Peter BJ, Kent HM, Mills IG, et al. BAR Domains as Sensors of Membrane Curvature: The Amphiphysin BAR Structure. *Science*. 2004;303(5657):495-499. doi:10.1126/science.1092586

114. Frost A, Unger VM, De Camilli P. The BAR Domain Superfamily: Membrane-Molding Macromolecules. *Cell*. 2009;137(2):191-196. doi:10.1016/J.CELL.2009.04.010

115. Itoh T, Takenawa T. Mechanisms of membrane deformation by lipid-binding domains. *Prog Lipid Res*. 2009;48(5):298-305. doi:10.1016/J.PLIPRES.2009.05.002

116. Suetsugu S, Toyooka K, Senju Y. Subcellular membrane curvature mediated by the BAR domain superfamily proteins. *Semin Cell Dev Biol*. 2010;21(4):340-349. doi:10.1016/J.SEMCDB.2009.12.002

117. Aspenström P. A Cdc42 target protein with homology to the non-kinase domain of FER has a potential role in regulating the actin cytoskeleton. *Curr Biol*. 1997;7(7):479-487. doi:10.1016/S0960-9822(06)00219-3

118. Taylor MJ, Perrais D, Merrifield CJ. A High Precision Survey of the Molecular Dynamics of Mammalian Clathrin-Mediated Endocytosis. *PLOS Biol*. 2011;9(3):e1000604. doi:10.1371/JOURNAL.PBIO.1000604

119. Hollopeter G, Lange JJ, Zhang Y, et al. The membrane-associated proteins FCHo and SGIP are allosteric activators of the AP2 clathrin adaptor complex. *Elife*. 2014;3. doi:10.7554/ELIFE.03648

120. Umasankar PK, Sanker S, Thieman JR, et al. Distinct and separable activities of the endocytic clathrin-coat components Fcho1/2 and AP-2 in developmental patterning. *Nat Cell Biol 2012 145*. 2012;14(5):488-501. doi:10.1038/ncb2473

121. Umasankar PK, Ma L, Thieman JR, et al. A clathrin coat assembly role for the muniscin protein central linker revealed by TALEN-mediated gene editing. *Elife*. 2014;3. doi:10.7554/ELIFE.04137

122. Henne WM, Boucrot E, Meinecke M, et al. FCHo proteins are nucleators of Clathrin-Mediated endocytosis. *Science*. 2010;328(5983):1281-1284. doi:10.1126/science.1188462

123. Reider A, Barker SL, Mishra SK, et al. Syp1 is a conserved endocytic adaptor that contains domains involved in cargo selection and membrane tubulation. *EMBO J*. 2009;28(20):3103-3116. doi:10.1038/EMBOJ.2009.248

124. Uezu A, Horiuchi A, Kanda K, et al. SGIP1α is an endocytic protein that directly interacts with phospholipids and Eps15. *J Biol Chem*. 2007;282(36):26481-26489. doi:10.1074/JBC.M703815200/ATTACHMENT/74522BA5-599E-4A6D-A3DE-1E0A5DD7AAD8/MMC1.ZIP

125. Ma L, Umasankar PK, Wrobel AG, et al. Transient Fcho1/2·Eps15/R·AP-2 Nanoclusters Prime the AP-2 Clathrin Adaptor for Cargo Binding. *Dev Cell*. 2015;37(5):428-443. doi:10.1016/J.DEVCEL.2016.05.003

126. Benmerah A, Bèguet B, Dautry-Varsat A, Cerf-Bensussan N. The Ear of α-Adaptin Interacts with the COOH-terminal Domain of the Eps15 Protein (∗). *J Biol Chem*. 1996;271(20):12111-12116.

doi:10.1074/JBC.271.20.12111

127. Iannolo G, Salcini AE, Gaidarov I, et al. Mapping of the Molecular Determinants Involved in the Interaction between eps15 and AP-21. *Cancer Res*. 1997;57(2):240-245.

128. Fung TS, Liu DX. Human Coronavirus : Host-Pathogen Interaction. 2019:529-560.

129. Tang T, Bidon M, Jaimes JA, Whittaker GR, Daniel S. Coronavirus membrane fusion mechanism offers a potential target for antiviral development. *Antiviral Res*. 2020;178(April):104792. doi:10.1016/j.antiviral.2020.104792

130. Hoffmann M, Kleine-Weber H, Schroeder S, et al. SARS-CoV-2 Cell Entry Depends on ACE2 and TMPRSS2 and Is Blocked by a Clinically Proven Protease Inhibitor. *Cell*. 2020;181(2):271-280.e8. doi:10.1016/j.cell.2020.02.052

131. Harrison SC. Viral membrane fusion. *Virology*. 2015;479-480:498-507. doi:10.1016/J.VIROL.2015.03.043

132. Lin Y, Yan X, Cao W, et al. Probing the structure of the SARS coronavirus using scanning electron microscopy. *Antivir Ther*. 2004;(9):287-289.

133. Ng ML, Lee JWM, Leong MLN, Ling AE, Tan HC, Ooi EE. Topographic Changes in SARS Coronavirus–infected Cells during Late Stages of Infection. *Emerg Infect Dis*. 2004;10(11). www.cdc.gov/eid.

134. Li Q, Wu J, Nie J, et al. The Impact of Mutations in SARS-CoV-2 Spike on Viral Infectivity and Antigenicity. *Cell*. 2020;182(5):1284-1294.e9. doi:10.1016/J.CELL.2020.07.012

135. Daly JL, Simonetti B, Klein K, et al. Neuropilin-1 is a host factor for SARS-CoV-2 infection. *Science*. 2020;370(6518):861-865. doi:10.1126/science.abd3072

136. Cai Y, Zhang J, Xiao T, et al. Distinct conformational states of SARS-CoV-2 spike protein. *Science*. 2020;369(6511). doi:10.1126//science.abd4251

137. Benton DJ, Wrobel AG, Xu P, et al. Receptor binding and priming of the spike protein of SARS-CoV-2 for membrane fusion. *Nat 2020 5887837*. 2020;588(7837):327-330. doi:10.1038/s41586-020-2772-0

138. Xia S, Liu M, Wang C, et al. Inhibition of SARS-CoV-2 (previously 2019-nCoV) infection by a highly potent pan-coronavirus fusion inhibitor targeting its spike protein that harbors a high capacity to mediate membrane fusion. *Cell Res*. 2020;2(February). doi:10.1038/s41422-020-0305-x

139. Walls AC, Tortorici MA, Bosch BJ, et al. Cryo-electron microscopy structure of a coronavirus spike glycoprotein trimer. *Nat 2016 5317592*. 2016;531(7592):114-117. doi:10.1038/nature16988

140. Xu Y, Lou Z, Liu Y, et al. Crystal structure of severe acute respiratory syndrome coronavirus spike protein fusion core. *J Biol Chem*. 2004;279(47):49414-49419. doi:10.1074/jbc.M408782200

Chapter 2

Methods

Due to the complexity of real biological membranes, researchers have often exploited model membranes, in the form of *in vitro* lipid model systems, to investigate membrane properties as well as study the interaction of lipids with proteins. Thus, finding an appropriate biomimetic model membrane is of outmost importance in the biophysical research field. Model membranes are simpler and controllable systems that can be optimized to mimic the biological membranes of interest[1,2]. Besides, different types of model membranes can be built and adapted to the use of specific techniques for characterization. The most commonly used systems as biomimetic model membranes are planar membranes, such as lipid monolayers and solid supported bilayers, and liposomes. This chapter provides a general overview of these *in vitro* lipid model systems, and the related techniques exploited for their characterization.

1. *In vitro* lipid model systems

1.1. Lipid monolayers

Lipid monolayers, formed at air/liquid interfaces, are widely exploited as models to replicate single leaflets of cellular membranes. Therefore, they are not well suited for studying transmembrane processes, even though lipid monolayers can be exploited for studying processes occurring at the biomembrane surface. Being phospholipids, sphingolipids and sterols poorly soluble in water, they readily form Langmuir monolayers when deposited from organic solvent solutions onto a water interface using a **Langmuir trough**[2–4]. Although they are considered the simplest among the *in vitro* lipid model membranes, Langmuir monolayers are versatile systems to study the physico-chemical characteristics of a membrane, as well as investigate its interaction with biologically relevant molecules[5], such as drugs[6], nanoparticles[7,8], antimicrobial peptides[9–11], as well as viral[12] and eukaryotic[13,14] proteins. Indeed the use of a lipid monolayer allows the combination of different techniques that provide complementary information on the system of interest, such as **surface pressure (Π) - area (A) isotherm** and time evolution of surface pressure at a fixed interfacial concentration, which provide evidences of protein-lipid interaction, as well as **ellipsometry**, **neutron reflectometry** (**NR**), and **Brewster angle microscopy** (**BAM**) that can

be coupled to the Langmuir trough (see **Figure 2.1**), and provide additional information related to the in-plane and out-of-plane organization of the molecules within the model membrane.

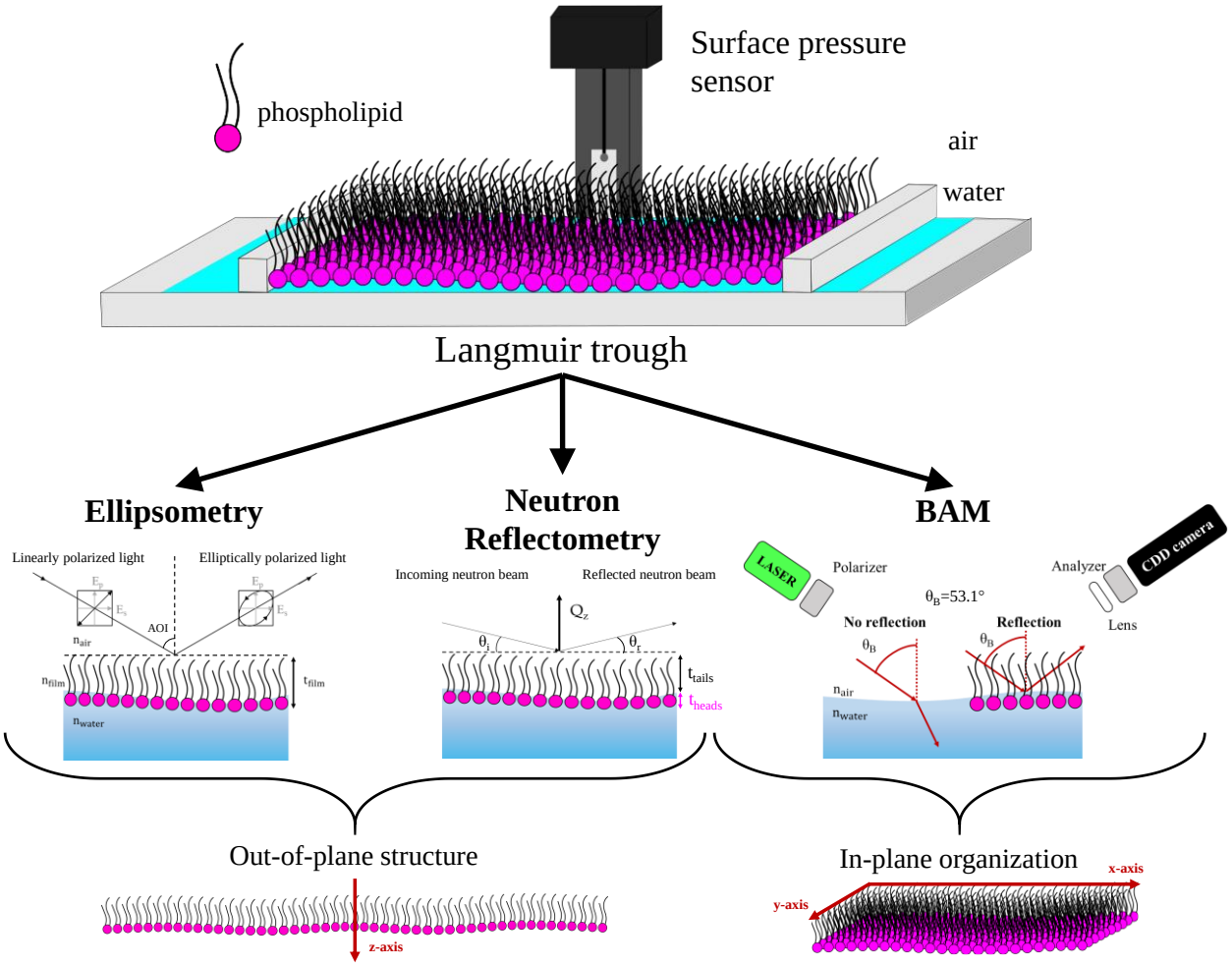

Figure 2.1 Representation of a Langmuir trough with a deposited lipid monolayer. The techniques that can be coupled to the trough are schematically shown, alongside with the information that could be obtained. Lipid tails are depicted in black and the headgroups in magenta.

1.2. Solid supported lipid bilayer

Compared to monolayers, bilayers are more complicated *in vitro* model systems, made of two lipid leaflets deposited onto a surface, usually a silicon wafer coated with a native thin silicon oxide layer (see **Figure 2.2**). Two main deposition methods are known: (1) Langmuir-Blodgett and Langmuir-Schaefer, which consists in sub-sequential transference of lipid layers from Langmuir monolayers spread at an air/liquid interface onto the solid surface, and (2) vesicle fusion, schematically shown in **Figure 2.2**. While the first is very useful when asymmetric bilayers need to be deposited, the latter is the easiest and fastest way to produce a lipid bilayer[2]. It relies on the

aptitude of small unilamellar vesicles (SUVs) to fuse upon reaching the surface, thus forming a lipid bilayer[2,15–19]. Given their nature, lipid bilayers are more representative of the biological membranes, with respect to lipid monolayers. However, the viscoelastic properties as well as response to external stimuli, such as the binding of a protein, may differ from the one of a real membrane, being affected by the presence of the solid support. Indeed, the proximity of the substrate influences the diffusion of lipids[2,20,21]. Moreover, the natural bilayer fluctuations are suppressed when deposited onto a solid support due to the strength of the interaction between the substrate and the lipids[22,23]. The solid supported lipid bilayers remain a very valuable model system to investigate structural membrane properties as well as protein binding and insertion. The main techniques used to study lipid bilayers, exploited in this PhD thesis, are **NR** and **Quartz Crystal Microbalance with Dissipation monitoring** (**QCM-D**).

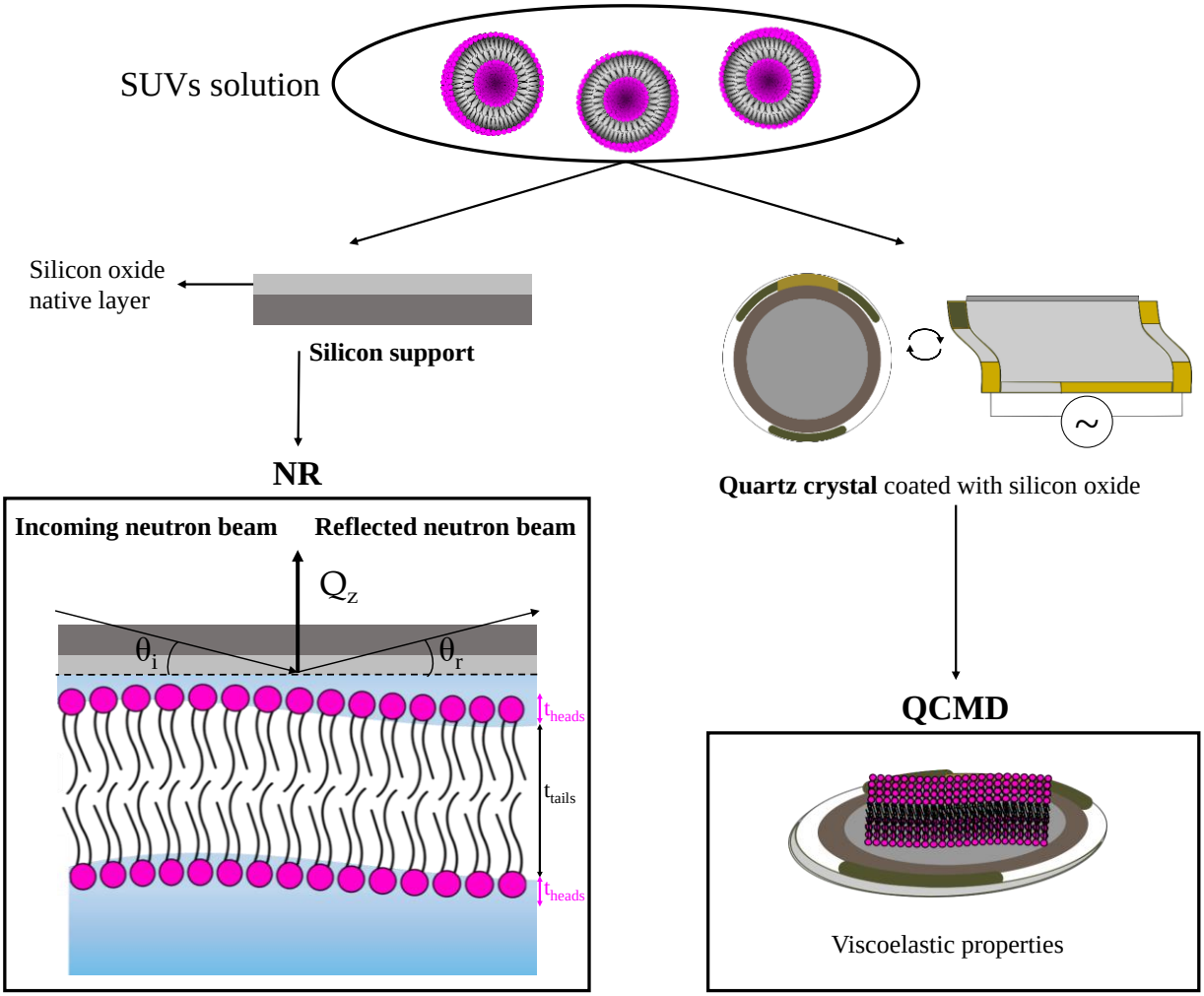

Figure 2.2 Representation of a lipid bilayer deposited on a solid support via vesicles fusion. The techniques exploited to characterize bilayers are schematically shown, alongside with the information that could be obtained. Lipid tails are depicted in black and the headgroups in magenta.

1.3. Liposomes

Other than planar *in vitro* model systems, liposomes could be used to replicate biological membranes. They are vesicles composed of one or multiple bilayers, thus they could be classified in function of their lamellarity, in uni- and multilamellar vesicles (ULVs and MLVs, respectively). Moreover, they could be classified by their size into small unilamellar vesicles (SUVs) with a size range of 20-100 nm, large unilamellar vesicles (LUVs) with a size range of 100-1000 nm and giant unilamellar vesicles (GUVs) with a size range of 1-200 μm[24]. Generally, liposomes preparation is very straightforward, only requiring a lipid film dispersed in an aqueous medium. Lipids then self-assemble in vesicles with the hydrophilic headgroups facing the aqueous environment, protecting the hydrophobic tails. Different methods are used to tune liposome size, such as tip sonication and extrusion[25]. The former is usually performed in pulsation, in order to break intermolecular interactions between lipids and force them to rearrange, in smaller vesicles. On the other hand, extrusion (see **Figure 2.3**) is an easily accessible technique that requires multiple passages of the multilamellar liposome dispersion through a membrane with a defined pore size. The possibility of using different pore size membranes presents the great advantage of choosing the average nominal liposome size. This is very useful when it comes to investigating the binding of curvature sensing proteins, which could interact with liposomes depending on their size[26]. It should be stressed that the reconstruction of liposomes by conventional approaches leads to lipid vesicles with a symmetric composition in both leaflets, which contrasts with the high asymmetry of real cell membranes. The absence of asymmetry is a very important limitation of the use of artificial lipid vesicles as biomembrane models[27]. To characterize such systems, light as well as neutron scattering techniques are exploited (**Figure 2.3**), such as **dynamic light scattering** (**DLS**) and **small-angle neutron scattering** (**SANS**), respectively. Indeed, they provide information regarding liposome shape, size and diffusion in bulk, thus giving information concerning the eventual influence of a protein on these properties.

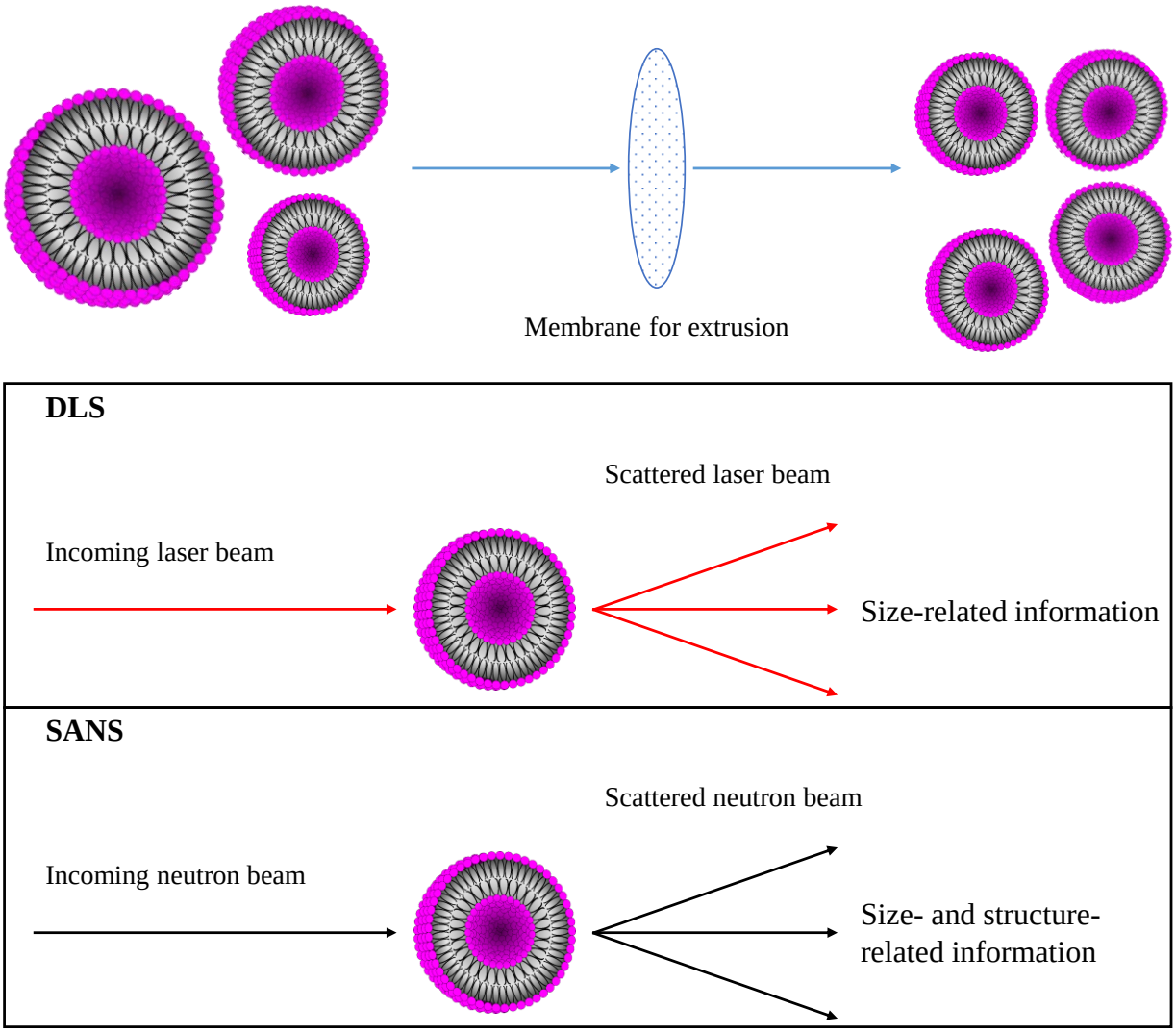

Figure 2.3 Schematic representation of extrusion, also reporting the techniques exploited to characterize liposomes and the information that could be obtained. Lipid tails are depicted in black and the headgroups in magenta.

2. Experimental techniques

2.1. Laboratory techniques

2.1.1. Langmuir trough: surface pressure (Π) - area (A) isotherm

Langmuir trough experiments are necessary to monitor the surface pressure (Π) of the monolayer at the air/water interface. The latter is defined following **Equation 2.1:**

$$\Pi = \gamma_0 - \gamma \qquad \textbf{2.1}$$

where γ_0 and γ are the surface tension of the bare water interface and the one of the interface enriched in amphiphilic molecules, respectively. **Equation 2.1** implies that the presence of lipid molecules at the air/water interface reduces the surface tension of the water. Nevertheless, the surface pressure is a key parameter in describing the packing state of lipid membranes[28], since it is strictly connected to the compressibility of the membrane as well as its stability and the lateral organization of lipids. Indeed, measuring surface pressure modifications upon changing the area available for the lipid molecules provides a surface pressure-area per molecule diagram (the so called compression isotherm) that can be considered analogous to a phase diagram for a three-dimensional system. This type of diagrams provides information related to the lateral organization of lipids at the air/water interface. In fact, the reduction of the area available for the molecules forces their reorganization, leading the system towards different physical states. **Figure 2.4** displays a sketch showing a Π-A diagram, and the corresponding idealized organization of the lipids at the interface in the different phases.

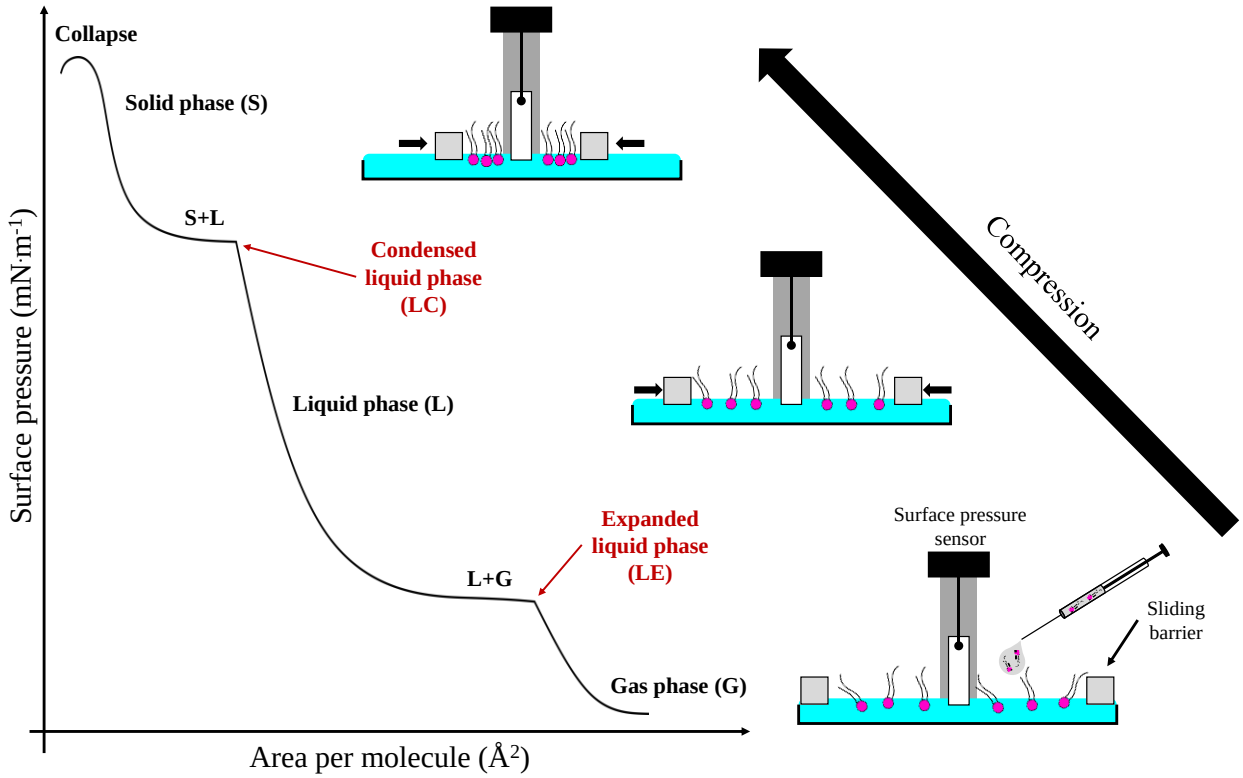

Figure 2.4 Idealized surface pressure-area per molecule diagram for a lipid monolayer and the different organization of the molecules at the interface.

The evolution of the surface pressure as a function of the average area available for each lipid molecule provides insightful information about the lipid phase behavior. The observed phase behavior of the monolayer is determined mainly by the physicochemical properties of the lipid molecules, the subphase temperature, and the subphase composition[1]. Π-A isotherms allow to distinguish if a lipid monolayer is in a gas (G), liquid (L) or solid (S) phase, each of them characterized by a different lateral packing of the lipid molecules. For example, a monolayer in the gas phase is much diluted, characterized by particularly high values of area per molecule (*i.e.*, hundreds of square angstroms). Thus it could be described as a two-dimensional gas[3]. With increasing surface pressure, by compressing the monolayer, the film proceeds into the liquid phase, which is divided into liquid expanded (LE, fluid-like) and liquid condensed (LC, gel-like) phase. These are the two most commonly observed monolayer states, which are analogous to the liquid-crystalline and gel states in bilayers, respectively[1,3]. The former is characterized by a tails conformational disorder[3], which gradually decrease when the condensed state is reached, upon further compression. Finally, the monolayer becomes less and less compressible, until the solid phase is reached. Furthermore, regions of coexistence can be identified from the slope of the

isotherm. In particular, the presence of a plateau in the surface pressure profile, monitored during compression, usually indicates the coexistence of two phases, thus implying the occurring of a transition from a phase more abundant in a less compressed monolayer, to another one that characterizes the film at higher compression states. Specifically, in the range of the liquid phase, the LC-LE phase transitions are fairly common, which can be described as disordered/ordered phase transitions of a two-dimensional fluid[29]. When working with multi component lipid monolayers, the phase of the film could be easily tuned by changing the lipid composition. For example, DPPC is known to produce bean-shaped condensed domains at the air/water interface[30], and cholesterol is often used as condensing agent[31–34], since it increases film rigidity. Conversely, Langmuir monolayers made of lipids with single or multiple double bonds (such as POPC and DOPC, respectively) are characterized by a minor rigidity, being the oleoyl chains intrinsically more disordered than the palmitoyl ones[34,35].

2.1.2. Ellipsometry

Ellipsometry is a non-destructive optical technique based on the determination of the polarization changes that light undergoes when it is reflected at an interface[36] (**Figure 2.1**). The reflection coefficients parallel (r_p) and perpendicular (r_s) to the plane of incidence are related to the ellipsometric angles Δ and Ψ, through **Equation 2.2**:

$$\rho = \frac{r_p}{r_s} = \tan\Psi e^{i\Delta} \qquad \textbf{2.2}$$

where the ellipticity ρ depends on the angle of incidence (AOI) and wavelength of the light beam. Moreover, it is also strictly correlated to the thickness (t_F) as well as refractive index (n_F) of the film present at the interface. Thus, once Δ and Ψ profiles as functions of the AOI are obtained, they could be interpreted by considering a model with a defined t_F and n_F. In particular, in this PhD thesis, a one-layer slab model is constructed, composed of a lipid monolayer (at the air/water interface), and the fit is performed by using a numeric nonlinear minimization procedure, specifically a trust-region reflective algorithm[37], by determining the ellipsometric angles of the model that minimizes the differences with those experimentally obtained[37–39]. To calculate Δ and Ψ of the model, a power series expansion to the first order of the relative film thickness is used (**Equation 2.3**):

$$\rho \approx \rho_0 + i\rho' \frac{2\pi t_F}{\lambda} \qquad \textbf{2.3}$$

where ρ_0 is the ellipsometric ratio of the ambient/substrate interface and can be calculated with Fresnel's reflection coefficients[40], and ρ' (defined following **Equation 2.4**) is a coefficient defined by the refractive indices of the air and the subphase, n_1 and n_2, respectively, and the incident and transmission angles, α_{inc} and α_{tra}, respectively.

$$\rho' = -2 \times \frac{n_1}{{n_2}^2 - {n_1}^2} \times \frac{\sin^2\alpha_{inc} \times \cos\alpha_{inc}}{\cos^2(\alpha_{inc} - \alpha_{tra})} \times \frac{({n_F}^2 - {n_1}^2) \times ({n_F}^2 - {n_2}^2)}{{n_F}^2} \qquad \textbf{2.4}$$

As previously reported by Drude[40,41], the thin-film approximation is invoked: since the thickness of the film (lipid monolayer) is very small (below the tens of nanometer range) , the terms of a higher order than the first are negligible (in **Equation 2.3**). Therefore, the reported equations can be used to calculate the values of Δ and Ψ, for given values of n_F and t_F. Moreover, from each (n_F, t_F) couple, the surface excess (Γ) of the molecules composing the film (*i.e.*, the number of lipid molecules per unit of area in the case of lipid monolayers) can be determined by applying the de Feijter equation[42], reported in **Equation 2.5**:

$$\Gamma = \frac{t_F(n_F - n_{bulk})}{dn/dc} \qquad \textbf{2.5}$$

where dn/dc is the refractive index increment and n_{bulk} is the refractive index of the bulk phase (usually water, for which n_{bulk}=1.335).

2.1.3. Brewster angle microscopy (BAM)

BAM is an imaging technique used to reveal lateral inhomogeneities of biomembrane systems at the air/water interface. When p-polarized laser light is directed to such interfaces at the Brewster angle (θ_B=53.1° for water), the reflected light is negligible. The Brewster angle is defined following the so called Brewster's law (**Equation 2.6**):

$$\theta_B = \arctan\left(\frac{n_2}{n_1}\right) \qquad \textbf{2.6}$$

where n_1 is the refractive index of the initial medium through which the light propagates (*i.e.*, air, n_1=1), and n_2 is the index of the medium on the interface of which the film is deposited (*i.e.*, water n_1≈1.33). Thus, any change in the interfacial refractive index, due to the presence of a surface film, will induce light reflection which can be detected by a CCD camera that provides real-time images of the interface (**Figure 2.1**). Moreover, spatial reflectivity modulations are correlated with optically different monolayer phases depending on lateral ordering and/or lipid packing density. Thus, BAM allows the visualization of domains of lipids characterized by a different local

refractive index. BAM imaging has been extensively used to study morphological features of lipid monolayers[43] or, in general, films at the air/liquid interface of amphiphilic molecules[44], proteins, DNA, drugs or nanoparticles[45], as well as investigating the binding processes involving peptides and proteins[2,46–50]. Finally, BAM images also prove the ability of peptides and proteins to interact with monolayers and influence the lipid lateral organization through a fluidizing effect[12].

2.1.4. Quartz-crystal microbalance with dissipation monitoring (QCM-D)

QCM-D is an essential technique to characterize solid supported lipid bilayers, investigating their viscoelastic properties, as well as to probe the protein-bilayer interaction with a very high sensitivity[2,51]. It relies on the deposition and consecutive fusion of SUVs onto a silicon oxide layer coated-quartz crystal (**Figure 2.2**), whose piezoelectric properties make it oscillate at a characteristic resonance frequency in response to an oscillating electric field. Thus, the deposition of SUVs change the resonance frequency (f) of the systems, and the obtained shift (Δf) is proportional to the deposited mass[52]. Besides, QCM-D allows measuring the energy dissipation (D), which is inversely proportional to the decay time constant[53,54]. However, viscoelastic films at the solid/liquid interface, as lipid bilayers, can dissipate a significant amount of energy, hence producing a shift in the dissipation factor during quartz crystal oscillation, $\Delta D=E_{dissipated}/E_{stored}$, with $E_{dissipated}$ and E_{stored} representing the dissipated and stored energies, respectively. Thus, the measure of the changes in both f and D obtained when lipids are deposited onto the crystal surface permits the determination of the mass as well as the viscoelastic properties of the film. In the simplest case involving the formation of a rigid bilayer (*i.e.*, $\Delta D\approx 0$), the Sauerbrey equation can be used to analyse the data of Δf and ΔD recorded over time. However, the latter only gives information regarding the amount of mass adsorbed on the crystal and is valid when the bilayer is laterally homogeneous and rigid. Generally, it is used when $^{\Delta D}/_{\Delta f} < 0.1 \cdot 10^{-6}\mathrm{Hz}^{-1}$, and it becomes inaccurate for $^{\Delta D}/_{\Delta f} > 0.1 \cdot 10^{-6}\mathrm{Hz}^{-1}$, which is an indication of a softer film[51]. Indeed, in the latter case, the Sauerbrey equation would provide with an underestimation of the mass deposited on the crystal[55]. The Voigt-Voinova viscoelastic model[54] should be used in these cases. The latter, which describes the bilayer as a solid undergoing reversible viscoelastic strain (*i.e.*, a viscoelastic material that conserve its shape and does not flow)[56,57], provides not only the exact mass adsorbed on the crystal, but also information regarding the viscoelasticity, shear modulus and density of the film deposited on the quartz crystal. Indeed, since the mechanical properties of

viscoelastic materials are related to energy storage and dissipation processes, the introduction of parameters such as shear viscosity and shear elasticity modulus helps in the description of viscoelastic material properties. In the Voigt-Voinova model, the viscoelastic element is described by a complex shear modulus: the real part (storage modulus) is independent of frequency, while the imaginary one (loss modulus) increases linearly with frequency[57]. In particular, considering a homogenous film with a uniform thickness surrounded by a semi-infinite Newtonian fluid (*i.e.*, a fluid whose stress response against rate of strain is linear, like water), and assuming no-slip conditions (relying on the strong coupling between the solid support and the lipid bilayer[58]), the complex shear modulus (G) of the adsorbed layer can be described by **Equation 2.7**:

$$\mathrm{G} = \mathrm{G}' + \mathrm{i}\mathrm{G}'' = \mu_f + \mathrm{i}2\pi\mathrm{f}\eta_f = \mu_f(1 + \mathrm{i}2\pi\mathrm{f}\tau_f) \qquad \textbf{2.7}$$

where G' is the storage modulus, G'' is the loss modulus, μ_f is the elastic shear modulus, η_f is the shear viscosity, $\tau_f = {\eta_f}/{\mu_f}$ is the characteristic relaxation time of the film. Then, Δf and ΔD can be given by **Equations 2.8** and **2.9**, respectively:

$$\Delta\mathrm{f} = \mathrm{Im}\left(\frac{\beta'}{2\pi\rho_q \mathrm{l}_q}\right) \qquad \textbf{2.8}$$

$$\Delta\mathrm{D} = -\mathrm{Re}\left(\frac{\beta'}{\pi\mathrm{f}\rho_q \mathrm{l}_q}\right) \qquad \textbf{2.9}$$

with $\beta' = \xi_1\left(\frac{2\pi\mathrm{f}\eta_f - \mathrm{i}\mu_f}{2\pi\mathrm{f}}\right)\left(\frac{1-\alpha'\exp(2\xi_1 \mathrm{h}_f)}{1+\alpha'\exp(2\xi_1 \mathrm{h}_f)}\right)$, $\alpha' = \left(\frac{\xi_1(2\pi\mathrm{f}\eta_f - \mathrm{i}\mu_f)}{\xi_2 2\pi\mathrm{f}\eta_f} + 1\right)\Big/\left(\frac{\xi_1(2\pi\mathrm{f}\eta_f - \mathrm{i}\mu_f)}{\xi_2 2\pi\mathrm{f}\eta_f} - 1\right)$, $\xi_1 = \sqrt{-\frac{(2\pi\mathrm{f}^2)\rho_f}{\mu_f + \mathrm{i}2\pi\eta_f}}$, and $\xi_2 = \sqrt{\mathrm{i}\frac{2\pi\mathrm{f}\rho_f}{\eta_l}}$, where ρ_f and h_f are the density and the thickness of the adsorbed film, respectively. Thus, the hydrodynamic thickness (h_f), the shear viscosity (η_f), and the shear modulus (μ_f) can be obtained by fitting the changes of Δf and ΔD at different overtones[54,59]. The subscripts *q*, *l* and *f* refer to the quartz crystal, the bulk liquid and the film, respectively.

2.1.5. Dynamic light scattering (DLS)

DLS experiments relies on the measurement of the normalized intensity or (second-order) autocorrelation function, $g^{(2)}(\mathbf{q},\mathrm{t})$, which can be related to the first-order autocorrelation function, $g^{(1)}(\mathbf{q},\mathrm{t})$, through the Siegert relationship[60], reported in **Equation 2.10**:

$$\mathrm{g}^{(2)}(\mathbf{q},\mathrm{t}) - 1 = \beta\left|\mathrm{g}^{(1)}(\mathbf{q},\mathrm{t})\right|^2 \qquad \textbf{2.10}$$

where t is the time, $q = \left(\frac{4\pi n}{\lambda}\right) \sin\left(\frac{\theta}{2}\right)$ is the scattering wave vector, and n the solution refractive index. β is an optical coherence factor, which commonly assumes values close to 1, except for systems characterized by a low intensity of the scattered light as result of small size of the scatters, low concentration or poor refractive index contrast between the scatters and the solvent. For scatters diffusing following a Brownian motion, it is possible to define the time evolution of the first-order autocorrelation function as an exponential decay (**Equation 2.11**):

$$g^{(1)}(\mathbf{q}, t) = \exp(-t/\tau) = \exp(-\mathcal{D}\mathbf{q}^2 t) \qquad \textbf{2.11}$$

with the characteristic decay time τ being directly related to the diffusion coefficient, $\mathcal{D}$. Assuming the intrinsic sample polydispersity, it should be considered that both the characteristic decay time and the diffusion coefficient are averaged magnitudes. For spherical Brownian scatters diffusing in a Newtonian medium, it is possible to correlate the diffusion coefficient with an apparent hydrodynamic radius of the scattering particles, R_h^{app}, using the Stokes-Einstein relationship (**Equation 2.12**):

$$\mathcal{D} = \frac{k_B T}{6\pi\eta R_h^{app}} \qquad \textbf{2.12}$$

with k_B being the Boltzmann constant, T the absolute temperature and η the shear viscosity of the solvent. Thus, this techniques provides information regarding sample size and eventual aggregation.

2.1.6. Circular dichroism (CD)

CD is an absorption spectroscopy method based on the differential absorption of left and right circularly polarized light. In fact, optically active molecules with a defined chirality or dissymmetry, such as folded proteins, preferentially absorb one of the two directions of the circularly polarized light. CD is defined as the difference in the absorption (A) of left- and right-handed circularly polarized light, following **Equation 2.13**:

$$CD = \Delta A_L - \Delta A_R \qquad \textbf{2.13}$$

where λ is the wavelength and the subscripts L and R stand for left and right, respectively. Thus, the Lambert-Beer law can be re-written as (**Equation 2.14**):

$$A = \Delta\varepsilon \cdot c \cdot l \qquad \textbf{2.14}$$

where the difference in molar absorptivity ($\Delta\varepsilon=\varepsilon_L-\varepsilon_R$) is known as the molar circular dichroism. The latter depends on the wavelength and on the absorbing molecule conformation, which makes

it a function of concentration, temperature, and chemical environment. This differential absorption results in an elliptically polarized radiation that emerges from the sample. A CD spectrum is often reported in degrees of ellipticity, θ, which is a measure of the ellipticity of the polarization given by **Equation 2.15**:

$$\tan\theta = \frac{E_L - E_R}{E_L + E_R} \qquad \textbf{2.15}$$

where E is the magnitude of the electric field vector. However, to remove the dependence on concentration and path length, CD spectra are usually reported in molar ellipticity [θ] (**Equation 2.16**):

$$[\theta] = \frac{100 \cdot \theta}{c \cdot l} \qquad \textbf{2.16}$$

whose historical units are $deg{\cdot}cm^{2}{\cdot}dmol^{-1}$. From the shape of a CD spectrum, information about protein secondary structure could be obtained, identifying, for example, the amount of α-helixes, β-sheets and random coil sections.

2.2. Neutron scattering techniques

Neutrons are particularly well suited for the study of soft and biological matter since they allow measurements at room-temperature and their wavelengths are similar to atomic spacings, thus able to provide structural information from the picometer to the hundreds micrometer range. Being neutral particles, they are highly penetrating and non-destructive, thus allowing work in physiological conditions. Furthermore, neutrons interact with the nuclei and they are very sensitive even to light atoms, such as Hydrogen. In particular, they interact very differently with hydrogen (^{1}H) and deuterium (^{2}H or D) nuclei. This effect is particularly exploited in neutron techniques, by substituting the two atoms (isotopic substitution), which allows underlining or hiding the signal originated from certain regions of the sample, and therefore highlighting structural and chemical differences in specific regions of interest.

Both neutron techniques used in this PhD thesis (*i.e.*, reflectometry and small-angle scattering) are based on the elastic interaction between the nuclear radiation and the sample. Thus, there is no energy change of the neutron radiation after interaction with the nuclei, and only scattering events are considered. Hence, taking into account that the size of the sample is much smaller than both the distances neutron source-sample and sample-detector, the wave field incident on the sample can be seen as a plane wave (Fraunhofer approximation), described by a wave vector

$\mathbf{k}$ ($|\mathbf{k}|=k=\frac{2\pi}{\lambda}$), whose direction indicates the direction of propagation. Thus, the scattering vector (also known as momentum transfer) can be defined following **Equation 2.17**:

$$\mathbf{Q} = \mathbf{k}' - \mathbf{k} \qquad \textbf{2.17}$$

whose magnitude is (**Equation 2.18**):

$$|\mathbf{Q}| = Q = \frac{4\pi}{\lambda}\sin\theta \qquad \textbf{2.18}$$

where $\mathbf{k}$ and $\mathbf{k}'$are the wave vectors of the incident and scattered radiation, respectively, λ is the wavelength of the neutrons and θ refers to the scattering angle.

A scattering experiment comprises the measurement of the intensity distribution (I) of the scattered radiation as a function of the scattering vector ($\mathbf{Q}$). The scattered intensity is proportional to the so called cross section (σ), which indicates the number of particles (neutrons) that are scattered per second, per unit of solid angle (Ω) and in a defined energy interval. However, since elastic scattering is considered and taking into account all the scattered neutrons that reach the detector (constant scattering solid angle of the detector), the total scattering cross section could be defined that is a measure of the total scattering probability, independent of changes in energy and scattering angle (**Equation 2.19**):

$$\sigma = \int_0^{4\pi} \frac{d\sigma}{d\Omega}\, d\Omega \qquad \textbf{2.19}$$

The latter is connected to the arrangement of the atoms in the sample. However, the output of a scattering experiment is simply the intensity distribution of the scattered radiation. Thus, the relationship between scattered intensity and sample structure needs to be described. This description results simpler when the Born approximation (also called “kinematic scattering theory”) is taken into account. It neglects refraction and attenuation of the beam (due to scattering events), as well as the existence of multiple scattering events. Thus, the total scattering amplitude ($A(\mathbf{Q})$) is given by the superimposition of scattering from all points within the sample, following **Equation 2.20**:

$$A(\mathbf{Q}) \approx A_0 \cdot \int_V V(\mathbf{r}) \cdot e^{i\mathbf{Q}\cdot\mathbf{r}} d^3r \qquad \textbf{2.20}$$

where A_0 is the amplitude of the incident wave, $V(\mathbf{r})$ is the interaction potential, $\mathbf{r}$ indicates the position of the scattering particles, and the product $\mathbf{Q}\cdot\mathbf{r}$ denotes the phase shift that occurs during scattering. The specification of $V(\mathbf{r})$ helps in the description of the interaction between sample and

radiation. For the neutron wavelengths used in this PhD thesis (3Å≤λ≤25Å) the Fermi-pseudo-potential can be used (**Equation 2.21**), which implies that the nuclei are seen as point-like scatters, thus the scatter is Q-independent. This approximation relies on the consideration that the neutron wavelengths are much larger than the nuclear radii.

$$V(\mathbf{r}) = \frac{2\pi\hbar^2}{m} b\delta(\mathbf{r}) \qquad \textbf{2.21}$$

where b, which is called "scattering length", is a phenomenological quantity describing the strength of the interaction potential. Indeed, the total cross section of a given nucleus can be described as $\sigma = 4\pi b^2$ and corresponds to the surface area of a sphere with radius b. The scattering length is different for each isotopes and also depends on the nuclear spin state. It usually adopts positive values, but could also be negative, indicating a phase shift of 180° during the scattering process. A blatant example of the dependence of b on the nuclear structure, is the case of the proton (^{1}H nucleus) against the deuterium nucleus. Indeed, the respective value of the scattering lengths are -3.74 fm and 6.67 fm. This is at the base of the so called contrast variation methods: it is indeed possible to exchange ^{1}H with ^{2}H in the sample to highlight the chemical structure with neutron scattering experiments, as well as investigate the same system but in different environment changing the ^{1}H percentage (as for example using different percentage of H_2O and D_2O), thus obtaining different intensity profiles for the same system. However, although b is a characteristic of each nucleus, techniques such as NR and SANS, exploited in this PhD thesis, do not allow distinguishing the exact position of each nucleus in the sample, with atomic precision, rather the molecules are characterized by a defined scattering length density (SLD), *i.e.*, the sum of the scattering length of all atoms (j) composing the molecule normalized with respect to the molecular volume (V_m), following **Equation 2.22**.

$$SLD = \frac{1}{V_m}\sum_j b_j \qquad \textbf{2.22}$$

The SLD can be seen as a measure of how well a molecule (or part of it) can scatter neutrons. Hence, the interaction potential can be rewritten following **Equation 2.23**:

$$V(\mathbf{r}) = \frac{2\pi\hbar^2}{m} SLD\delta(\mathbf{r} - \mathbf{R}) \qquad \textbf{2.23}$$

However, as already explained, only the scattered intensity ($I(\mathbf{Q}) \approx |A(\mathbf{Q})|^2$) can be measured from a scattering experiment. Thus, the phase information is lost, and the deduction of the potential $V(\mathbf{r})$, using a Fourier transform, is no longer possible. This is the so called "phase loss problem",

which is overcome by defining models in order to fit the data. Indeed, a molecular model representing the system under study can be defined from scratch (or starting from known information), which is used to interpreted the intensity distribution obtained from the scattering experiment.

2.2.1. Neutron reflectometry (NR)

NR experiments reported in this PhD thesis were performed at the horizontal reflectometer FIGARO[61] and at the vertical reflectometer D17[62,63], at the Institut Laue-Langevin (Grenoble). For both cases, and for every planar membranes under study (both mono- and bilayer of lipids), grazing angles of incidence of the neutron beam impinging on the sample are exploited and specular reflection is taken into account, *i.e.*, the angle of incidence (θ_i) between the neutron beam and the interface is equal to the angle between the reflected neutron beam and the interface (θ_r). In this case, the momentum transfer vector **Q**, defined in **Equations 2.17** and **2.18** (with **k** and **k′** being the wave vector of the incoming and reflected neutron beams, respectively), only possesses a component in the direction normal to the plane of the interface (z). Furthermore, considering a neutron beam impinging on an interface between two media with different SLD (**Figure 2.5**), total reflection is observed for certain values of SLD and angles of incidence, smaller than a defined critical angle.

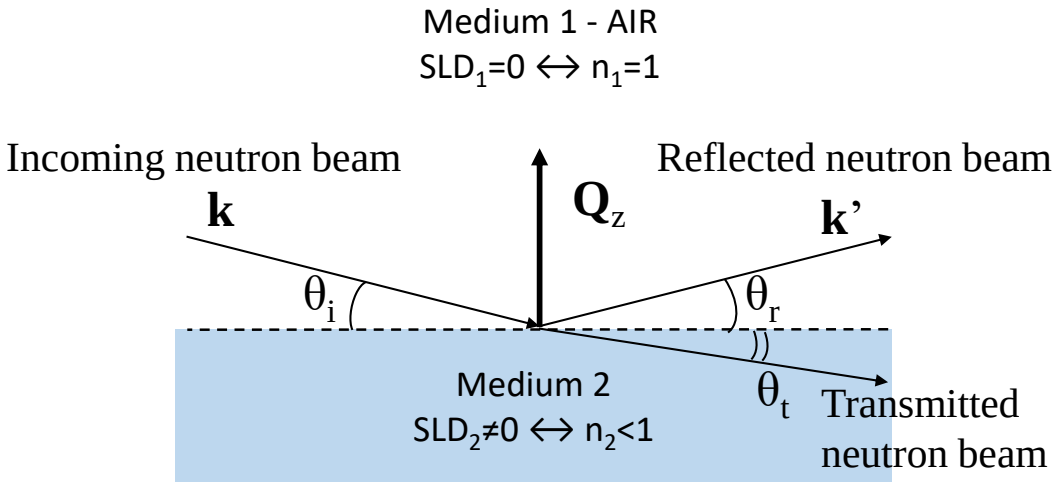

Figure 2.5 Example of a reflectometry experiment. Reflected and transmitted (with an angle of θ_t) neutron beam from a bare interface is shown.

This phenomenon can be understood by taking into account the relation between the SLD and the refractive index of a medium, which is explained by **Equation 2.24**:

$$n \approx 1 - \frac{\lambda^2}{2\pi} SLD \qquad \textbf{2.24}$$

In the case of air (SLD=0) n=1. Otherwise, a medium with SLD≠0 is characterised by a refractive index n<1. The value of the critical angle can be calculated by invoking Snell's law of refraction ($\cos\theta_c = n$, where n is the refractive index of the medium on which the neutron beam is reflected, coming from vacuum), and taking into account that $(\cos\theta)^2 = 1 - (\sin\theta)^2$, a critical angle ($\theta_c$) value can be calculated following **Equation 2.25**:

$$\theta_c \approx \lambda \sqrt{\frac{SLD}{\pi}} \qquad \textbf{2.25}$$

However, **Equation 2.25** applies to an incoming neutron beam in vacuum (n=0). In the case of a neutron beam coming from medium 1 ($n_1 \neq 0$) and being reflected from an interface defined by medium 1/medium 2, **Equation 2.25** can be rewritten as follows (**Equation 2.26**):

$$\theta_c = \approx \lambda \sqrt{\frac{\Delta SLD}{\pi}} \qquad \textbf{2.26}$$

where the quantity $\Delta SLD = SLD_2 - SLD_1$, called "contrast", is simply the difference between the SLD of the two media. Thus, for a given interface, defined by two media whose contrast is ΔSLD, for every incident angle $\theta < \theta_c$ total external reflection is observed. A blatant example of this is the reflection of a neutron beam coming from air (SLD=0) and impinging on an air/D_2O (SLD=$6.36 \cdot 10^{-6}$ Å^{-2}) interface. It is worth mentioning the dependence of θ_c on the neutron wavelength λ, since, in the case of the NR experiments presented here, the neutron beam exploited was polychromatic and only a discrete number of incident angles were used.

In the case of multi-layer interfaces, interference effects can arise from the reflection of the neutron beam at each interface, thus modulating the intensity profile. Moreover, the distance between such interfaces (*i.e.*, the thickness of the layers defining the interfaces) is strictly correlated with the interference phenomena in the Q_z space, producing fringes in the reflectivity (R) profiles, which are called "Kiessig fringes" (**Figure 2.6**). In particular, the optical path difference (d) between a beam that has been reflected from the first interface and a beam that has

been transmitted and then reflected from the second interface, can be calculated as follows (**Equation 2.27**):

$$d = 2t \sin \theta_i \qquad \textbf{2.27}$$

with t being the layer thickness and θ_i the incident angle. Taking into account that θ_i is a grazing angle (thus it is valid the approximation $\sin \theta \approx \theta$), and considering the cases in which Δ differs by one wavelength ($d = \lambda$), the following relationship between Q_z and t is obtained (**Equation 2.28**):

$$\Delta Q \approx \frac{2\pi}{t} \qquad \textbf{2.28}$$

where ΔQ indicated the distance between two interference maxima.

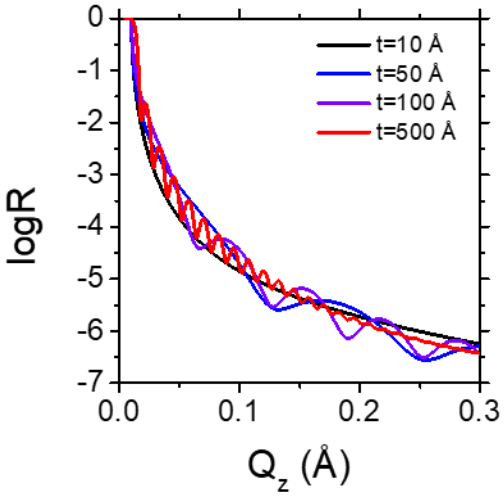

Figure 2.6 Simulated reflectivity profiles of a silicon oxide layer of various thickness on a silicon substrate. The Kiessig fringes are visible when t=50, 100 and 500Å.

Once obtained a profile of intensity distribution of the reflected radiation (*i.e.*, a reflectivity profile), which is normalized with respect to the incoming radiation and plotted against Q_z, and since the information about the phase is lost, a model has to be built to interpret the reflectivity data. Such model consists of multi-layers of constant SLD (which is in-plane averaged taking into account the different molecules present in the layer), whose reflectivity is calculated using the Parratt's recursive method[64] and compared to the experimental data. However, real interfaces are characterized by a finite roughness, whose minimum value depends on the capillary waves of the subphase[65,66]. Therefore, the change in SLD along the z-axis of a real interface has to be described by the SLD profile of the ideal interface (no roughness) modulated by an error function, ERF, which is defined by **Equation 2.29**[67]:

$$\mathrm{ERF}\left(\frac{z - z_0}{r/\sqrt{2}}\right) = \frac{2}{\sqrt{\pi}} \int_0^{\frac{z-z_0}{r/\sqrt{2}}} e^{-t^2} dt \qquad \textbf{2.29}$$

where z_0 and r indicate the position and the roughness, respectively, of the interface between the layers.

Finally, the same system is usually measured in different conditions, exploiting the contrast variation. Hence, using mixtures of H_2O and D_2O in various percentages, bulk phases with different SLD are obtained. As a consequence, several reflectivity curves can be measured from the same system, and interpreted together with the same molecular model (tuning the layers SLD accordingly). Indeed data analysis is usually performed by co-refinement of all data sets obtained, thus reducing the ambiguity in the modelling. In this PhD thesis, AuroreNR[68], Motofit[69] and Refnx[70] software were exploited to perform data analysis. To conclude, NR provides information along the z-axis of the planar membrane (direction perpendicular to the plane of the membrane) regarding thickness and composition of each layer present at the interface. In particular, in the case of planar membranes, the models used to interpret the data are usually made of layers composed by lipid headgroups and layers of hydrophobic tails. Constraints were used to ensure the same number of tails moiety and headgroups, *i.e.*, ensuring the same area per molecule (A) of tails and headgroups, following **Equation 2.30**:

$$A_i = \frac{\Sigma b_i}{SLD_i \cdot t_i \cdot (1 - f_{wi})} \qquad \textbf{2.30}$$

where SLD_i, t_i, Σb_i and f_{wi} are, respectively, the scattering length density, the thickness, the total scattering length and the water volume fraction of the *i*-th layer (tails or headgroups). Besides, upon protein binding, the interaction of the protein as well as its insertion in the membrane, and its influence on the membrane stability, could be probed with NR.

NR has been a key technique of this PhD thesis, allowing to unravel the structure of planar membranes in the direction perpendicular to the membrane plane, as well as to obtain structural information about proteins upon lipid binding. Each chapter reported in this manuscript recalls the basic principles of this technique, particularly explaining the data modelling.

2.2.2. Small-angle neutron scattering (SANS)

SANS measurements reported in this PhD thesis were carried out on D11[71], at the Institut Laue-Langevin (Grenoble). SANS probes the shape, the spatial distribution and the interactions between solute particles by detecting the neutrons scattered by the sample as a function of

momentum transfer (**Q**). This technique also provides information about the internal structure of the studied systems. Indeed the differential scattering cross section of a SANS experiment[72,73] (expressed in **Equation 2.31**) contains a form factor ($P(\mathbf{Q})$) component that accounts for the particle internal structure, and a structure factor[74] ($S(\mathbf{Q})$) that gives information regarding the inter-particle interactions in solution.

$$\frac{d\sigma}{d\Omega}(\mathbf{Q}) = n(\Delta SLD)^2 V_{part}^2 P(\mathbf{Q}) S(\mathbf{Q}) \qquad \textbf{2.31}$$

where n is the particle number density, ΔSLD is the contrast between the solvent and the particles, and V_{part} is the volume of a single particle. From a SANS profile, information on different length scales can be obtained. In particular, in the low-Q region (Guinier region), the relation $I(Q)/Q^{-D}$ can be used, where the fractal dimension *D* of the system provides structural information on the system in question[74–76]. Hence, the overall size of the scattering particles can be calculated, by determining the so called Guinier radius. From the slope of the I(Q) profile in the mid-Q region, it is possible to deduce the shape of the scattering particles. Finally, the high-Q region (Porod region) provides information about the small length scales. In the case of liposomes, the thickness of the bilayer can be obtained. Finally, from the slope of the curve in the high-Q region, the Porod volume of the scattering particles can be determined. This is usually compared with the hypothesized volume (calculated from the overall size obtained from the Guinier region), to get additional structural information. For example, the comparison between the Porod volume and the volume calculated taking into account the overall liposome size provides information about eventual multilamellarity of the vesicles. For the analysis of the SANS data recorded in this PhD thesis, SASfit[77,78] and SasView Version 5.0.4[79] software were used. The former was employed to determine the Guinier radius and the Porod volume, and the latter to build an appropriate model used to fit the experimental data.

References

1. Rojewska M, Smułek W, Kaczorek E, Prochaska K. Langmuir Monolayer Techniques for the Investigation of Model Bacterial Membranes and Antibiotic Biodegradation Mechanisms. *Membr 2021, Vol 11, Page 707*. 2021;11(9):707. doi:10.3390/MEMBRANES11090707

2. Clifton LA, Campbell RA, Sebastiani F, et al. Design and use of model membranes to study biomolecular interactions using complementary surface-sensitive techniques. *Adv Colloid Interface Sci*. 2020;277. doi:10.1016/j.cis.2020.102118

3. Kaganer VM, Möhwald H, Dutta P. Structure and phase transitions in Langmuir monolayers. *Rev Mod Phys*. 1999;71(3):779-819. doi:10.1103/RevModPhys.71.779

4. Maestro A, Gutfreund P. In situ determination of the structure and composition of Langmuir monolayers at the air/water interface by neutron and X-ray reflectivity and ellipsometry. *Adv Colloid Interface Sci*. 2021;293:102434. doi:10.1016/j.cis.2021.102434

5. Bertsch P, Bergfreund J, Windhab EJ, Fischer P. Physiological fluid interfaces: Functional microenvironments, drug delivery targets, and first line of defense. *Acta Biomater*. 2021;130:32-53. doi:10.1016/j.actbio.2021.05.051

6. Ortiz-Collazos S, Picciani PHS, Oliveira ON, Pimentel AS, Edler KJ. Influence of levofloxacin and clarithromycin on the structure of DPPC monolayers. *Biochim Biophys Acta - Biomembr*. 2019;1861(10):182994. doi:10.1016/j.bbamem.2019.05.016

7. Guzmán E, Santini E. Lung surfactant-particles at fluid interfaces for toxicity assessments. *Curr Opin Colloid Interface Sci*. 2019;39:24-39. doi:10.1016/j.cocis.2019.01.003

8. Ravera F, Miller R, Zuo YY, et al. Methods and models to investigate the physicochemical functionality of pulmonary surfactant. *Curr Opin Colloid Interface Sci*. 2021;55:101467. doi:10.1016/j.cocis.2021.101467

9. Ciumac D, Gong H, Campbell RA, Campana M, Xu H, Lu JR. Structural elucidation upon binding of antimicrobial peptides into binary mixed lipid monolayers mimicking bacterial membranes. *J Colloid Interface Sci*. 2021;598:193-205. doi:10.1016/j.jcis.2021.04.037

10. Gong H, Hu X, Liao M, et al. Structural Disruptions of the Outer Membranes of Gram-Negative Bacteria by Rationally Designed Amphiphilic Antimicrobial Peptides. *ACS Appl Mater Interfaces*. 2021;13(14):16062-16074. doi:10.1021/ACSAMI.1C01643/ASSET/IMAGES/LARGE/AM1C01643_0006.JPEG

11. Gong H, Sani MA, Hu X, et al. How do Self-Assembling Antimicrobial Lipopeptides Kill Bacteria? *ACS Appl Mater Interfaces*. 2020;12(50):55675-55687. doi:10.1021/ACSAMI.0C17222/ASSET/IMAGES/LARGE/AM0C17222_0007.JPEG

12. Santamaria A, Batchu KC, Matsarskaia O, et al. Strikingly Different Roles of SARS-CoV-2 Fusion Peptides Uncovered by Neutron Scattering. *J Am Chem Soc*. 2022. doi:10.1021/jacs.1c09856

13. Bartkowiak A, Rojewska M, Prochaska K. Study of mucin interaction with model phospholipid membrane at the air–water interface. *Colloids Surfaces A Physicochem Eng Asp*. 2019;578(March):123587. doi:10.1016/j.colsurfa.2019.123587

14. Ege C, Lee KYC. Insertion of Alzheimer's Aβ40 peptide into lipid monolayers. *Biophys J*. 2004;87(3):1732-1740. doi:10.1529/biophysj.104.043265

15. Lind TK, Cárdenas M. Understanding the formation of supported lipid bilayers via vesicle fusion—A case that exemplifies the need for the complementary method approach (Review). *Biointerphases*. 2016;11(2):020801. doi:10.1116/1.4944830

16. Lind TK, Wacklin H, Schiller J, et al. Formation and Characterization of Supported Lipid Bilayers Composed of Hydrogenated and Deuterated Escherichia coli Lipids. *PLoS One*. 2015;10(12):e0144671. doi:10.1371/JOURNAL.PONE.0144671

17. Åkesson A, Lind T, Ehrlich N, Stamou D, Wacklin H, Cárdenas M. Composition and structure of mixed phospholipid supported bilayers formed by POPC and DPPC. *Soft Matter*. 2012;8(20):5658-5665. doi:10.1039/c2sm00013j

18. Cho NJ, Frank CW, Kasemo B, Höök F. Quartz crystal microbalance with dissipation monitoring of supported lipid bilayers on various substrates. *Nat Protoc*. 2010;5(6):1096-1106. doi:10.1038/nprot.2010.65

19. Richter RP, Bérat R, Brisson AR. Formation of solid-supported lipid bilayers: An

integrated view. *Langmuir*. 2006;22(8):3497-3505. doi:10.1021/la052687c

20. Macháň R, Hof M. Lipid diffusion in planar membranes investigated by fluorescence correlation spectroscopy. *Biochim Biophys Acta - Biomembr*. 2010;1798(7):1377-1391. doi:10.1016/J.BBAMEM.2010.02.014

21. Wu HL, Tong Y, Peng Q, Li N, Ye S. Phase transition behaviors of the supported DPPC bilayer investigated by sum frequency generation (SFG) vibrational spectroscopy and atomic force microscopy (AFM). *Phys Chem Chem Phys*. 2016;18(3):1411-1421. doi:10.1039/C5CP04960A

22. Alessandrini A, Facci P. Phase transitions in supported lipid bilayers studied by AFM. *Soft Matter*. 2014;10(37):7145-7164. doi:10.1039/C4SM01104J

23. Monzel C, Sengupta K. Measuring shape fluctuations in biological membranes. *J Phys D Appl Phys*. 2016;49(24). doi:10.1088/0022-3727/49/24/243002

24. Walde P, Cosentino K, Engel H, Stano P. Giant Vesicles: Preparations and Applications. *ChemBioChem*. 2010;11(7):848-865. doi:10.1002/CBIC.201000010

25. Lapinski MM, Castro-Forero A, Greiner AJ, Ofoli RY, Blanchard GJ. Comparison of liposomes formed by sonication and extrusion: Rotational and translational diffusion of an embedded chromophore. *Langmuir*. 2007;23(23):11677-11683. doi:10.1021/LA7020963/ASSET/IMAGES/MEDIUM/LA7020963N00001.GIF

26. Miller SE, Mathiasen S, Bright NA, et al. CALM Regulates Clathrin-Coated Vesicle Size and Maturation by Directly Sensing and Driving Membrane Curvature. *Dev Cell*. 2015;33(2):163-175. doi:10.1016/j.devcel.2015.03.002

27. London E. Membrane Structure-Function Insights from Asymmetric Lipid Vesicles. *Acc Chem Res*. 2019;52(8):2382-2391. doi:10.1021/ACS.ACCOUNTS.9B00300/ASSET/IMAGES/MEDIUM/AR9B00300_0005.GIF

28. Marsh D. Lateral pressure in membranes. *Biochim Biophys Acta - Rev Biomembr*. 1996;1286(3):183-223. doi:10.1016/S0304-4157(96)00009-3

29. Arriaga LR, Löpez-Montero I, Ignés-Mullol J, Monroy F. Domain-growth kinetic origin of nonhorizontal phase coexistence plateaux in langmuir monolayers: Compression rigidity of a raft-like lipid distribution. *J Phys Chem B*. 2010;114(13):4509-4520. doi:10.1021/jp9118953

30. McConlogue CW, Vanderlick TK. A close look at domain formation in DPPC monolayers. *Langmuir*. 1997;13(26):7158-7164. doi:10.1021/LA970898E/ASSET/IMAGES/LARGE/LA970898EF00007.JPEG

31. Gershfeld NL, Pagano RE. The Condensing Effect of Cholesterol. A Critical Examination of Mixed-Film Studies. 1972;76(9):1244-1249.

32. Shah DO, Schulman JH. Influence of calcium, cholesterol, and unsaturation on lecithin monolayers. *J Lipid Res*. 1967;8(3):215-226. doi:10.1016/s0022-2275(20)40140-3

33. Müller-Landau F, Cadenhead DA. Molecular packing in steroid-lecithin monolayers, part II: Mixed films of cholesterol with dipalmitoylphosphatidylcholine and tetradecanoic acid. *Chem Phys Lipids*. 1979;25(3):315-328. doi:10.1016/0009-3084(79)90114-2

34. Chakraborty S, Doktorova M, Molugu TR, et al. How cholesterol stiffens unsaturated lipid membranes. *Proc Natl Acad Sci U S A*. 2020;117(36):21896-21905. doi:10.1073/pnas.2004807117

35. Almeida PFF. Thermodynamics of lipid interactions in complex bilayers. *Biochim Biophys Acta - Biomembr*. 2009;1788(1):72-85. doi:10.1016/j.bbamem.2008.08.007

36. Azzam RMA, Bashara NM. *Ellipsometry and Polarized Light*. New York: North-Holland Publishing Company; 1977.

37. Conn AR, Scheinberg K, Vicente LN. *Introduction to Derivative-Free Optimization*. Society for Industrial and Applied Mathematics; 2009. doi:10.1137/1.9780898718768

38. Dutta S. Trust-Region Methods. In: *Optimization in Chemical Engineering*. Cambridge: Cambridge University Press; 2016:74-85. doi:10.1017/CBO9781316134504.005

39. Yuan YX. Recent advances in trust region algorithms. *Math Program*. 2015;151(1):249-281. doi:10.1007/s10107-015-0893-2

40. Nestler P, Helm CA. Determination of refractive index and layer thickness of nm-thin films via ellipsometry. *Opt Express*. 2017;25(22):321-327.

41. Drude P. *The Theory of Optics*. Longmans, Green and Co.; 1902.

42. De Feijter JA, Benjamins J, Veer FA. Ellipsometry as a tool to study the adsorption behavior of synthetic and biopolymers at the air–water interface. *Biopolymers*. 1978;17(7):1759-1772. doi:10.1002/bip.1978.360170711

43. Wydro P, Flasiński M, Broniatowski M. Molecular organization of bacterial membrane lipids in mixed systems—A comprehensive monolayer study combined with Grazing Incidence X-ray Diffraction and Brewster Angle Microscopy experiments. *Biochim Biophys Acta - Biomembr*. 2012;1818(7):1745-1754. doi:10.1016/J.BBAMEM.2012.03.010

44. Campbell RA, Tummino A, Noskov BA, Varga I. Polyelectrolyte/surfactant films spread from neutral aggregates. *Soft Matter*. 2016;12(24):5304-5312. doi:10.1039/c6sm00637j

45. Daear W, Mahadeo M, Prenner EJ. Applications of Brewster angle microscopy from biological materials to biological systems. *Biochim Biophys Acta - Biomembr*. 2017;1859(10):1749-1766. doi:10.1016/j.bbamem.2017.06.016

46. Ciumac D, Campbell RA, Xu H, et al. Implications of lipid monolayer charge characteristics on their selective interactions with a short antimicrobial peptide. *Colloids Surfaces B Biointerfaces*. 2017;150:308-316. doi:10.1016/j.colsurfb.2016.10.043

47. Castano S, Desbat B. Structure and orientation study of fusion peptide FP23 of gp41 from HIV-1 alone or inserted into various lipid membrane models (mono-, bi- and multibi-layers) by FT-IR spectroscopies and Brewster angle microscopy. *Biochim Biophys Acta - Biomembr*. 2005;1715(2):81-95. doi:10.1016/J.BBAMEM.2005.07.008

48. Clifton LA, Sanders M, Kinane C, et al. The role of protein hydrophobicity in thionin–phospholipid interactions: a comparison of α1 and α2-purothionin adsorbed anionic phospholipid monolayers. *Phys Chem Chem Phys*. 2012;14(39):13569-13579. doi:10.1039/C2CP42029E

49. Foglia F, Fragneto G, Clifton LA, Lawrence MJ, Barlow DJ. Interaction of amphotericin

B with lipid monolayers. *Langmuir*. 2014;30(30):9147-9156. doi:10.1021/LA501835P/ASSET/IMAGES/LARGE/LA-2014-01835P_0004.JPEG

50. Alvares DS, Wilke N, Ruggiero Neto J, Fanani ML. The insertion of Polybia-MP1 peptide into phospholipid monolayers is regulated by its anionic nature and phase state. *Chem Phys Lipids*. 2017;207:38-48. doi:10.1016/J.CHEMPHYSLIP.2017.08.001

51. Nielsen SB, Otzen DE. Quartz Crystal Microbalances as Tools for Probing Protein–Membrane Interactions. *Methods Mol Biol*. 2013;974:1-21. doi:10.1007/978-1-62703-275-9_1

52. Sauerbrey G. The use of quarts oscillators for weighing thin layers and for microweighing. *Z Phys*. 1959;155(206). https://cir.nii.ac.jp/crid/1571417124278253824. Accessed May 25, 2022.

53. Rodahl M, Kasemo B. On the measurement of thin liquid overlayers with the quartz-crystal microbalance. *Sensors Actuators A Phys*. 1996;54(1-3):448-456. doi:10.1016/S0924-4247(97)80002-7

54. Voinova M V, Rodahl M, Jonson M, Kasemo B. Viscoelastic Acoustic Response of Layered Polymer Films at Fluid-Solid Interfaces: Continuum Mechanics Approach. *Phys Scr*. 1999;59(5):391-396. doi:10.1238/physica.regular.059a00391

55. Voinova M V., Jonson M, Kasemo B. “Missing mass” effect in biosensor’s QCM applications. *Biosens Bioelectron*. 2002;17(10):835-841. doi:10.1016/S0956-5663(02)00050-7

56. Ferry JD. *Viscoelastic Properties of Polymers*. 3rd ed. New York; 1980. https://books.google.fr/books?hl=fr&lr=&id=9dqQY3Ujsx4C&oi=fnd&pg=PA1&dq=Ferry,+J.+D.,+%60%60Viscoelastic+properties+of+polymers%27%27+(3rd+ed.+New+York+1980).&ots=FiB2UG_UJk&sig=a5DZ_awcURh9YJrNA6j-nhcSBGI&redir_esc=y#v=onepage&q=Ferry%2C J. D.%2C %60%60Viscoelastic properties of polymers’’ (3rd ed. New York 1980).&f=false. Accessed May 25, 2022.

57. Philippoff W. Relaxations in Polymer Solutions, Liquids, and Gels. *Phys Acoust*. 1965;2(PB):1-90. doi:10.1016/B978-0-12-395662-0.50011-4

58. Voinova M V., Jonson M, Kasemo B. Dynamics of viscous amphiphilic films supported by elastic solid substrates. *J Phys Condens Matter*. 1997;9(37):7799-7808. doi:10.1088/0953-8984/9/37/011

59. Liu G, Zhang G. *QCM-D Studies on Polymer Behavior at Interfaces*.; 2013. doi:10.1007/978-3-642-39790-5

60. Pecora R. *Dynamic Light Scattering - Applications of Photon Correlation Spectroscopy* . (Plenum Press NY and L, ed.).; 1985. doi:10.1002/BBPC.19870910455

61. Campbell RA, Wacklin HP, Sutton I, Cubitt R, Fragneto G. FIGARO: The new horizontal neutron reflectometer at the ILL. *Eur Phys J Plus*. 2011;126(11):1-22. doi:10.1140/epjp/i2011-11107-8

62. Cubitt R, Fragneto G. D17: the new reflectometer at the ILL. 2002;331:329-331.

63. Gutfreund P, Saerbeck T, Gonzalez MA, et al. Towards generalized data reduction on a chopperbased time-of-flight neutron reflectometer. *J Appl Crystallogr*. 2018. doi:10.1107/S160057671800448X

64. Parratt LG. Surface studies of solids by total reflection of x-rays. *Phys Rev*. 1954;95(2):359-369. doi:10.1103/PhysRev.95.359

65. Braslau A, Deutsch M, Pershan PS, Weiss AH, Als-Nielsen J, Bohr J. Surface roughness of water measured by x-ray reflectivity. *Phys Rev Lett*. 1985;54(2):114-117. doi:10.1103/PhysRevLett.54.114

66. Sinha SK, Sirota EB, Garoff S, Stanley HB. X-ray and neutron scattering from rough surfaces. *Phys Rev B*. 1988;38(4):2297-2311. doi:10.1103/PhysRevB.38.2297

67. Maranville BB, Green A, Kienzle PA. Distributed Error-Function Roughness in Refl1d Reflectometry Fitting Program. 2018;XXX(1):1-4.

68. Gerelli Y. Aurore: New software for neutron reflectivity data analysis. *J Appl Crystallogr*. 2016;49:330-339. doi:10.1107/S1600576716000108

69. Nelson A. Co-refinement of multiple-contrast neutron/X-ray reflectivity data using MOTOFIT. *J Appl Crystallogr*. 2006;39(2):273-276. doi:10.1107/S0021889806005073

70. Nelson ARJ, Prescott SW. Refnx: Neutron and X-ray reflectometry analysis in python. *J Appl Crystallogr*. 2019;52(1):193-200. doi:10.1107/S1600576718017296/RG5158SUP5.ZIP

71. Lindner P, Schweins R. The D11 Small-Angle Scattering Instrument: A New Benchmark for SANS. *https://doi.org/101080/10448631003697985*. 2010;21(2):15-18. doi:10.1080/10448631003697985

72. Pedersen JS. Analysis of small-angle scattering data from colloids and polymer solutions: modeling and least-squares fitting. *Adv Colloid Interface Sci*. 1997;70(1-3):171-210. doi:10.1016/S0001-8686(97)00312-6

73. Lindner P, Zemb T. *Neutron, X-Rays and Light. Scattering Methods Applied to Soft Condensed Matter - 1st Edition*. (Elsevier: Amsterdam, ed.). Boston; 2002. https://www.elsevier.com/books/neutron-x-rays-and-light-scattering-methods-applied-to-soft-condensed-matter/zemb/978-0-444-51122-5. Accessed May 6, 2022.

74. Guinier A, Walker CB, York N, Wiley J. Small-angle scattering of X-rays. 1955.

75. Teixeira J, IUCr. Small-angle scattering by fractal systems. *urn:issn:0021-8898*. 1988;21(6):781-785. doi:10.1107/S0021889888000263

76. Anitas EM. Small-Angle Scattering from Weakly Correlated Nanoscale Mass Fractal Aggregates. *Nanomater 2019, Vol 9, Page 648*. 2019;9(4):648. doi:10.3390/NANO9040648

77. Breßler I, Kohlbrecher J, Thünemann AF. SASfit: A tool for small-angle scattering data analysis using a library of analytical expressions. *J Appl Crystallogr*. 2015;48(5):1587-1598. doi:10.1107/S1600576715016544/VG5026SUP2.ZIP

78. Kohlbrecher J, Studer A. Transformation cycle between the spherically symmetric correlation function, projected correlation function and differential cross section as implemented in SASfit. *urn:issn:1600-5767*. 2017;50(5):1395-1403. doi:10.1107/S1600576717011979

79. Doucet M, et al. SasView Version 5.0.4. doi:http://doi.org/10.5281/zenodo.4467703

Chapter 3

Unravelling the orientation of the inositol-biphosphate ring and its dependence on PI(4,5)P_2 cluster formation in model membranes[a]

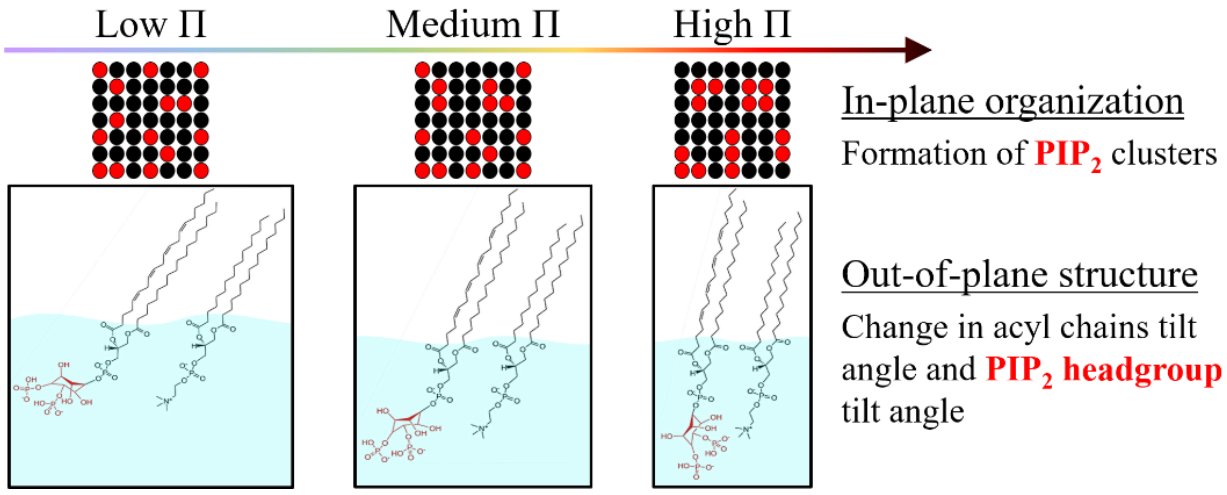

[a] This work has been submitted to the *Journal of colloids and interface science* (see the Publication List at page 279).

Abstract

Inositol phospholipids are responsible for the interaction and recruitment of proteins in different key biological processes like, for example, endocytosis. Importantly, they are well known to form clusters in the inner leaflet of cellular membranes. However, the correlation between the PIP_2 headgroup orientation with respect to the membrane and its lateral packing density, yielding transient clusters, has not been described yet. Therefore, given the paramount importance of PIP_2 clusters as docking sites in the membrane, we consider that the elucidation of the relation between lateral (in-plane) and perpendicular (out-of-plane) molecular organization of PIP_2 deserves further investigation. Here, we study phosphatidylinositol 4,5-bisphosphate (PIP_2) planar model membranes in the form of Langmuir monolayers by surface pressure-area isotherms, Brewster angle microscopy and neutron reflectometry. The lateral organization of the lipids was controlled through monolayer compression, to characterize lipid organization and structure at several values of area per lipid molecule. The multi-technique approach exploited here allowed us to correlate the formation of transient PIP_2 clusters (in-plane lipid organization) with the change in orientation of the inositol-biphosphate headgroup (out-of-plane structure). Moreover, the dependence of the latter on monolayer surface pressure was experimentally determined by neutron reflectometry.

1. Introduction

Despite inositol phospholipids (IPs) are scarcely present in eukaryotic cell membranes, their spatial assembly forming docking sites on the inner leaflet of membranes is crucial for the recruitment of specific proteins from the cytosol[1–3]. The organization of IPs in clusters is well rationalized due to their electrostatic interaction with intracellular divalent cations. Interestingly, recent experimental[4,5] and numerical[6] studies focused on phosphatidylinositol 4,5-bisphosphate (PI(4,5)P_2 or, hereinafter, PIP_2) have demonstrated that a purely electrostatic, multivalent ion-mediated mechanism is enough to induce PIP_2 clustering in biomimetic model membranes. The effects of divalent cations on the in-plane organization of PIP_2 containing membranes were previously studied by imaging, spectroscopy[5,7] and atomistic molecular dynamic simulations[6]. The existence of PIP_2 domains was attributed to the capacity of divalent cations, most predominantly Ca^{2+} and Mg^{2+}, to interact with PIP_2 headgroups and act as a bridge between PIP_2 molecules, yielding well-defined clusters. Nevertheless, the question of how the orientation of the PIP_2

headgroup with respect to the membrane correlates with its lateral packing density in presence of divalent cations was not addressed.

Since PIP_2 is the most abundant phosphoinositide in the plasma membrane inner leaflet of mammalian cells (~ 1-2% in mol)[3,8–10], recent research focused on its role in model membranes[7,11] as well as its interaction with proteins[10,12–14]. PIP_2 is characterized by a net negative electrostatic charge in the headgroup, as well as an acyl chain asymmetry with a high degree of unsaturation. Its phosphorylated inositol ring headgroup enables specific proteins to bind via electrostatic interaction, triggering or contributing to a plethora of important biological pathways, such as the attachment of the cytoskeleton to the plasma membrane, membrane trafficking, and ion channel and enzyme activation[3,8–10,15]. Moreover, since PIP_2 is characterized by a large headgroup to acyl chain ratio, it has an inverted conical shape, thereby favouring the bending of the membrane into a positive curvature, *i.e.* bending the monolayer away from the headgroups[16]. Such curvature is often sensed and aided by the presence of proteins, which can induce pits or tubules formation[13,17–19]. Since the key feature of all these molecular processes is the interaction with the inositol-biphosphate, unravelling the ring orientation in biological membranes prior to the presence of proteins is essential. Although molecular dynamic simulations of PIP_2 suggested a preferred tilt angle of ~40° [3,20,21], defined as the angle between the vector connecting C1 and C4 of the inositol-biphosphate ring and the membrane normal (See **Figure 3.1 B**), there is a lack of experimental validation. Previous *in vitro* studies focused primarily on the influence of PIPs on model membranes and not on determining preferred tilt angles[11,14,22].

Therefore, given the importance of PIP_2 docking sites, and the likely influence of preferred headgroup orientations on membrane-protein interactions, it is essential to elucidate the relation between lateral (in-plane) and perpendicular (out-of-plane) molecular organization of PIP_2. To this end, we designed a simple, *in vitro* model based on Langmuir monolayers composed of 30% in mol of PIP_2 and 70% in mol of a zwitterionic phospholipid (1,2-dipalmitoyl-sn-glycero-3-phosphocholine, DPPC). Although the overall PIP_2 concentration in the inner leaflet of the mammalian plasma membrane is much lower (~1% mol), this model reflects the high local concentration of the PIP_2 present at the docking sites on the cell membrane[23]. DPPC was chosen because its structure is well known to form stable monolayers and bears structural similarities to a large diversity of phospholipids in biological membranes. Indeed, Langmuir monolayers have been widely used to mimic cellular membranes *in vitro*[24–30]. The lipid monolayer configuration in a

Langmuir trough allows the *in situ* use of neutron reflectometry (NR), ellipsometry and Brewster angle microscopy (BAM). While the latter is used to visualize the in-plane interfacial organization of lipid monolayers, NR and ellipsometry can be exploited to obtain information about monolayer composition and structure in the direction perpendicular to the plane of the interface. In particular, NR is well suited for the structural study of planar biomimetic membranes with sub-nanometric resolution. Besides, as neutrons interact very differently with hydrogen and deuterium, it was possible to exploit isotopic substitution, using lipid with hydrogenous and deuterated aliphatic tails, to highlight structural differences in between the hydrophobic tails and the polar headgroups (including the associated water molecules) constituting DPPC:PIP_2 monolayers. These experiments were crucial for determining the tilt angle of the inositol-biphosphate ring and its dependence on the lipid surface pressure (Π) and area per molecule (A). Since membrane deformation is known to be modulated through membrane area/pressure changes, a broad range of surface pressures was explored through compression, allowing to find a correlation between the lateral PIP_2 distribution (which influences transient PIP_2 cluster formation), and the variation of the PIP_2 tilt angle.

2. Materials and methods

2.1. Materials

1,2-dipalmitoyl-sn-glycero-3-phosphocholine (h-DPPC), chain-deuterated DPPC (d62-DPPC) and brain L-α-phosphatidylinositol-4,5-bisphosphate (ammonium salt) PI(4,5)P_2 (PIP_2) were purchased as powder from Avanti Polar Lipids (purity >99%, Alabaster, AL, USA). **Figure S3.1** shows the lipid molecular structure. Solutions of 1 mg·mL^{-1} of h-DPPC, d62-DPPC and PIP_2 were prepared in chloroform stabilized with ethanol (purity 99.8%; Sigma-Aldrich, St. Louis, MO, USA). These solutions were used as stock solutions in order to prepare mixtures with the desired compositions, *i.e.*, h-DPPC:PIP_2 and d62-DPPC:PIP_2 7:3 molar ratio, at 0.1 mg·mL^{-1}. Ultra-pure water was generated by passing deionized water through a Milli-Q unit (total organic content = 4 ppb; resistivity = 18 mΩ·cm, Milli-Q, Merck KGaA, Darmstadt, Germany). D_2O (99.9% of isotopical purity) was purchased from Sigma-Aldrich and used as received. Experiments were performed in HKM buffer (25 mM HEPES pH 7.2, 125 mM potassium acetate, 5 mM magnesium acetate, 1 mM DTT). HEPES (in solution, 1 M in H_2O, and powder, purity 99.5%), potassium

acetate (purity≥99.0%), magnesium acetate (purity≥99.0%) and DTT (purity≥99.0%) were purchased from Sigma Aldrich.

2.2. Preparation of Langmuir lipid monolayers: surface pressure - area isotherm

The surface pressure (Π) - area per molecule (A) isotherms were measured using a Langmuir trough (KIBRON, Helsinki, Finland) with a maximum area of 166.4 cm^2. The trough was carefully cleaned with Decon90, ethanol and Milli-Q water before filling it with 120 mL of HKM buffer. Subsequently, the lipid solution with a concentration of 0.1 $mg \cdot mL^{-1}$ was spread on the clean subphase using a Hamilton microsyringe with a precision of ±1 µL. After the chloroform was evaporated for about 20 min, the variation of surface pressure during compression was recorded using a contact probe (paper Wilhelmy plate), at a barrier speed of 8 $cm^2 \cdot min^{-1}$. In all the experiments performed, the temperature of the subphase was maintained at 21.0 ± 0.5 °C.

2.3. Brewster angle microscopy

In situ visualization of the morphology of Langmuir monolayers at the air/water interface was performed using a BAM Nanofilm EP3 (Accurion, GmbH, Göttingen, Germany) coupled to the previously described Langmuir trough. In brief, spatial reflectivity modulations are correlated with optically different monolayer phases depending on lateral ordering and/or lipid packing density. The instrument was equipped with a 50 mW laser emitting p-polarized light at a wavelength 532 nm directly focalized on the air/water interface at the Brewster angle (53.1°), a 10x magnification objective and a polarizer which drive the reflected light to a CCD camera. The spatial resolution of BAM images was 2 µm and the field of view 350 × 275 μm^2. Further analysis of the BAM images was performed by using the software ImageJ[31]. In short, the relative areas occupied by the condensed phases were calculated by applying a threshold before processing the images. The error was determined from the precision of the threshold and the statistical analysis over several images and samples. Gaussian distributions were used to fit the experimental areas obtained. The experiments were performed using HKM buffer as subphase.

2.4. Neutron Reflectometry

Neutron reflectometry (NR) experiments were performed on FIGARO, a time-of-flight reflectometer[32–34] at the Institut Laue-Langevin, Grenoble (France), using two different angles of incidence (θ_1 = 0.6° and θ_2 = 3.8°). A wavelength resolution of 7% $d\lambda/\lambda$ was used, yielding a

momentum transfer of 0.01 $Å^{-1}$<Q_z<0.25 $Å^{-1}$, normal to the interface, and defined as $Q_z = (4\pi/\lambda)\sin\theta$, where λ (from 3 to 20 Å) is the wavelength of the neutron beam. In a typical experiment, Reflectivity (R), defined as the ratio of the intensity of the neutrons scattered from the air/water interface over the intensity of the incident neutron beam, is measured in specular conditions (*i.e.*, the incident angle of the neutron beam is equal to the reflected angle, denoted as θ) as a function of Q_z. The raw time-of-flight experimental data at the two angles of incidence were calibrated with respect to the incident wavelength distribution and the efficiency of the detector, yielding the resulting R(Q_z) profile using, COSMOS[35]. This profile is linked to an in-plane averaged scattering length density (SLD) distribution perpendicular to the interface, which is a measure of the coherent scattering cross-section of the molecular species that constitutes each interfacial layer.

NR experiments were performed using two subphases, providing different contrasts to neutrons: 8.1% D_2O *v/v* and 100 % D_2O. The former is known as air contrast matched water (ACMW), since its scattering length density is equal to the one of air, which is zero. A Langmuir trough was used to deposit lipid monolayers as explained above.

3. Results and discussion

3.1. Phase behaviour of DPPC:PIP_2 monolayers: surface pressure - area per molecule isotherm and compressional elastic modulus

The benefit of working with lipid monolayers (**Figure 3.1 A**) with regard to lipid bilayers is that a much large region of the lipids interfacial phase diagram can be explored from their Π-A compression isotherm. The evolution of lateral pressure as a function of the average area available for each lipid molecule provides insightful information about the lipid phase behavior. Indeed, it allows to distinguish if a lipid monolayer is in a liquid expanded (LE, fluid-like) phase or in a liquid condensed (LC, gel-like) phase. Furthermore, from the slope of the Π-A isotherm it is possible to determine the lateral compressibility of the monolayer, *i.e.*, its mechanical resistance against a dilational deformation in terms of the compressional elastic modulus (C_s^{-1}) of the film (**Equation S3.1**).

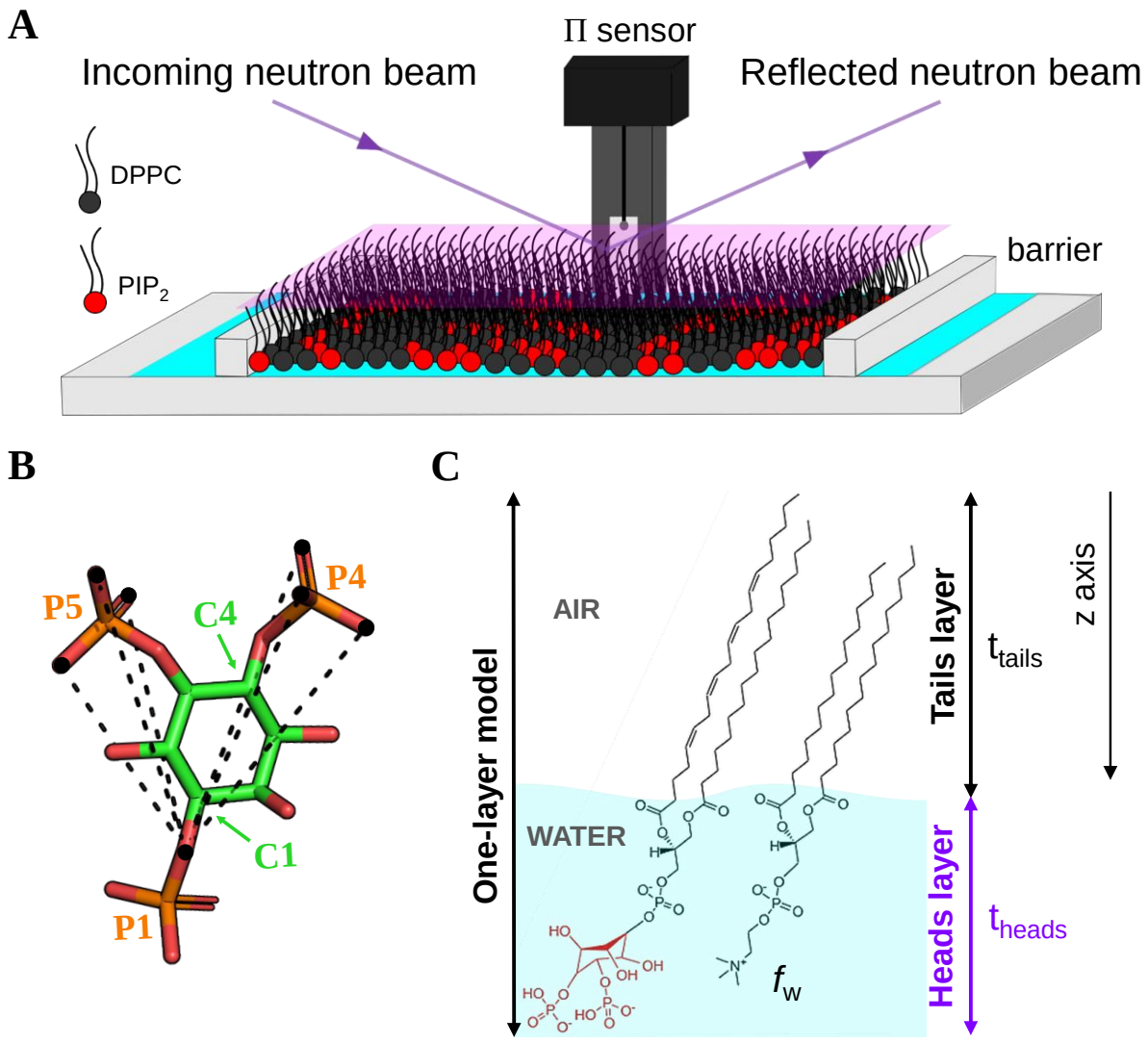

Figure 3.1 A Cartoon representing a mixed DPPC:PIP_2 Langmuir lipid monolayer spread on a Langmuir trough. Incoming and reflected neutron beams are showed to illustrate the *in-situ* characterization by Neutron Reflectometry. **B** Molecular structure of inositol-triphosphate from PBD ID 1HFA[12]. The distances between the oxygen atom bound to C1 and the oxygen atoms bound to P4 and P5 are shown as dashed black lines; the position of the relative oxygen atoms are shown as black circles. **C** Sketch representing the one-layer and two-layer models used to fit the Neutron reflectometry data.

The Π-A isotherm at 21°C of a DPPC:PIP_2 (7:3) mixed monolayer and, as reference, the isotherms corresponding to pure DPPC[36] and pure PIP_2, all of them deposited on a buffer solution containing divalent cations (Mg^{2+}), are shown in **Figure 3.2 A**. The corresponding representation of the compressional elastic modulus (C_s^{-1}) versus Π and A are reported in **Figure 3.2 B** and **C**, respectively. Interestingly, the aspect of the DPPC:PIP_2 isotherm shown in **Figure 3.2 A** appears similar to the one of pure DPPC, in agreement with previous results by Dietrich et al.[14]: both

display a LE phase at low values of surface pressure ($\Pi < 5$ mN·m^{-1}) characterized by a lack of in-plane spatial and orientational organization of the lipid molecules. Further compression yielded an increase in lateral density and both monolayers showed a coexistence of the LE phase with a more ordered, condensed state (LC) that consists of tightly packed lipids. There is, therefore, a LE-LC transition that can be described as a disordered/ordered phase transition of a 2D fluid[37]. Here, the LE-LC coexistence region, whose identification *a priori* was not straightforward from the visualization of the Π-A isotherm of both monolayers, was evident from the appearance of a minimum in the C_s^{-1} profile. This minimum has been already reported for DPPC monolayers spread onto both pure water[33] and buffer (rich in Mg^{2+})[36] subphases. Further compression yielded a LC phase for both DPPC and DPPC:PIP_2 monolayers. Finally, the emergence of a pseudo-plateau in the isotherm of the mixture at $\Pi \approx 43$ mN·m^{-1} was observed, which may be associated with a change in the miscibility of the lipids in the monolayer. After this plateau, the DPPC:PIP_2 isotherm was shifted to even lower molecular areas than those of pure DPPC. The small values of C_s^{-1} at larger areas per molecule corresponding to both monolayers were rationalized by the existence of a high compressibility LE region, whilst higher values of C_s^{-1} (130 mN·m^{-1} for DPPC and 100 mN·m^{-1} for DPPC:PIP_2 monolayers at smaller areas per molecule) correspond to the LC phase. The introduction of PIP_2 to the monolayer lead to a reduction in the elasticity by a factor of ~2.5, in the surface pressure range 30-50 mN·m^{-1}, which corresponds to the LC DPPC phase.

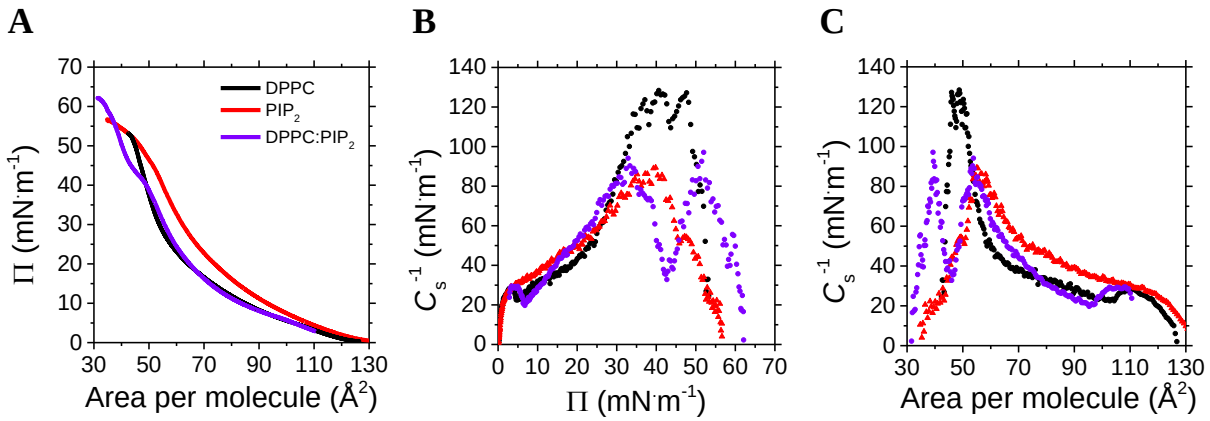

Figure 3.2 A Surface pressure - area isotherms of DPPC (black line), PIP_2 (red line) and DPPC:PIP_2 (violet line) monolayers. Compressional elastic modulus profiles of DPPC (black circles), PIP_2 (red triangles) and DPPC:PIP_2 (violet circles) monolayers plotted versus **B** Π and **C** area per molecule

To summarize, two observations can be made from the Π-A isotherms: firstly, as previously reported for DPPC:PIP_2 mixed monolayers[14], the presence of PIP_2 does not drastically influence the DPPC isotherm. This low impact of PIPs on model membranes has been also

observed in bilayers[11,21]. Secondly, in buffer with Mg^{2+} ions, the values of C_s^{-1} corresponding to the LC phase for DPPC:PIP_2 monolayers are much lower in comparison with the DPPC monolayer[36]. However, in both systems, the values of C_s^{-1} are remarkably smaller in comparison to those measured for DPPC monolayers in water[33]. This effect can be attributed to the presence of divalent Mg^{2+} cations that decrease the lipid packing density in mono- and bilayers[36,38,39]. Furthermore, it is worth mentioning that the steric hindrance associated with the size of the PIP_2 headgroup may hinder partially the maximum lipid packing in DPPC:PIP_2 monolayers, and hence contributes to the reduction of C_s^{-1} with respect to DPPC monolayers, independently of the ionic content of the subphase.

3.3. In-plane organization of DPPC:PIP_2 monolayer investigated through Brewster angle microscopy

A series of BAM images taken during the lateral compression of pure DPPC and mixed DPPC:PIP_2 monolayers are reported in **Figure 3.3**. Different lateral organization of the lipids at the interface was observed depending on the specific composition and compression state, *i.e.*, lipid area per molecule. Indeed, BAM is sensitive to the phase behaviour within the plane of the monolayer and it does not require the use of fluorescent dyes that could introduce artefacts to the observation of lipid miscibility. Particularly, the orientational order related to lipid condensed phases results in modulations of the polarization state of the reflected light[40,41]. As a consequence, dark areas in the BAM images are attributed to fluid regions while more condensed phases are seen as bright micro-domains.

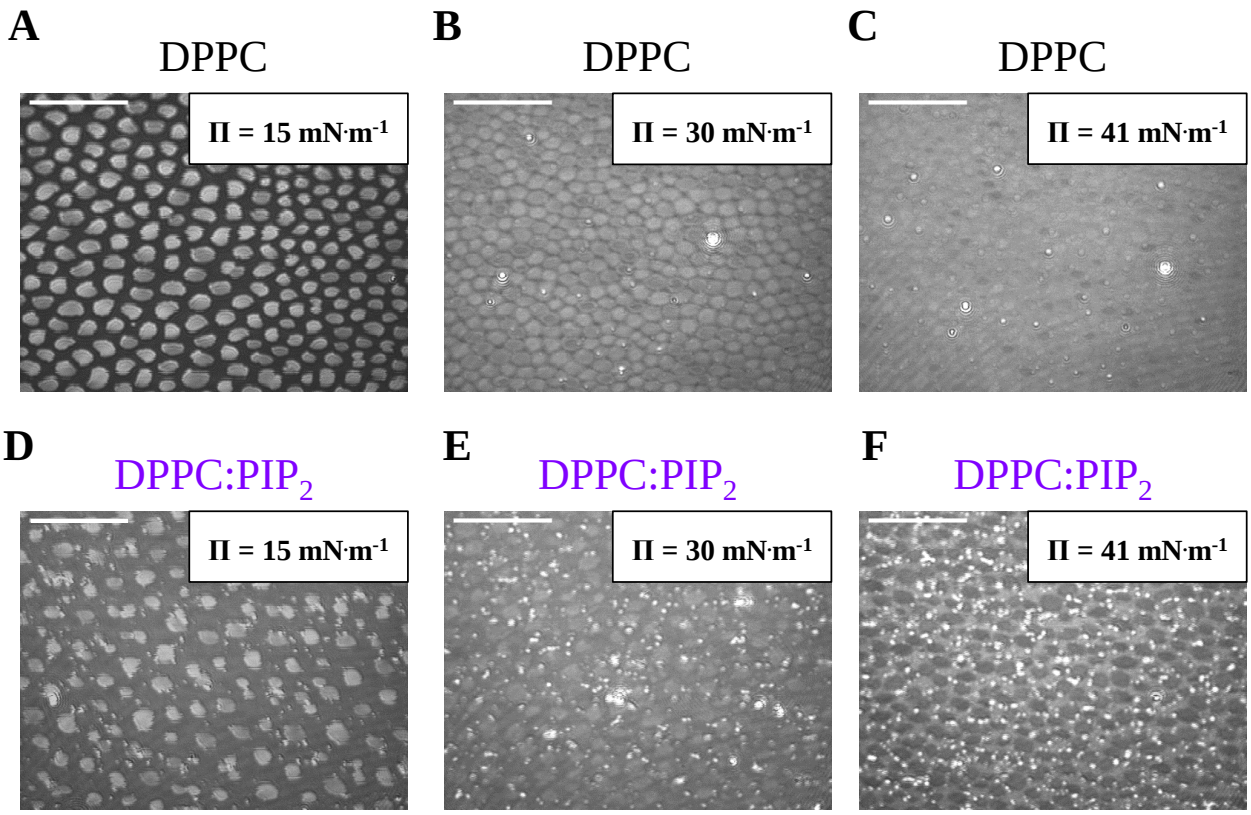

Figure 3.3 BAM image of DPPC monolayer in HKM buffer at **A** 15 mN·m^{-1}, **B** 30 mN·m^{-1} and **C** 41 mN·m^{-1}. BAM image of DPPC:PIP_2 mixed monolayer in HKM buffer at **D** 15 mN·m^{-1}, **E** 30 mN·m^{-1} and **F** 41 mN·m^{-1}

At Π=15 mN·m^{-1}, bean-shaped domains are visible for DPPC monolayer in Mg^{2+} ions containing buffer (**Figure 3.3 A**), which appears less condensed than DPPC monolayer spread on pure water (**Figure S3.2**). This morphological difference is likely due to the presence of divalent cations (here, Mg^{2+}) in the subphase, which have been shown to increase lateral compressibility as well as permeability of the monolayer[36,38,39]. BAM images became brighter at increasing Π indicating a reduction of the area occupied by the fluid phase. At Π=30 mN·m^{-1}, it is still possible to observe condensed domains in the DPPC monolayer that are coalescing as the lateral packing is increasing due to compression (**Figure 3.3 B**). At very high surface pressures (Π=41 mN·m^{-1}) the emergence of a condensed phase for DPPC characterized by a rather homogenous film is observed (**Figure 3.3 C**). In the presence of pure water, DPPC monolayer is in condensed state at lower pressures as it can be seen in **Figure S3.2**.

In the case of DPPC:PIP_2 monolayer, similar domains as for DPPC monolayers were found at Π=15 mN·m^{-1} (**Figure 3.3 D**). In particular, the dark areas in the image were assigned to a fluid phase that includes both DPPC and PIP_2 molecules while the bright, large domains to ordered

DPPC molecules. In addition, bright, small domains (size < 30 μm^2, see **Figure 3.4 B**) also appeared in the image. Interestingly, in DPPC:PIP_2 monolayers at Π=30 $mN \cdot m^{-1}$ (**Figure 3.3 E**), condensed domains are also clearly visible but strikingly coexist with small bright spots, uniformly dispersed within the LE region in a larger number with respect to Π=15 $mN \cdot m^{-1}$ (**Figure 3.3 D**). We attributed those small bright spots to PIP_2 clusters, which have been already reported in the literature[4,5]. This aggregation of PIP_2 molecules within the mixed monolayer may be ascribed to the presence of Mg^{2+} ions in the subphase, which bridge different PIP_2 molecules together, thus excluding other lipids[42]. The small size of these PIP_2 clusters in relation to DPPC domains is the result of diffusion limitations[7]. Therefore, at Π=30 $mN \cdot m^{-1}$ (**Figure 3.3 E**) it was possible to identify up to three different coexisting phases: (1) a fluid phase region containing both DPPC and PIP_2, (2) large DPPC condensed domains, and (3) small bright PIP_2 clusters. Charge shielding and cluster formation did not prevent the formation of condensed DPPC domains that fuse at higher pressures. However, these effects force a random orientation of the molecules at the interface, yielding more disorganized monolayers. Finally, at Π=41 $mN \cdot m^{-1}$ (**Figure 3.3 F**), for which the Π-A isotherm of DPPC:PIP_2 monolayer showed a pseudo-plateau, fusion of the condensed DPPC domains occurred, forming a honeycomb structure in which the fraction of area occupied by the LE phase decreased dramatically. It is also interesting to note that the size of PIP_2 domains increased with the pressure, from 30 to 41 $mN \cdot m^{-1}$ (**Figure 3.4 A** and **B**). Besides, the position of PIP_2 clusters is clearly in the darker (more fluid) zone at 30 $mN \cdot m^{-1}$, while at 41 $mN \cdot m^{-1}$ PIP_2 domains reorganised themselves at the interface between fused condensed DPPC domains (medium bright regions) and more liquid phases (dark regions). At high surface pressures (30 and 41 $mN \cdot m^{-1}$), the phase separation between DPPC and PIP_2, may play an important role in PIP_2 function, as PIP_2 clustering directly increases its local concentration, thereby influencing its interaction with other molecules, like peripheral membrane proteins[7,10].

Moreover, BAM images were quantitatively analysed to gain further insight into the evolution of DPPC micro-domains and PIP_2 clusters with the increase in surface pressure, and, therefore, the decrease in area per molecule. The domain size distribution, in terms of the relative area with respect to the total area, of both DPPC and PIP_2 domains was calculated for different surface pressures and plotted in **Figure 3.4 A**. The characteristic size of each population is reported in **Figure 3.4 B**, together with the corresponding histograms fitted to a normal Gaussian distribution (**Figure 3.4 C**, **D** and **E**). On one side, the number of DPPC condensed domains

remains relatively constant, ~25% of the total area (represented as orange area in **Figure 3.4 A** and **B**) until a pressure of Π≈35 mN·m^{-1} is reached. Above that pressure (cyan area in area in **Figure 3.4 A** and **B**), LC domains start to coalesce and the LE phase (represented as blue triangle in **Figure 3.4 A**, **B** and **E**) reached a final distribution of 50% of the total area. The fraction of area corresponding to the PIP_2 clusters increases with pressure, alongside with their average size (**Figure 3.4**). In this case, the clusters may be formed by a nucleation/growth mechanism that is characterized by the nucleation of novel clusters (corresponding to an increase in the area fraction with pressure) and the growth of the ancient ones already formed. Interestingly, a reduction in DPPC domains size was observed from 15 to 30 mN·m^{-1}. We attributed this result to an enhanced packing of the DPPC molecules within the domains, with their orientation being more perpendicular to the plane of the monolayer.

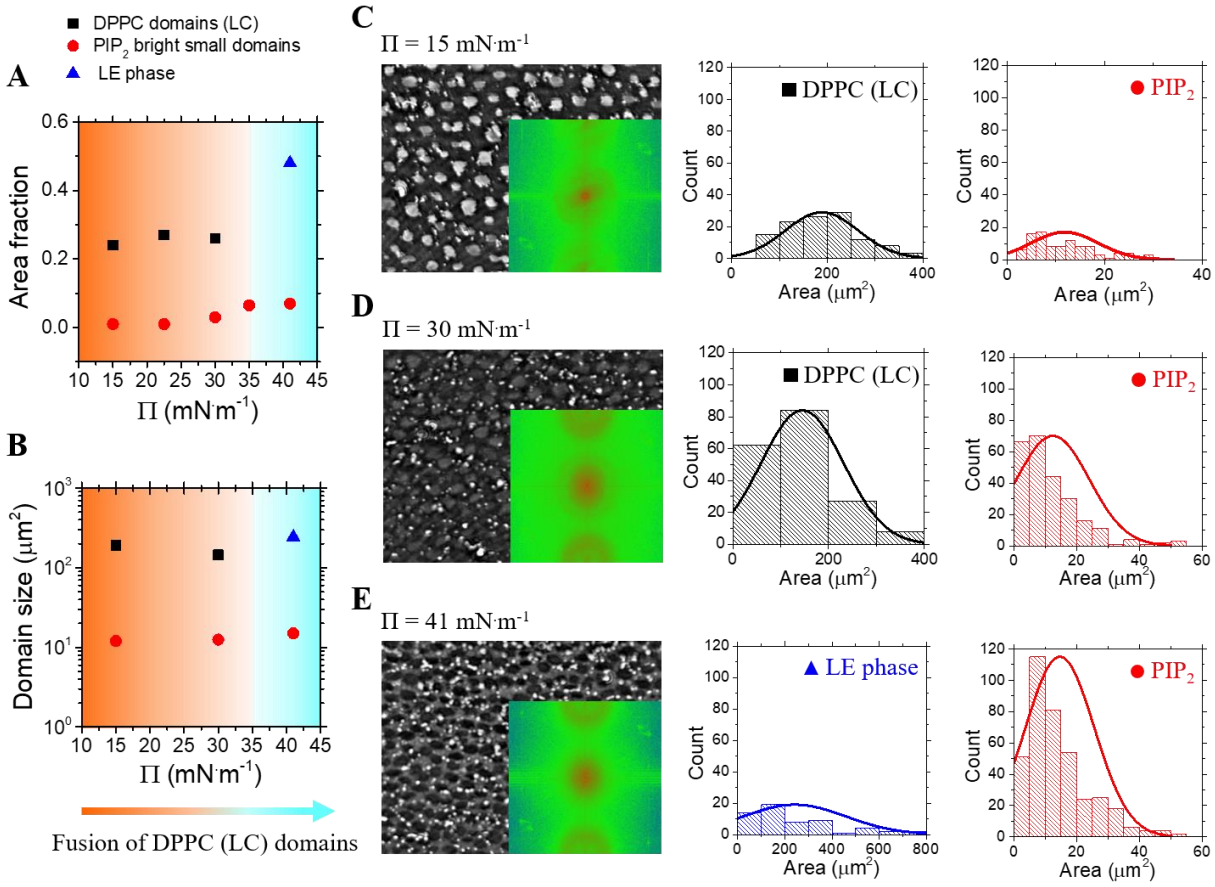

Figure 3.4 Quantitative analysis of BAM images. DPPC domains are depicted as black squares, PIP_2 domains are represented as red circles and finally liquid expanded areas as blue triangles. **A** Area fraction occupied by each domain versus surface pressure. **B** Domain size versus surface pressure. Histograms related to domain size fitted to a normal Gaussian distribution at **C** 15 mN·m^{-1}, **D** 30 mN·m^{-1} and **E** 41mN·m^{-1} BAM images. Insets in **C**, **D** and **E** corresponds to the 2D-FFT power spectra

Finally, to get insights regarding the lipid miscibility, the excess in area per molecule (A_{exc}) as well as the total Gibbs energy of mixing (ΔG_{mix}) were calculated (**Equations S3.2** and **S3.3**) and plotted in **Figure 3.5**. The resultant negative values indicate the presence of attractive interactions between the molecules, which enhance the cohesion of lipids within the mixed monolayer[43]. However, it is interesting to note that, although still negative, the values peak at Π=30 mN·m^{-1} lies between the ones of 15 and 41 mN·m^{-1}. This can be due to steric effects, triggered by the insertion of PIP_2 molecules in DPPC domains. The more condensed LC domains tend to exclude PIP_2 molecules, which in turn, form clusters in the LE phase of the monolayer due to the presence of Mg^{2+} ions. Finally, at Π=41 mN·m^{-1}, the lower ΔG_{mix} suggests a better mixing between lipids. Indeed, BAM images clearly show that PIP_2 domains are not only confined to the LE phase but are in close contact with LC DPPC domains.

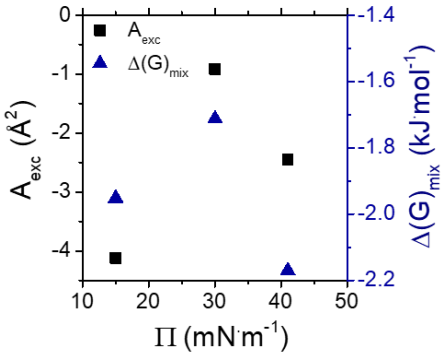

Figure 3.5 Panel showing the excess area per molecule (A_{exc}, black squares) and the Gibbs energy of mixing (ΔG_{mix}, dark blue triangles) calculated at the three pressures for the mixed monolayer

3.3. Out-of-plane structure of DPPC:PIP_2 monolayers and determination of the tilt angles by neutron reflectometry

NR allowed the determination of both the out-of-plane structure and the exact composition of the lipid monolayer. Indeed, the experimental determination of monolayer composition was necessary to accurately determine the molecular volumes and scattering length densities, SLD, values of the DPPC:PIP_2 mixture. Thus, experimental data at a limited momentum transfer range (0.01 Å^{-1}<Q_z<0.03 Å^{-1}) were collected and analysed by a one-layer model that is only sensitive to the composition of the monolayer[44,45] (**Figure 3.1 C** and **Supporting Information**). By using two different isotopic contrasts, h-DPPC:PIP_2 and d62-DPPC:PIP_2 in HKM-buffered ACMW, the relative amount of DPPC and PIP_2 at three surface pressures (15, 30 and 41 mN·m^{-1}) was

determined, yielding values very close to the nominal lipid composition (**Table S3.2**). From these molar compositions, and using the values shown in **Table S3.1**, the values of molecular volumes and SLD for both h-DPPC:PIP_2 and d62-DPPC:PIP_2 mixtures at the three pressures were calculated. These values, shown in **Table S3.3**, were then included in the model of the experimental data at the fully accessible Q_z-range, to obtain information relative to the monolayer out-of-plane structure. In this case, four different isotopic contrasts were exploited, employing both hydrogenous and deuterated tails phospholipid. Thus, by spreading monolayers of h-DPPC:PIP_2 and d62-DPPC:PIP_2 onto both HKM-buffered ACMW and D_2O subphases (see **Figure S3.3** for experimental curves), it was possible to define a two-layer model to fit the data, rationally divided into polar headgroups facing the bulk phase and aliphatic tails in contact with air (**Figure 3.1 C** and **Figure 3.6**). The parameters optimised during the fitting process (**Table S3.4**) were: thickness of both headgroups and tails (t_{heads} and t_{tails}, respectively), water volume fraction in the headgroups layer (f_{wh}) and roughness (r) of the three interfaces (air/tails layer, tails layer/headgroups layer, headgroups layer/subphase), which were constrained to be equal[33,36]. The values of roughness obtained were compatible with that corresponding to water capillary waves (~3Å)[46–48] and did not significantly vary in the range of surface pressures studied. Besides, each of the models used to fit the data ensure the same area per molecule of tails and headgroups, whose values were consistent with the ones obtained from isotherm and ellipsometry (**Table S3.5** and **Figure S3.7**). The optimised value of f_{wh} was in perfect agreement with the value calculated according to **Equation S3.7**. This finding further assures the goodness of our two-layer models.

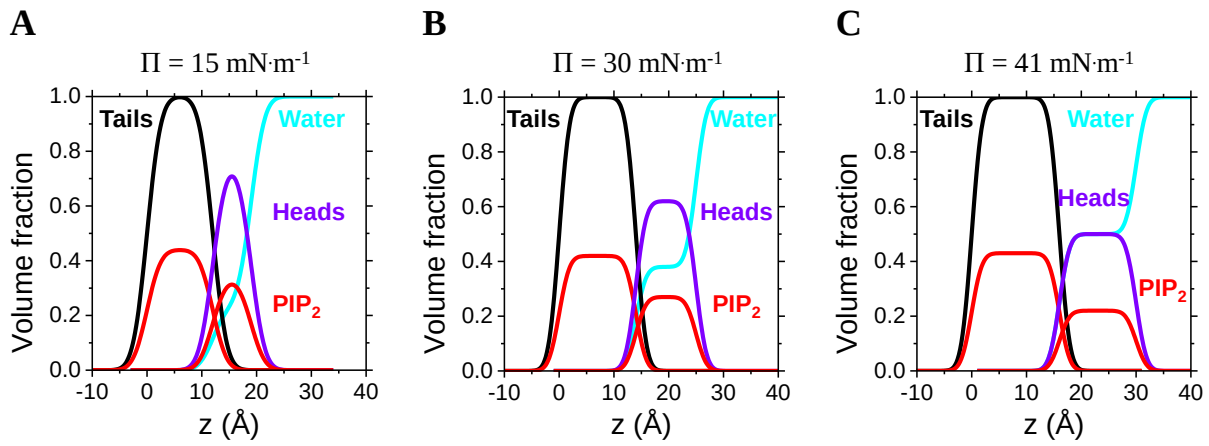

Figure 3.6 Data derived from fitting of reflectivity profiles plotted in **Figure S3.4**. The panels show the volume fraction profiles normal to the interface underlying the distribution of tails (black), headgroups (olive blue) and water (cyan), at the surface pressure value of **B** 15 mN·m^{-1}, **C** 30 mN·m^{-1} and **D** 41 mN·m^{-1}. PIP_2 volume fraction, in both tails- and headgroups-layer, is shown as red lines.

The use of four different isotopic contrasts allowed to optimize simultaneously the different structural parameters (illustrated in **Figure 3.1 C**) reported in **Figure 3.7 A** and **B**, which clearly depend on the monolayer compression. As expected, the increase in surface pressure produced an increase in the thickness of the aliphatic tails as shown in **Figure 3.7 A**. This can be rationalized because further compression diminishes the area available per lipid molecule, yielding an increase of the tilt angle of the hydrophobic tails, as already reported in literature[14]. Here, the tilt angle (ϕ) of the tails with respect to the membrane normal, calculated as $\phi = \cos^{-1}(t_{\text{tails}}/t_{\text{pal}})$ with t_{pal} the thickness of the palmitoyl chain (19.5Å[49]), resulted in ϕ = 52°, 44° and 35° for Π = 15, 30 and 41 $mN \cdot m^{-1}$, respectively (plotted against the corresponding A in **Figure 3.7 F**). Both values of ϕ and A are larger with respect to the ones of PIP_2 containing monolayer in the absence of divalent salts (*i.e.*, in purely HEPES-NaCl-EDTA buffer)[14] confirming thus a decrease in the packing density of the monolayers in the presence of divalent salts, as already observed in purely DPPC monolayers[36].

Despite previous NR studies on DPPC monolayers report a constant value of the headgroups thickness at different surface pressures[33,50], here the values of t_{heads} obtained experience an increase with Π (see **Figure 3.7 A**), attributed to a change in PIP_2 headgroup tilt angle. Besides, the increase in f_{wh} observed (**Figure 3.7 B**) can be rationalized by the change of the headgroup tilt angle. Particularly, the systematic increase in both t_{heads} and f_{wh} were assumed to be determined by the change in the orientation of the inositol ring, which was further calculated below. Although it was already demonstrated by NR that the inositol-triphosphate ring assumes a preferred orientation close to the surrounding lipid headgroups in bilayers[11], the tilt angle of the ring has been never experimentally determined, to the best of our knowledge. Molecular dynamic (MD) simulations on lipid bilayers[3,20,21] suggested that PIP_2 adopts a preferred orientation of ~40° with respect to the membrane normal. Noteworthy, these simulations demonstrated that the solvent-accessible surface area of the PIP_2 headgroup increases as the tilt angle decreases, since fewer water molecules can be present in the solvation shell of the inositol ring when oriented closer to the membrane. Our experimental results from NR gave similar outcomes concerning the PIP_2 headgroup hydration (**Table S3.4** and **Figure 3.7 B**): as surface pressure increases, although the headgroup layer thickens as the tilt angle decreases, its water content increases.

To calculate the PIP_2 tilt angle, denoted as τ, the inositol-(1,4,5)triphosphate ring average size ~7Å (t_{IP_2}) was estimated from its atomic structure (as found in the crystal structure PDB ID:

1HFA[12]), measuring the distances between the oxygen atom bound to C1 and P1 and the oxygen atoms bound to P4 and P5 (**Figure 3.1 B**). The phosphate P1 was considered to be at the same position (along z) than the phosphate of DPPC, as reported by Wu et al.[21]. Assuming this model, at Π=15 mN·m^{-1} the inositol-biphosphate ring would lie parallel to the monolayer (τ=90°), as the headgroups thickness obtained (t_{heads} = 7Å) is similar to the value for a pure DPPC monolayer[51,52].

The linear dependence in the headgroups thickness with Π, defined as $\Delta t_{heads} = t_{heads}(\Pi) - t_{heads}(15 mN{\cdot}m^{-1})$, and reported in **Figure 3.7 C**, could be attributed exclusively to the change in the molecular orientation of the inositol-biphosphate ring. Thus, a protrusion of PIP_2 headgroup happens. It is important to underline that similar protrusions were already observed by MD simulation for DPPC:PIP_2 bilayers[3]. Considering t_{IP_2} the inositol-biphosphate ring length and Δt_{heads} the projection of t_{IP_2} onto the z-axis, normal to the monolayer (**Figure S3.4**), the PIP_2 tilt angle τ can be calculated as $\tau = \cos^{-1}(\Delta t_{heads}/t_{IP_2})$. Its dependence on the monolayer compression and, therefore, on the surface pressure, could be empirically described by:

$$\tau = \cos^{-1}\frac{a * \Pi + b}{t_{IP_2}}, \qquad \textbf{3.1}$$

where, *a* and *b* are constants defined by the linear relationship between Δt_{heads} and Π. The trajectory described by τ at varying Π due to monolayer compression, shown in **Figure 3.7 D**, is in excellent agreement with the calculated values of τ obtained from previous MD simulations[3,20,21]. Indeed, a bilayer with an area per molecule of ~50Å^2 and characterized by a hypothetical surface pressure of 35 mN·m^{-1} (extrapolated from the isotherm), yields a calculated PIP_2 tilt angle of τ≈40° (blue circle in **Figure 3.7 D**). This value of area per molecule is compatible with the one of a DPPC bilayer at 20°C (gel phase)[53].

To summarize, the aliphatic tails (ϕ) and inositol ring (τ) tilt angles calculated were plotted against A as shown in **Figure 3.7 F**. The values of A were also calculated by NR and ellipsometry (**Supporting Information** and **Figure S3.7**). As the lipid leaflet was compressed, lipids gain in compaction and thus reduce their surface area. This is reflected not only in the decrease of ϕ, but also in the re-orientation of PIP_2 headgroups towards the bulk phase, illustrated by the decrease of τ with A. This tendency can be correlated with the in-plane structure observed in the BAM images, in which there is an increase in PIP_2 clustering at larger areas per molecule possibly due to the re-

organization of the PIP_2 headgroups occupying lower volume and favouring less steric hindrance between them.

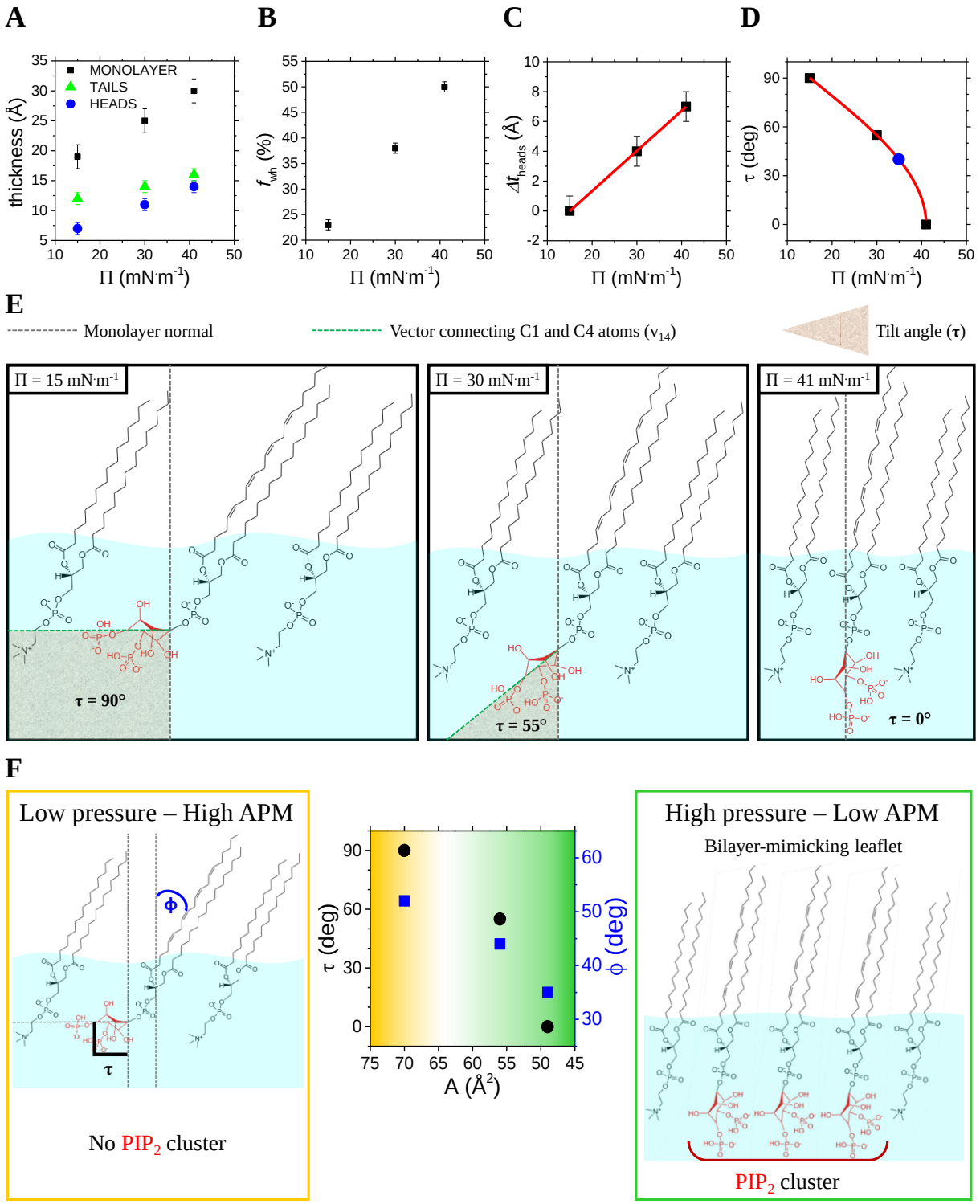

Figure 3.7 A Thickness of tails (green triangles) and headgroups (blue circles) plotted versus surface pressure, together with total thickness of the monolayer (black squares). **B** Volume fraction of water in the headgroups layer

plotted versus surface pressure. **C** Plot showing the thickness increment of the headgroups-layer obtained from the fit versus surface pressure. The linear dependence is shown as a red line. **D** The calculated values of tilt angle (θ) versus surface pressure are shown as black squares. The fit performed using a $\cos^{-1}$ function (**Equation 3.1**) is shown as a red line. The interpolated point (35 $mN \cdot m^{-1}$; 40°)[20,21] is shown in blue. **E** Sketches representing mixed DPPC:PIP_2 monolayer at the three pressures. The inositol-biphosphate (IP_2) ring is depicted in red. The normal to the monolayer (dashed grey line) and the vector connecting C1 and C4 of the inositol-biphosphate (IP_2) ring (v_{14}, dashed green line) are shown. The tilt angle (θ), which is calculated between the normal and v_{14}, is shown and depicted as light brown area. **F** Comparison between out-of-plane structure and in-plane organization of DPPC:PIP_2 mixed monolayers at the three surface pressures. The central panel reports the values of PIP_2 inositol ring tilt angles (θ) and tails tilt angles (φ) versus area per molecule. Left panel shows the monolayer structure at a low area per molecule value as well as the graphical definition of θ and φ. Right panel reports a sketch of PIP_2 cluster in the mixed monolayer at larger areas.

4. Conclusions

We designed a simple, *in vitro* model based on Langmuir monolayers composed of PIP_2 and DPPC to mimic the inner leaflet of plasma membrane. Our multi-technique approach allowed us to compare the results regarding both in-plane organization and out-of-plane structure of the DPPC:PIP_2 monolayer at different compression states, *i.e.*, different areas per molecule. The evolution of PIP_2 clusters in our planar model system, when divalent cations are present in bulk, have been experimentally studied as a function of monolayer compression. We focused on the relation between PIP_2 domain formation and the monolayer out-of-plane structure determined by neutron reflectometry. PIP_2 cluster formation depends not only on the presence of Mg^{2+} ions, but also on the surface pressure, which influences the out-of-plane structure of the lipids. Moreover, neutron reflectometry allowed the determination of the inositol-phosphate ring orientation, in terms of its tilt angle. We observed that when the inositol-biphosphate ring moves away from the membrane, the formation of clusters is favored, and larger PIP_2 islands can form. This behavior is also identified from the quantitative analysis of the BAM images. Indeed, PIP_2 clusters (with an area > 1%) form from Π=30 $mN \cdot m^{-1}$ and their number increases until a plateau at Π=35 $mN \cdot m^{-1}$ is reached. Therefore, our results clearly show the dependence between the orientation of the inositol-biphosphate ring and the PIP_2 cluster formation. Moreover, an empirical equation has been proposed to determine the trajectory of the PIP_2 headgroups tilt angle with the surface pressure and the level of monolayer compression. The orientation of PIP_2 headgroup can thus be estimated at different molecular areas and experimental conditions.

The investigation of the lipid in-plane organization, by means of BAM, showed the formation of PIP_2 cluster in presence of divalent cations, which have been already reported in literature[4,5,42]. However, in this work we were able to correlate cluster formation with the out-of-plane structure

of the monolayer, *i.e.*, tilting of both acyl chains and PIP_2 inositol-biphosphate ring. Moreover, our experimental outcomes agree with previous MD simulations that determined the preferred inositol-biphosphate ring orientation in PIP_2-containing lipid bilayers[3,20,21] (~40°, with respect to the membrane normal). Indeed, by using **Equation 3.1**, this value leads to a surface pressure of 35 $mN{\cdot}m^{-1}$, corresponding to the typical bilayer area per molecule[53]. To the best of our knowledge, this is the first time that the orientation of an inositol-phosphate ring has been determined experimentally.

Finally, we consider that our work will help to a better understanding of both PIP_2-protein interaction and PIP_2 role in membrane curvature. Indeed, the PIP_2 headgroup variation of orientation found here might facilitate changes in membrane curvature. Particularly, we explored the limiting case at a very low surface area characterized by an orthogonal position of the inositol ring with respect to the acyl chains that turns into an almost parallel orientation at larger areas. This gradual PIP_2 headgroup protrusion in the bulk phase observed at decreasing surface areas, might have a direct influence on membrane curvature modulating the binding of different peripheral membrane proteins.

SUPPORTING INFORMATION

Surface pressure - area isotherm: calculation of compressional elastic modulus and Gibbs energy of mixing

From the isotherm, the compressional elastic modulus (C_s^{-1}) of a lipid film can been calculated according to the following expression

$$C_s^{-1} = -A \cdot \left(\frac{\partial \Pi}{\partial A}\right) \quad \textbf{S3.1}$$

where A is the area per molecule and Π is the surface pressure. Comparing the isotherms of pure components and mixed monolayers, the total Gibbs energy of mixing of the different lipid molecules can be calculated[43]. Firstly, the excess in area per molecule (A_{exc}) at fixed values of the surface pressure can be obtained as follows:

$$A_{exc} = A_{DPPC:PIP_2} - A^{id}_{DPPC:PIP_2} \quad \textbf{S3.2}$$

where $A_{DPPC:PIP_2}$is obtained at a fixed value of Π from the DPPC:PIP_2 isotherm and $A^{id}_{DPPC:PIP_2}$ is the A of the monolayer evaluated at the same Π considering ideal miscibility, *i.e.*, the absence of interactions between the lipids forming the monolayer, and thus is calculated taking into account the molar fraction (x) of each components obtained by neutron reflectometry ($A^{id}_{DPPC:PIP_2} = A_{DPPC} \cdot x_{DPPC} + A_{PIP_2} \cdot x_{PIP_2}$). Then, the total Gibbs energy of mixing was obtained following:

$$\Delta G_{mix} = \Delta G_{exc} + \Delta G_{id} \quad \textbf{S3.3}$$

where ΔG_{exc} is the excess Gibbs energy of mixing, which can be expressed as $\Delta G_{exc} = N_A \int_0^{\pi} A_{exc}\, d\pi$ (N_A is the Avogadro's number), and ΔG_{id} is the ideal Gibbs energy of mixing. The latter can be expressed as $\Delta G_{id} = RT[x_{DPPC} \cdot \ln(x_{DPPC}) + x_{PIP_2} \cdot \ln(x_{PIP_2})]$, where R is the gas constant and T is the temperature in Kelvin.

Neutron reflectometry: data collection and analysis

The data analysis was performed using Motofit software[54]. Quantification of the membrane composition was done exploiting the low-Q_z range approach, *i.e.*, by collecting data at a limited Q_z range, 0.01 Å^{-1}<Q_z<0.03 Å^{-1}, which allows a relatively fast acquisition time. A one-layer model of the monolayer (**Figure 3.1 C**) was exploited to determine the area per molecule (A) of both phospholipids at different values of Π following[44]. The A is given by $A = {\sum b}/{SLD \cdot t}$, where

$\sum b$ and SLD are the scattering length and the scattering length density of each component, respectively, and t is the film thickness. Here the product of SLD and t can be considered as additive and, therefore, expressed as:

$$\mathrm{SLD} \cdot \mathrm{t} = \left(\frac{\Sigma \mathrm{b}_{\mathrm{DPPC}}}{\mathrm{A}_{\mathrm{DPPC}}} + \frac{\Sigma \mathrm{b}_{\mathrm{PIP_2}}}{\mathrm{A}_{\mathrm{PIP_2}}} \right) \qquad \textbf{S3.4}$$

where A_{DPPC} and A_{PIP_2} are the area per molecule of DPPC and PIP_2 molecules, respectively. The data analysis was performed by fitting the product of SLD and t. This was done for both h-DPPC:PIP_2 and d62-DPPC:PIP_2 monolayers in ACMW subphase, thus obtaining a set of two equations with two unknown parameters: A_{DPPC} and A_{PIP_2}. Finally, taking into account that the amount of material is proportional to the lipid A, the film composition was determined, and the relative molar fraction of DPPC and PIP_2 were calculated (**Table S3.2**).

To elucidate the structure of the monolayer, data were collected at the fully accessible full-Q_z range. In this case, a two-layer model was used to fit the data (**Figure 3.1 C**), dividing the phospholipid molecules in two different regions in the direction perpendicular to the interface: one including the polar headgroups, and the other corresponding to the aliphatic tails. The choice of this model was rationalized by the differences in SLD between these two regions[33]. The fixed parameters used in the fitting procedure (**Table S3.3**) were the molecular volumes of headgroups (V_{heads}) and tails (V_{tails}) and the total scattering length density of headgroups (SLD_{heads}) and tails (SLD_{tails}). The roughness (*r*) of the three interfaces (air/tails layer, tails layer/headgroups layer, headgroups layer/subphase) was assumed identical as previously reported[33,36]. Besides, its value was consistent with the presence of water capillary waves[46–48]. The change in SLD along the *z*-axis of each interface is modulated by an error function, ERF[55], defined as:

$$\mathrm{ERF}\left(\frac{z - z_0}{r/\sqrt{2}}\right) = \frac{2}{\sqrt{\pi}} \int_0^{\frac{z-z_0}{r/\sqrt{2}}} \mathrm{e}^{-t^2} \mathrm{d}t \qquad \textbf{S3.5}$$

where z_0 indicate the position of the interface.

As previously reported in the case of liquid condensed phase DPPC (as it is for the pressures here reported), a contraction of the tails volume of 15% occurs, which changes the SLD of the tails-layer[33]. The volumes and SLD showed in **Table S3.1** reported the corrected values, which are taken (or calculated) from literature values[56,57]. Experimental data of the same monolayer in the different contrasts were fitted together. Using this approach, the variables determined through the

fitting procedure were the surface roughness (*r*), the thickness of both the tails layer (t_{tails}) and the headgroups layer (t_{heads}), and the water volume fraction in the headgroups layer (f_{wh}), which is defined as $f_{wh}+ f_{heads} = 1$. Each model used to fit the data ensures that there is the same area per molecule, of tails A_{tails} and headgroups A_{heads}, calculated as:

$$A_i = \frac{\Sigma b_i}{SLD_i \cdot t_i \cdot f_i} = \frac{V_i}{t_i f_i} \qquad \textbf{S3.6}$$

where Σb_i, f_i and V_i are the total scattering length, the volume fraction and the molecular volume of the *i*-th component (tails or headgroups), respectively. The tails volume fraction f_{tails} was fixed to unity. This lead to the following equation:

$$f_w = 1 - \frac{t_t \cdot V_h}{t_h \cdot V_t} \qquad \textbf{S3.7}$$

where f_w is the water volume fraction in the headgroups-layer, t and V are the thickness and molecular volumes, and the subscripts h and t indicate headgroups and tails, respectively.

A Langmuir trough was used to deposit lipid monolayers as explained above. All the experiments were performed at 21 ± 0.5 °C and using HKM buffer solution (made of ACMW or D_2O solvents) as subphase

Neutron reflectometry: determination of PIP_2 inositol ring orientation

As already explained in the main text, to calculate the PIP_2 tilt angle, the inositol-(1,4,5)triphosphate ring average size ~7Å (t_{IP_2}) was estimated from its atomic structure (as found in the crystal structure PDB ID: 1HFA[12]), measuring the distances between the oxygen atom bound to C1 and P1 and the oxygen atoms bound to P4 and P5 (**Figure 3.1 B**). The phosphate P1 was considered to be at the same position (along z) than the phosphate of DPPC, as reported by Wu et al.[21]. Assuming this model, at 15 $mN \cdot m^{-1}$ the inositol-biphosphate ring would lie parallel to the monolayer (θ=90°), as the headgroups thickness obtained (7Å) is similar to the DPPC headgroup thickness[51,52]. A further increase in surface pressure leads to an increase in headgroups layer thickness. If the thickness increment (Δt_{heads}) is considered to be attributed exclusively to the inositol-biphosphate (IP_2) ring, the change in thickness Δt_{heads} can be determined as defined as $\Delta t_{heads} = t_{heads}(\Pi) - t_{heads}(15 mN \cdot m^{-1})$, where $t_{heads}(15 mN \cdot m^{-1}) = 7$Å. Thus, a protrusion of PIP_2 headgroup happens. It is important to underline that similar protrusions were already observed by MD simulation for DPPC:PIP_2 bilayers[3]. **Figure 3.7 C** shows a linear fit of

thickness increment with respect to surface pressure, according to the linear equation:

$$\Delta t_{heads} = a * \Pi + b \quad \textbf{S3.8}$$

where *a* is the slope and *b* is the intercept of the linear fit. Knowing the inositol-biphosphate ring length (t_{IP_2}) and considering Δt_{heads} as the projection of t_{IP_2} on the z-axis (normal to the monolayer) as shown in **Figure S3.4**, the tilt angle τ can be calculated according to $\tau = \cos^{-1}(\Delta t_{heads}/t_{IP_2})$, which, if combined with **Equation S3.8**, can be translated in the following (called **Equation 3.1** in the main text):

$$\tau = \cos^{-1}\frac{a * \Pi + b}{t_{IP_2}} \quad \textbf{3.1}$$

In the linear fit related to **Equation S3.8** and the sinusoidal fit related to **Equation 3.1**, the parameters *a* and *b* were unconstrained, leading to the same values.

Ellipsometry

Ellipsometry is a non-destructive optical technique based on the determination of the polarization changes that light undergoes when it is reflected at an interface[58]. The experiments were performed on a Picometer Light ellipsometer (Beaglehole Instruments, Kelburn, New Zealand) fitted with a He-Ne laser with λ = 632 nm. The Langmuir trough (KIBRON, Helsinki, Finland) was coupled with the ellipsometer to measure the surface pressure of the lipid monolayer during the measurements of the ellipsometric angles. We deposited the monolayer at the air/water (HKM buffer) interface and measured the ellipsometric angles as a function of the angle of incidence (AOI). The range of AOI was 40°-70° with a step of 0.25°. The reflection coefficients parallel and perpendicular to the plane of incidence, r_p and r_s respectively, are related to the ellipsometric angles Delta, Δ, and Psi, Ψ. This relationship is known as ellipticity, ρ, and is defined by:

$$\rho = {}^{r_p}/_{r_s} = tan\,\Psi e^{i\Delta} \quad \textbf{S3.9}$$

where ρ depends on the AOI, the wavelength of the incident light and both the thickness and the dielectrical properties of the material on which the reflection of the light beam occurs. Although the ellipsometric measurements are experimentally easily performed, they do not provide direct determination of the refractive index (n_F) and the thickness (t_F) of the film spread at the interface (lipid monolayer). These values have to be determined indirectly by optimizing a model linking angles Δ and Ψ with the AOI. The model used in this work consisted of one slab formed by the lipid monolayer characterized by t_F and n_F. Once constructed the model, the fit of Δ and Ψ vs. AOI

was carried on using a numeric non-linear minimization procedure, a trust-region reflective algorithm[59]. This method, already exploited in literature[36,60], is based on the determination of the ellipsometric angles of the model that minimizes the differences with those experimentally obtained.

The area per molecule that characterizes any lipid monolayer at a given surface pressure has been classically determined through surface pressure - area isotherms, neutron reflectometry or X-ray reflectometry. Here we propose a novel approach to determine the A using ellipsometry. The analysis of the ellipsometry data provides values of A compatible with those obtained by neutron reflectometry. Ellipsometry measurements allowed us to explore the variation of the ellipsometric angles Δ and Ψ as a function of the angle of incidence (AOI). The HKM buffer had a similar refractive index to pure water, hence the same profile of ellipsometric angles versus AOI. **Figure S3.5** shows the superimposition of Δ profiles versus AOI of pure water, HKM buffer and DPPC:PIP_2 monolayer at the three surface pressures 15, 30 and 41 $mN \cdot m^{-1}$. As expected, the increase in surface pressure produced a significant difference in the Δ profile, due to the change in the state of polarization of the light beam after reflection on the monolayer interface. This is due to a change in the monolayer thickness (t_F). To fit the experimental data, a one-layer optically isotropic model for the DPPC:PIP_2 monolayer with an average refractive index (n_F) was used. We simultaneously fitted the variation of Δ and Ψ with AOI with different $n_F - t_F$ initial values covering a wide range of n_F (from 1.34, corresponding to the bulk phase, to 1.54) and t_F (from 1 to 3 nm), to achieve the lowest χ^2 value. The combination of 300 values of both parameters resulted in 9×10^4 $n_F - t_F$ pairs of solutions with a given χ^2. This approach resulted in a matrix, shown as a colormap, for each of the studied surface pressures (**Figure S3.6**). The lowest values of χ^2 are coloured dark blue. As already described by Carrascosa-Tejedor et al[36], the de Feijter's, equation[61] was used to determine the number of lipid molecules per unit area at each surface pressure (called surface excess, Γ) of DPPC:PIP_2 at 15, 30 and 41 $mN \cdot m^{-1}$, taking into account the molecular weight (MW) of the mixture:

$$\Gamma = \frac{t_F(n_F - n_{bulk})}{(dn/dc) * MW} \qquad \textbf{S3.10}$$

where dn/dc is the refractive index increment and n_{bulk} is the refractive index of the bulk phase, here we used a value of 1.335 that corresponds to pure water. Considering that the composition of the interface is ~70% DPPC, the dn/dc value for DPPC found in literature[62], 0.138 $mL \cdot g^{-1}$, was

used. **Figure S3.6** reports the distribution of Γ calculated for the different pairs of (n_F, t_F) values yielding the lowest χ^2. These values satisfy $\chi^2 \leq 1.5\chi^2_{min}$, where χ^2_{min} accounts for the best value. The tendency shown by Γ has been modelled by a normal distribution (red line in **Figure S3.6**), leading to the most probable value of surface excess. Once the surface excess at the three surface pressures had been determined (**Figure S3.7 A**), the A can be calculated (**Figure S3.7 A** and **B**, **Table S3.5**), taking into account that $A = (\Gamma * N_A)^{-1}$, where N_A is the Avogadro's number. The outcomes obtained are plotted in **Figure S3.7 B** and are in agreement with values obtained from isotherm and neutron reflectometry.

It is important to emphasize the self-consistency of the results obtained from isotherm, ellipsometry and neutron reflectometry (**Figure S3.7 B** and **Table S3.5**). Even though a similar multi-technique approach was used with pure DPPC monolayers at a single pressure[36], the ability to determine A through ellipsometry has now been extended to more complex lipid monolayers, measured over a wide range of surface pressures. A fundamental consequence is that this experimental approach can be used to infer the A of any Langmuir monolayer, providing important microscopic information through an easily accessible benchtop technique. Although a simple isotherm could give information about lipid A, unlike ellipsometry, it does not describe the interfacial behaviour of lipid- as well as surfactant-based model systems at the air/water interface. This is particularly true when further compression leads to loss of material at the interface. In this case, extended structures in the bulk water could form, whose presence is undetectable from the surface sensor of a typical Langmuir trough.

Tables

Table S3.1 Fixed parameters used for data modelling.

Parameters	h-DPPC	d62-DPPC	PIP_2
V_{heads} (Å^3)	319	319	472.5
SLD_{heads} (10^{-6} Å^{-2})	1.88	1.88	3.05
V_{tails} (Å^3)	701	701	1014
SLD_{tails} (10^{-6} Å^{-2})	-0.46	8.74	-0.075
f_{tails} (%)	1	1	1

Table S3.2 Relative DPPC and PIP_2 molar composition in the monolayer at the three surface pressures explored in this study. Data obtained from the low-Q_z analysis of the neutron reflectometry data. From the relative lipid amount, the molecular weight of the mixture has been calculated at each Π.

Π (mN·m^{-1})	**DPPC molar ratio**	**PIP_2 molar ratio**	**Molecular Weight, MW (g·mol^{-1})**
15	0.65	0.35	861.2
30	0.67	0.33	855.4
41	0.66	0.34	858.3
Nominal composition	0.7	0.3	842.7

Table S3.3 Fixed parameters of h-DPPC:PIP_2 and d62-DPPC:PIP_2, calculated from low-Q_z. The values between brackets refers to d62-DPPC:PIP_2.

Fixed Parameters	**15 mN·m^{-1}**	**30 mN·m^{-1}**	**41 mN·m^{-1}**
V_{heads} (Å^3)	372.9	370.4	371.6
SLD_{heads} (10^{-6} Å^{-2})	2.40	2.38	2.39
V_{tails} (Å^3)	810.9	805.8	808.4
SLD_{tails} (10^{-6} Å^{-2})	-0.29 (4.87)	-0.30 (5.03)	-0.30 (4.95)
f_{tails} (%)	1	1	1

Table S3.4 Optimised parameters. Results obtained from full-Q_z neutron reflectometry analysis.

Fitting Parameters	15 mN·m^{-1}	30 mN·m^{-1}	41 mN·m^{-1}
t_{tails} (Å)	12±1	14±1	16±1
t_{heads} (Å)	7±1	11±1	14±1
$t_{monolayer}$ (Å)	19±2	25±2	30±2
f_{wh} (%)	23±2	38±1	50±1
r (Å)	4±1	3±1	3±1

Table S3.5 Values of area per molecule (A) obtained from the different techniques exploited in this work.

Π (mN·m^{-1})	Area per molecule, A (Å^2)				
	Isotherm	*Ellipsometry*	*NR (low-Q_z)*	*NR (full-Q_z)*	
				tails	*headgroups*
15	72	75±8	70±1	70±6	70±12
30	56	60±5	56±1	58±4	55±6
41	48	55±5	49±1	49±3	53±5

Figures

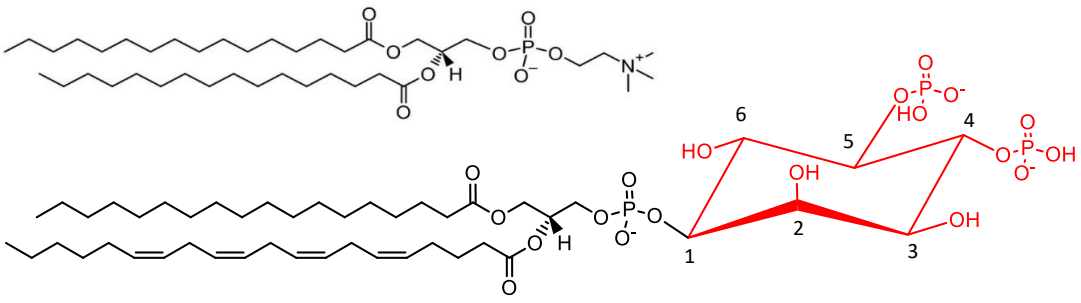

Figure S3.1 Molecular structures of DPPC (top) and PIP_2 (bottom) taken from Avanti Polar lipids. The inositol-biphosphate ring is highlighted in red.

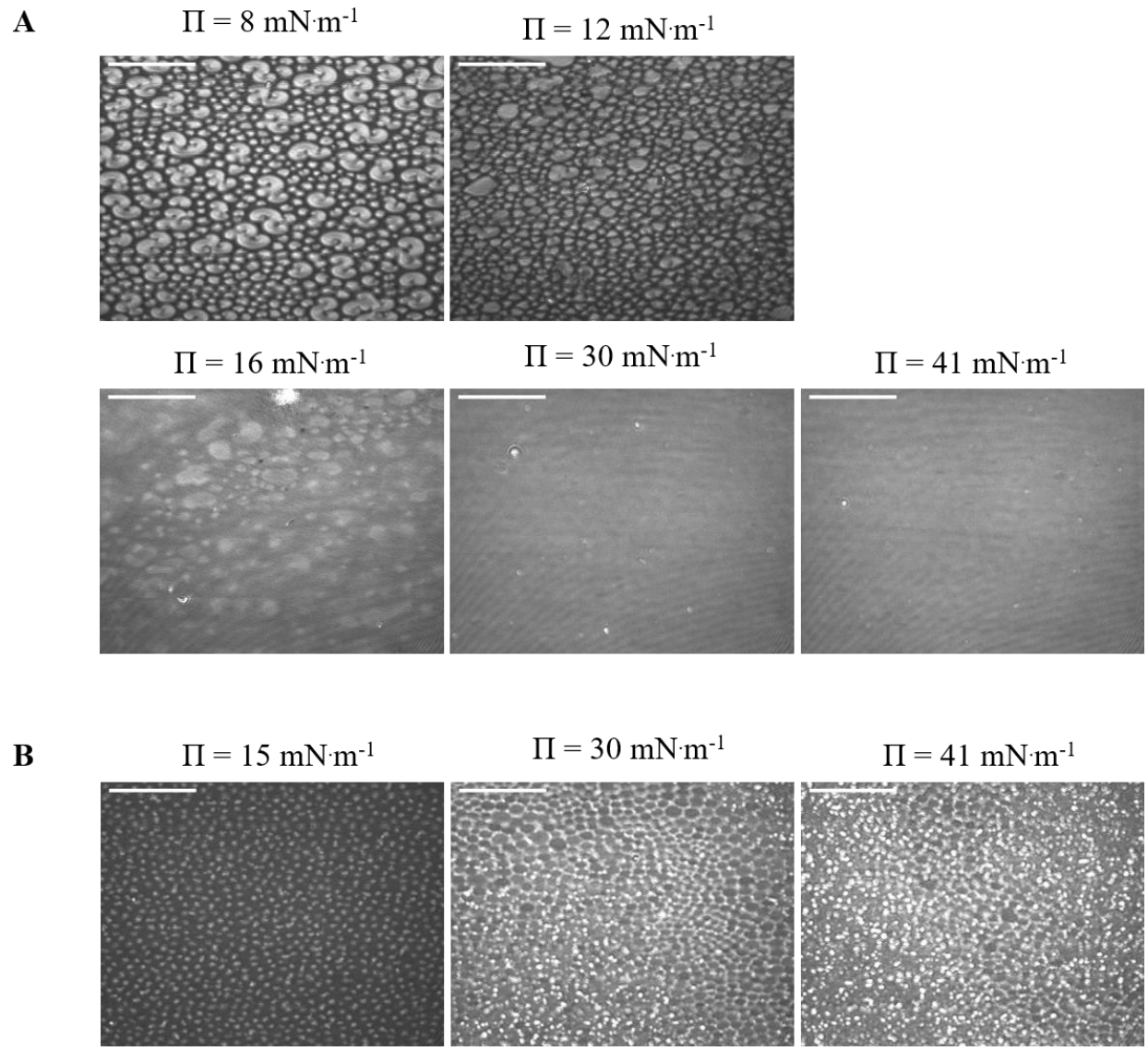

Figure S3.2 A BAM images of DPPC on pure water. As surface pressure increases, the typical bean-shaped domains of DPPC tend to fuse, indicating the transition from LE to LC phase. **B** BAM image of DPPC:PIP_2 mixed monolayer on pure water. The incorporation of PIP_2 into DPPC monolayers spread on a pure water subphase hinders the condensation of DPPC domains within the whole surface pressure range, leading to the formation of smaller domains than those found in pure DPPC monolayers[14]. This leads to the formation of a 2D emulsion-like organization of the lipids at the air/water interface, where the dispersed phase is expected to be mostly formed by DPPC in condensed phase which is surrounded by a continuous phase including DPPC in expanded phase and PIP_2 molecules (bright spots). Indeed, it has to be taken into account that the refractive index of PIP_2 headgroups (1.65 is the predicted refractive index of inositol monophosphate ring as generated using the ACD/Labs Percepta Platform - PhysChem Module) is higher than the one of DPPC headgroups, leading to brighter spots. The formation of this interfacial morphology is associated with the high negative charge of the inositol-biphosphate ring which leads to a repulsive interaction within the monolayer[63], hindering DPPC condensation. Similar interfacial morphology was also report in DPPC monolayers upon the incorporation of negatively charged silicon dioxide particles[64].

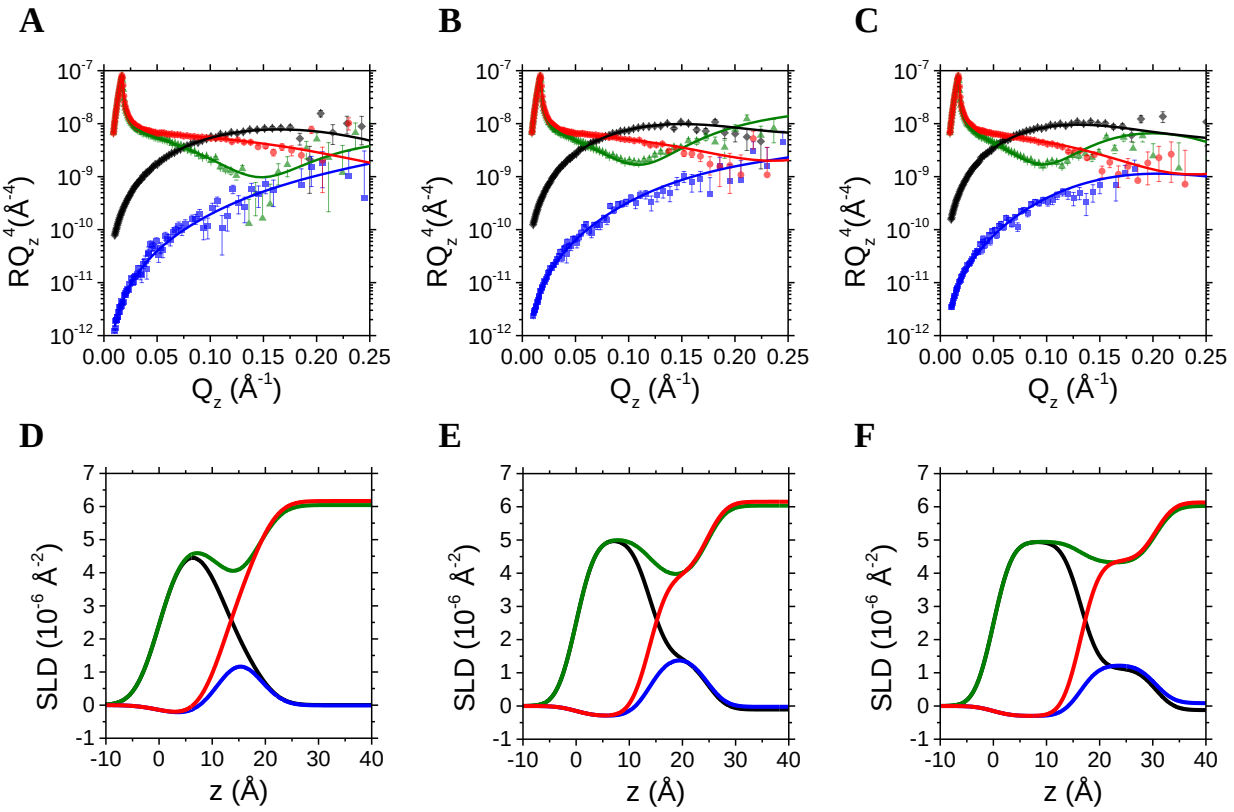

Figure S3.3 Experimental data (symbols) of neutron reflectometry of h-DPPC:PIP_2 in ACMW (blue square) and D_2O (red circles) and d62-DPPC:PIP_2 in ACMW (black diamonds) and D_2O (green triangles) monolayers, at the surface pressure value of **A** 15 mN·m^{-1}, **B** 30 mN·m^{-1} and **C** 41 mN·m^{-1}. Fitting curves (solid lines) of h-DPPC:PIP_2 in ACMW (blue) and D_2O (red) and d62-DPPC:PIP_2 in buffered ACMW (black) and D_2O (green) monolayers, at the surface pressure value of **A** 15 mN·m^{-1}, **B** 30 mN·m^{-1} and **C** 41 mN·m^{-1}. Figures are displayed on an RQ_z^4 scale to show the quality of the fits at high Q_z values. SLD profiles of h-DPPC:PIP_2 in ACMW (blue) and D_2O (red) and d62-DPPC:PIP_2 in ACMW (black) and D_2O (green) monolayers, at the surface pressure value of **D** 15 mN·m^{-1}, **E** 30 mN·m^{-1} and **F** 41 mN·m^{-1}.

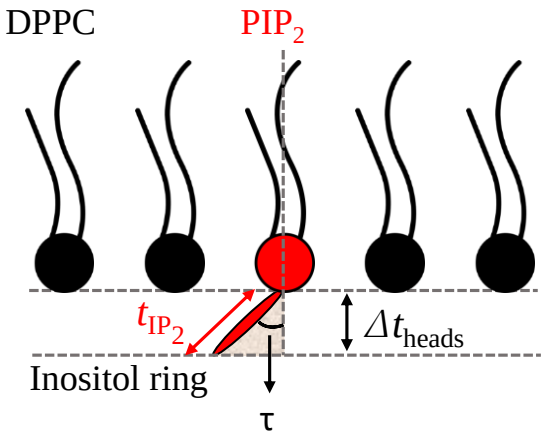

Figure S3.4 Sketch showing the procedure used to calculate the PIP_2 headgroup tilt angle (τ).

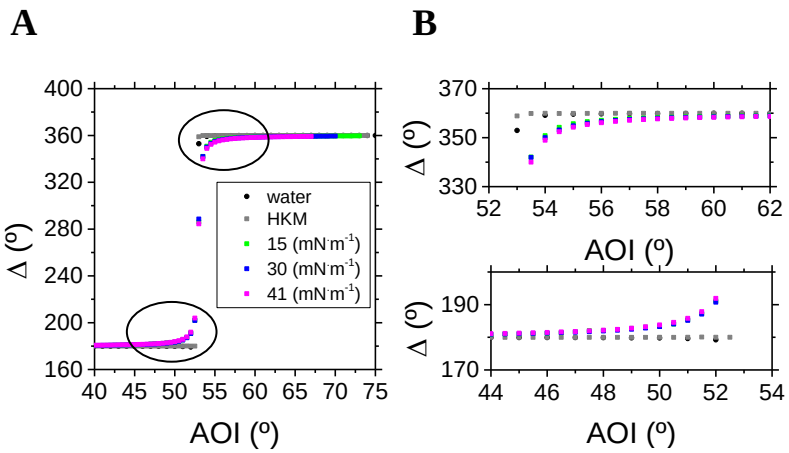

Figure S3.5 A Profiles of Δ versus AOI for bare interface using water (black circles) and HKM buffer (grey squares) as subphases; profiles of Δ versus AOI for DPPC:PIP_2 spread monolayer on HKM subphase at 15 mN·m^{-1} (green squares), 30 mN·m^{-1} (blue squares), 41 mN·m^{-1} (magenta squares). The data in the two black circles around the Brewster angle have been zooming in and shown in **B** the panels on the right.

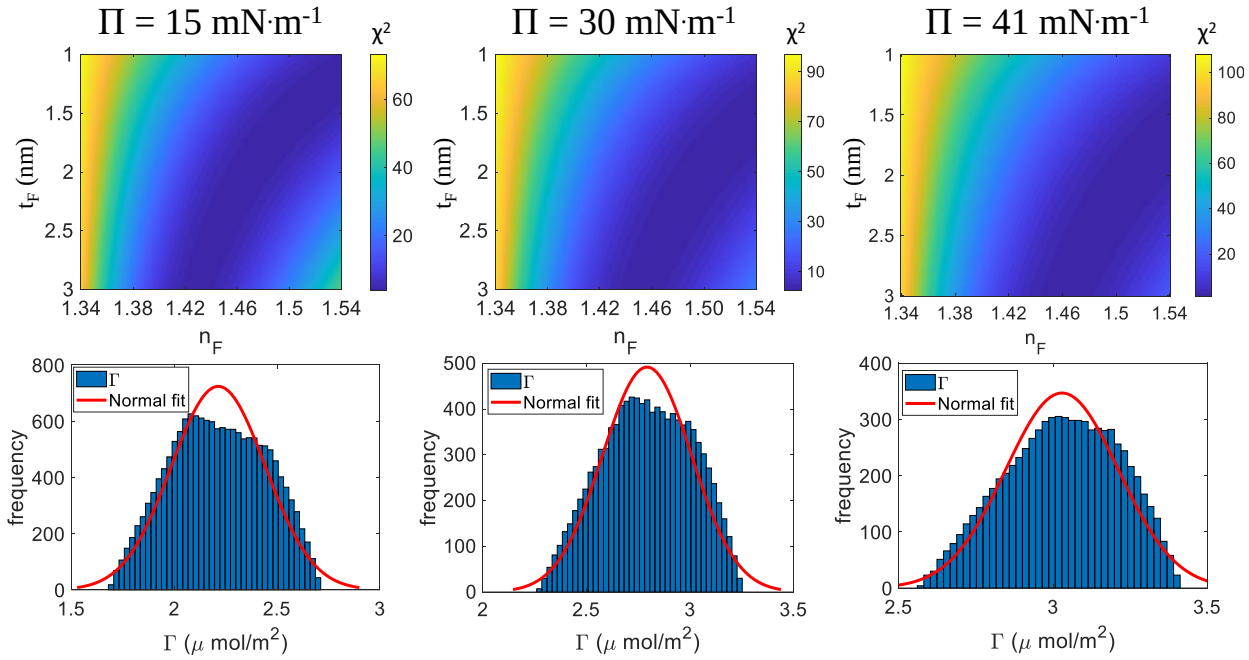

Figure S3.6 Colormaps with a range of n_F = 1.34-1.54 and t_F = 1-3 nm, matrix of 300x300 values of n_F and t_F, and tolerance of 30, and respective histograms modelled by a normal distribution (red line).

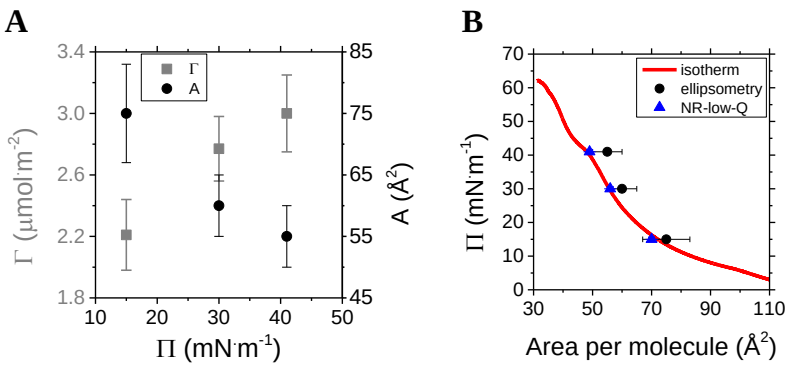

Figure S3.7 A surface excess and area per molecule (A) obtained from ellipsometry. **B** comparison between isotherm (red line) and A values obtained from ellipsometry (black circles) and NR-lowQ_z approach (blue triangles).

References

1. Czech MP. PIP2 and PIP3: Complex roles at the cell surface. *Cell*. 2000;100(6):603-606. doi:10.1016/S0092-8674(00)80696-0

2. Falkenburger BH, Jensen JB, Dickson EJ, Suh BC, Hille B. Phosphoinositides: Lipid regulators of membrane proteins. *J Physiol*. 2010;588(17):3179-3185. doi:10.1113/jphysiol.2010.192153

3. Lupyan D, Mezei M, Logothetis DE, Osman R. A molecular dynamics investigation of lipid bilayer perturbation by PIP2. *Biophys J*. 2010;98(2):240-247. doi:10.1016/j.bpj.2009.09.063

4. Ellenbroek WG, Wang YH, Christian DA, Discher DE, Janmey PA, Liu AJ. Divalent cation-dependent formation of electrostatic PIP2 clusters in lipid monolayers. *Biophys J*. 2011;101(9):2178-2184. doi:10.1016/j.bpj.2011.09.039

5. Wang YH, Collins A, Guo L, et al. Divalent cation-induced cluster formation by polyphosphoinositides in model membranes. *J Am Chem Soc*. 2012;134(7):3387-3395. doi:10.1021/ja208640t

6. Bilkova E, Pleskot R, Rissanen S, et al. Calcium Directly Regulates Phosphatidylinositol 4,5-Bisphosphate Headgroup Conformation and Recognition. *J Am Chem Soc*. 2017;139(11):4019-4024. doi:10.1021/jacs.6b11760

7. Levental I, Christian DA, Wang YH, Madara JJ, Discher DE, Janmey PA. Calcium-dependent lateral organization in phosphatidylinositol 4,5-bisphosphate (PIP2)- and cholesterol-containing monolayers. *Biochemistry*. 2009;48(34):8241-8248. doi:10.1021/bi9007879

8. McLaughlin S, Murray D. Plasma membrane phosphoinositide organization by protein electrostatic. *Nature*. 2005;438. doi:10.1038/nature04398.

9. Graber ZT, Jiang Z, Gericke A, Kooijman EE. Phosphatidylinositol-4,5-bisphosphate ionization and domain formation in the presence of lipids with hydrogen bond donor capabilities. *Chem Phys Lipids*. 2012;165(6):696-704. doi:10.1016/j.chemphyslip.2012.07.003

10. McLaughlin S, Wang J, Gambhir A, Murray D. PIP2 and proteins: Interactions, organization, and information flow. *Annu Rev Biophys Biomol Struct*. 2002;31:151-175. doi:10.1146/annurev.biophys.31.082901.134259

11. Luchini A, Nzulumike ANO, Lind TK, et al. Towards biomimics of cell membranes: Structural effect of phosphatidylinositol triphosphate (PIP 3) on a lipid bilayer. *Colloids Surfaces B Biointerfaces*. 2019;173(March 2018):202-209. doi:10.1016/j.colsurfb.2018.09.031

12. Ford MGJ, Pearse BMF, Higgins MK, et al. Simultaneous binding of PtdIns (4,5) P2 and clathrin by AP180 in the nucleation of clathrin lattices on membranes. *Science*. 2001;291(5506):1051-1055. doi:10.1126/science.291.5506.1051

13. Miller SE, Mathiasen S, Bright NA, et al. CALM Regulates Clathrin-Coated Vesicle Size and Maturation by Directly Sensing and Driving Membrane Curvature. *Dev Cell*. 2015;33(2):163-175. doi:10.1016/j.devcel.2015.03.002

14. Dietrich U, Krüger P, Gutberlet T, Käs JA. Interaction of the MARCKS peptide with PIP2 in phospholipid monolayers. *Biochim Biophys Acta - Biomembr*. 2009;1788(7):1474-1481. doi:10.1016/j.bbamem.2009.04.001

15. Golebiewska U, Kay JG, Masters T, et al. Evidence for a fence that impedes the diffusion of phosphatidylinositol 4,5-bisphosphate out of the forming phagosomes of macrophages. *Mol Biol Cell*. 2011;22(18):3498-3507. doi:10.1091/mbc.E11-02-0114

16. McMahon HT, Boucrot E. Membrane curvature at a glance. *J Cell Sci*. 2015;128(6):1065-1070. doi:10.1242/jcs.114454

17. Ford MGJ, Mills IG, Peter BJ, et al. Curvature of clathrin-coated pits driven by epsin. *Nature*. 2002;419(6905):361-366. doi:10.1038/nature01020

18. Owen DJ, Collins BM, Evans PR. ADAPTORS FOR CLATHRIN COATS: Structure and Function. *Annu Rev Cell Dev Biol*. 2004;20(1):153-191. doi:10.1146/annurev.cellbio.20.010403.104543

19. McMahon HT, Gallop JL. Membrane curvature and mechanisms of dynamic cell membrane remodelling. *Nature*. 2005;438(7068):590-596. doi:10.1038/nature04396

20. Li Z, Venable RM, Rogers LA, Murray D, Pastor RW. Molecular dynamics simulations of PIP2 and PIP3 in lipid bilayers: Determination of ring orientation, and the effects of surface roughness on a Poisson-Boltzmann description. *Biophys J*. 2009;97(1):155-163. doi:10.1016/j.bpj.2009.04.037

21. Wu EL, Qi Y, Song KC, Klauda JB, Im W. Preferred orientations of phosphoinositides in bilayers and their implications in protein recognition mechanisms. *J Phys Chem B*. 2014;118(16):4315-4325. doi:10.1021/jp500610t

22. Baumann MK, Amstad E, Mashaghi A, Textor M, Reimhult E. Characterization of supported lipid bilayers incorporating and phosphoinositol-3,4,5-triphosphate by complementary techniques. *Biointerphases*. 2010;5(4):114-119. doi:10.1116/1.3516485

23. Ghosh SK, Castorph S, Konovalov O, Jahn R, Holt M, Salditt T. In vitro study of interaction of synaptic vesicles with lipid membranes. *New J Phys*. 2010;12. doi:10.1088/1367-2630/12/10/105004

24. Bertsch P, Bergfreund J, Windhab EJ, Fischer P. Physiological fluid interfaces: Functional microenvironments, drug delivery targets, and first line of defense. *Acta Biomater*. 2021;130:32-53. doi:10.1016/j.actbio.2021.05.051

25. Ortiz-Collazos S, Picciani PHS, Oliveira ON, Pimentel AS, Edler KJ. Influence of levofloxacin and clarithromycin on the structure of DPPC monolayers. *Biochim Biophys Acta - Biomembr*. 2019;1861(10):182994. doi:10.1016/j.bbamem.2019.05.016

26. Guzmán E, Santini E. Lung surfactant-particles at fluid interfaces for toxicity assessments. *Curr Opin Colloid Interface Sci*. 2019;39:24-39. doi:10.1016/j.cocis.2019.01.003

27. Ravera F, Miller R, Zuo YY, et al. Methods and models to investigate the physicochemical functionality of pulmonary surfactant. *Curr Opin Colloid Interface Sci*. 2021;55:101467. doi:10.1016/j.cocis.2021.101467

28. Bartkowiak A, Rojewska M, Prochaska K. Study of mucin interaction with model phospholipid membrane at the air–water interface. *Colloids Surfaces A Physicochem Eng Asp*. 2019;578(March):123587. doi:10.1016/j.colsurfa.2019.123587

29. Ege C, Lee KYC. Insertion of Alzheimer's Aβ40 peptide into lipid monolayers. *Biophys J*.

2004;87(3):1732-1740. doi:10.1529/biophysj.104.043265

30. Santamaria A, Batchu KC, Matsarskaia O, et al. Strikingly Different Roles of SARS-CoV-2 Fusion Peptides Uncovered by Neutron Scattering. *J Am Chem Soc*. 2022. doi:10.1021/jacs.1c09856

31. Schneider CA, Rasband WS, Eliceiri KW. NIH Image to ImageJ: 25 years of image analysis. *Nat Methods 2012 97*. 2012;9(7):671-675. doi:10.1038/nmeth.2089

32. Campbell RA, Wacklin HP, Sutton I, Cubitt R, Fragneto G. FIGARO: The new horizontal neutron reflectometer at the ILL. *Eur Phys J Plus*. 2011;126(11):1-22. doi:10.1140/epjp/i2011-11107-8

33. Campbell RA, Saaka Y, Shao Y, et al. Structure of surfactant and phospholipid monolayers at the air/water interface modeled from neutron reflectivity data. *J Colloid Interface Sci*. 2018;531:98-108. doi:10.1016/j.jcis.2018.07.022

34. Braun L, Uhlig M, von Klitzing R, Campbell RA. Polymers and surfactants at fluid interfaces studied with specular neutron reflectometry. *Adv Colloid Interface Sci*. 2017. doi:10.1016/j.cis.2017.07.005

35. Gutfreund P, Saerbeck T, Gonzalez MA, et al. Towards generalized data reduction on a chopperbased time-of-flight neutron reflectometer. *J Appl Crystallogr*. 2018. doi:10.1107/S160057671800448X

36. Carrascosa-Tejedor J, Santamaria A, Pereira D, Maestro A. Structure of DPPC Monolayers at the Air/Buffer Interface: A Neutron Reflectometry and Ellipsometry Study. *Coatings 2020, Vol 10, Page 507*. 2020;10(6):507. doi:10.3390/COATINGS10060507

37. Arriaga LR, Löpez-Montero I, Ignés-Mullol J, Monroy F. Domain-growth kinetic origin of nonhorizontal phase coexistence plateaux in langmuir monolayers: Compression rigidity of a raft-like lipid distribution. *J Phys Chem B*. 2010;114(13):4509-4520. doi:10.1021/jp9118953

38. Nagle JF, Scott HL. Lateral compressibility of lipid mono- and bilayers. Theory of membrane permeability. *BBA - Biomembr*. 1978;513(2):236-243. doi:10.1016/0005-2736(78)90176-1

39. Adams EM, Casper CB, Allen HC. Effect of cation enrichment on dipalmitoylphosphatidylcholine (DPPC) monolayers at the air-water interface. *J Colloid Interface Sci*. 2016;478:353-364. doi:10.1016/j.jcis.2016.06.016

40. Hénon S, Meunier J. Microscope at the Brewster angle: Direct observation of first-order phase transitions in monolayers. *Rev Sci Instrum*. 1991;62(4):936-939. doi:10.1063/1.1142032

41. Daear W, Mahadeo M, Prenner EJ. Applications of Brewster angle microscopy from biological materials to biological systems. *Biochim Biophys Acta - Biomembr*. 2017;1859(10):1749-1766. doi:10.1016/j.bbamem.2017.06.016

42. Wen Y, Vogt VM, Feigenson GW. Multivalent Cation-Bridged PI(4,5)P2 Clusters Form at Very Low Concentrations. *Biophys J*. 2018;114(11):2630-2639. doi:10.1016/j.bpj.2018.04.048

43. Jurak M, Szafran K, Cea P, Martín S. Analysis of Molecular Interactions between Components in Phospholipid-Immunosuppressant-Antioxidant Mixed Langmuir Films. *Langmuir*. 2021;37(18):5601-5616. doi:10.1021/acs.langmuir.1c00434

44. Campbell RA, Tummino A, Noskov BA, Varga I. Polyelectrolyte/surfactant films spread from neutral aggregates. *Soft Matter*. 2016;12(24):5304-5312. doi:10.1039/c6sm00637j

45. Llamas S, Fernández-Penã L, Akanno A, et al. Towards understanding the behavior of polyelectrolyte-surfactant mixtures at the water/vapor interface closer to technologically-relevant conditions. *Phys Chem Chem Phys*. 2018;20(3):1395-1407. doi:10.1039/c7cp05528e

46. Braslau A, Deutsch M, Pershan PS, Weiss AH, Als-Nielsen J, Bohr J. Surface roughness of water measured by x-ray reflectivity. *Phys Rev Lett*. 1985;54(2):114-117. doi:10.1103/PhysRevLett.54.114

47. Sinha SK, Sirota EB, Garoff S, Stanley HB. X-ray and neutron scattering from rough surfaces. *Phys Rev B*. 1988;38(4):2297-2311. doi:10.1103/PhysRevB.38.2297

48. Maestro A, Gutfreund P. In situ determination of the structure and composition of Langmuir monolayers at the air/water interface by neutron and X-ray reflectivity and

ellipsometry. *Adv Colloid Interface Sci*. 2021;293:102434. doi:10.1016/j.cis.2021.102434

49. Vaknin D, Kjaer K, Als-Nielsen J, Lösche M. Structural properties of phosphatidylcholine in a monolayer at the air/water interface: Neutron reflection study and reexamination of x-ray reflection measurements. *Biophys J*. 1991;59(6):1325-1332. doi:10.1016/S0006-3495(91)82347-5

50. Naumann C, Brumm T, Rennie AR, Penfold J, Bayerl TM. Hydration of DPPC Monolayers at the Air/Water Interface and Its Modulation by the Nonionic Surfactant C12E4: A Neutron Reflection Study. *Langmuir*. 1995;(11):3948-3952.

51. Nagle JF, Wiener MC. Structure of fully hydrated bilayer dispersions. *BBA - Biomembr*. 1988;942(1):1-10. doi:10.1016/0005-2736(88)90268-4

52. Vacklin HP, Tiberg F, Thomas RK. Formation of supported phospholipid bilayers via co-adsorption with β-D-dodecyl maltoside. *Biochim Biophys Acta - Biomembr*. 2005;1668(1):17-24. doi:10.1016/j.bbamem.2004.11.001

53. Sun WJ, Suter RM, Knewtson MA, et al. Order and disorder in fully hydrated unoriented bilayers of gel-phase dipalmitoylphosphatidylcholine. *Phys Rev E*. 1994;49(5):4665-4676. doi:10.1103/PhysRevE.49.4665

54. Nelson A. Co-refinement of multiple-contrast neutron/X-ray reflectivity data using MOTOFIT. *J Appl Crystallogr*. 2006;39(2):273-276. doi:10.1107/S0021889806005073

55. Maranville BB, Green A, Kienzle PA. Distributed Error-Function Roughness in Refl1d Reflectometry Fitting Program. 2018;XXX(1):1-4.

56. Armen RS, Uitto OD, Feller SE. Phospholipid component volumes: Determination and application to bilayer structure calculations. *Biophys J*. 1998;75(2):734-744. doi:10.1016/S0006-3495(98)77563-0

57. Nagle JF, Tristram-Nagle S. Structure of lipid bilayers. *Biochim Biophys Acta - Rev Biomembr*. 2000. doi:10.1016/S0304-4157(00)00016-2

58. Azzam RMA, Bashara NM. *Ellipsometry and Polarized Light*. New York: North-Holland Publishing Company; 1977.

59. Conn AR, Scheinberg K, Vicente LN. *Introduction to Derivative-Free Optimization*. Society for Industrial and Applied Mathematics; 2009. doi:10.1137/1.9780898718768

60. Guzmán E, Ritacco H, Ortega F, Svitova T, Radke CJ, Rubio RG. Adsorption kinetics and mechanical properties of Ultrathin polyelectrolyte multilayers: Liquid-supported versus solid-supported films. *J Phys Chem B*. 2009;113(20):7128-7137. doi:10.1021/jp811178a

61. De Feijter JA, Benjamins J, Veer FA. Ellipsometry as a tool to study the adsorption behavior of synthetic and biopolymers at the air–water interface. *Biopolymers*. 1978;17(7):1759-1772. doi:10.1002/bip.1978.360170711

62. Erbe A, Sigel R. Tilt angle of lipid acyl chains in unilamellar vesicles determined by ellipsometric light scattering. *Eur Phys J E*. 2007;22(4):303-309. doi:10.1140/epje/e2007-00038-5

63. Levental I, Janmey PA, Cebers A. Electrostatic contribution to the surface pressure of charged monolayers containing polyphosphoinositides. *Biophys J*. 2008;95(3):1199-1205. doi:10.1529/biophysj.107.126615

64. Guzmán E, Orsi D, Cristofolini L, Liggieri L, Ravera F. Two-Dimensional DPPC based emulsion-like structures stabilized by silica nanoparticles. *Langmuir*. 2014;30(39):11504-11512. doi:10.1021/la502183t

Chapter 4

Investigation on the relationship between lipid composition and structure in model membranes composed of extracted natural phospholipids[a]

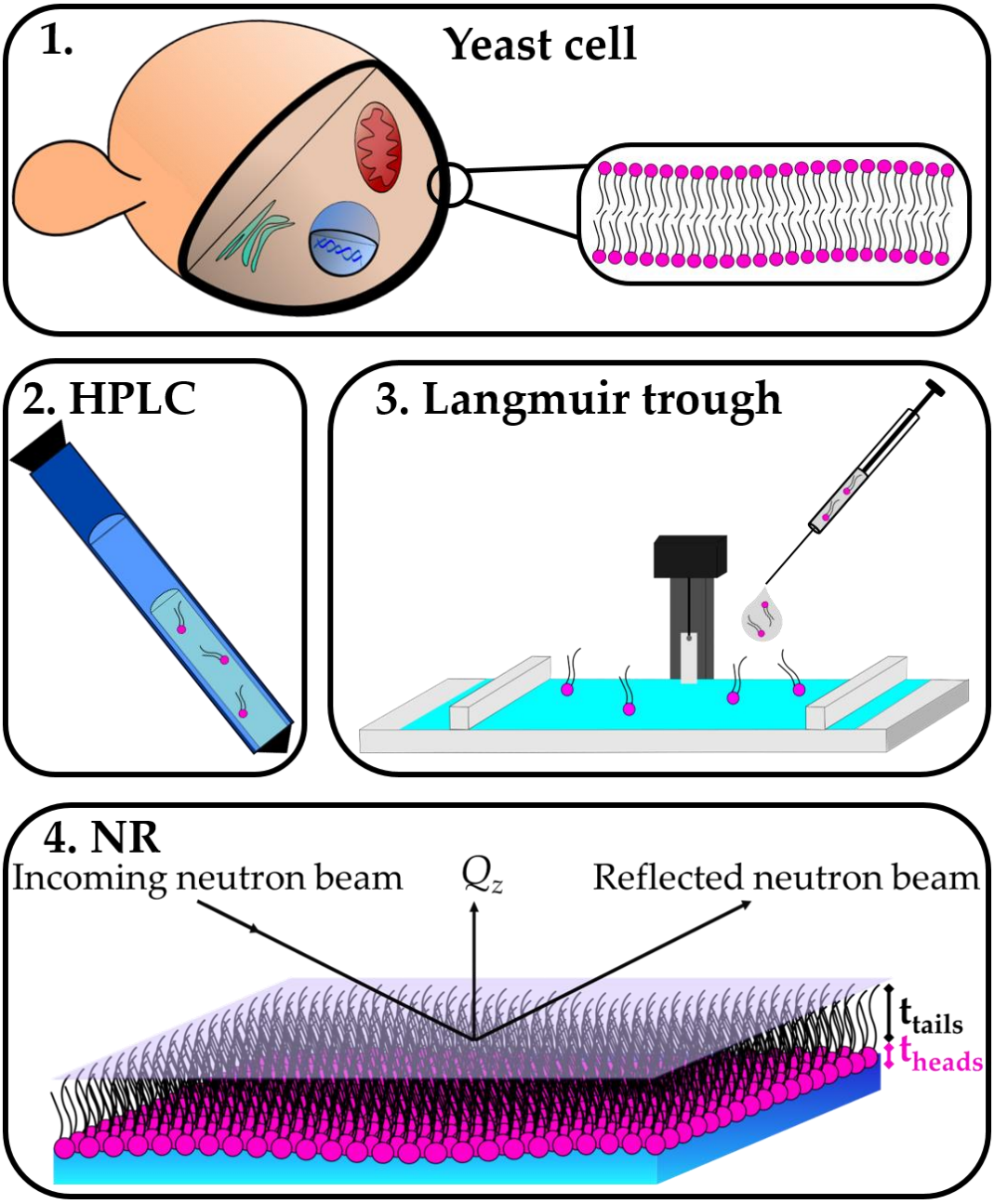

[a] This work has been submitted to the *Journal of colloids and interface science* (see the Publication List at page 279).

Abstract

Unravelling the structural diversity of cellular membranes is a paramount challenge in life sciences. In particular, lipid composition affects the membrane collective behaviour, and its interactions with other biological molecules. Here, the relationship between membrane composition and resultant structural features was investigated by surface pressure-area isotherms, Brewster angle microscopy and neutron reflectometry on *in vitro* membrane models of the mammalian plasma and endoplasmic-reticulum-Golgi intermediate compartment membranes in the form of Langmuir monolayers. Natural extracted yeast lipids were used because, unlike synthetic lipids, the acyl chain saturation pattern of yeast and mammalian lipids are similar. The structure of the model membranes, orthogonal to the plane of the membrane, as well as their lateral packing, was found to depend strongly on their specific composition, with cholesterol having a major influence on the in-plane morphology, yielding a coexistence of liquid-order and liquid-disorder phases.

1. Introduction

Lipid molecules constitute the building blocks of cellular membranes. The main constituents of mammalian membranes are glycerophospholipids, including zwitterionic phosphatidylcholines (PC) and phosphatidylethanolamines (PE), and lower proportions of anionic phosphatidylserines (PS) and phosphatidylinositols (PI). The lipid hydrophobic moiety consists of a diacylglycerol that contains saturated or *cis*-unsaturated fatty acyl chains of variable extent and unsaturation degree[1]. Due to their unique chemistry, including hydrophobic acyl chains and polar headgroups, these phospholipids spontaneously self-assemble as bilayers with the hydrophobic acyl chains facing each other and the polar headgroups interacting with the external aqueous phase. In particular, PC is well known to provide a stable, fluid environment due to its liquid crystalline arrangement, while PE, due to its relatively small polar headgroup, creates defects in the membrane bilayer that facilitates fusion as well as the interaction with peripheral membrane proteins[2]. Finally, PS and PI, even at low concentrations, provide the negative charge of the membranes, which is a key factor in the interaction with positively charged patches of proteins[2–4]. Synthetic versions of PC, PE, PS and PI phospholipids, usually with 16- or 18-carbon acyl chains, which are the most abundant in cell membranes[5,6], have been used to mimic eukaryotic membranes[7–9]. However, the latter are much more complex systems, being characterized by differently unsaturated acyl chains as well as

by the presence of sterols and sphingolipids, such as sphingomyelin (SM). Another important feature of the plasma membrane (PM) is the high levels of cholesterol[10,11] (~ 50% in mol), and the formation of lipid rafts, due to the immiscibility of cholesterol (and saturated lipids) with unsaturated lipids[12]. These rafts would help to concentrate proteins as well as lipids locally, enabling cellular processes such as budding of enveloped viruses and sorting of lipids and proteins to the Golgi complex[12]. The endoplasmic-reticulum-Golgi intermediate compartment, ERGIC, membrane (EM) is also a membrane of biological interest, which contains a lower amount of cholesterol, as it provides an anchoring point for viral proteins[13]. The ERGIC is an organelle that lies between the endoplasmic reticulum and the Golgi complex, mediating trafficking between them and facilitating the sorting of cargo[14].

In the present work, Langmuir lipid monolayers were exploited to accurately replicate the EM[15,16] and the PM[10]. Indeed, the structural characterization of these membranes may shed light on their function and malfunction. A simpler lipid mixture, lacking cholesterol and sphingomyelin, was also prepared in order to characterize a monolayer uniquely composed of three natural phospholipids, PC-PE-PS (**Figure 4.1 A** shows the molar lipid compositions used in this work). Previously, synthetic lipid monolayers, for example using DPPC (1,2-dipalmitoyl-sn-glycerol-3-phosphocholine) and POPC (1-palmitoyl-2-oleoyl-glycero-3-phosphocholine), or complex mixtures such as the so called canonical mixture (containing POPC, sphingomyelin and cholesterol), were employed to mimic cellular membranes as well as lung surfactants[17–26]. The versatility of Langmuir monolayers allows the lipid structure and organisation at the air/water interface to be investigated with a plethora of interfacial *in situ* techniques[27–29]. Here, Langmuir monolayers composed of natural lipids were studied by surface pressure-area isotherms, Brewster angle microscopy (BAM) and neutron reflectometry (NR). The latter technique is especially suited for the study of biological interfaces. Indeed, neutrons are non-destructive, thus allowing structural characterisation with sub-nanometric resolution in physiological conditions and temperatures. Moreover, neutrons interact very differently with hydrogen and deuterium nuclei, therefore, through isotopic substitution, it is possible to highlight structural and chemical differences in specific regions of interest such as, for example, identifying the presence of water molecules and the position and orientation of hydrophobic tails and polar headgroups.[27]

The combined experimental approach used in this work shed light on the interfacial structure of *in vitro* model systems of the plasma and ERGIC membranes, with emphasis on the structural

effects associated with the incorporation of cholesterol in the membranes. Although natural lipids were previously used in the form of bi- and multilayers to mimic eukaryotic cell membranes, which were then characterized by neutron reflectometry[30,31] and diffraction[32,33], to the best of our knowledge, this is the first report describing the use of natural lipids extracted from yeast and studied in the form of monolayers at the air/water interface, in order to mimic biological relevant membranes, and to provide direct structural evidences about the role of cholesterol. The possibility of tuning and controlling the composition and surface density of phospholipids makes Langmuir films effective models for mimicking single leaflets of cell membranes under different environmental conditions. Such *in vitro* lipid model systems could potentially be exploited to study the interaction of cell membranes with external stimuli, such as viral proteins[34] or antimicrobial peptides[35–37].

2. Materials and Methods

2.1. Natural lipid extraction and purification

The phospholipids were extracted from perdeuterated and hydrogenous *Pichia pastoris* biomasses. Harvested cells were suspended into 10 mL deionised water and lysed by probe sonication on an ice bath for 3×5 min with 30 s intervals, 25% duty cycle. The resulting cell lysate was poured into boiling ethanol containing 1% butylated hydroxytoluene (BHT) followed by vigorous stirring to denature lipases. The total lipid mixtures were then extracted according to the method proposed by Folch et al.[38], followed by evaporation of the organic phase under a N_2 stream and their final reconstitution in $CHCl_3$. Purification of the various classes of phospholipid mixtures containing molecular species of mixed acyl chain lengths was achieved through sequential purifications steps, first by passing the lipid extracts through an amino-bonded solid-phase extraction column followed by a diol-modified silica stationary phase column coupled to a High-performance Liquid Chromatography-Evaporative light scattering detector (HPLC-ELSD) (Agilent 1260, United Kingdom) system. The mobile phase employed was a gradient of solvent A ($CHCl_3$/CH_3OH/NH_4OH, 80:20.5:0.5 *v/v*) and solvent B ($CHCl_3$/CH_3OH/H_2O/NH_4OH, 60:35:5.5:0.5 *v/v*)[39]. TLC analysis was carried out on a High-Performance Thin-Layer Chromatography (HP-TLC) system (CAMAG, Muttenz, Switzerland) to assess the identity and purity of each of the purified classes. Fatty acid compositions of such purified mixtures were measured by Gas Chromatography-Flame Ionization Detection (GC-FID), see **Table S4.1**.

2.2. Other lipids and reagents

Cholesterol (purity≥99.0%) and natural extracted sphingomyelin (egg, chicken, purity≥99.0%) were purchased from Avanti Polar Lipids (Alabaster, AL, USA). Deuterated cholesterol was obtained from the National Deuteration Facility (NDF) in ANSTO (Australia). Ultra-pure water was generated by passing deionized water through a Milli-Q unit (total organic content=4 ppb; resistivity=18 mΩ·cm, Milli-Q, Merck KGaA, Darmstadt, Germany). D_2O (99.9% of isotopical purity) was purchased from Sigma Aldrich and used as received. HEPES-NaCl buffer (5 mM HEPES, 150 mM NaCl, pH=7) was used for the experiments. HEPES (in solution, 1 M in H_2O, and powder, purity 99.5%), and sodium chloride (purity≥99.0%) were purchased from Sigma Aldrich.

2.3. Lipid mixture solutions preparation

Lipid stock solutions were prepared in chloroform stabilized with ethanol (purity 99.8%; Sigma Aldrich, St. Louis, MO, USA), and stored at -20°C. Solutions with the desired composition (shown in **Figure 4.1 A** and **Table S4.2**) of 0.2 mg·mL^{-1} were then prepared and used to perform all the experiments. The relative percentage of 16- and 18-carbon chains of each lipid could be estimated from their molar ratios and acyl chain composition (see **Table S4.3**).

2.4. Surface pressure (Π)-area (A) isotherm

The surface pressure (Π)-area per molecule (A) isotherms were measured using a Langmuir trough (KIBRON, Helsinki, Finland) with a maximum area of 166.4 cm^2 coupled to a force balance fitted with a contact probe. The trough was carefully cleaned with Decon90, ethanol and Milli-Q water before filling it with 120 mL of HEPES-NaCl buffer. Subsequently, the lipid solutions were spread on the clean subphase using a Hamilton micro-syringe with a precision of ±1 µL. After the chloroform was evaporated for about 20 min, the variation of surface pressure during compression was recorded using a Wilhelmy plate made of filter paper as contact probe and applying a barrier speed of 8 cm^2·min^{-1}. The temperature of the subphase was maintained at 21.0±0.5 °C. Measurements always started after temperature stabilization. From the Π-A isotherms, the corresponding compressional elastic modulus (C_s^{-1}) was calculated as follows:

$$C_s^{-1} = -\mathrm{A} \cdot \left(\frac{\partial \Pi}{\partial \mathrm{A}}\right) \qquad \textbf{4.1}$$

2.5. Neutron reflectometry data acquisition

Neutron reflectometry (NR) experiments were performed on FIGARO, a time-of-flight reflectometer[40–42] at the Institut Laue-Langevin, Grenoble (France) using two different angles of incidence (θ_1=0.6° and θ_2=3.8°). The wavelength resolution of 7% $d\lambda/\lambda$ was used, yielding a momentum transfer of 0.007 $Å^{-1} < Q_z < 0.25$ $Å^{-1}$, normal to the interface, and defined as:

$$Q_z = \frac{4\pi}{\lambda}\sin(\theta) \qquad \textbf{4.2}$$

where λ (from 3 to 20 Å) is the wavelength of the neutron beam. Reflectivity, $R(Q_z)$, is defined as the ratio of the intensity of the neutrons scattered from the air/water interface over the incident intensity of the neutron beam. The raw time-of-flight experimental data at these two angles of incidence were calibrated with respect to the incident wavelength distribution and the efficiency of the detector yielding the resulting $R(Q_z)$ profile, using COSMOS[43]. NR experiments were performed under different contrast conditions, using pH buffered subphases: 8.1% D_2O *v/v* and 100% D_2O. The former is generally known as air contrast matched water (ACMW) since its scattering length density is equal to the one of air, which is zero.

2.6. Neutron reflectometry data modelling

The measured $R(Q_z)$ profile can be linked to an in-plane averaged scattering length density (SLD) profile perpendicular to the interface, which is a measure of the coherent scattering cross-section of the molecular species that constitute each interfacial layer, and is linked to their chemical composition and molecular volume, V, as $SLD = \sum_i(b_i \cdot n_i)$, where $n_i = 1/V_i$ is the number density and b_i is the scattering length of each molecular species. Data modelling was performed by minimizing the difference between the experimental data points and the calculated reflectivity profile. The latter was obtained by a model consisting of two layers of constant SLD using Parratt's recursive method[44], with an error function connecting adjacent layers[45]. The two-layer model (see **Figure 4.1 B**) can be rationalized by dividing phospholipid molecules between polar headgroups in contact with the liquid subphase and aliphatic tails facing the air phase as they have different averaged SLDs. Molecular volumes of the lipid headgroups (V_h) and tails (V_t) and the total scattering length of headgroups (Σb_h) and tails (Σb_t) were fixed parameters in the fitting procedure (see **Table S4.4**). The roughness of the three interfaces (air/tails-layer, tails-layer/heads-layer, and heads-layer/subphase), whose minimum value depends on the capillary waves of the aqueous subphase[46,47], was assumed identical following the approach reported by Campbell et al.[41]

Molecular volumes were calculated taking into account the different percentages of unsaturation in the acyl chains (see **Table S4.1**). Data analysis (using AuroreNR v5.0[48], MOTOFIT[49] and Refnx[50] programs) was completed by simultaneous co-refinement of all data sets obtained with a global minimization of a least-squares function χ^2 to reduce the ambiguity in the modelling. Experimental data of the same monolayer in the different isotopic contrasts were fitted together. Using this approach, the fitting variables determined through the fitting procedure were the interfacial roughness (r), the thicknesses of tails- and headgroups-layer (t_t and t_h, respectively), the water volume fraction in the headgroups-layer (f_{wh}), whose value was constrained to ensure the same area per molecule of tails (A_t) and headgroups (A_h) following:

$$A_i = \frac{\Sigma b_i}{SLD_i \cdot t_i \cdot (1 - f_{wi})} \quad \textbf{4.3}$$

where SLD_i, t_i, Σb_i and f_{wi} are, respectively, the scattering length density, the thickness, the total scattering length and the water volume fraction of the *i*-th layer (tails or headgroups). The water volume fraction in the tails-layer (f_{wt}) was fixed to zero, leading to the following expression:

$$f_{wh} = 1 - \frac{t_t \cdot V_h}{t_h \cdot V_t} \quad \textbf{4.4}$$

In addition, to account for the existence of lateral inhomogeneities of the lipid monolayers on the length scale of the in-plane neutron coherence length (on the order of 10-30 μm[27]), the experimental curves were also fitted using a mixed area reflectivity model based on the incoherent sum of reflectivity corresponding to areas with different lipids content. In this approach, the overall reflectivity was considered a weighted average of the reflectivity from two regions of different lipid coverage, denoted as α and β, as $R = f_\alpha \cdot R_\alpha + f_\beta \cdot R_\beta$, where $f_\alpha + f_\beta = 1$.

2.7. Brewster angle microscopy

In situ visualization of the morphology of Langmuir monolayers at the air/water interface was performed using a Brewster angle microscope Nanofilm EP3 (Accurion, GmbH, Göttingen, Germany) coupled to the previously described Langmuir trough. In brief, spatial reflectivity modulations are correlated with optically different monolayer phases depending on lateral ordering and/or lipid packing density. The instrument was equipped with a 50 mW laser emitting p-polarized light at a wavelength 532 nm focused directly at the air/water interface at the Brewster angle (53.1°). The reflected light is captured by a CCD camera through a 10x magnification objective and a polarizer. The spatial resolution was 2μm and the field of view 350 × 275 μm^2.

3. Results

Stable monolayers composed of natural lipids were studied. Briefly, phospholipids extracted from yeast were mixed together with cholesterol and sphingomyelin, in molar ratios to mimic the plasma and ERGIC membranes, and then deposited at the air/water interface (**Figure 4.1 A** and **Table S4.2**). A simpler mixture was also prepared without cholesterol and sphingomyelin (PC-PE-PS). The resultant Langmuir monolayers were characterized by Π-A isotherms (**Figure 4.2**), BAM (**Figure 4.3**) and NR (**Figures 4.4** and **4.5**). While the isotherms provided information concerning lipid phase, lateral packing and cohesion of the film spread at the air/water interface, BAM was used to visualize the in-plane interfacial organization of lipid monolayers and NR yielded the out-of-plane structure of the monolayers, including their thickness and water content (**Figure 4.7** and **Table S4.5**).

Thanks to the possibility of tuning lipid composition in Langmuir monolayers, these are remarkably simple model systems that report structural similitudes with single leaflets composing bilayers in cellular membranes. Here, concretely, PM and EM model systems, with average lipid compositions between those corresponding to both inner and outer leaflets, were studied. However, there are some limitations of the Langmuir lipid monolayers used here, as, for example, to address the effect of bilayer asymmetry and inter-leaflet coupling in model membranes[51]. These are beyond the scope of this work.

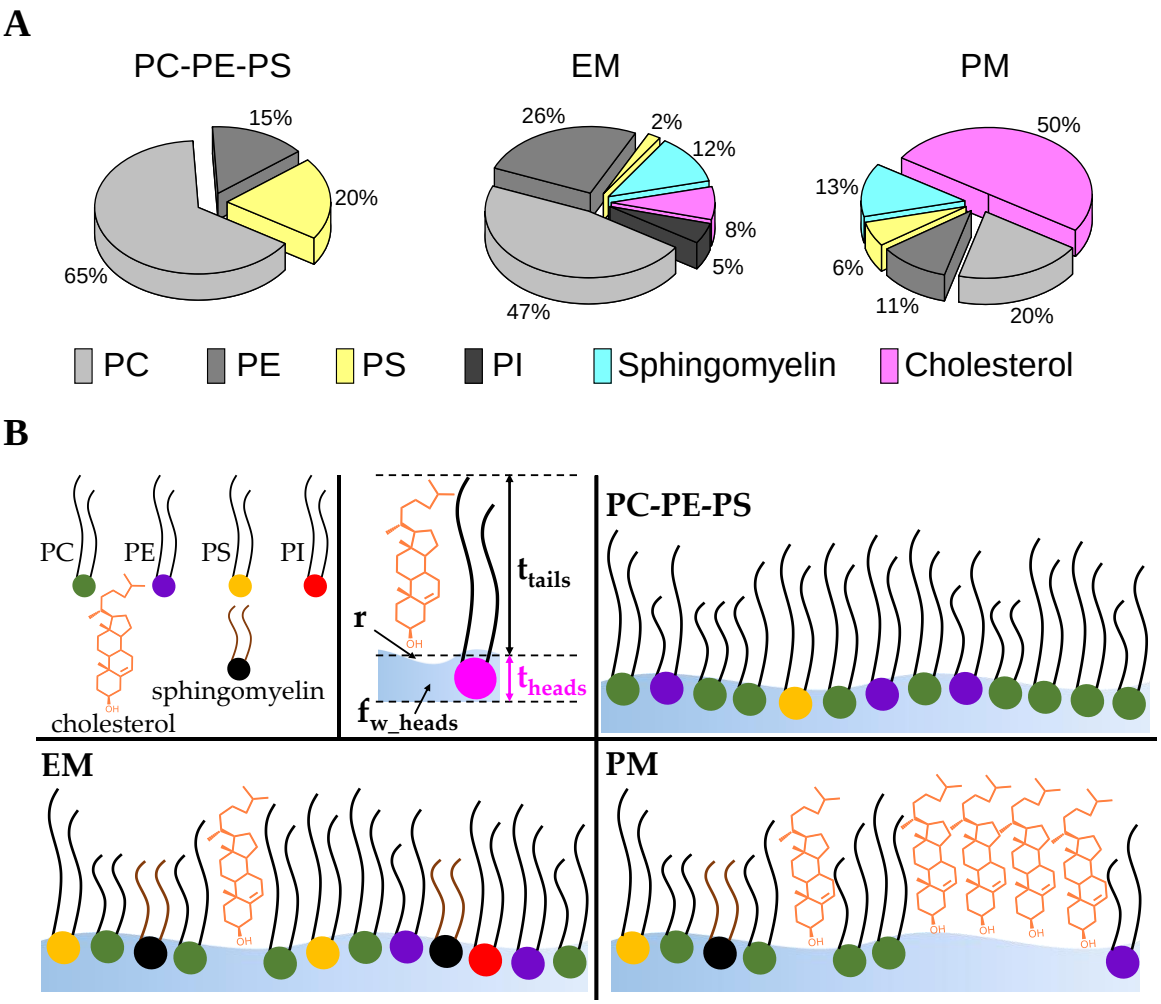

Figure 4.1 A Pie charts representing the different lipid compositions used in this study: PC-PE-PS mixture, ERGIC membrane[15,16] and plasma membrane[10] mimicking monolayers. **B** Sketch representing the Langmuir monolayers with the different lipid composition and the models used for the NR analysis that consist in dividing the lipids in polar headgroups-layer and acyl chains-layer, with constant scattering length density.

3.1. Langmuir monolayer composed of solely natural lipid extracted from yeast: surface pressure-area isotherm and out-of-plane structure.

The relationship between the area per molecule and the surface pressure of Langmuir monolayers composed of natural lipids spread at the air/water interface was investigated. The Π-A isotherm for monolayers of hydrogenous lipids at 21°C is shown in **Figure 4.2 A**. The corresponding compressional elastic modulus C_s^{-1}, derived from the Π-A isotherms and calculated according to **Equation 4.1**, is shown in **Figure 4.2 B** and **C**. As the pressure increases in a continuous manner, the Π-A isotherm of the PC-PE-PS lipid monolayer shows a lift-off at a molecular area of ~100 Å^2, thus displaying a liquid expanded (LE) phase, until the appearance of a discontinuity in the compression isotherm at Π≈22 mN·m^{-1}. This discontinuity indicates the onset

of the transition to the liquid condensed (LC) phase. There is no indication of film collapse at the minimal area of the Langmuir trough. The compressional elastic modulus C_s^{-1} against the surface pressure (shown in **Figure 4.2 B**) shows a continuous behaviour at low surface pressures (Π<25 mN·m^{-1}; LE phase) with a plateau at $\Pi\approx10$ mN·m^{-1}, until a minimum is reached at $\Pi\approx25$ mN·m^{-1}. This drop in C_s^{-1} values can be rationalized as a discontinuity in the lateral packing at phase boundaries and constitutes the hallmark of the LE to LC phase transition[52,53].

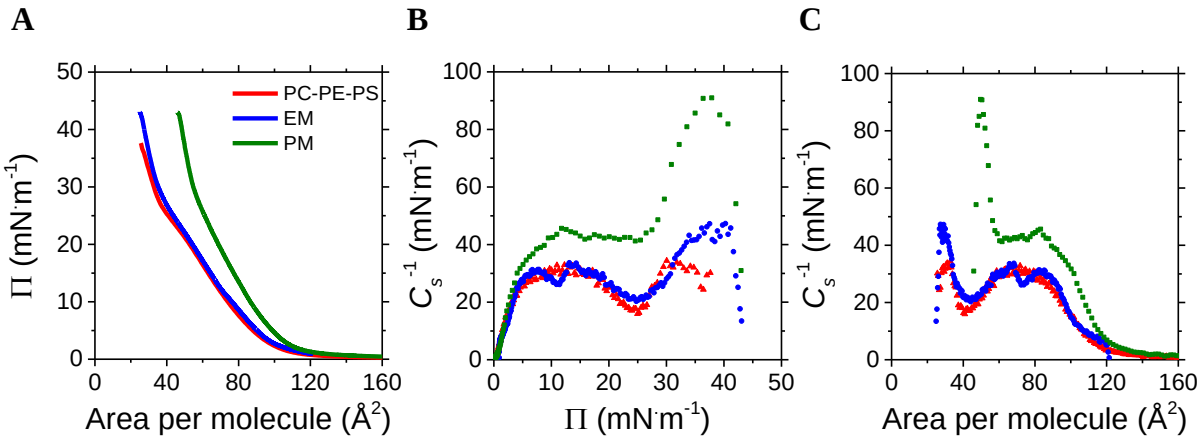

Figure 4.2 A Π-A isotherms of PC-PE-PS, EM and PM monolayers. Corresponding compressional elastic modulus profile C_s^{-1} of PC-PE-PS (red triangles), EM (blue circles) and PM (green squares) monolayers as a function of **B** Π and **C** area per molecule.

To further characterize the lipid phase behaviour within the plane of the monolayer, *in situ* morphology of the PC-PE-PS membrane was investigated by BAM. Importantly, this technique does not require the use of fluorescent dyes, which may introduce phase artefacts. BAM images taken during the lateral compression of the monolayer are reported in **Figure 4.3 A** (and **Figure S4.1**). Since the orientational order related to lipid condensed phases results in modulations of the polarization state of the reflected light[54,55], dark areas are attributed to fluid, LE regions whereas more condensed phases are seen as bright micro-domains. Given the nature of PC-PE-PS mixture, rich in unsaturated lipids, the monolayer at Π=10 mN·m^{-1} displays an overall dark region, consistent with the existence of a LE phase. At Π=22 mN·m^{-1}, bright spots can be observed, indicating the presence of LC domains, due to the favourable interaction between saturated acyl chains molecules that exclude unsaturated phospholipids, coexisting within the LE phase. At larger pressures (*e.g.*, at Π=38 mN·m^{-1}), the existence of a condensed phase with brighter domains is visible in agreement with the compressional modulus tendency shown in **Figure 4.2 B**.

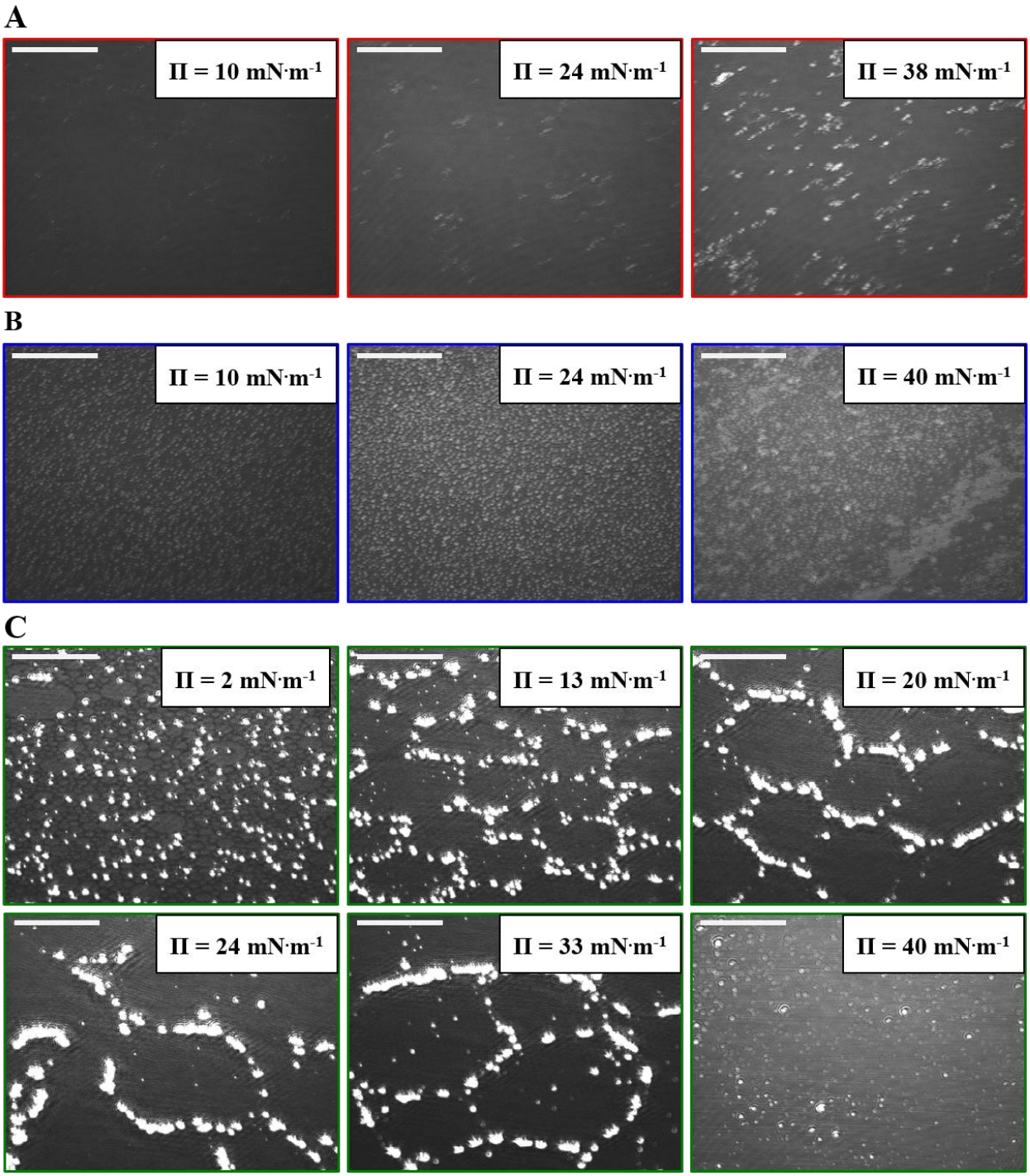

Figure 4.3 Brewster angle microscopy images of the different Langmuir monolayers at selected surface pressures: **A** PC-PE-PS, **B** EM, and **C** PM monolayers. Scale bar: 100 µm.

The out-of-plane interfacial structure of PC-PE-PS lipid monolayer was resolved by NR at two different surface pressures (14 and 24 $mN \cdot m^{-1}$). Three isotopic contrast data sets were recorded and analysed together: hydrogenous lipid mixture in buffered D_2O and ACMW, and deuterated

lipid mixture in buffered D_2O (**Figure 4.4 A** and **D**). Because of these samples yielded laterally homogeneous interfaces on the length scale of the in-plane neutron coherence length (on the order of ~10-30 μm[27]) according to BAM (**Figure 4.3 A**), the measured reflectivity curves can be correlated with an in-plane averaged SLD profile across the interface. The out-of-plane structure of the lipid monolayers as a function of the distance from the interface can be, therefore, determined. This is done by simultaneous fitting all contrasts, to obtain a single set of structural parameters. A two-layer model describing the aliphatic tails and the polar headgroups provides a suitable description of the experimental data. The optimized parameters (**Table S4.5**) were the thickness of the headgroups- and the tails-layer, and the roughness. The water molecules associated to the headgroups were calculated by **Equation 4.4**. In the LE phase, at Π=14 $mN \cdot m^{-1}$, the tails-layer has a thickness of 14±1 Å, while the headgroups-layer, has a thickness of 5±1 Å. In the onset of the LC state, at Π=24 $mN \cdot m^{-1}$, the tails thickness increases by 6 Å, from 14 to 20 Å. As expected for a more compact monolayer, the content of water is reduced from 12 to 10% in the headgroups-layer, leading also to a smaller value of A, from 70 to 46 $Å^2$, that is comparable with previously published data of both hydrogenous and perdeuterated natural lipid bilayers[30]. For both surface pressures, the areas obtained are compatible (within the experimental error) with the values obtained from the Π-A isotherms. From the optimized fit obtained (**Figure 4.4 A** and **D**), the corresponding neutron SLD distribution (**Figure 4.4 B** and **E**), and the volume fraction profiles of tails and headgroups (**Figure 4.4 C** and **F**) were derived. The observed roughness values (5Å, **Table S4.5**) are higher than that obtained for the bare interface (~2.8Å), which agrees with the theoretical value expected for thermally excited capillary waves (k_BT/γ_0)[27,46,47], where γ_0=72.8 $mN \cdot m^{-1}$ is the interfacial tension of the bare interface. However, the calculation of the expected roughness according to $r=r_0(\gamma_0/\gamma)^{1/2}$, for both values of interfacial tension γ studied here, leads to values of 3.1Å and 3.4 Å, respectively ($\gamma=\gamma_0$- Π=58.8 and 48.8 $mN \cdot m^{-1}$, respectively for Π=14 and 24 $mN \cdot m^{-1}$). Thus, the presence of a natural PC-PE-PS lipid monolayer at the air/water interface produces an additional roughness, which seems to be independent of surface pressure, and could potentially be explained by considering the intrinsic variability in the natural lipid acyl chains. Indeed, in the case of heterogeneous methyl-branched fatty acid monolayers, the much larger than expected perturbation in the out-of-plane height of the air/water interface can be attributed to a 3D nano-texturization of the interface[56].

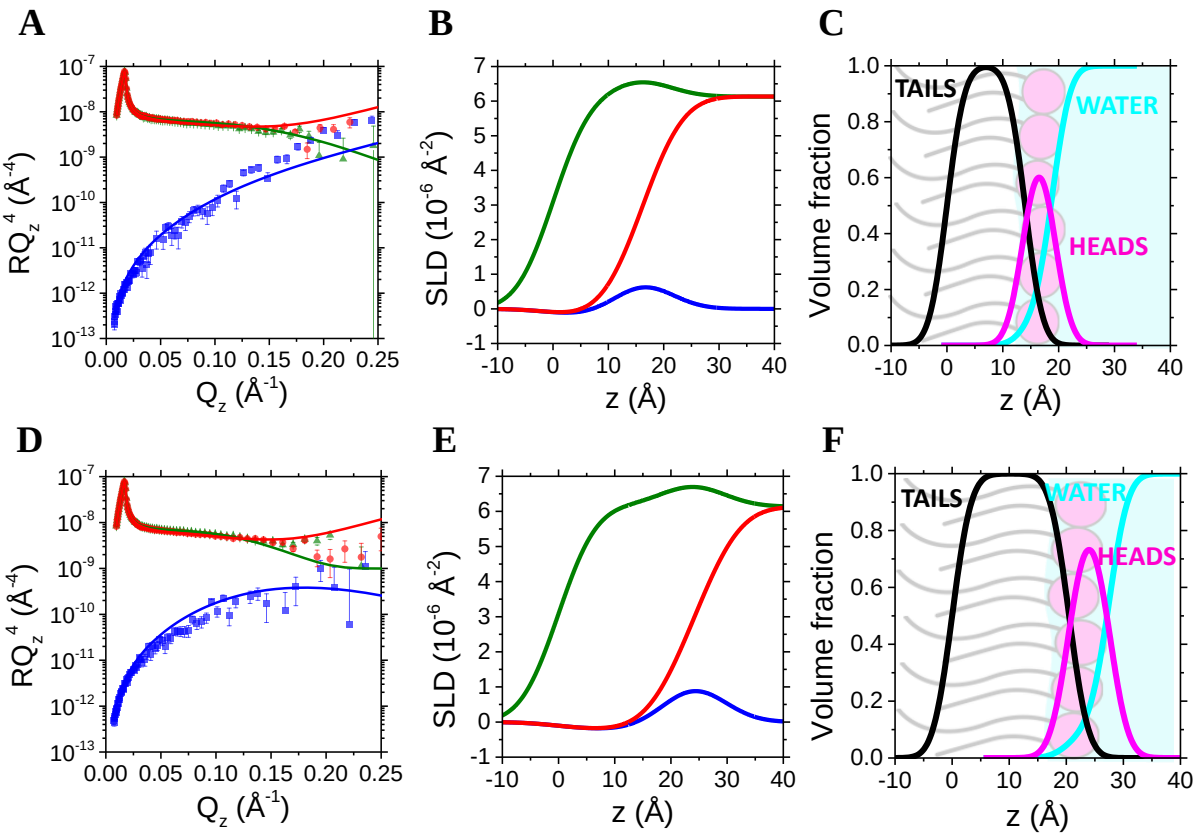

Figure 4.4 NR data of PC-PE-PS monolayers at two selected surface pressures: **A** Π=14 mN·m^{-1} and **D** Π=24 mN·m^{-1}. The experimental data relative to hydrogenous lipids in ACMW and D_2O are depicted as blue squares and red circles, respectively, together with the data of deuterated lipids in D_2O (green triangles). Straight lines correspond to the simulated curves according to the two-layer model proposed. The figures are displayed on an RQ_z^4 scale to highlight the quality of the fits at high Q_z values. Corresponding SLD profiles normal to the interface (**B** Π=14 mN·m^{-1} and **E** Π=24 mN·m^{-1}). The curves relative to hydrogenous lipids in ACMW and D_2O are shown in blue and red, respectively, together with the curve of deuterated lipids in D_2O, which is shown in green. Derived volume fraction profiles normal to the interface from the SLD distributions at **C** Π=14 mN·m^{-1}and **F** Π=24 mN·m^{-1} that illustrate the distribution of tails (black) and headgroups (magenta). The contributions of water (cyan) is also shown. A sketch of the proposed lipid monolayer structure is included in the panel.

3.2. Towards more complex Langmuir lipid monolayers: replicate ERGIC membrane and plasma membrane

Langmuir monolayers whose lipid composition resembled the one of mammalian ERGIC and plasma membranes were subsequently characterized. The aim was to evaluate how differences in lipid composition (and especially cholesterol content) could affect the membrane organization which in turn influence the biological function. Indeed, in agreement with previous studies, the increase of the cholesterol content in PM in relation to EM (and PC-PE-PS) monolayers shifts the Π-A isotherm to larger areas. This change was postulated to be due to the strong effect of cholesterol in the packing of lipids at the interface, affecting headgroup and tail regions[57,58]. In particular, the hydrogen bond formation between cholesterol and sphingomyelin favours a specific conformation of the latter at the interface, which contributes to the expansion of the area per molecule in PM monolayer[59]. For EM monolayer, the obtained Π-A isotherm and compressional elastic modulus curve are remarkably similar to the PC-PE-PS ones, even if EM contains 8% mol of cholesterol. This difference in composition affects the compressional elastic modulus profile only at high pressures. The EM monolayer shows a discontinuity in the compressional isotherm at Π≈25 $mN \cdot m^{-1}$ that proves the existence of an LE-LC phase transition. There is however no clear indication of this discontinuity in the case of the plasma membrane monolayer, whose compressional elastic modulus profile shows a plateau regime from 15 until 26 $mN \cdot m^{-1}$. Then, as surface pressure reaches ~27 $mN \cdot m^{-1}$, C_s^{-1} also increases, which may be linked to the onset of the LC phase. Here, the compressional elastic modulus of the PM monolayer, containing 50% mol of cholesterol, is more than 2-fold higher than the one of the PC-PE-PS monolayer, unlike the compressional elastic modulus of the EM monolayer, which is only 1.5-fold higher than the one of PC-PE-PS monolayer. Indeed, it is known that cholesterol is a condensing agent[60–62], thus leading to an increase in the rigidity of the monolayer, which is translated in an increase in the compressional elastic modulus. The higher values of the compressional elastic modulus for PM in comparison to EM monolayer are compatible with the expected effect due to the increase in cholesterol content, as measured for PC-SM-cholesterol monolayers by Pereira et al.[58]. Finally, in both EM and PM monolayers, the compressional modulus of the film increases rapidly when Π≈27 $mN \cdot m^{-1}$ and then it decreases at Π≈40 $mN \cdot m^{-1}$. This decrease tentatively indicates film collapse, as the lipids are concentrated into the minimal area of the Langmuir trough.

In order to evaluate the influence of cholesterol on the lipid in-plane organization, BAM images were taken during the lateral compression of EM and PM monolayers (**Figure 4.3 B** and **C** respectively, and **Figure S4.2** and **S4.3**). For PM monolayer (**Figure 4.3 C**), dark areas are attributed to liquid-disordered (L_d) regions coexisting with densely packed liquid-ordered (L_o) phases that are seen as bright micro-environments rich in cholesterol and SM. The visualization of L_o/L_d coexisting phases is rationalized because (i) cholesterol, as a hydrophobic disk-shaped lipid, is confined preferably into the L_o region and (ii) long-range orientational order in cholesterol-rich phases results in modulations of the polarization state of the reflected light. Interestingly, the evolution of the L_o /L_d coexistence in PM monolayer, containing 50% mol cholesterol, starts from the nucleation of bright spots at 2 $mN \cdot m^{-1}$ coalescing because of the reduction in the available area of the Langmuir trough into a honeycomb-like network at $\Pi \approx 13$ $mN \cdot m^{-1}$. Both cholesterol and SM are well known to form rigid structures due to the hydrophobic interaction between rigid sterol rings and the SM acyl chains[63]. In fact, the strong affinity of sterol rings for SM drives the formation of tightly packed domains stabilized through hydrogen bonds, and essential for the formation of domains in biomembranes and L_o phases in model systems[64]. Therefore, it may be expected that cholesterol and SM may be mostly excluded from the L_d phase, which plays a very important role in the modulation of specific molecular interactions within the plane of the membrane[65]. Further compression towards $\Pi = 20$ $mN \cdot m^{-1}$ leads to an evolution of the network losing the hexagonal order at $\Pi \approx 24$ $mN \cdot m^{-1}$, which can be interpreted as the onset of a LC phase. Remodelling of the L_o phase is visible at $\Pi = 30$ $mN \cdot m^{-1}$ towards a more compact phase and at the limit pressure of 40 $mN \cdot m^{-1}$ a homogeneous film, with no phase separation, was observed. Interestingly, important structural differences can be observed comparing BAM images of PM with those obtained from EM monolayer, characterized by a lower amount of cholesterol (8% in mol). Firstly, at $\Pi = 10$ $mN \cdot m^{-1}$ there is a clear coexistence of two phases, hypothesized as L_o domains embedded in an L_d phase. Those L_o domains are smaller to those observed in PM at the same pressure and at $\Pi = 12$ $mN \cdot m^{-1}$ (**Figure S4.2**) they do not present the hexagonal structures observed for PM monolayer. The coalescence of such L_o domains is clearly observed as pressure is increased, since the image becomes brighter with increasing Π. Finally, these domains partially collapse yielding a 2D, heterogonous compact regime at larger pressures, as it can be observed at $\Pi = 40$ $mN \cdot m^{-1}$, **Figure 4.3 B**. From the comparison of EM and PM, we can conclude that when the cholesterol percentage is increased up to 50% in mol, the L_o domains formed by cholesterol-

SM-saturated phospholipids are much brighter, and bigger, appearing even at low Π (**Figure 4.3 C**). This can be understood considering a maximization of the cholesterol-SM-saturated phospholipids hydrophobic interactions, resulting in a tight packing of the ordered domains, mediated by the hydrophobic mismatch between the planar sterol nucleus and the flexible acyl chains of SM and lipids[63,66]. Even though a preferential interaction between cholesterol and SM was expected, alternative current voltammetry measurements showed that interactions between cholesterol and other long-chain lipids may also affect the formation of the ordered domains, but were not as important[57].

The out-of-plane structures of both EM and PM monolayers were investigated by neutron reflectometry at Π≈23±1 $mN \cdot m^{-1}$. At this pressure, the average area per molecule (obtained by both NR and the Π-A isotherm) is equivalent to the one of a typical bilayer[11,67]. Hydrogenous and perdeuterated lipid monolayers were fitted together (**Figure 4.5 A** and **D**). Three isotopic contrast data sets were recorded in the case of EM and PM monolayers (hydrogenous lipids in D_2O and ACMW buffers, and deuterated lipids in D_2O buffer), whilst an extra one was also measured for PM monolayer (deuterated lipids in ACMW). The resultant model built with four data sets demonstrated that cholesterol is present in the tails-layer without extending into the lipid headgroups-layer, as previously observed in the case of mixed POPC:POPE:cholesterol bilayers[68]. The resultant SLD distribution (**Figure 4.5 B** and **E**) and the corresponding volume fraction profiles of tails, including the presence of cholesterol, and headgroups are plotted in **Figure 4.5 C** and **F**, respectively for EM and PM. The obtained structural parameters of PC-PE-PS, EM and PM monolayers are shown in **Figure 4.7** (and summarized in **Table S4.5**). The averaged values of area per molecule are compatible (within the experimental error) with the values obtained from the Π-A isotherms, besides, the one for PM monolayers also agrees with that measured for DOPC monolayers doped with a similar high level cholesterol content[69].

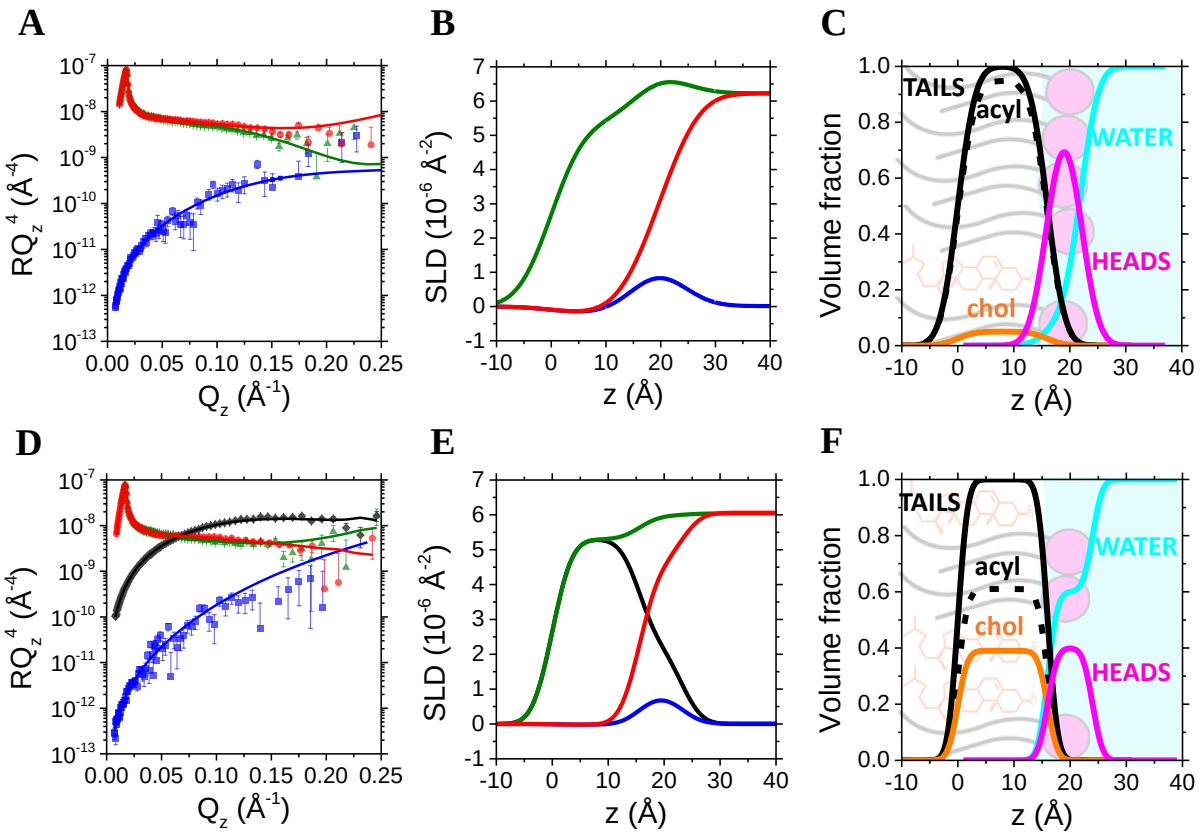

Figure 4.5 NR data of **A** EM and **D** PM monolayers. The data relative to hydrogenous lipids in ACMW and D_2O are depicted as blue squares and red circles, respectively, together with the data of deuterated lipids in ACMW and D_2O, which are represented as black diamonds and green triangles, respectively. The lines correspond to the relative simulated curves. The figures are displayed on an RQ_z^4 scale to highlight the quality of the fits at high Q_z values. Corresponding SLD profiles normal to the interface are plotted in **B** and **E,** for EM and PM, respectively. The curves relative to hydrogenous lipids in ACMW and D_2O are shown in blue and red, respectively, together with the curves of deuterated lipids in ACMW and D_2O, which are shown in black and green, respectively. Derived volume fraction profiles normal to the interface of **C** EM and **F** PM monolayers to highlight the distribution of tails (black) and headgroups (magenta). The contributions of water (cyan), cholesterol (orange) and solely acyl chains (dashed black) are shown. A sketch of the lipid monolayers is included.

In the case of EM monolayer, the L_o/L_d coexistence of phases observed by BAM (**Figure 4.3 B**) yields a homogeneous lateral structure on the length scale of the in-plane neutron coherence length[27], therefore the measured NR can be correlated with an in-plane averaged SLD. However, the L_o domains observed in PM monolayer (**Figure 4.3 C**), although they do not cover a significant fraction of the interface (9% from BAM, **Figure S4.4**), are larger than the neutron coherence length. Therefore, the experimental NR curves were also fitted using a mixed reflectivity model based on the incoherent sum of reflectivity for L_o and L_d regions, denoted as α and β, respectively (see **Methods**). The model used took into account a contribution from the L_o phase (f_α=12%) that is in agreement with the calculated area from BAM (**Figure 6A**). This implied that half of the total

amount of cholesterol and sphingomyelin was segregated in the L_o phase (**Figure 6B**). From the model, the relative amount of each lipids in the two phases was calculated (**Figure 4.6 B**).

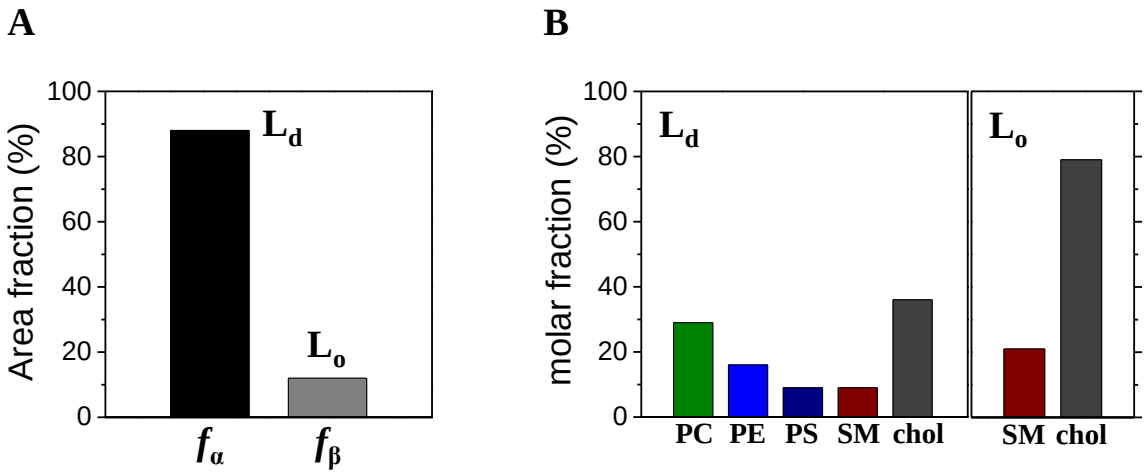

Figure 4.6 A Fraction of L_d (black column) and L_o (grey column) and domains obtained from the NR data analysis. **B** molar percentage of each lipid component in the two phases.

4. Discussion. *In vitro* models of plasma and ERGIC membranes: structural differences and effect of lipid composition on organelle function and morphology.

Although the influence of cholesterol on different lipid monolayers has been extensively studied[69,70], the work presented here is the first characterization of mixed cholesterol and natural yeast lipids monolayers deposited at the air/water interface. Structural differences between complex model systems, such as EM and PM monolayers, are shown in **Figure 4.7**. Although the observed differences in aliphatic chains are believed to be primarily due to the influence of cholesterol and sphingomyelin, the existence of phospholipids with longer acyl chains in the PC pool (see **Table S4.1**) leads to an increase in tails thickness for PC-PE-PS (**Figure 4.7 A**), whose PC content is higher than the EM and PM mixtures (see **Tables S4.2** and **S4.3**). Moreover, the NR data showed a 4Å reduction in the thickness of the acyl chains (from 20 to 16Å) with respect to the PC-PE-PS monolayer measured in similar conditions, *i.e.*, in the onset of the LC phase. The presence of cholesterol, however, could also potentially increase the average tilting of the acyl chains of the lipids constituting the monolayer. The decrease of monolayer thickness by the presence of cholesterol has already been reported in DPPC monolayers with 10% mol of cholesterol[70].

Regarding the PM monolayer, the associated increase in water present in the headgroups-layer is much higher than for EM and PC-PE-PS monolayers (**Figure 4.7 B**). This can be rationalized

by the incorporation of a rigid, hydrophobic molecule like cholesterol into the aliphatic tails-layer, which can develop a steric hindrance in between them, yielding an increase in the distance between polar headgroups. This is also supported by the in-plane phase coexistence observed by BAM (**Figure 4.3 C**). Moreover, there is not only a significant reduction in the tails-layer thickness but also a decrease in roughness (from 5 to 3Å), which was not observed with EM monolayers (**Figure 4.7 C**). We attribute this reduction in PM monolayer roughness to the high cholesterol content. Importantly, cholesterol molecules alter the molecular packing within lipid monolayers, as observed by BAM and NR, also yielding an increase in film rigidity, which reflects in an increase of the compressional elastic modulus. In addition, following the work of Daillant et al.[71], in which the roughness due to capillary waves was linked to the interplay between surface tension and bending elasticity modulus, the decrease of the roughness observed for PM can be interpreted as an increase in bending rigidity of the monolayer. This effect was also recently observed in mixed cholesterol-DOPC membranes by neutron spin-echo (NSE) spectroscopy and solid-state deuterium NMR (^{2}H NMR) spectroscopy[72]. The local increase in membrane bending rigidity by cholesterol was interpreted as an increase in the bilayer packing density similar with what was observed here.

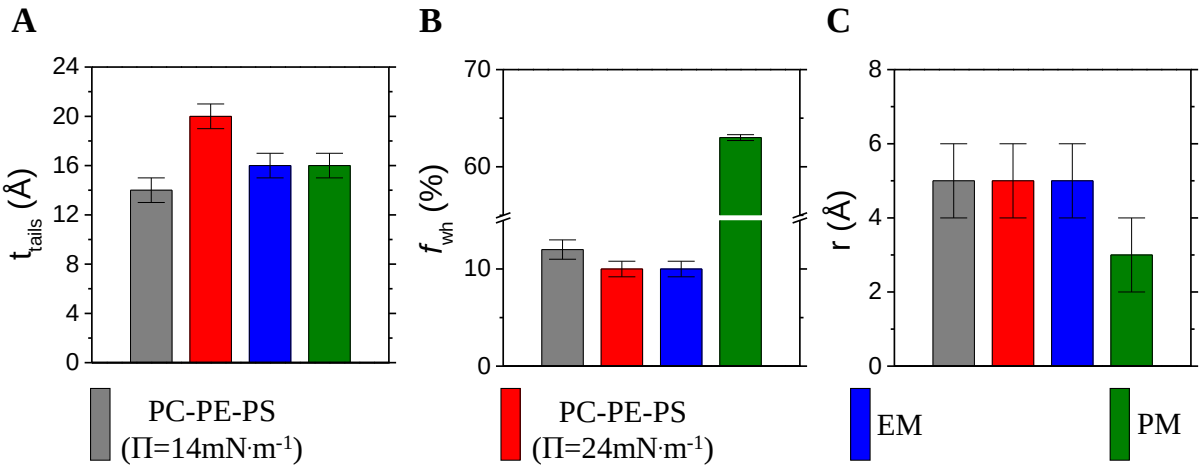

Figure 4.6 Comparison of results derived from NR analysis: bar diagrams showing **A** thickness of tails, **B** water volume fraction in the headgroups-layer and **C** roughness of each monolayer.

Different hypotheses have been postulated regarding the interaction between phospholipids and cholesterol. For example the existence of phospholipid/cholesterol complexes[69,73], whose stoichiometry would depend on the phospholipid nature, while it has also been suggested that phospholipid headgroups act as "umbrellas", protecting cholesterol from water[74,75], which should lead to a decrease of the water fraction content within the headgroups-layer, emerging

incompatible with our experimental findings. Here, BAM and NR experiments on PM monolayer (**Figure 4.3 C** and **Figure 4.6**) have showed the existence of densely packed L_o phases rich in cholesterol and SM. Cholesterol, as a hydrophobic disk-shaped lipid, has been demonstrated to be confined preferably into the L_o region formed by saturated acyl chains lipids[66,76]. In fact, both cholesterol and SM are well known to form rigid structures due to the hydrophobic interaction between rigid sterol rings and the SM acyl chains[63]. A molecular explanation of the formation of such clusters can come from the ability of cholesterol to preferentially associate with phospholipids with saturated acyl chains, as well as segregate away from unsaturated phospholipids. The balance of both forces is determined by the number of hydrocarbon contacts and attractive van der Waals interactions formed between the cholesterol and the rest of lipids, as was reported by molecular dynamics simulations[66,76].

It is important to underline that the lipid composition of cellular organelles is designed to suit specific functions[77]. In particular, spatial organization of lipid molecules not only in the context of the bilayer structure, but also within leaflets is of paramount importance. The membrane leaflet thickness is determined by the acyl chain length, while the presence of cholesterol increases membrane rigidity. In PM monolayer, enriched in sphingolipids and sterols (cholesterol) with respect to the PC-PE-PS mixture, lipids are found to be packed at higher density yielding a more rigid environment. On the contrary, EM yields a more fluid and loosely packed membrane, as expected for the lower percentage of cholesterol. These results are consistent with the ERGIC membrane role in the insertion and transport of newly synthesized lipids and proteins.

5. Conclusions

In the present work, surface pressure-area isotherms combined with BAM and NR were used to characterize the in-plane morphology and out-of-plane structure of Langmuir monolayers composed of natural lipids. By mixing natural lipids extracted from yeast cells, it was possible to mimic biological relevant mammal cell membranes, *i.e.*, ERGIC membrane and plasma membrane. A simpler membrane, uniquely composed of natural PC, PE and PS phospholipids was also investigated. These experiments shed light on the correlation between lipid composition and membrane properties: the presence of cholesterol is associated with a decrease in film thickness as well as an increase in rigidity, while the lipid monolayer without cholesterol (PC-PE-PS) had reduced rigidity and increased roughness. We attribute the latter to the intrinsic heterogeneity in

natural chain composition and the presence of cholesterol. BAM imaging helped to elucidate the coexistence of a densely packed liquid-ordered phase (cholesterol-rich) and liquid-disordered domains in the plasma membrane model, which also influences the structure normal to the membrane and its rigidity.

To the best of our knowledge, this is the first work dedicated to the study of Langmuir monolayer of natural lipids mimicking single membrane leaflets, characterized by BAM and NR. These *in vitro* lipid model systems could potentially be exploited to study the interaction of cell membranes with biological relevant molecules, such as for example novel molecules and colloids as well as bacterial and viral proteins. Moreover, the use of strategies for the production and purification of deuterated natural lipids emerges as a very important advance for the characterization of structural features of lipid monolayers, opening an important avenue towards a better understanding of the organization of lipids within model membranes.

Investigation on the relationship between lipid composition and
structure in model membranes composed of extracted natural phospholipids

SUPPORTING INFORMATION

Tables

Table S4.1 Fatty acids composition in molar percentage.

Fatty	**PC**		**PE**		**PS**		**PI**	
Acids	**h**	**d**	**h**	**d**	**h**	**d**	**h**	**d**
16:0	4.4	1.3	14.1	11.2	37.5	29.1	30.4	25.0
16:1	6.7	0.7	3.2	0.8	1.6	2.4	2.4	0.2
18:0	7.3	2.2	5.4	4.3	6.3	7.5	8.6	11.4
18:1	39.8	66.0	29.2	48.0	34.1	51.1	33.1	51.1
18:2	33.2	25.1	40.2	32.7	19.4	9.0	22.9	11.5
18:3	8.6	4.6	7.9	3.0	1.2	0.8	2.7	0.9

Table S4.2 Lipid mixtures composition[10,15,16]. Cholesterol and natural extracted sphingomyelin (egg, chicken) were purchased from Avanti Polar Lipids.

Composition	**Extracted Natural Lipids**					
in mol%	*PC pool*	*PE pool*	*PS pool*	*PI pool*	*Sphingomyelin*	*Cholesterol*
PC-PE-PS	65	15	20	0	0	0
EM	47	26	2	5	12	8
PM	20	11	6	0	13	50

Table S4.3 Acyl chain composition in molar percentage.

Phospholipid acyl chain	**Hydrogenous**		**Deuterated**	
composition	**16C**	**18C**	**16C**	**18C**
PC-PE-PS	17.6	82.4	9.4	90.5
EM	24.4	74.6	17.7	81.2
PM	35.3	62.6	29.6	68.3

Table S4.4 Fixed parameters used for data modelling.

Fixed Parameters	PC-PE-PS		EM		PM	
	h	d	h	d	h	d
V_h (Å^3)	309.6	309.6	302.7	302.7	304.6	304.6
SLD_h (10^{-6} Å^{-2})	2.12	7.39	2.05	7.37	2.00	5.48
V_t (Å^3)	951.2	965.9	914.6	931.5	764.1	803.2
SLD_t (10^{-6} Å^{-2})	-0.21	6.17	-0.19	5.37	-0.02	5.30
f_{wt} (%)	0		0		0	

Table S4.5 Fitted and calculated parameters. *corresponding to an area per molecule of solely phospholipids of 53 Å^2, in agreement with the isotherm. **corresponding to an area per molecule of solely phospholipids of 59 Å^2, in agreement with the isotherm.

Parameters	PC-PE-PS (Π=14 mN·m^{-1})	PC-PE-PS (Π=24 mN·m^{-1})	EM	PM
t_t (Å)	14±1	20±1	16±1	16±1
t_h (Å)	5±1	7±1	6±1	8±1
f_{wh} (%)	12±1	10±1	10±1	60±1
r (Å)	5±1	5±1	5±1	3±1
A_t (Å^2)	69±5	46±2	*56±3	**49±7
A_h (Å^2)	70±15	49±8	*51±9	**49±7

Figures

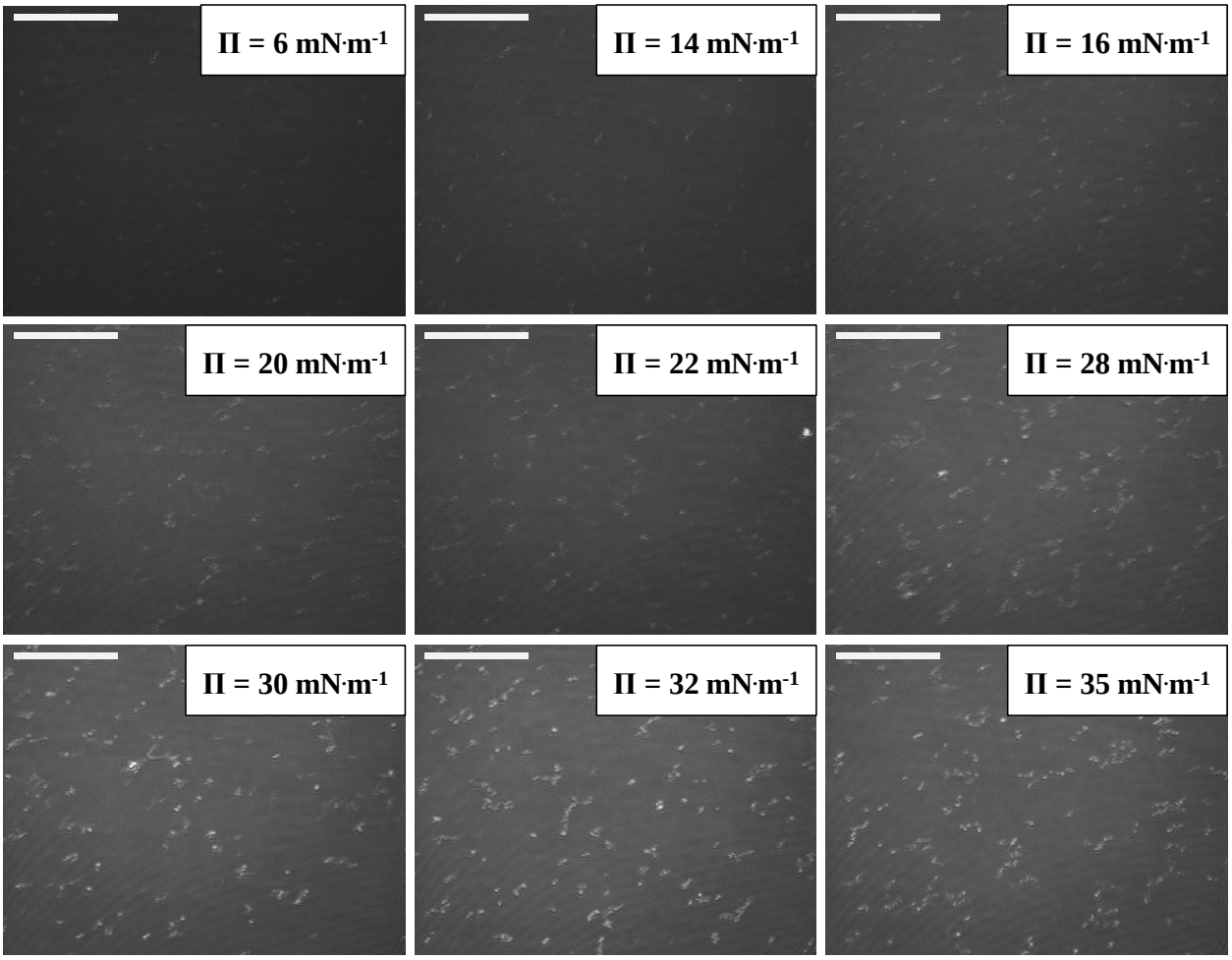

Figure S4.1 BAM images of PC-PE-PS monolayer. Scale bar: 100 µm.

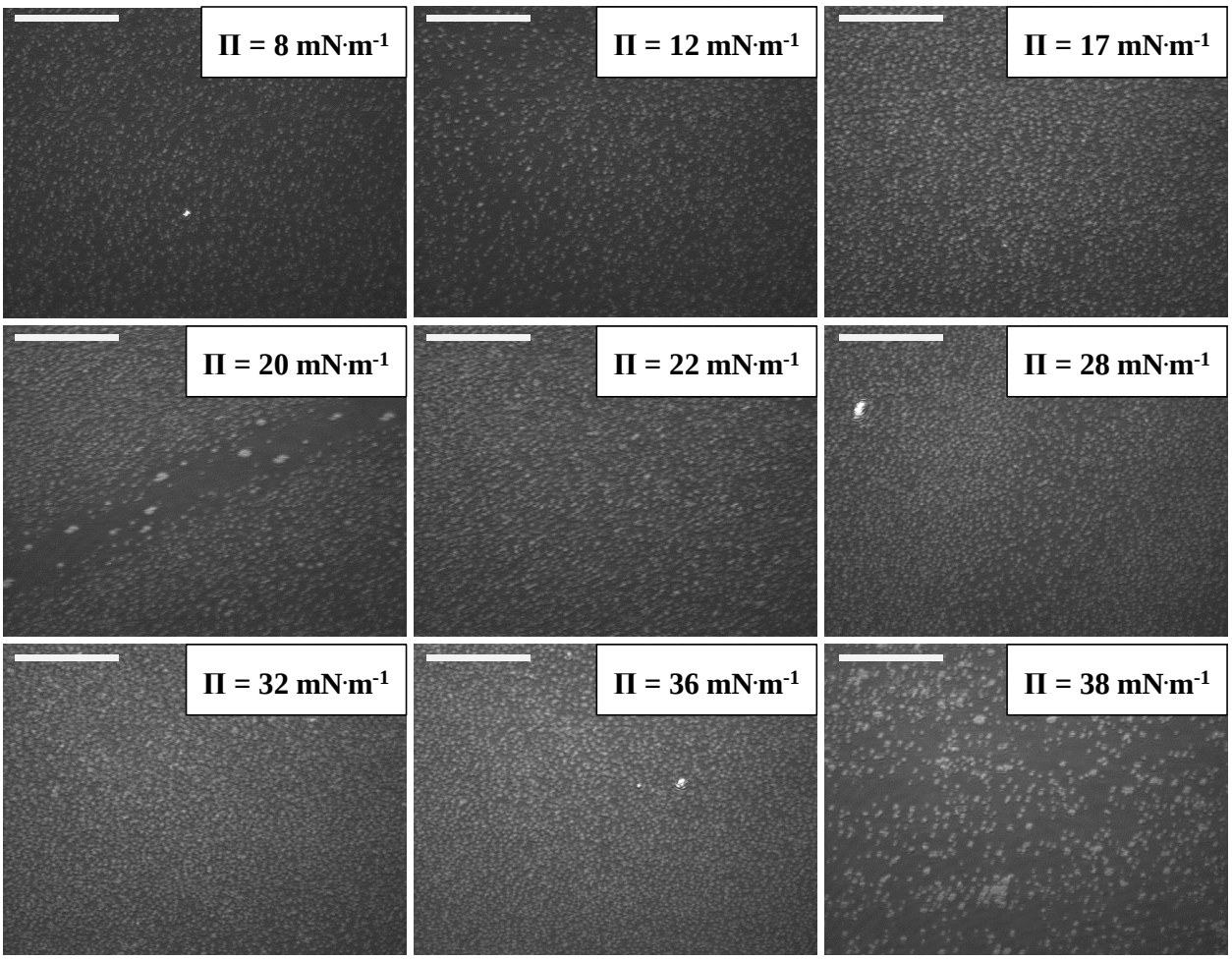

Figure S4.2 BAM images of EM monolayer. Scale bar: 100 µm.

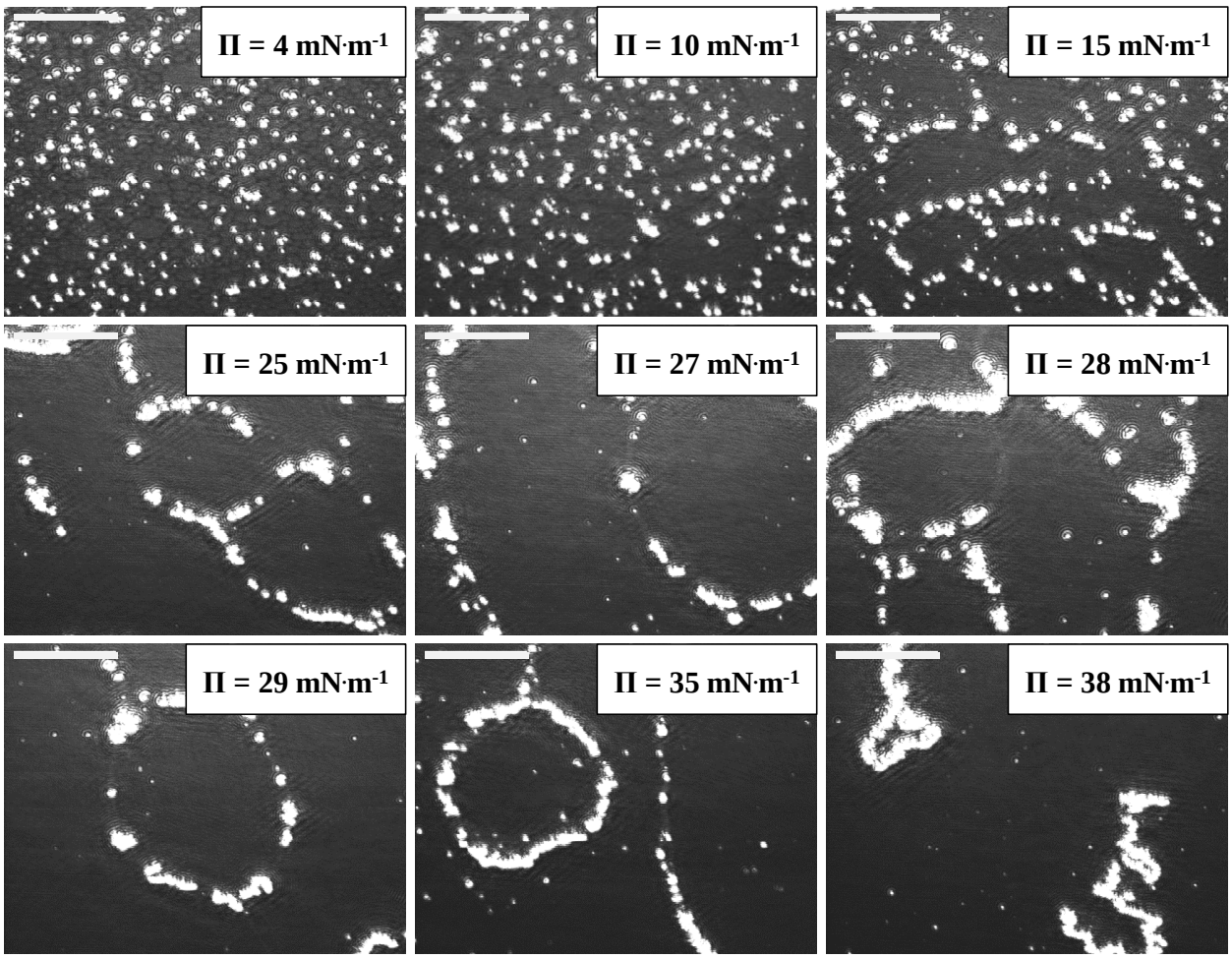

Figure S4.3 BAM images of PM monolayer. Scale bar: 100 µm.

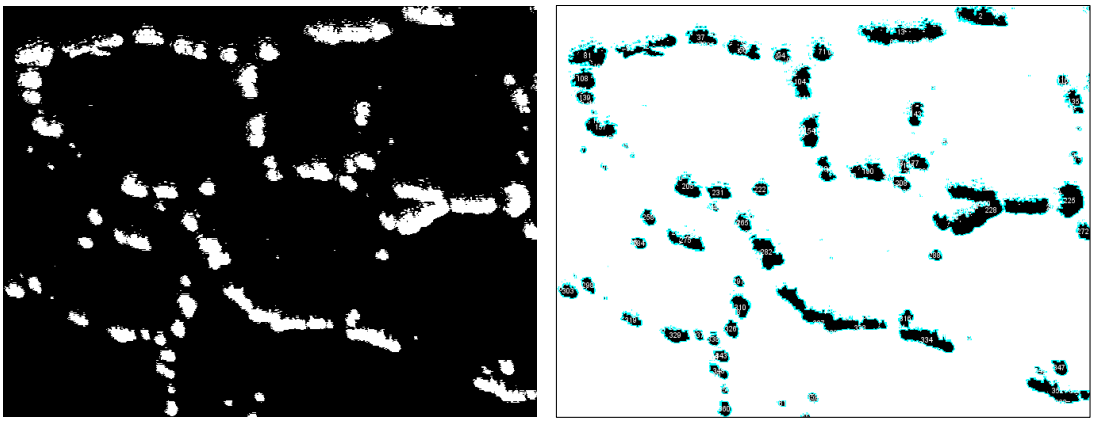

Figure S4.3 Left: BAM image of PM monolayer at Π=22mN·m^{-1}. Right: image analysis done with ImageJ[78]. The total relative area occupied by the L_o phase was calculated by inverting the background colour of the image (from black to white) and by applying a threshold function before processing the images.

References

1. Van Meer G, Voelker DR, Feigenson GW. Membrane lipids: Where they are and how they behave. *Nat Rev Mol Cell Biol*. 2008;9(2):112-124. doi:10.1038/nrm2330

2. Holthuis JCM, Menon AK. Lipid landscapes and pipelines in membrane homeostasis. *Nature*. 2014;510(7503):48-57. doi:10.1038/nature13474

3. Grinstein S. Imaging signal transduction during phagocytosis: Phospholipids, surface charge, and electrostatic interactions. *Am J Physiol - Cell Physiol*. 2010;299(5):876-881. doi:10.1152/AJPCELL.00342.2010

4. Magalhaes MAO, Glogauer M. Pivotal Advance: Phospholipids determine net membrane surface charge resulting in differential localization of active Rac1 and Rac2. *J Leukoc Biol*. 2010;87(4):545-555. doi:10.1189/JLB.0609390

5. Lodish H, Berk A, Zipursky LS. "Biomembranes: Structural Organization and Basic Functions." In: *Molecular Cell Biology*. 4th ed. New York: Scientific American Books.; 2000.

6. G. M. Cooper. Structure of the Plasma Membrane. In: *The Cell: A Molecular Approach*. 2nd ed. Washington, D.C.: Sunderland, Mass. : Sinauer Associates; 2000.

7. Miller SE, Mathiasen S, Bright NA, et al. CALM Regulates Clathrin-Coated Vesicle Size and Maturation by Directly Sensing and Driving Membrane Curvature. *Dev Cell*. 2015;33(2):163-175. doi:10.1016/j.devcel.2015.03.002

8. Lai AL, Millet JK, Daniel S, Freed JH, Whittaker GR. The SARS-CoV Fusion Peptide Forms an Extended Bipartite Fusion Platform that Perturbs Membrane Order in a Calcium-Dependent Manner. *J Mol Biol*. 2017;429(24):3875-3892. doi:10.1016/j.jmb.2017.10.017

9. Ghosh A, Bhattacharyya D, Bhunia A. Structural insights of a self-assembling 9-residue peptide from the C-terminal tail of the SARS corona virus E-protein in DPC and SDS micelles: A combined high and low resolution spectroscopic study. *Biochim Biophys Acta - Biomembr*. 2018;1860(2):335-346. doi:10.1016/j.bbamem.2017.10.015

10. Raghava S, Giorda KM, Romano FB, Heuck AP, Hebert DN. The SV40 late protein VP4 is a viroporin that forms pores to disrupt membranes for viral release. *PLoS Pathog*. 2011;7(6). doi:10.1371/journal.ppat.1002116

11. Ingólfsson HI, Melo MN, Van Eerden FJ, et al. Lipid organization of the plasma membrane. *J Am Chem Soc*. 2014;136(41):14554-14559. doi:10.1021/ja507832e

12. Scheve CS, Gonzales PA, Momin N, Stachowiak JC. Steric pressure between membrane-bound proteins opposes lipid phase separation. *J Am Chem Soc*. 2013;135(4):1185-1188. doi:10.1021/ja3099867

13. Nieto-Torres JL, DeDiego ML, Álvarez E, et al. Subcellular location and topology of severe acute respiratory syndrome coronavirus envelope protein. *Virology*. 2011;415(2):69-82. doi:10.1016/j.virol.2011.03.029

14. Appenzeller-Herzog C, Hauri HP. The ER-Golgi intermediate compartment (ERGIC): In search of its identity and function. *J Cell Sci*. 2006;119(11):2173-2183. doi:10.1242/jcs.03019

15. Sarkar M, Saha S. Structural insight into the role of novel SARSCoV-2 E protein: A potential target for vaccine development and other therapeutic strategies. *PLoS One*. 2020;15(8 August):1-25. doi:10.1371/journal.pone.0237300

16. Kapoor K, Chen T, Tajkhorshid E. Post-Translational Modifications Optimize the Ability of SARS-CoV-2 Spike for Effective Interaction with Host Cell Receptors. *bioRxiv*. 2021. doi:10.1101/2021.12.02.470852

17. Ravera F, Miller R, Zuo YY, et al. Methods and models to investigate the physicochemical functionality of pulmonary surfactant. *Curr Opin Colloid Interface Sci*. 2021;55:101467. doi:10.1016/j.cocis.2021.101467

18. Guzmán E, Santini E. Lung surfactant-particles at fluid interfaces for toxicity assessments. *Curr Opin Colloid Interface Sci*. 2019;39:24-39. doi:10.1016/j.cocis.2019.01.003

19. Guzmán E, Liggieri L, Santini E, Ferrari M, Ravera F. Mixed DPPC-cholesterol Langmuir monolayers in presence of hydrophilic silica nanoparticles. *Colloids Surfaces B Biointerfaces*. 2013;105:284-293. doi:10.1016/j.colsurfb.2013.01.020

20. Bertsch P, Bergfreund J, Windhab EJ, Fischer P. Physiological fluid interfaces: Functional microenvironments, drug delivery targets, and first line of defense. *Acta Biomater*. 2021;130:32-53. doi:10.1016/j.actbio.2021.05.051

21. Bartkowiak A, Rojewska M, Prochaska K. Study of mucin interaction with model phospholipid membrane at the air–water interface. *Colloids Surfaces A Physicochem Eng Asp*. 2019;578(March):123587. doi:10.1016/j.colsurfa.2019.123587

22. Ege C, Lee KYC. Insertion of Alzheimer's Aβ40 peptide into lipid monolayers. *Biophys J*. 2004;87(3):1732-1740. doi:10.1529/biophysj.104.043265

23. Ortiz-Collazos S, Picciani PHS, Oliveira ON, Pimentel AS, Edler KJ. Influence of levofloxacin and clarithromycin on the structure of DPPC monolayers. *Biochim Biophys Acta - Biomembr*. 2019;1861(10):182994. doi:10.1016/j.bbamem.2019.05.016

24. Videv P, Mladenov N, Andreeva T, et al. Condensing effect of cholesterol on hBest1/POPC and hBest1/SM langmuir monolayers. *Membranes (Basel)*. 2021;11(1):1-8. doi:10.3390/membranes11010052

25. Zhang Z, Hao C, Qu H, Sun R. Studied on the dynamic adsorption process of Lycium barbarum polysaccharide in the POPC/DPPC monolayers. *Colloids Surfaces B Biointerfaces*. 2019;178(February):38-43. doi:10.1016/j.colsurfb.2019.02.046

26. Veatch SL, Keller SL. Organization in Lipid Membranes Containing Cholesterol. *Phys Rev Lett*. 2002;89(26):1-4. doi:10.1103/PhysRevLett.89.268101

27. Maestro A, Gutfreund P. In situ determination of the structure and composition of Langmuir monolayers at the air/water interface by neutron and X-ray reflectivity and ellipsometry. *Adv Colloid Interface Sci*. 2021;293:102434. doi:10.1016/j.cis.2021.102434

28. Oliveira ON, Caseli L, Ariga K. The Past and the Future of Langmuir and Langmuir-Blodgett Films. *Chem Rev*. 2022;122(6):6459-6513. doi:10.1021/ACS.CHEMREV.1C00754/ASSET/IMAGES/LARGE/CR1C00754_0036.JPEG

29. Clifton LA, Campbell RA, Sebastiani F, et al. Design and use of model membranes to study biomolecular interactions using complementary surface-sensitive techniques. *Adv*

Colloid Interface Sci. 2020;277. doi:10.1016/j.cis.2020.102118

30. De Ghellinck A, Fragneto G, Laux V, et al. Lipid polyunsaturation determines the extent of membrane structural changes induced by Amphotericin B in Pichia pastoris yeast. *Biochim Biophys Acta - Biomembr*. 2015;1848(10):2317-2325. doi:10.1016/j.bbamem.2015.06.006

31. Luchini A, Micciulla S, Corucci G, et al. Lipid bilayer degradation induced by SARS-CoV-2 spike protein as revealed by neutron reflectometry. *Sci Rep*. 2021;11(1). doi:10.1038/s41598-021-93996-x

32. Luchini A, Delhom R, Demé B, et al. The impact of deuteration on natural and synthetic lipids: A neutron diffraction study. *Colloids Surfaces B Biointerfaces*. 2018;168:126-133. doi:10.1016/j.colsurfb.2018.02.009

33. Luchini A, Corucci G, Chaithanya Batchu K, et al. Structural Characterization of Natural Yeast Phosphatidylcholine and Bacterial Phosphatidylglycerol Lipid Multilayers by Neutron Diffraction. *Front Chem*. 2021;9(March):1-11. doi:10.3389/fchem.2021.628186

34. Santamaria A, Batchu KC, Matsarskaia O, et al. Strikingly Different Roles of SARS-CoV-2 Fusion Peptides Uncovered by Neutron Scattering. *J Am Chem Soc*. 2022. doi:10.1021/jacs.1c09856

35. Ciumac D, Gong H, Campbell RA, Campana M, Xu H, Lu JR. Structural elucidation upon binding of antimicrobial peptides into binary mixed lipid monolayers mimicking bacterial membranes. *J Colloid Interface Sci*. 2021;598:193-205. doi:10.1016/j.jcis.2021.04.037

36. Gong H, Hu X, Liao M, et al. Structural Disruptions of the Outer Membranes of Gram-Negative Bacteria by Rationally Designed Amphiphilic Antimicrobial Peptides. *ACS Appl Mater Interfaces*. 2021;13(14):16062-16074. doi:10.1021/ACSAMI.1C01643/ASSET/IMAGES/LARGE/AM1C01643_0006.JPEG

37. Gong H, Sani MA, Hu X, et al. How do Self-Assembling Antimicrobial Lipopeptides Kill Bacteria? *ACS Appl Mater Interfaces*. 2020;12(50):55675-55687. doi:10.1021/ACSAMI.0C17222/ASSET/IMAGES/LARGE/AM0C17222_0007.JPEG

38. Folch J, Lees M, Sloane stanley GH. A simple method for the isolation and purification of

total lipides from animal tissues. *J Biol Chem*. 1957;226(1):497-509. doi:10.1016/s0021-9258(18)64849-5

39. Boselli E, Pacetti D, Lucci P, Frega NG. Characterization of phospholipid molecular species in the edible parts of bony fish and shellfish. *J Agric Food Chem*. 2012;60(12):3234-3245. doi:10.1021/jf205159a

40. Campbell RA, Wacklin HP, Sutton I, Cubitt R, Fragneto G. FIGARO: The new horizontal neutron reflectometer at the ILL. *Eur Phys J Plus*. 2011;126(11):1-22. doi:10.1140/epjp/i2011-11107-8

41. Campbell RA, Saaka Y, Shao Y, et al. Structure of surfactant and phospholipid monolayers at the air/water interface modeled from neutron reflectivity data. *J Colloid Interface Sci*. 2018;531:98-108. doi:10.1016/j.jcis.2018.07.022

42. Braun L, Uhlig M, von Klitzing R, Campbell RA. Polymers and surfactants at fluid interfaces studied with specular neutron reflectometry. *Adv Colloid Interface Sci*. 2017. doi:10.1016/j.cis.2017.07.005

43. Gutfreund P, Saerbeck T, Gonzalez MA, et al. Towards generalized data reduction on a chopperbased time-of-flight neutron reflectometer. *J Appl Crystallogr*. 2018. doi:10.1107/S160057671800448X

44. Parratt LG. Surface studies of solids by total reflection of x-rays. *Phys Rev*. 1954;95(2):359-369. doi:10.1103/PhysRev.95.359

45. Maranville BB, Green A, Kienzle PA. Distributed Error-Function Roughness in Refl1d Reflectometry Fitting Program. 2018;XXX(1):1-4.

46. Braslau A, Deutsch M, Pershan PS, Weiss AH, Als-Nielsen J, Bohr J. Surface roughness of water measured by x-ray reflectivity. *Phys Rev Lett*. 1985;54(2):114-117. doi:10.1103/PhysRevLett.54.114

47. Sinha SK, Sirota EB, Garoff S, Stanley HB. X-ray and neutron scattering from rough surfaces. *Phys Rev B*. 1988;38(4):2297-2311. doi:10.1103/PhysRevB.38.2297

48. Gerelli Y. Aurore: New software for neutron reflectivity data analysis. *J Appl Crystallogr*.

2016;49:330-339. doi:10.1107/S1600576716000108

49. Nelson A. Co-refinement of multiple-contrast neutron/X-ray reflectivity data using MOTOFIT. *J Appl Crystallogr*. 2006;39(2):273-276. doi:10.1107/S0021889806005073

50. Nelson ARJ, Prescott SW. Refnx: Neutron and X-ray reflectometry analysis in python. *J Appl Crystallogr*. 2019;52(1):193-200. doi:10.1107/S1600576718017296/RG5158SUP5.ZIP

51. Nickels JD, Smith JC, Cheng X. Lateral organization, bilayer asymmetry, and inter-leaflet coupling of biological membranes. *Chem Phys Lipids*. 2015;192:87-99. doi:10.1016/J.CHEMPHYSLIP.2015.07.012

52. Mouritsen OG, Ipsen JH, Zuckermann MJ. Lateral density fluctuations in the chain-melting phase transition of lipid monolayers. *J Colloid Interface Sci*. 1989;129(1):32-40. doi:10.1016/0021-9797(89)90413-X

53. Nagle JF, Scott HL. Lateral compressibility of lipid mono- and bilayers. Theory of membrane permeability. *BBA - Biomembr*. 1978;513(2):236-243. doi:10.1016/0005-2736(78)90176-1

54. Hénon S, Meunier J. Microscope at the Brewster angle: Direct observation of first-order phase transitions in monolayers. *Rev Sci Instrum*. 1991;62(4):936-939. doi:10.1063/1.1142032

55. Daear W, Mahadeo M, Prenner EJ. Applications of Brewster angle microscopy from biological materials to biological systems. *Biochim Biophys Acta - Biomembr*. 2017;1859(10):1749-1766. doi:10.1016/j.bbamem.2017.06.016

56. Bergendal E, Campbell RA, Pilkington GA, Müller-Buschbaum P, Rutland MW. 3D texturing of the air-water interface by biomimetic self-assembly. *Nanoscale Horizons*. 2020;5(5):839-846. doi:10.1039/c9nh00722a

57. Lecompte MF, Gaibelet G, Lebrun C, Tercé F, Collet X, Orlowski S. Cholesterol and Sphingomyelin-Containing Model Condensed Lipid Monolayers: Heterogeneities Involving Ordered Microdomains Assessed by Two Cholesterol Derivatives. *Langmuir*. 2015;31(43):11921-11931. doi:10.1021/ACS.LANGMUIR.5B02646

58. Pereira AR, Shimizu FM, Oliveira ON. Cholesterol modulates the interaction between paclitaxel and Langmuir monolayers simulating cell membranes. *Colloids Surfaces B Biointerfaces*. 2021;205. doi:10.1016/J.COLSURFB.2021.111889

59. Lemma T, Marques Ruiz GC, Oliveira ON, Constantino CJL. The pesticide picloram affects biomembrane models made with Langmuir monolayers. *Colloids Surfaces B Biointerfaces*. 2019;181:953-958. doi:10.1016/J.COLSURFB.2019.06.060

60. Gershfeld NL, Pagano RE. The Condensing Effect of Cholesterol. A Critical Examination of Mixed-Film Studies. 1972;76(9):1244-1249.

61. Shah DO, Schulman JH. Influence of calcium, cholesterol, and unsaturation on lecithin monolayers. *J Lipid Res*. 1967;8(3):215-226. doi:10.1016/s0022-2275(20)40140-3

62. Müller-Landau F, Cadenhead DA. Molecular packing in steroid-lecithin monolayers, part II: Mixed films of cholesterol with dipalmitoylphosphatidylcholine and tetradecanoic acid. *Chem Phys Lipids*. 1979;25(3):315-328. doi:10.1016/0009-3084(79)90114-2

63. Slotte JP. Sphingomyelin - Cholesterol interactions in biological and model membranes. *Chem Phys Lipids*. 1999;102(1-2):13-27. doi:10.1016/S0009-3084(99)00071-7

64. Wydro P. Sphingomyelin/phosphatidylcholine/cholesterol monolayers - analysis of the interactions in model membranes and Brewster Angle Microscopy experiments. *Colloids Surfaces B Biointerfaces*. 2012;93:174-179. doi:10.1016/j.colsurfb.2011.12.035

65. De La Serna JB, Perez-Gil J, Simonsen AC, Bagatolli LA. Cholesterol rules: Direct observation of the coexistence of two fluid phases in native pulmonary surfactant membranes at physiological temperatures. *J Biol Chem*. 2004;279(39):40715-40722. doi:10.1074/jbc.M404648200

66. Krause MR, Regen SL. The structural role of cholesterol in cell membranes: From condensed bilayers to lipid rafts. *Acc Chem Res*. 2014;47(12):3512-3521. doi:10.1021/ar500260t

67. Marsh D. Lateral pressure in membranes. *Biochim Biophys Acta - Rev Biomembr*. 1996;1286(3):183-223. doi:10.1016/S0304-4157(96)00009-3

68. Vanegas JM, Heinrich F, Rogers DM, et al. Insertion of Dengue E into lipid bilayers studied by neutron reflectivity and molecular dynamics simulations. *Biochim Biophys Acta - Biomembr*. 2018;1860(5):1216-1230. doi:10.1016/j.bbamem.2018.02.012

69. Dynarowicz-ŁĄtka P, Hąc-Wydro K. Interactions between phosphatidylcholines and cholesterol in monolayers at the air/water interface. *Colloids Surfaces B Biointerfaces*. 2004;37(1-2):21-25. doi:10.1016/j.colsurfb.2004.06.007

70. Wojciechowski K, Orczyk M, Gutberlet T, Geue T. Complexation of phospholipids and cholesterol by triterpenic saponins in bulk and in monolayers. *Biochim Biophys Acta - Biomembr*. 2016;1858(2):363-373. doi:10.1016/j.bbamem.2015.12.001

71. Daillant J, Bosio L, Benattar JJ, Meunier J. Capillary waves and bending elasticity of monolayers on water studied by x-ray reflectivity as a function of surface pressure. *Epl*. 1989;8(5):453-458. doi:10.1209/0295-5075/8/5/010

72. Chakraborty S, Doktorova M, Molugu TR, et al. How cholesterol stiffens unsaturated lipid membranes. *Proc Natl Acad Sci U S A*. 2020;117(36):21896-21905. doi:10.1073/pnas.2004807117

73. Rubio RG, Guzmán E, Ortega F, Liggieri L. Monolayers of Cholesterol and Cholesteryl Stearate at the Water/Vapor Interface: A Physico-Chemical Study of Components of the Meibum Layer. *Colloids and Interfaces*. 2021;5(2):30. doi:10.3390/COLLOIDS5020030

74. Huang J, Feigenson GW. A microscopic interaction model of maximum solubility of cholesterol in lipid bilayers. *Biophys J*. 1999;76(4):2142-2157. doi:10.1016/S0006-3495(99)77369-8

75. Simons K, Vaz WLC. Model systems, lipid rafts, and cell membranes. *Annu Rev Biophys Biomol Struct*. 2004;33:269-295. doi:10.1146/annurev.biophys.32.110601.141803

76. Regen SL. The Origin of Lipid Rafts. *Biochemistry*. 2020;59(49):4617-4621. doi:10.1021/acs.biochem.0c00851

77. Casares D, Escribà P V, Rossello CA. Membrane Lipid Composition Effect on Membrane and Organelle Structure, Function and Compartmentalization and Therapeutic Avenues. *Int J Mol Sci*. 2019;20(9):2167. doi:10.3390/ijms20092167

78. Schneider CA, Rasband WS, Eliceiri KW. NIH Image to ImageJ: 25 years of image analysis. *Nat Methods 2012 97*. 2012;9(7):671-675. doi:10.1038/nmeth.2089

Chapter 5

Untangling structural molecular details of the endocytic adaptor protein CALM upon binding with PIP_2-containing model membranes[a]

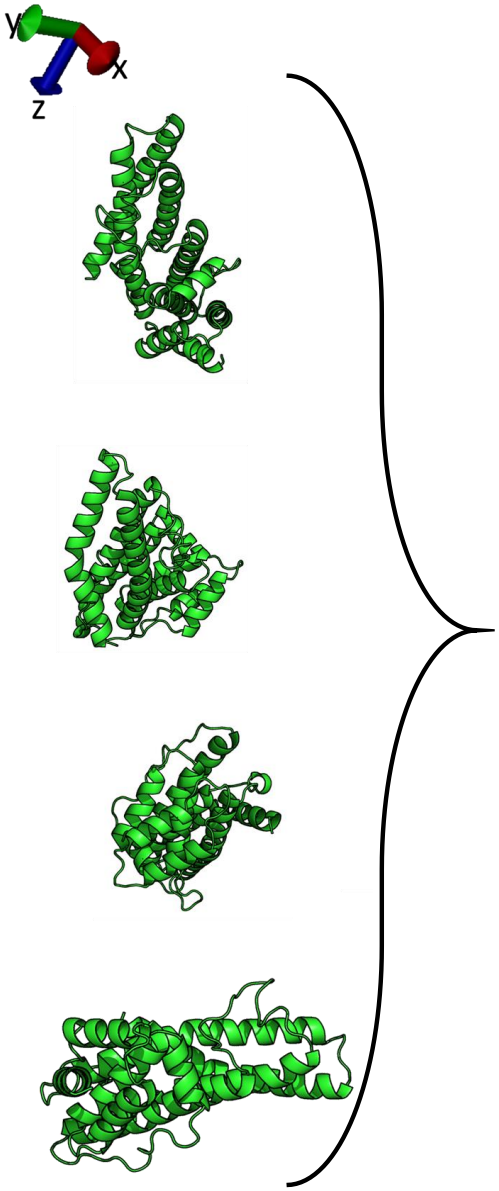

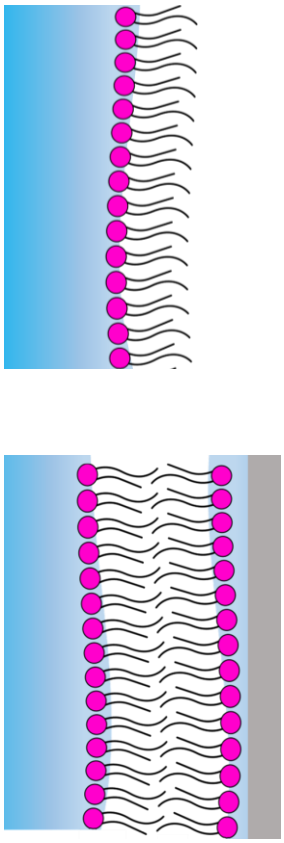

Studying the interaction with model membrane enriched in PIP_2 to find out the orientation of the protein upon binding

[a] This work will be submitted to *Nature Communications* (see Publication List at page 279).

Abstract

CALM (clathrin assembly lymphoid myeloid leukemia protein) is one of the principal proteins involved in the clathrin-mediated endocytosis pathway. Indeed, it is responsible for recognizing and sorting the cargoes that need to be internalized through the endocytic pathway, as well as for recruiting clathrin molecules. Moreover, CALM can bind the inner leaflet of the plasma membrane by electrostatic interactions with phosphatidylinositol 4,5-bisphosphate, whose headgroups are negatively charged. Biochemical and structural studies allowed to identify the amino acid residues involved in the binding of both PIP_2 and the cargoes. However, the interaction between CALM and the membrane was yet to be investigated. Protein insertion in the membrane has been only hypothesized, but never directly experimentally proven. In this work, a biophysical approach was exploited to investigate CALM interaction with PIP_2 containing model membranes. In particular, neutron reflectometry experiments shed light on the insertion of the protein in the membrane, as well as on its three-dimensional orientation upon lipid binding.

1. Introduction

Clathrin-mediated endocytosis (CME), is the main endocytic pathway used by cells to internalize membrane protein (named cargoes)[1–3]. It is defined as a receptor-mediated endocytic pathway, since it needs the interaction of several proteins, named adaptor and modulator, with the inner leaflet of cell membrane. Indeed, the latter presents negatively charged lipids, such as phosphatidylinositol 4,5-bisphosphate (PIP_2), that can interact with positive patches of endocytic proteins. PIP_2 polar headgroup contains a cyclic polyol myo-inositol $(CHOH)_6$[4] ring whose hydroxyl groups in position 4 and 5 are phosphorylated, thus providing the required negative charges for protein binding.

CME is a very complicated biological pathway (see **Figure 1.6**) which has been studied for years. It requires the cross-interaction between different adaptor and modulator proteins, which form large protein complexes, localized at the inner leaflet of the plasma membrane. The function of adaptor proteins, such as AP2 and CALM, is to bind both the lipid membrane and the cargo, as well as clathrin molecules, whose recruitment leads to self-association in polygonal lattices. The latter coat the plasma membrane progressing into a deeply invaginated bud of the bilayer. Indeed, acting as a mechanical scaffold, the clathrin coat deforms the surface membrane forming clathrin-coated pits (CCPs). Thus, the coupling between cargo recognition and clathrin coat assembly,

which is tightly regulated by the adaptor proteins, is a key step in the CME pathway[5]. The resultant intricate network of protein-protein and protein-lipid cross-interactions aims to form stable protein-cargo complexes localized at the inner leaflet of the cell membrane that could then lead to maturated CCP. As last step of the CME pathway, the GTPase dynamin, localised at the plasma membrane, assemble into collar-like structures at the necks of CCPs, where it catalyses membrane fission[6]. Hence, the clathrin-coated vesicle (CCV), which contains the cargo and a small volume of extracellular fluid, is released and enter freely in the cell[5,6].

Malfunctioning during any step of this complex biological machinery can result in diseases such as Alzheimer[7] and Stiff man diseases[8]. Thus, recently the CME has been a much studied process and many of the most important cross interactions between proteins have been unravelled[7,9–12]. Molecular biology and proteomic approaches have been essential to fully understand the CME pathway and biocrystallography was also exploited to obtain the crystal structure of many of the protein involved, such as CALM.

CALM (clathrin assembly lymphoid myeloid leukemia protein) is one of the most abundant clathrin adaptors in endocytic CCVs isolated from tissue culture cells (30%-35% of the adaptors in a CCV[13,14]), and it binds to and sorts the small proteins R-SNAREs VAMPs 2, 3, and 8[7,15]. It possesses a relatively small, compact stacked-helical domain, called AP180 N-terminal homology (ANTH) domain and defined as residues 19-289[16] (crystallographic structure shown in **Figure 1.7**), with large, natively unstructured, C-terminal appendages containing a clathrin binding site[16–18]. Both PIP_2 and cargo binding sites are located in the ANTH domain, Lysines 28, 38 and 40[16] and Methionine 244[7] respectively[10]. Moreover, CALM is characterized by a membrane-inserting amphipathic helix at the N-terminus (amphipathic helix 0, AH0, residues 5-18)[10], whose 3D orientation is thought to change upon membrane binding. The absence of AH0 leads to the formation of flat clathrin lattices on lipid monolayers and not invaginated clathrin-coated pits[9,16]. Indeed, it was shown that CALM senses and induces membrane curvature[10,19], being also able to drive pearlized liposomes tubulation, thanks to the insertion of AH0 in the membrane[10]. Although the insertion of the helix in the membrane was hypothesized, it was not experimentally proved[10].

Thus, many questions remain unanswered concerning the interaction between CALM and lipids, which represents the very first steps of the CME, as well as the protein insertion and orientation with respect to the membrane. Here, we exploited neutron reflectometry (NR) to

investigate CALM-model membrane systems. NR probes the structure of planar membranes in the direction perpendicular to their plane, obtaining information about film thickness and composition, as well as about protein interaction and insertion in the membrane.

The main aim of this work has been to unravel the determination of CALM insertion in the membrane and its orientation. In order to assess the insertion of the AH0 in the membrane, the wild type ANTH domain of the protein (hereinafter CALM wild type, $CALM_{wt}$) and the mutant missing the AH0 ($CALM_{\Delta AH0}$) were compared. Moreover, the relation between PIP_2-inositol ring orientation (with respect to the plane of the membrane) and CALM binding was also investigated.

2. Materials and methods

2.1. Protein expression and purification

All the hydrogenous protein constructs used in this work were kindly provided by Dr. David J. Owen of the Cambridge Institute for Medical Research (University of Cambridge). The deuterated CALM was a kind gift of the ILL D-Lab. The proteins expression and purification protocols can be found in Refs[7,10]. The sequence is GSPIGIPMSGQSLTDRITAAQHSVTGSAVSKTVCKATTHEIMGPKKKHLDYLIQCTNEMN VNIPQLADSLFERTTNSSWVVVFKSLITTHHLMVYGNERFIQYLASRNTLFNLSNFLDKS GLQGYDMSTFIRRYSRYLNEKAVSYRQVAFDFTKVKRGADGVMRTMNTEKLLKTVPII QNQMDALLDFNVNSNELTNGVINAAFMLLFKDAIRLFAAYNEGIINLLEKYFDMKKNQ CKEGLDIYKKFLTRMTRISEFLKVAEQVGIDRGDISGSGSGHMDRVRNLQSEVEGVKNI MTQNVERILARGENL.

2.2. Materials

1,2-dipalmitoyl-sn-glycero-3-phosphocholine (DPPC), 1,2-dipalmitoyl-sn-glycero-3-phosphoethanolamine (DPPE) 1,2-dioleoyl-sn-glycero-3-phosphocholine (DOPC), 1,2-dioleoyl-sn-glycero-3- phosphoethanolamine (DOPE) and brain L-α-phosphatidylinositol-4,5-bisphosphate (ammonium salt) $PI(4,5)P_2$ (PIP_2) were purchased as powder from Avanti Polar Lipids (purity >99%, Alabaster, AL, USA). Solutions of 3 $mg \cdot mL^{-1}$ of DPPC, DPPE, DOPC and DOPE and a solution of 1 $mg \cdot mL^{-1}$ PIP_2 were prepared in chloroform stabilized with ethanol (purity 99.8%; Sigma-Aldrich, St. Louis, MO, USA). These solutions were used as stock solutions in order to prepare mixtures with the desired compositions, *i.e.*, PC:PE:PIP_2 7:2:1 molar ratio, either with

DPPC, DPPE for monolayer studies, or DOPC, DOPE for bilayer and liposome studies. Ultra-pure water was generated by passing deionized water through a Milli-Q unit (total organic content = 4 ppb; resistivity = 18 mΩ·cm, Milli-Q, Merck KGaA, Darmstadt, Germany). D_2O (99.9% of isotopical purity) was purchased from Sigma-Aldrich (St. Louis, MO, USA) and used as received. Experiments were performed in HKM buffer (25 mM HEPES pH 7.2, 125 mM potassium acetate, 5 mM magnesium acetate, 1 mM DTT) or HEPES-NaCl buffer (5 mM HEPES pH 7.0, 150 mM sodium chloride). HEPES (in solution, 1 M in H_2O, and powder, purity 99.5%), potassium acetate (purity≥99.0%), magnesium acetate (purity≥99.0%), DTT (purity≥99.0%), sodium chloride (purity≥99.0%) and magnesium chloride (purity≥98.0%) were purchased from Sigma Aldrich (St. Louis, MO, USA).

2.3. Langmuir monolayer

A solution of lipids in chloroform with a composition DPPC:DPPE:PIP_2 7:2:1 molar ratio was prepared at 0.1 $mg{\cdot}mL^{-1}$ concentration, and used for all the experiments with lipid monolayers. A Langmuir trough (Kibron, Helsinki, Finland) with a maximum area of 166.4 cm^2 equipped with two dependent symmetric sliding barriers was used to measure the surface pressure (Π) – area (A) isotherms of lipid monolayers. The variation of surface pressure was recorded using a Wilhelmy plate made of filter paper (Whatman CHR1 chromatography paper. The subphase used was made of HKM buffer (120 mL) and the temperature was maintained at 21.0 ± 0.5 °C.

2.4. Liposomes preparation

Small unilamellar vesicles (SUV) were prepared by dissolving DOPC:DOPE:PIP_2 (7:2:1 molar ratio) in chloroform, dried under gentle Argon flow and placed in vacuum overnight to ensure evaporation of all solvent. The resulting lipid films were rehydrated at room temperature in water with 2 mM magnesium chloride up to 0.1 $mg{\cdot}mL^{-1}$, or in HEPES-NaCl buffer solution up to 1 $mg{\cdot}mL^{-1}$, for Quartz crystal microbalance with dissipation monitoring (QCM-D) and bilayer NR studies, respectively. Immediately before use for lipid bilayer formation, the suspension was tip sonicated for 5 min at pulses of 1 s on/off to produce a visually clear dispersion of SUVs. For QCM-D experiments, the SUV were tip sonicated for 5 min at pulses of 1 s on/off and then extruded at room temperature through 100 nm pore-size Millipore polycarbonate membranes. For SANS experiments, liposomes were prepared in HEPES 5 mM NaCl 10 mM (pH=7) buffer solution. They were tip sonicated for 5 min at pulses of 1 s on/off and finally extruded at room

temperature through 100 nm pore-size Millipore polycarbonate membranes. The concentration of NaCl was gradually increased up to 150mM.

2.5. Quartz crystal microbalance with dissipation monitoring (QCM-D)

QCM-D experiments were performed using a commercial Q-Sense E4 instrument (Q-Sense, Biolin Scientific AB, Sweden). SiO_2-coated 5 MHz AT-cut quartz sensors (QSX 303, Q-Sense, Biolin Scientific AB, Sweden) were employed. The latter were cleaned before the experiments with organic solvents (chloroform, acetone, ethanol) and water, with the use of an ultra-sonication bath. Finally, they were dried under gentle Nitrogen flow and exposed to UV-ozone cleaning in aProCleaner™ Plus instrument (BioForce Nanosciences, Virginia Beacrh, VI, USA) for 30 minutes. The crystals were inserted in the QCM-D flow module, which is connected to a peristaltic pump (Multichannel Peristaltic Pump IPC-N 4, Ismatec, Switzerland). Before acquisition, the fundamental frequency and six overtones (3^{rd}, 5^{th}, 7^{th}, 11^{th} and 13^{th}) were recorded and the system was equilibrated in the appropriate buffer at 22 °C for at least 10 min, *i.e.*, until a stable baseline was obtained. A solution 0.1 $mg \cdot mL^{-1}$ of small unilamellar vesicles (DOPC:DOPE:PIP_2, 7:2:1 molar ratio) in water with 2 mM magnesium chloride was introduced in the flow cell at 0.1 $mL \cdot min^{-1}$ and the typical signal corresponding to the vesicle fusion and lipid bilayer formation was followed. Osmotic shock was exploited to force vesicle rupture and bilayer formation, by introducing in the flow cell a solution 500 mM of sodium chloride at 0.1 $mL \cdot min^{-1}$. After the formation of the lipid bilayer, buffer solution was flowed through the system to remove partially or weakly bound unilamellar lipid vesicles. Protein solution (9.6 µM) was introduced in the flow cell at 0.1 $mL \cdot min^{-1}$. After 5 hours incubation, buffer was flowed at 0.1 $mL \cdot min^{-1}$ to remove unbound and physisorbed protein molecules. The system was let equilibrate overnight and finally buffer was flowed at 0.1 $mL \cdot min^{-1}$ until a stable baseline was reached.

The QCM-D allows monitoring, simultaneously, the changes of the resonance frequency (Δf) and dissipation energy (ΔD) over time. The data were analysed using the software Q-Tools (version 3.0.10, Q-Sense, Biolin Scientific AB, Sweden), by using the Voigt viscoelastic model adapted by Voinova et al.[20], which describes the bilayer as a solid undergoing reversible viscoelastic strain. This model provides the exact mass adsorbed on the crystal, and gives information regarding the viscoelasticity, shear modulus and density of the different layers deposited on the quartz crystal. An extensive explanation of the Voigt-Voinova viscoelastic model,

and the equations used to describe it (**Equations S5.1** to **S5.3**), is reported in the **Supporting Information**. For the fitting, the fluid density and viscosity were fixed at $1 \cdot 10^3$ kg·m^{-3} and $1 \cdot 10^{-3}$ kg·m^{-1}·s^{-1}, respectively; the density of the lipid bilayer was fixed at $1.1 \cdot 10^3$ kg·m^{-3}, which is consistent with previous studies[21]. The density of the protein layer was fixed first at $1.0 \cdot 10^3$ kg·m^{-3}, and then at $1.36 \cdot 10^3$ kg·m^{-3}, which correspond to the density of the solvent and the one of the dry protein[b], respectively. In both cases, the obtained values for the mass of $CALM_{wt}$ adsorbed on the bilayer was the same, and the values of protein layer shear modulus and shear viscosity were in the range of ~0.01-2.5 MPa and ~0.001-0.02 kg·m^{-1}·s^{-1}, respectively, which agree with estimated values for protein[22].

2.6. Neutron reflectometry on mono- and bilayer model membranes

NR experiments with monolayer and bilayer model membranes were performed on the reflectometers FIGARO[23] and D17[24,25] at the ILL. Two different angles of incidence were employed: 0.62° and 3.8° for Langmuir monolayers, and 0.8° and 3.2° (or 3°) for solid supported lipid bilayers in FIGARO (or D17). The wavelength resolution used was 7% $d\lambda/\lambda$. The momentum transfer, $Q_z=(4\pi/\lambda)\sin\theta$, range was from 0.001 to 0.25 Å^{-1}. Lipid monolayers were prepared in home-built Langmuir troughs, filled with 42 mL of HKM buffer solution, and after their characterization, protein was injected in the bulk phase to a final concentration of 5 µM that corresponds to the protein K_D[3]. Three buffered isotopic solvent contrasts were employed, characterized by different scattering length density (SLD): 100% D_2O (SLD=$6.36 \cdot 10^{-6}$ Å^{-2}), 60% D_2O *v/v* (SLD=$3.59 \cdot 10^{-6}$ Å^{-2}) and 8.1% D_2O *v/v* (SLD=0), denominated air contrast matched water (ACMW), since its SLD is equal to that of the air. For NR experiments on bilayers, solid/liquid flow cells available at the ILL with polished silicon crystals (111) with a surface area of 5×8 cm^2 were used. The silicon crystals were carefully cleaned with organic solvents (chloroform, acetone, ethanol) and polished for 2 minutes with a Plasma cleaner PDC-002 (230V) (Harrick Plasma, New York, US). Substrate surface was characterized in two different isotopic solvent contrasts, (100% H_2O and 100% D_2O), before bilayer deposition. Bilayers were formed through vesicle fusion, aided by osmotic shock, and then characterized in three different buffered isotopic solvent contrasts: 100% H_2O (SLD=$-0.56 \cdot 10^{-6}$ Å^{-2}), 38% D_2O *v/v* (called silica contrast matched water,

[b] Obtained through the Biomolecular Scattering Length Density Calculator tool available on the STFC-ISIS online platform (http://psldc.isis.rl.ac.uk/Psldc/).

SiMW, SLD=$2.07 \cdot 10^{-6}$ $Å^{-2}$) and 100% D_2O. Then, the protein was injected in the flow cell, up to a 20 µM concentration. After appropriate kinetics, the unbounded and physisorbed protein molecules were washed away by a buffer solution washing step, and the bilayer+protein system was characterized in three buffered isotopic solvent contrasts: 100% H_2O, 38% D_2O and 100% D_2O *v/v* for experiments with hydrogenous CALM, and 100% H_2O, 38% D_2O and 62% D_2O *v/v* for experiments with deuterated CALM. HEPES 5mM, NaCl 150mM (pH=7) buffer solution was used for NR bilayer experiments. The NR data were reduced and normalized using COSMOS[26]. Subsequent data analysis was performed using AuroreNR[27] and Motofit[28] software, by minimizing the difference between the experimental data points and the calculated reflectivity profile, which was obtained employing a multi-layer slab model. The latter is made of layers characterized by an in-plane averaged SLD, whose value depend of the volume fraction (*f*) of each component, leading to $SLD_{model} = f_{solvent} \cdot SLD_{solvent} + f_{lipid} \cdot SLD_{lipid} + f_{protein} \cdot SLD_{protein}$[c]; where $f_{solvent} + f_{lipid} + f_{protein} = 1$. Moreover, data analysis was performed using constrains between layer parameters, *i.e.*, taking into account that lipid headgroups and tails must have the same area per molecule. To this purpose, the fraction of water in the headgroups-layer (f_{wh}) was calculated following **Equation 5.1**:

$$f_{wh} = 1 - \frac{t_t \cdot V_h}{t_h \cdot V_t} \qquad \textbf{5.1}$$

where t_t and t_h are the thicknesses of tails- and headgroups-layer, respectively, and V_t and V_h are the molecular volumes of tails and headgroups, respectively. All the fixed parameters are tabulated in **Tables S5.1**. The roughness of the interfaces was also fitted; in the case of purely lipid molecules containing layer, the roughness of the different interfaces were linked.

2.7. Dynamic Light Scattering (DLS)

A Zetasizer Nano ZS90 (Malvern Instruments Ltd., U.K.) using a He-Ne laser 633nm (max 5mW) and a scattering angle of 90° was used in this work to determine the size and polydispersity of the liposome samples for SANS and QCM-D. DLS experiments relies on the measurement of the normalized intensity or (second-order) autocorrelation function, which can be related to the field (or first-order) autocorrelation function, allowing the determination of the diffusion coefficient of the scattering particles. For spherical Brownian scattering particles diffusing in a

[c] The SLD of the protein has been determined using the Biomolecular Scattering Length Density Calculator tool available on the STFC-ISIS online platform (http://psldc.isis.rl.ac.uk/Psldc/).

Newtonian medium, it is possible to correlate the diffusion coefficient with an apparent hydrodynamic radius (**Equations S5.4** to **S5.6** in the **Supporting Information**). Thus, this techniques provides information regarding sample size and eventual aggregation. A quartz cell with a 90° window was exploited, with reduced volume (50 µL). Liposome sample for QCM-D experiments were measured after extrusion. The same samples measured with SANS (purely lipid samples and lipids+protein samples) were then measured with DLS.

2.8. Small-angle neutron scattering (SANS)

Small-angle neutron scattering (SANS) probes the shape, the spatial distribution and the interactions between dispersed particles by detecting the radiation scattered by the sample as a function of momentum transfer Q. SANS measurements were carried out on D11[29] at the ILL, using Hellma quartz 120-QS cells of 200 µL volume and 1 mm pathway for 100% D_2O contrast, and 400 µL volume and 2 mm pathway for 42% D_2O *v/v* (SLD=$2.35 \cdot 10^{-6}$ $Å^{-2}$) contrast, to match out the protein. Samples were measured over a Q-range of 2.5 10^{-3} to 0.6 $Å^{-1}$ at a single wavelength of 6.0 Å (FWHM 10 %), with 3 sample-to-detector distances (1.5, 17.6 and 43 m). Absolute scale was obtained from the flux using the attenuated direct beam. Data correction was performed using GRASP (Graphical Reduction and Analysis SANS Program for Matlab developed at ILL by Charles Dewhurst), accounting for transmission, flat field, detector noise (measurement of boron carbide absorber); the contribution from the solvent was subtracted. The differential scattering cross-section of a SANS experiment can be expressed as[30,31]

$$\frac{d\sigma}{d\Omega}(Q) = n(\Delta SLD)^2 V_{part}^2 P(Q) S(Q) \qquad \textbf{5.2}$$

where n is the particle number density, ΔSLD is the difference in SLD between the solvent and the particles (*i.e.*, the contrast), and V_{part} is the volume of a single particle. The term P(Q) is the particle form factor, determined by the particle conformation. S(Q) is the structure factor[32], which gives information regarding the inter-particle interactions in solution. The form factors used in this work are explained in detail in the **Supporting Information** (**Equations from S5.7** to **S5.10**).

Experiments were performed at 22°C in HEPES 5 mM NaCl 150 mM (pH=7) buffer, with a protein:lipid molar ratio of 1:25. The protein stock solution contained 50% *v/v* of glycerol. Liposomes after extrusion in two different contrast were measured: 100% D_2O at a concentration of 0.6 $mg \cdot mL^{-1}$, and 42% D_2O *v/v* at a concentration of 0.7 $mg \cdot mL^{-1}$, adding 11.5% and 7.7% glycerol (*v/v*), respectively. Liposomes+$CALM_{wt}$ samples were measured in the same contrasts:

100% D_2O (+11.5% glycerol, *v/v*), containing 0.6 mg·mL^{-1} lipids and 28 µM $CALM_{wt}$; 42% D_2O (+7.7% glycerol, *v/v*) containing 0.7 mg·mL^{-1} lipids and 36 µM $CALM_{wt}$. The data were analyzed with SASfit[33,34] and SasView Version 5.0.4[35] software. The former was employed to determine the Guinier Radius and the Porod Volume, at low-Q and high-Q, respectively. From this analysis, the total size of the liposomes was calculated, which was used to estimate the volume occupied by the scattering molecules. From the ratio between this volume and the Porod Volume (<1), and taking into account the characteristic bump at mid-Q in the SANS profiles, we deduced that the data could be modelled considering two different populations: bilamellar vesicles[36] and nanodisks (cylinders[30,37,38]). Thus, an appropriate model was implemented in SasView and used to fit the experimental data (see **Supporting Information**). Due to the sample dilution, any kind of structure factor was used.

3. Results and Discussion

3.1. Binding of $CALM_{wt}$ to model planar membranes enriched in PIP_2

Although the overall PIP_2 concentration in the inner leaflet of the mammalian plasma membrane is about ~1-2% in mol[39–42], in order to better investigate CALM-membranes interaction, *in vitro* lipid model systems containing 10% mol of PIP_2 were chosen. This composition reflects the high local concentration of PIP_2 present at the docking sites of the cell membrane[43]. Besides it has been reported in literature[44–47], as well as demonstrated in **Chapter 3** of this manuscript, that divalent cations (as Mg^{2+}) induce cluster formation of PIP_2 within the membrane plane, thus improving protein binding. Indeed, PIP_2 molecules are free to laterally diffuse within mono- and bilayer interfaces, forming electrostatically stabilized complexes with the divalent cations[45,48]. Moreover, since PIP_2 molecules are mostly present in liquid disordered phase of a lipid monolayer[48] (as reported in **Chapter 3**), their diffusion in the plane of the membrane is facilitated[49]. However, in the case of liposome dispersion with 10% mol PIP_2 in presence of 5 mM Mg^{2+}, we experienced aggregation and precipitation of the lipid sample, probably due to the bridging effect of the divalent cation on PIP_2 molecules. Thus, a simpler buffer solution without Mg^{2+} has been employed for neutron studies with liposomes as well as bilayers. Indeed, different model membranes were employed in this chapter. Planar membranes such as lipid mono- and bilayers were firstly used to investigate $CALM_{wt}$ binding in presence, and absence, of divalent

cations (Mg^{2+}). Later on, vesicles were exploited to study $CALM_{wt}$ interaction with curved membranes, with the aim of investigating the liposomes tubulation[10].

In the case of lipid monolayers, a composition of DPPC:DPPE:PIP_2, in molar ratio 7:2:1, was employed. The composition was chosen to replicate the inner leaflet of the plasma membrane, whose phospholipid content is enriched in phosphatidylcholine (PC) and phosphatidylethanolamine (PE)[50–52]. Such composition of phospholipid headgroup family was already used for biochemical studies with CALM[10]. Importantly, the use of saturated palmitoyl chains avoided the problem of oxidation of phospholipid tails, which may occur at the air/water interface when multiple unsaturations are present, as for example with di-oleoyl phospholipids. Nonetheless, DOPC and DOPE were used for bilayer as well as liposomes, as the risk of oxidation is reduced. These lipids mimic better the flexibility of the plasma membrane as they are characterized by a lower melting temperature, hence higher flexibility of acyl chains.

Firstly, the surface pressure (Π) - area (A) per molecule compression isotherm of the DPPC:DPPE:PIP_2 monolayer was recorded, at 21°C, and plotted in **Figure 5.1 A**, together with the isotherm of purely DPPC[53] monolayer measured in the same condition of temperature and buffer solution. **Figure 5.1 B** shows the corresponding compressional elastic moduli (C_s^{-1}), calculated according to **Equation 5.3**.

$$C_s^{-1} = -\mathrm{A} \cdot \left(\frac{\partial \Pi}{\partial \mathrm{A}}\right) \qquad \textbf{5.3}$$

where A is the area per molecule and Π is the surface pressure. Recording the compression isotherm allowed us to explore a large region of the lipid interfacial phase diagram, providing insightful knowledge about the monolayer phase behaviour. Indeed, the isotherm helps distinguish between liquid expanded (LE, fluid-like) phase, characterized by a lack of in-plane spatial and orientational organization of the lipid molecules, and liquid condensed (LC, gel-like) phase that consists of tightly packed lipids. Thus, information regarding lateral compressibility could be obtained. Both isotherms shown in **Figure 5.1 A**, similar to the one of DPPC:PIP2 7:3 molar ratio shown in **Chapter 3**, display a LE phase at low values of surface pressure (Π < 3-5 $mN \cdot m^{-1}$), followed by an increase in lateral density upon further compression and the emerging of an LE-LC phase coexistence. There is, therefore, a disordered/ordered phase transition corresponding to the LE-LC transition, whose identification was not straightforward from the visualization of the Π -A isotherms. However, the phase transition produced a minimum in the C_s^{-1} profile at Π ≈ 3

$mN \cdot m^{-1}$ and $\Pi \approx 5$ $mN \cdot m^{-1}$, for mixed and DPPC monolayers, respectively, which is typically visible in isotherms of purely DPPC monolayers[53,54]. Further compression yielded a LC phase for both DPPC and DPPC:DPPE:PIP_2 monolayers. Indeed the slope of the C_s^{-1} profile increases when $\Pi \approx 25$ $mN \cdot m^{-1}$, indicating increasing rigidity of the film, thus increasing in the LC phase. We could conclude that the introduction of DPPE (20% in mol) and PIP_2 (10% in mol) in the monolayer, does not produce drastic changes in the isotherm, which is mostly influenced by DPPC phases. Only a shift of the isotherm at smaller values of area per molecules, as well as a shift of the C_s^{-1} profile minimum related to the LE-LC phase transition (from 5 to 3 $mN \cdot m^{-1}$), are visible. We attributed these to the presence of DPPE lipid molecules that possess a smaller headgroup moiety compared to the PC, thus occupying less area. It has already been discussed in **Chapter 3** that the presence of PIP_2 does not drastically influence the DPPC isotherm. Finally, as reported in **Chapter 3**, smaller values of C_s^{-1} at larger areas per molecule compared to DPPC isotherm in pure water[54] are observed. This behaviour was explained taking into account the presence of divalent cations (Mg^{2+}) in the bulk phase, which decrease the lipid packing density in both mono- and bilayers[53,55,56].

Two different initial lipid surface pressure (Π_0) were chosen, 15 and 25 $mN \cdot m^{-1}$, in order to evaluate the influence of lipid area per molecule on $CALM_{wt}$ binding, through the recording of the increase in surface pressure upon protein injection in the bulk phase. As expected, starting from a less packed monolayer, *i.e.*, when $\Pi_0 = 15$ $mN \cdot m^{-1}$, allowed a larger increase in the surface pressure upon protein binding, due to a major partitioning of $CALM_{wt}$ at the interface (**Figure 5.1 C** and **Figure S5.1 A** and **B**). However, NR was necessary to unravel the coverage of the protein interacting with the membrane.

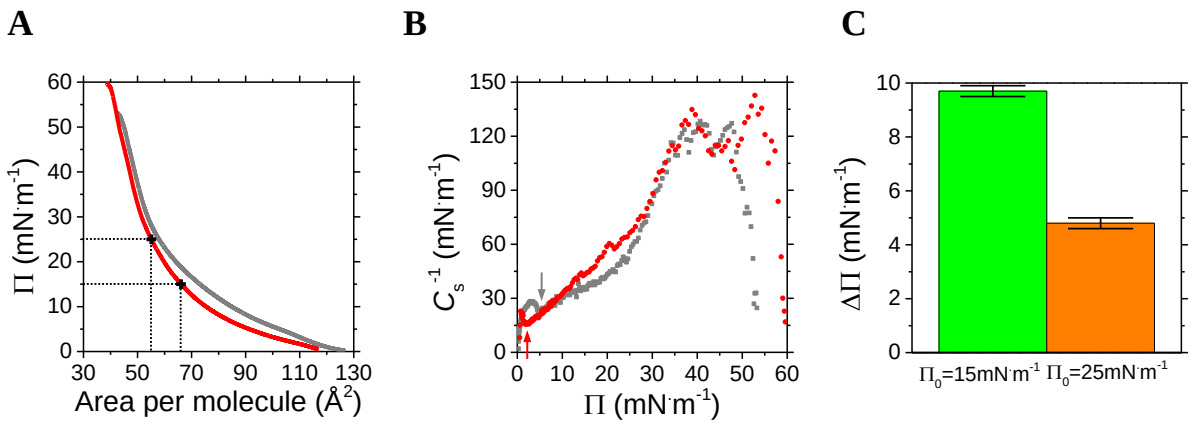

Figure 5.1 A Compression isotherms of DPPC:DPPE:PIP_2, 7:2:1 molar ratio (red line) and pure DPPC (grey line) monolayers; the two pressures exploited for binding studies with the protein are shown as black cross. **B** Compressional elastic moduli (C_s^{-1}) of DPPC:DPPE:PIP_2 (red circles) and pure DPPC (grey squares) monolayers. The arrows indicate the minima in the profiles, corresponding to the LE-LC phase transition. **C** Increase in surface pressure ($\Delta\Pi$) obtained after $CALM_{wt}$ injection in the bulk underneath the lipid monolayer at Π_0=15mN·m^{-1} (green column) and Π_0=25mN·m^{-1} (orange column).

The binding of $CALM_{wt}$ to lipid bilayer was also investigated, firstly through QCM-D experiments, and then with NR. The former technique relies on the aptitude of SUVs to fuse upon reaching the surface of SiO_2-coated quartz crystals, thus forming a lipid bilayer[21,22,57–63]. QCM-D is widely exploited to determine viscoelastic properties of lipid bilayers, or more generally, to find out the mass of the film deposited on the crystal[20,63–65], by measuring the frequency of resonance of the crystal as well as the energy dissipated. After PIP_2–containing liposomes injection and fusion on the crystal, the formation of the bilayer was monitored. Once a stable signal of both frequency shift and energy dissipation related to the bilayer was obtained, $CALM_{wt}$ was injected in the flow cell to a final concentration of 9.6 µM. A final washing step with appropriate buffer was necessary to wash away the unbounded and physisorbed protein molecules (see all the steps in **Figure S5.2 A** to **D**), and then the extra mass due to protein binding was determined, by using the viscoelastic model proposed by Voinova and coworkers[20,64,65] (see **Methods** and **Supporting Information**). To evaluate the influence of Mg^{2+} cations on protein binding, the experiments were performed in both HEPES-NaCl (no Mg^{2+}) and HKM (5 mM Mg^{2+}) buffer solutions, whose profiles are displayed in **Figure 5.2 A** and **B**, respectively. Six different overtones (3rd, 5th, 7th, 9th, 11th, 13th) were recorded for each experiment, and five of them (from 5th to 13th) were employed for the analysis (the fundamental frequency, 1st, and the 3rd overtones were not used in the analysis due to the piezoelectric stiffness of the AT-cut quartz crystals which reduces the signal sensitivity).

Figure 5.2 C shows the values of adsorbed mass obtained in the two buffer solutions. As already explained in the **Methods** section, the density of the lipid bilayer was fixed at $1.1 \cdot 10^3$ $kg \cdot m^{-3}$, which is consistent with previous studies[21], and the one of the protein layer was fixed first at $1.0 \cdot 10^3$ $kg \cdot m^{-3}$, and then at $1.36 \cdot 10^3$ $kg \cdot m^{-3}$, which correspond to the density of the solvent and the one of the dry protein, respectively. In both cases, the obtained values for the mass of $CALM_{wt}$ adsorbed on the bilayer was the same, and the values of protein layer shear modulus and shear viscosity were in the range of ~0.01-2.5 MPa and ~0.001-0.02 $kg \cdot m^{-1} \cdot s^{-1}$, respectively, which agree with estimated values for protein layers[22]. Anyway, from NR studies we obtained a hydration percentage of the protein layer of at least 88% (*v/v*), that would lead to a layer density close to the one of the pure solvent (*i.e.*, $1.0 \cdot 10^3$ $kg \cdot m^{-3}$). **Figure S5.2** shows the fit obtained using $1.0 \cdot 10^{-3}$ $kg \cdot m^{-3}$ as density value. From the ratio between bilayer mass and $CALM_{wt}$ mass deposited on the crystal, a PIP_2:$CALM_{wt}$ molecular ratio of 2±1 and 6±2 in HEPES-NaCl and HKM buffer solution, respectively, was obtained. However it has to be underlined that to obtain the mass of the protein, all the viscoelastic parameters regarding the bilayer were fixed, thus not considering an effect of CALM on the membrane viscoelastic properties. Although it has been reported that the presence of divalent cations increases PIP_2-protein binding by inducing PIP_2 clusters in both lipid monolayers and not supported lipid bilayers, here we experienced a larger shift in frequency, correlated to a large amount of adsorbed mass (**Figure 5.2 C**) in the case of absence of Mg^{2+}, hence suggesting an improvement in CALM binding. This results could be explained taking into account the reduced lipid diffusion in the case of supported lipid bilayer[57,66,67]. Indeed, the strength of the interaction between the substrate and the lipids influences viscoelastic properties as well as natural bilayer fluctuations[68,69], thus preventing the formation of PIP_2-clusters bridged by Mg^{2+}. Hence, in this case, divalent cations tend to shield negative charges of isolated PIP_2 molecules. Anyway, the bigger increase in frequency in the case of absence of Mg^{2+} ions led us to use the same HEPES-NaCl (no Mg^{2+}) buffer solution for NR experiments with lipid bilayer, from which we recalculated a more accurate PIP_2:$CALM_{wt}$ ratio.

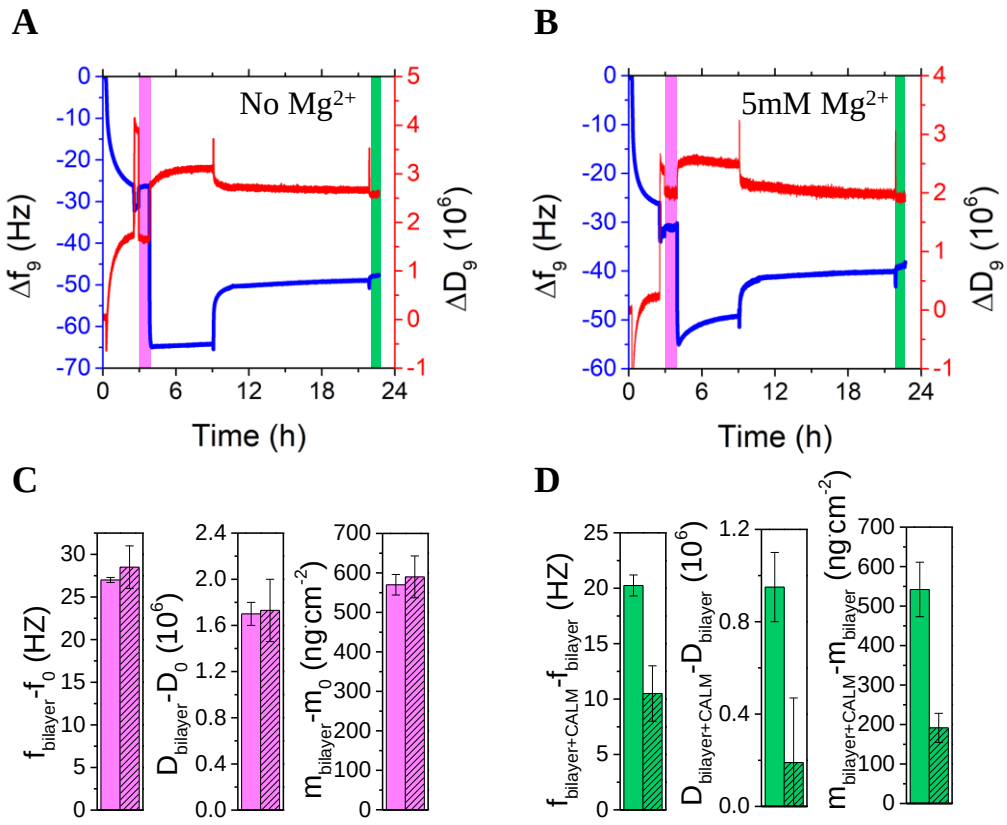

Figure 5.2 QCM-D profiles of DOPC:DOPE:PIP_2 bilayer, followed by $CALM_{wt}$ injection, in **A** HEPES-NaCl (no Mg^{2+}) and **B** HKM (5 mM Mg^{2+}) buffer solutions. Frequency and dissipation energy shifts of the 9th overtone are depicted as blue and red lines respectively (see **Figure S5.2** for all the overtones). The magenta and green shading represent the data used for the fit, related to bilayer and bilayer+$CALM_{wt}$, respectively. Shifts in frequency and dissipation, as well as fitted mass, due to **C** pure lipid adsorption (bilayer formation, pink columns) and **E** $CALM_{wt}$ addition (green columns) in the two buffer solution. Parameters related to HEPES-NaCl (no Mg^{2+}) are shown as plain columns, while the ones related to HKM buffer solution as hachured columns.

3.2. Interaction of $CALM_{wt}$ with liposomes enriched in PIP_2

DLS and SANS were employed to investigate the binding of CALM with PIP_2-containing 100 nm sized liposomes, and at a protein:lipid ratio of 1:25. This size was chosen since it is closer to the preferred size for CALM[10]. **Figure 5.3 A** reports the exponential-like intensity autocorrelation functions for purely lipids and lipids in presence of $CALM_{wt}$: the presence of the protein shifts the decay of the function to higher values of the time, thus suggesting an increase in the average size of the scattering particles, as can be clearly observed in the intensity distributions shown in **Figure 5.3 B**. However, the expected structural complexity emerging from the interaction of the liposomes with $CALM_{wt}$ makes difficult to perform a quantitative comparative in terms of the apparent hydrodynamic radius, or the diffusion coefficient. SANS profiles of lipids in two different contrast were measured: 100% D_2O and 42% D_2O *v/v*. The obtained intensity

curves, plotted against the momentum transfer (Q), were modelled taking into account two different population: bilamellar vesicles of a total diameter of ~60 nm, which is compatible with the size of the membrane used for extrusion (100 nm), and nanodisks of lipids with a radius of ~18 nm (see **Figure 5.3 C** and **D**, and **Table S5.3** for fitting parameters). When $CALM_{wt}$ was added to the liposomes solution, changes in the profile were observed, especially at low-Q and mid-Q. It is interesting to note the faster decay ($\sim Q^{-2}$) in the low-Q range (**Figure 5.3 E** and **F**), compared to profiles of pure lipid samples (Q^0), thus suggesting the presence of scattering objects bigger than 100 nm. We concluded that $CALM_{wt}$ has indeed an effect on liposome shape and size. However, we could not deduce whether the lipid+$CALM_{wt}$ sample contains larger vesicle, from fusion processes, or large tubules. Time-resolved measurements were performed, showing no effect (**Figure S5.4 A** and **C**). Moreover precipitation was observed in the sample after the addition of the protein, which led to a decrease in the signal (**Figure S5.4 C** and **F**).

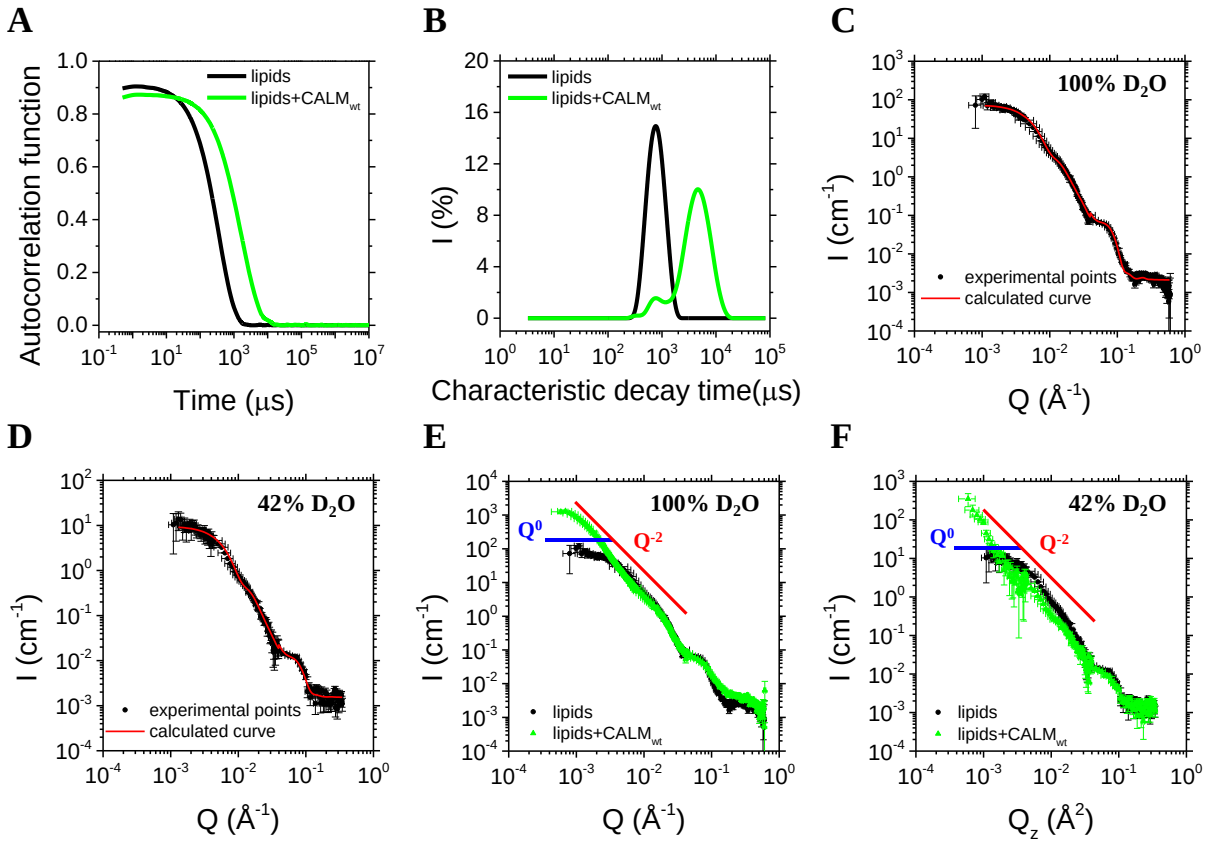

Figure 5.3 A Intensity autocorrelation functions for solely lipid sample (black line) and lipids in presence of $CALM_{wt}$ (green line). **B** intensity distributions plotted versus the characteristic decay time of solely lipid sample (black line) and lipids+$CALM_{wt}$ sample (green line). Panels **C** to **F** show the recorded SANS profiles: solely lipid samples in **C** 100% D_2O and **D** 42% D_2O *v/v*; comparisons of lipid sample and lipid+$CALM_{wt}$ sample profiles in **E** 100% D_2O and

F 42% D_2O *v/v*. The experimental data points related to lipid and lipid+$CALM_{wt}$ samples are depicted as black circles and green triangles respectively. The model used to fit the lipid profiles is shown as red line.

3.3. Neutron reflectometry as tool to determine $CALM_{wt}$ orientation toward model membranes

Although the molecular structure of the protein is known (PDB ID: 3zyk[7]), its orientation with respect to the lipid membrane upon binding was yet to be investigated. NR offered a precious tool to determine the degree of insertion of $CALM_{wt}$ in mono- and bilayer, as well as its three-dimensional orientation.

The $CALM_{wt}$ structure on lipid monolayers (Π_0=15mN·m^{-1}) was investigated in presence of Mg^{2+} cations, and the data obtained were modelled through a multilayer slab model that takes into account lipid tails- and headgroups- layers, and three extra layers for the protein, considered underneath the monolayer (**Table 5.2**). It has to be noted that insertion of the protein in the headgroups-layer was observed (13±1% *v/v*, **Figure 5.4 A**, **Table 5.1** and **Table 5.1 Table 5.2**), which is consistent with our multilayer model since the PIP_2 inositol ring is considered as included in the headgroups-layer. Moreover the fraction of water that characterizes this layer ensured that tails and headgroups have the same area per molecule, even after $CALM_{wt}$ insertion. To validate this model, the binding of $CALM_{wt}$ with lipid bilayer in absence of Mg^{2+} cations was also investigated through NR, and both hydrogenous and fully deuterated protein (h-$CALM_{wt}$ and d-$CALM_{wt}$, respectively) were tested. However, although it is still possible to obtain the same total thickness of $CALM_{wt}$, as well as to observe its insertion in the headgroups-layer (4±1% and 3±1% *v/v* for h-$CALM_{wt}$ and d-$CALM_{wt}$, respectively), the volume fraction of the protein binding to the bilayer is much lower (4±1% *v/v* for both, **Table S5.2** and **Figure S5.3**) then the one found with lipid monolayers. It is important to underline that the absence of Mg^{2+} cations does not reduce $CALM_{wt}$ binding, as inferred from the QCM-D experiment. Moreover, both model membranes, mono- and bilayers, are characterised by the same lipid area per molecule, thus the same PIP_2 inositol ring tilt angle (as explained in **Chapter 3** of this manuscript). We concluded that the difference in the binding is mostly due to the rigidity of the bilayer model system. Indeed, $CALM_{wt}$ is a curvature sensing/driving protein, whose binding to membranes depends on the bilayer curvature[10]. Anyway, the bilayer physico-chemical properties, as well as natural fluctuation are largely affected by the proximity of the solid support and by the strong interaction between the latter and the lipids[68,69].

Importantly, the software SLDMOL[70,71] was employed to orient the crystallographic structure of CALM on the lipid monolayer. This software is a freely distributed open source program written in python that can be run independently using command lines or a GUI, and is available on the online SASSIE package platform (https://sassie-web.chem.utk.edu/sassie2), alongside with other useful tools for extended molecular modelling[70,72]. The SLDMOL program is intended as a tool to facilitate refinement of reflectivity results with atomistic protein models. Indeed, it requires the experimental SLD profile obtained from reflectivity measurements, containing the protein contribution, which is then compared with the calculated SLD profiles of several differently oriented crystallographic structures of the protein of interest. Thus, a file (with .dcd extension, see **Figure S5.6**) was produced by VMD software[73] by combining multiple structures for $CALM_{wt}$ oriented along the x- and y-axis, at 10° increments (the angles are indicated as α and β, respectively). Hence, rigid body rotations of the crystallographic structure were performed around the centre of mass of the protein. Orientations along the angle related to the z-axis are irrelevant because the neutron reflection is invariant against rotational symmetry around this axis. As a result, SLDMOL provides a detailed molecular interpretation of reflectivity data, with the aim of finding the protein conformation and orientation that best fits the experimental data. Importantly, since the position of AH0 upon binding remains unknown, the crystal structure of $CALM_{wt}$ used as input in SLDMOL (taken from PDB ID: 3ZYK[7]) lacked the helix, containing amino acids from 19 to 258. Finally, SLDMOL calculated the SLD profile of each orientation and compared them with respect to the experimental one, providing a parameters (χ^2) that indicates the similarity between the profiles. This allowed us to build a colormap (**Figure 5.4 B**) in order to individuate the orientation that can best fit the experimental data (blue area in the colormap). The latter is represented in **Figure 5.4 C**, alongside with the comparison between its SLD profile and the experimental one (**Figure 5.4 D**). Looking at the colormap, two different orientation were considered as best orientations compared to the experimental data (α=330°, β=10° and α=150°, β=170°, see **Figure S5.5 A**), and they are indistinguishable for NR, since the latter is only sensitive to the structure along the z-axis. Moreover, SLDMOL allows the determination of parameters as protein depth penetration and surface coverage. $CALM_{wt}$ was found inserted in the headgroups-layer as expected, with a total surface coverage of 12% *v/v*, which is similar to the coverage obtained by Miller et al with PIP_2 containing liposomes (16%[10]).

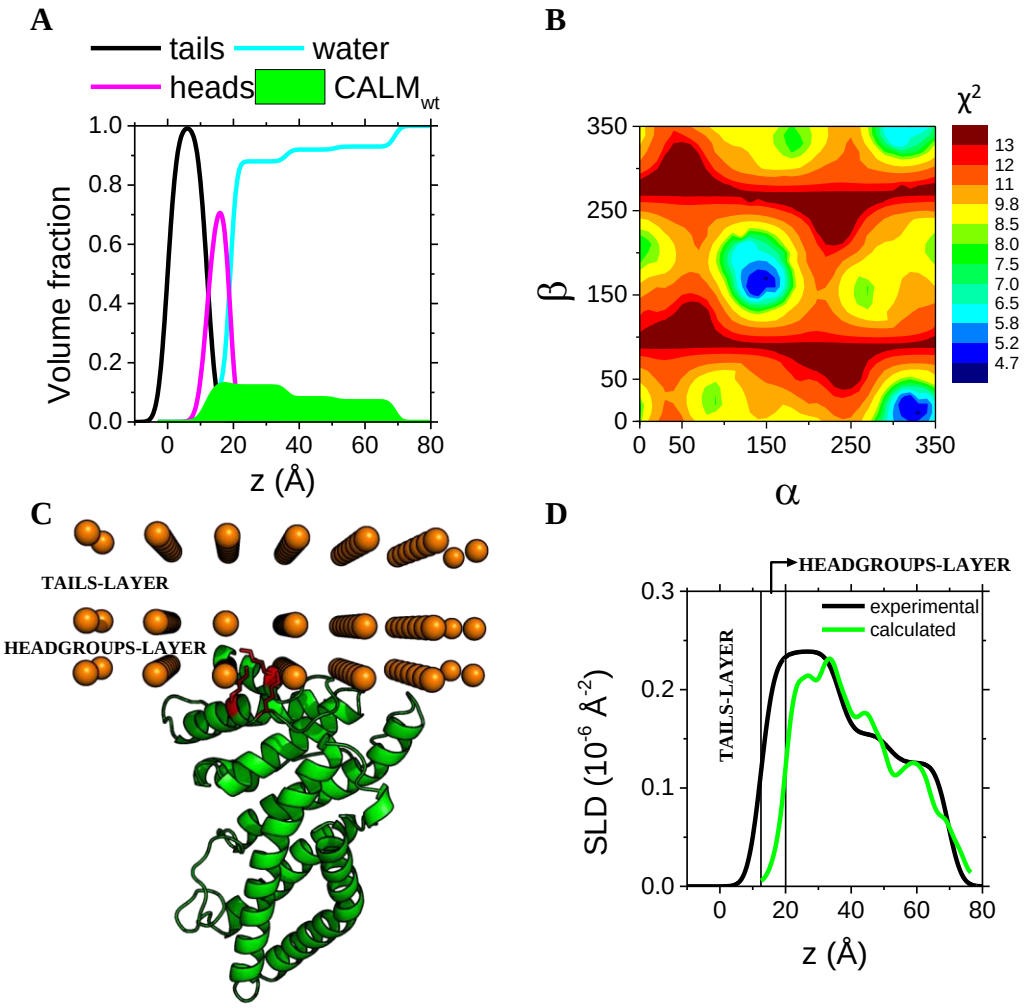

Figure 5.4 Volume fraction profile obtained from the fitting of the NR data and showing the contribution of tails (black line), headgroups (magenta line), water (cyan line) and $CALM_{wt}$ (green area). **B** Colormap showing the orientation of CALM that can best fit the data (blue area, i.e., lowest χ^2). **C** Molecular cartoon representation of the best orientation (α=330°, β=10°). The PIP_2 binding site, which is depicted in red, points towards the membrane. The orange spheres indicate the interfaces between the slabs, *i.e.*, air/tails-layer, tails-layer/headgroups-layer, headgroups-layer/bulk. **D** comparison of experimental SLD profile (black line) and calculated one for the best orientation (green line).

3.4. Influence of PIP_2 tilt angle on $CALM_{wt}$ binding to lipid monolayers

After the observation that $CALM_{wt}$ partitioning at the interface is increased when Π_0=15 $mN \cdot m^{-1}$, NR was employed to determine the protein volume fraction present at the interface after binding, at the two different pressures. The obtained reflectivity curves before and after protein injection at Π_0=15 $mN \cdot m^{-1}$ showed a major difference, compared to the ones at Π_0=25 $mN \cdot m^{-1}$ whose differences were almost negligible (**Figure 5.5 A** and **C**). As explained in the previous paragraph, the results show that, when injected underneath a monolayer of Π_0=15 $mN \cdot m^{-1}$,

$CALM_{wt}$ is able to insert in the membrane, precisely in the headgroups-layer, with a 13±1% volume fraction, and its total volume fraction upon binding is 12% (**Table 5.1** and **Figure 5.5**). However, when Π_0=25 $mN{\cdot}m^{-1}$, no $CALM_{wt}$ was observed inserted in the membrane, and only 2±1% of the protein is present underneath the monolayer (**Figure 5.5, Table 5.1** and **Table S5.2**).

Chapter 3 of this PhD thesis reported that in PIP_2-containing membranes the monolayer surface pressure influences the tilt angle of the inositol ring with respect the monolayer normal. Thus, our outputs allowed us to correlate the inositol ring orientation with the binding of $CALM_{wt}$, with monolayer model membranes. Following the approach explained in **Chapter 3**, the two initial surface pressures Π_0=15 $mN{\cdot}m^{-1}$ and 25 $mN{\cdot}m^{-1}$ would correspond to PIP_2 inositol ring tilt angle of 60° and 30°, respectively. Indeed from these values of Π, the APM could be determined, which can be correlated with the APM (and the Π) of DPPC:PIP2 (7:3) monolayer exploited in **Chapter 3**. Hence, the respective tilt angles were determined, using the model proposed in **Chapter 3** (empirical **Equation 3.1**). Thus, the different orientation of the phosphorylated ring, direct partner of $CALM_{wt}$ binding, together with the slight increase in lipid packing degree (*i.e.*, decrease in APM) from 15 $mN{\cdot}m^{-1}$ to 25 $mN{\cdot}m^{-1}$ (C_s^{-1}=40 and 60 $mN{\cdot}m^{-1}$, respectively), greatly influence $CALM_{wt}$ binding to model membranes. To conclude, we hypothesised that when the inositol ring moves closer to the membrane, *i.e.*, positions itself towards a parallel orientation with respect to the monolayer, the binding of $CALM_{wt}$ is more favourable. However, it has to be taken into account that the increased binding at Π_0=15 $mN{\cdot}m^{-1}$ could be also influenced by the increased APM of the lipids at this surface pressure, compared to the APM at Π_0=25 $mN{\cdot}m^{-1}$ (see **Table 5.1**).

Table 5.1 Thickness and protein volume fraction, for $CALM_{wt}$ interacting with monolayers at Π_0=15 and 25 $mN{\cdot}m^{-1}$. The area per molecule (APM) of lipids is also reported. *obtained volume fraction from SLDMOL.

	Π_0=15$mN{\cdot}m^{-1}$			Π_0=25$mN{\cdot}m^{-1}$		
	t (Å)	$CALM_{wt}$ % (*v/v*)	APM (Å^2)	t (Å)	$CALM_{wt}$ % (*v/v*)	APM (Å^2)
Tails-layer	12±1	0	59±5	15±1	0	47±3
Headgroups-layer	7±1	(13±1 in heads)	56±9	9±1	0	46±6
CALM-layers	50±3	12*		57±1	2±1	

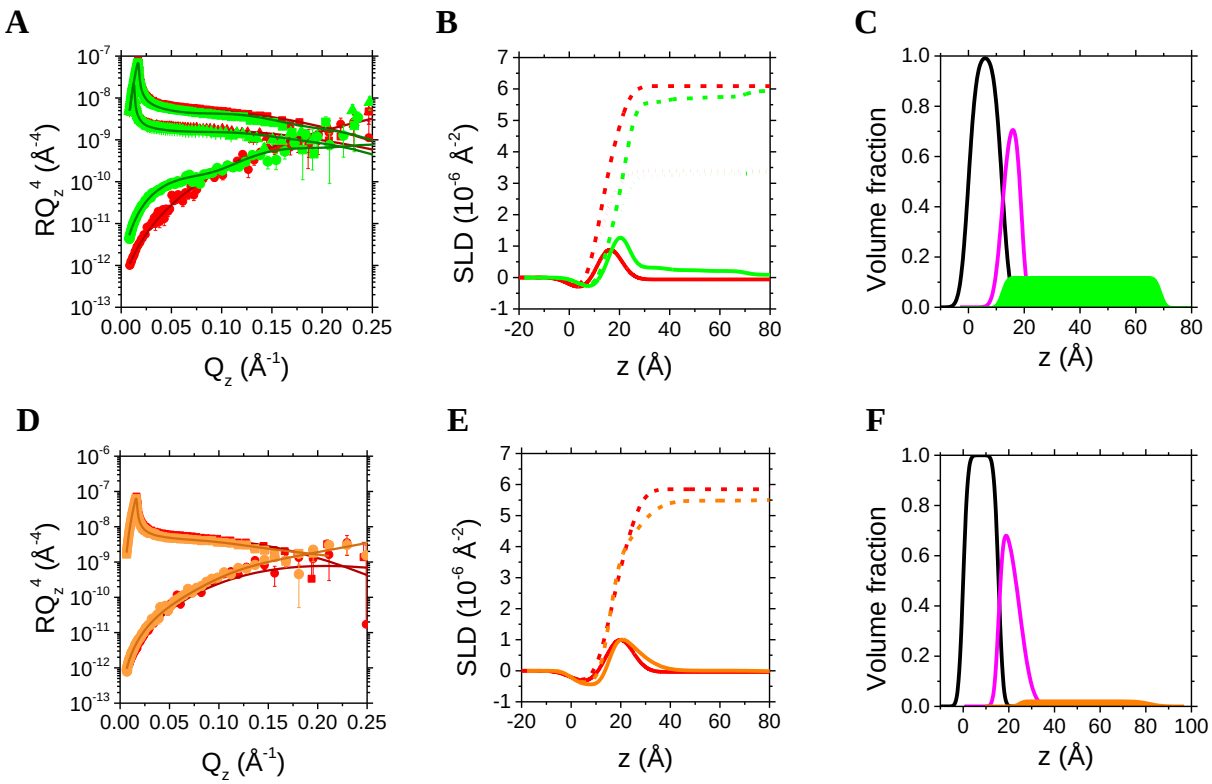

Figure 5.5 NR profiles of DPPC:DPPE:PIP_2 monolayers at **A** Π_0=15 mN·m^{-1} and **D** Π_0=25 mN·m^{-1} are displayed in red. The reflectivity profiles recorded upon $CALM_{wt}$ binding are displayed in green and orange. Experimental points recorded in ACMW, 60% D_2O and 100% D_2O are depicted as circles, triangles and squares, respectively, and simulated curves as lines. Figures are displayed on an RQ_z^4 scale to show the quality of the fits at high Q_z values. SLD profiles corresponding to fits are plotted in **B** and **D**. Continuous, short dotted, short dashed lines indicate the SLD profiles in ACMW, 60% D_2O and 100% D_2O isotopic contrasts, respectively. Red lines in **B** and **D** refer to purely monolayer profiles at Π_0=15 mN·m^{-1} and Π_0=25 mN·m^{-1}, respectively, green and orange lines refer to monolayer+$CALM_{wt}$ SLD profiles. Volume fraction profiles derived from the fit highlight the distribution of tails (black), heads (magenta), and $CALM_{wt}$ underneath **C** a Π_0=15 mN·m^{-1} monolayer (green) and **F** a Π_0=25 mN·m^{-1} monolayer (orange). Panel **C** takes into account the volume fraction obtained with SLDMOL.

3.5. Insertion of the amphipathic helix 0 (AH0) in the lipid membrane

The interaction of amphipathic helixes (AH) with biomembranes has recently been considered an important topic to deeply understand several cellular pathways that require protein-lipids interaction, as well as curvature of membranes, induced by the AH. Such as with other similar AH[74–76], AH0 of CALM have been hypothesized to insert in the membrane[10]. In fact, biochemical and microscopy experimental outcomes showed its interaction with lipids, as well as its propensity to sense and induce membrane curvature, thus predicting its insertion[10]. However, the insertion has yet to be directly proved, alongside with the helix position upon binding, which remains unknown. Thus, we aimed to investigate whether the AH0 is inserted in the membrane and its degree of insertion, *i.e.*, if it interacts only with the polar lipid headgroups or also with the

acyl chains. To this purpose, after the characterization of $CALM_{wt}$ binding to lipid monolayers, a mutant that lacks the AH0 ($CALM_{\Delta AH0}$) was employed and its interaction with PIP_2-containng model membranes was investigating.

Firstly, the binding to lipid monolayers (Π_0=15 $mN \cdot m^{-1}$) was followed measuring the increase in surface pressure upon protein injection. $CALM_{wt}$ and $CALM_{\Delta AH0}$ produced the same increase in surface pressure when injected underneath the monolayer (**Figure 5.6 A**), thus suggesting that the binding between lipids and CALM is not directly influenced by the AH0, but mainly relies on the electrostatic interaction between PIP_2 and Lysines 28, 38 and 40[16]. Since the AH0 represent only the 4% of the whole protein volume, the same multilayer slab model was used to fit $CALM_{wt}$ and $CALM_{\Delta AH0}$ reflectivity data. Thus obtaining similar total thicknesses for $CALM_{wt}$ and $CALM_{\Delta AH0}$ (57±4 Å and 63±4 Å, respectively), as well as similar volume fraction percentage underneath the monolayer (12% and 15% *v/v* obtained with SLDMOL, respectively). Moreover, SLDMOL was exploited, and the outcomes pointed out that the orientations of $CALM_{wt}$ and $CALM_{\Delta AH0}$ with respect to the monolayer are the same (see colormap in **Figure 5.6 B**, SLD profile in **Figure 5.6 C** and comparison between $CALM_{wt}$ and $CALM_{\Delta AH0}$ SLD profiles in **Figure S5.5 B**). However, the volume fraction percentage of $CALM_{\Delta AH0}$ inserted in the headgroups-layer was found to be only 5±1% *v/v* (**Figure 5.6 D**), with respect to the 13±1% *v/v* of $CALM_{wt}$, coherent with the presence of less amino acid residues in the membrane (**Table 5.2**).

Thus, comparing the structures obtained upon binding with both constructs and using the same experimental as well as data analysis procedures, we conclude that the AH0 of CALM is completely inserted in the headgroups-layer. Finally, it is interesting to note the increase in roughness of the protein layers, experienced with $CALM_{\Delta AH0}$ (8 Å against the 3 Å in the case of $CALM_{wt}$, **Table 5.2**), which may suggest a weaker interaction due to the absence of the anchoring moiety.

Table 5.2 Thickness and volume fraction of water (f_w) and protein (fitting parameters), for $CALM_{wt}$ and $CALM_{\Delta AH0}$ interacting with monolayers at Π_0=15mN·m^{-1}. The roughness (r) of the interfaces and the area per molecule (APM) of lipids is also reported. The total protein coverage obtained with SLDMOL is 12% and 15% (*v/v*) for $CALM_{wt}$ and $CALM_{\Delta AH0}$, respectively.

	t (Å)	f_w (%)	$CALM_{wt}$ % (*v/v*)	r (Å)	APM (Å^2)	t (Å)	f_w (%)	$CALM_{\Delta AH0}$ % (*v/v*)	r (Å)	APM (Å^2)
Tails-layer	12±1		0	5±1	59±5	12±1		0	3±1	59±5
Headgroups-layer	7±1	11±1	13±1	5±1	56±9	8±1	28±1	5±1	3±1	58±9
CALM-layers	17±1	88±1	12±1	3±1		20±1	84±1	16±1	8±1	
	15±1	92±1	8±1	3±1		15±1	90±1	10±1	8±1	
	18±1	93±1	7±1	3±1		20±1	92±1	8±1	8±1	

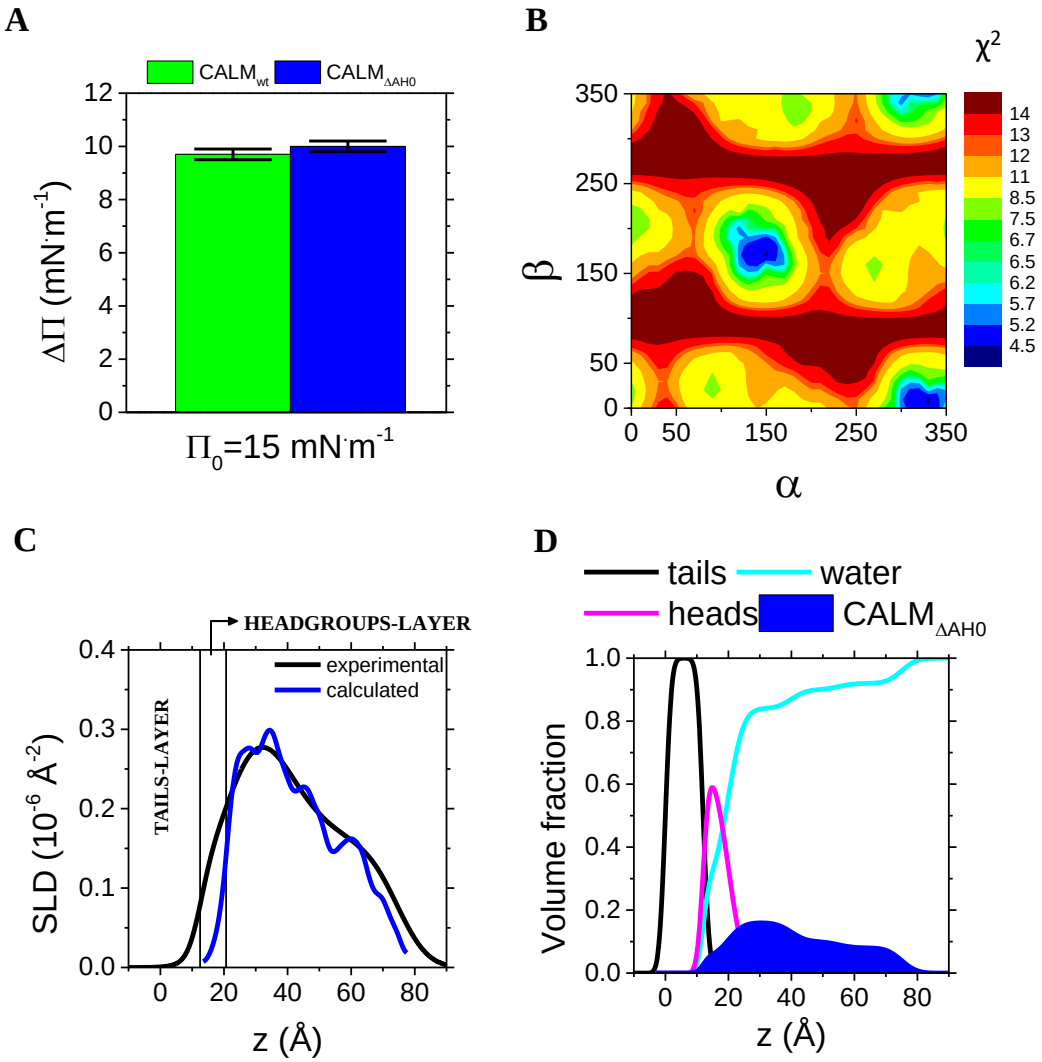

Figure 5.6 A Increase in surface pressure (ΔΠ) obtained after $CALM_{wt}$ (green column) and $CALM_{\Delta AH0}$ (blue column) injection in the bulk underneath the lipid monolayer (Π_0=15mN·m^{-1}). **B** colormap showing the orientation of CALM

that can best fit the data (blue area, *i.e.*, lowest χ^2). **C** comparison of experimental SLD profile (black line) and calculated one for the best orientation (blue line), *i.e.*, α=330°, β=10°. **D** Volume fraction profile obtained from the fitting of the NR data and showing the contribution of tails (black line), headgroups (magenta line), water (cyan line) and $CALM_{\Delta AH0}$ (blue).

3.6. CALM binds to cluster of PIP_2

The unravelling of the orientation of the protein and the position of the AH0 through NR experiments with lipid monolayers in Mg^{2+}-containing buffer solution allowed us to define the PIP_2:CALM ratio. Indeed, from the best orientation obtained from SLDMOL, the volume of the residues inserted in the headgroups-layer was calculated (963 $Å^3$), and summed to the volume of the AH0 (1822 $Å^3$) in the case of $CALM_{wt}$. This volume was then compared to the one implemented in the multilayer slab model (57.5±7.5 $Å^3$), defined as volume of the protein in the headgroups moiety. Thus, from the ratio (963+1822)/57.5=48, we conclude that there is one molecule of $CALM_{wt}$ each ~48 lipid molecules, which means a PIP_2:$CALM_{wt}$ ratio of ~5±1 (since PIP_2 represent 10% in moles of the lipid molecules). Regarding $CALM_{\Delta AH0}$, the same orientation is obtained, but only 25±6 $Å^3$ are inserted in the headgroups-layer, and the AH0 is missing. Hence (963)/25=38.5, and the PIP_2:$CALM_{\Delta AH0}$ ratio is ~4±1. On the other hand, QCM-D experiments showed a ratio of ~2±1 and ~6±2, in the absence and presence of Mg^{2+}, respectively. However, these calculations were performed assuming a homogenous distribution of PIP_2 in the two leaflet, a value of protein density layer of $1.0 \cdot 10^3$ $kg \cdot m^{-3}$, and hypothesizing that the values related to bilayer density, viscosity and shear modulus were fixed. The value calculated in presence of Mg^{2+} are similar to those obtained with NR with lipid monolayer, showing a reduction in binding with lipid bilayer rather than with lipid monolayer, which could be explained taking into account their rigidity and proximity to the substrate. However, although the absence of Mg^{2+} ions seem to increase CALM binding to supported lipid bilayer, allowing us to record NR profiles with CALM bound to them, it is important to underline that Mg^{2+} ions are required during the CME for clathrin binding, thus their absence does not provide a an environment that can well mimic the biological picture.

Finally, as already explained before, we want to underline the great sensitivity of neutron techniques when it comes to describe protein-lipid binding, *e.g.*, determine the lipid:protein ratio.

4. Conclusion

In this work, we presented a detailed investigation on the binding of the endocytic adaptor protein CALM to model membranes rich in PIP_2. Two main outstanding results are reported: the orientation of the protein with respect to the membrane upon binding and the position of CALM amphipathic helix 0.

A combination of NR experiments, as well as wet lab techniques (such as Langmuir trough and QCM-D), allowed to identify the best condition to study CALM binding with planar model membranes, containing 10% mol of PIP_2. In particular NR shed light on the coverage of the protein on lipid membrane, as well as on its orientation upon binding. Nonetheless, the orientation obtained makes biological sense because the PIP_2 binding site (Lysines 28, 38 and 40) points towards the membrane, and is actually partially inserted in it, thus allowing the interaction with the phosphate groups of the inositol ring. Moreover, experiments with both mono- and bilayer provided the same results, in terms of protein insertion in the headgroups-layer and total thickness of the protein, validating the goodness of the model used to fit the experimental data.

Scattering techniques in solution were employed to investigate $CALM_{wt}$ binding to vesicle lipid models. Anyway, the complex picture emerging after protein-lipids interaction was confirmed by the absence of a true Gaussian-like profile in the intensity distribution for the sample of liposome+$CALM_{wt}$, suggesting a polydisperse system. The DLS results are in agreement with the SANS outcomes obtained. Although SANS could provide a structural description of the purely lipid sample, it did not supply with more detailed structural information about the effect of $CALM_{wt}$ on the bilayer, a part from suggesting an increase in the average size of the scattering particles. Therefore, we concluded that the protein definitively affect the overall size of the vesicles, also modifying the structural organization of the lipid system by increase the sample polydispersity, probably as a result of a $CALM_{wt}$ induced aggregation of the liposomes.

Similarly to $CALM_{wt}$, a mutant lacking the AH0 ($CALM_{\Delta AH0}$), was employed in the experiments, to determine by comparison the position of the AH0. In fact, although the crystal structure of $CALM_{wt}$, containing the AH0, is known[7], its position upon binding is thought to change. It was previously suggested, from biochemical experiments, that the AH0 is able to insert in the membrane[10]. However, this hypothesis was only indirectly inferred, and not yet proven experimentally. Our NR results with lipid monolayer clearly show that the AH0 is inserted in the

headgroups-layer, thus positioning itself closer to the headgroup-tails interface rather than laying outside the membrane or inserting in the tails-layer.

Moreover, we found out that the orientation of PIP_2 inositol ring affect the binding of $CALM_{wt}$, whose interaction with the phosphate groups is stronger when the ring tends to position itself parallel to the membrane. Finally, from NR with monolayer we determined that each $CALM_{wt}$ molecule is able to bind to a cluster or 4-5 PIP_2 lipids, whose formation is induced by the presence of divalent cations (Mg^{2+}).

SUPPORTING INFORMATION

Tables

Table S5.1 Fixed parameters for mono- and bilayers used for the NR data analysis[77,78]. The exchange of protons in contrast with different D_2O content was taken into account. In the case of lipid monolayer, the volume contraction for palmitoyl tails was taken into account[54]. *used for SLD value for SANS data analysis.

Fixed Parameters	DPPC:DPPE:PIP_2 (7:2:1) monolayer	DOPC:DOPE:PIP_2 (7:2:1) bilayer
V_h (Å^3)	320.9	320.9
SLD_h (10^{-6} Å^{-2})	2.17	2.17
V_t (Å^3)	732.3	987
SLD_t (10^{-6} Å^{-2})	-0.42	-0.2*

Table S5.2 Fitting parameters of lipid monolayers and lipid bilayers. The χ^2 of all fits reported here are below 10.

Monolayer	Π_0=15mN·m^{-1}				Π_0=25mN·m^{-1}			
	t (Å)	f_w (%)	r (Å)	APM (Å^2)	t (Å)	f_w (%)	r (Å)	APM (Å^2)
Tails-layer	12±1		4±1	63±5	15±1		5±1	49±3
Headgroups-layer	8±1	35±1	4±1	59±8	9±1	24±1	5±1	47±5

Monolayer	Π_0=25mN·m^{-1} + $CALM_{wt}$				
	t (Å)	f_w (%)	$CALM_{wt}$ % (*v/v*)	r (Å)	APM (Å^2)
Tails-layer	15±1		0	3±1	49±3
Headgroups-layer	9±1	24±1	0	3±1	47±5
CALM-layer	57±1	98±1	2±1	8±1	

Bilayer	t (Å)	f_w (%)	r (Å)	APM (Å^2)	t (Å)	f_w (%)	$CALM_{wt}$ % (*v/v*)	r (Å)	APM (Å^2)
Water-layer	6±1	100	4±1		4±1	100	0	4±1	
Headgroups-layer	8±1	39±1	4±1	64±9	9±1	48±1	0	4±1	71±9
Tails-layer	16±1	5±1	4±1	63±5	15±1	6±1	0	4±1	70±5
Tails-layer	16±1	11±1	4±1	68±5	16±1	16±1	0	4±1	74±6
Headgroups-layer	7±1	50±1	4±1	71±12	8±1	48±1	3±1	4±1	78±11
d- CALM-layer					56±1	96±1	4±1	10±1	

Bilayer	t (Å)	f_w (%)	r (Å)	APM (Å^2)	t (Å)	f_w (%)	$CALM_{wt}$ % (*v/v*)	r (Å)	APM (Å^2)
Water-layer	4±1	100	3±1		5±1	100	0	3±1	
Headgroups-layer	8±1	44±1	3±1	70±10	8±1	43±1	0	3±1	70±10
Tails-layer	30±1	54±1	3±1	69±3	14±1	3±1	0	3±1	71±6
Tails-layer					14±1	6±1	0	3±1	73±6
Headgroups-layer	8±1	44±1	3±1	70±10	8±1	39±1	3±1	5±1	75±11
h-CALM-layer					56±1	96±1	7±1	5±1	

Quartz Crystal Microbalance with Dissipation energy monitoring (QCM-D): the Voigt-Voinova viscoelastic model

The mechanical properties of viscoelastic materials are related to energy storage and dissipation processes. Thus, the introduction of parameters such as shear viscosity and shear elasticity modulus helps in the description of viscoelastic material properties, which could be described with the Maxwell model or the Voigt model[20]. The former is used in the case of liquid material with elastic deformations, while the latter represents a solid-like material that undergoes reversible viscoelastic strain, *i.e.*, viscoelastic materials that conserve their shape and do not flow[79,80], such as supported lipid bilayers. In this case, the viscoelastic element is described by a complex shear modulus: the real part (storage modulus) is independent of frequency, while the imaginary one (loss modulus) increases linearly with frequency[80].

The quartz crystal used for the experiment has piezoelectric properties that make it oscillate at a characteristic resonant frequency in response to an oscillating electric field. The resonant frequency changes (Δf) if there is mass absorbed on the crystal. This changes would be proportional to the deposited mass[81]. Besides, the QCM-D allows to measure the energy dissipation, which is inversely proportional to the resonant frequency and the decay time constant[20,82]. However, viscoelastic films at the solid/liquid interface, as lipid bilayer, can dissipate a significant amount of energy during quartz crystal oscillation, hence producing a shift in the dissipation factor $\Delta D=E_{dissipated}/E_{stored}$, with $E_{dissipated}$ and E_{stored} represent the dissipated and stored energies, respectively. Thus, the measure of the changes in both f and D obtained when lipids are deposited onto the crystal surface permits the determination of the mass as well as the viscoelastic properties of the film. Considering a homogenous film with a uniform thickness surrounded by a semi-infinite Newtonian fluid (*i.e.*, a fluid whose stress response against rate of strain is linear, like water), and assuming no-slip conditions (relying on the strong coupling between the solid support and the lipid bilayer[65]), the complex shear modulus (G) of the adsorbed layer can be described by:

$$G = G' + iG'' = \mu_f + i2\pi f\eta_f = \mu_f(1 + i2\pi f\tau_f) \qquad \textbf{S5.1}$$

where G' is the storage modulus, G'' is the loss modulus, μ_f is the elastic shear modulus, η_f is the shear viscosity, $\tau_f = {\eta_f}/{\mu_f}$ is the characteristic relaxation time of the film. Then, Δf and ΔD can be given by:

$$\Delta f = \mathrm{Im}\left(\frac{\beta'}{2\pi\rho_q l_q}\right) \qquad \textbf{S5.2}$$

$$\Delta D = -\mathrm{Re}\left(\frac{\beta'}{\pi f\rho_q l_q}\right) \qquad \textbf{S5.3}$$

with $\beta' = \xi_1\left(\frac{2\pi f\eta_f - i\mu_f}{2\pi f}\right)\left(\frac{1-\alpha'\exp(2\xi_1 h_f)}{1+\alpha'\exp(2\xi_1 h_f)}\right)$, $\alpha' = \left(\frac{\xi_1(2\pi f\eta_f - i\mu_f)}{\xi_2 2\pi f\eta_f} + 1\right)\Big/\left(\frac{\xi_1(2\pi f\eta_f - i\mu_f)}{\xi_2 2\pi f\eta_f} - 1\right)$, $\xi_1 = \sqrt{-\frac{(2\pi f^2)\rho_f}{\mu_f + i2\pi\eta_f}}$, and $\xi_2 = \sqrt{i\frac{2\pi f\rho_f}{\eta_l}}$, where ρ_f and h_f are density and thickness of the adsorbed layer, respectively. Thus, the hydrodynamic thickness (h_f), the shear viscosity (η_f), and the shear modulus (μ_f) can be obtained by fitting the changes of Δf and ΔD at different overtones[20,83]. The subscripts *q*, *l* and *f* refer to the quartz crystal, the bulk liquid and the film, respectively.

Dynamic light scattering (DLS)

DLS experiments relies on the measurement of the normalized intensity or (second-order) autocorrelation function, $g^{(2)}(\mathbf{q},t)$, which can be related to the field (or first-order) autocorrelation function, $g^{(1)}(\mathbf{q},t)$, through the Siegert relationship[84], reported in **Equation S5.4**:

$$g^{(2)}(\mathbf{q},t) - 1 = \beta\left|g^{(1)}(\mathbf{q},t)\right|^2 \qquad \textbf{S5.4}$$

where t is the time, $q = \left(\frac{4\pi n}{\lambda}\right)\sin\left(\frac{\theta}{2}\right)$ is the scattering wave vector, and n the solution refractive index. β is an optical coherence factor, which commonly assumes values close to 1, except for systems characterized by a low intensity of the scattered light as result of small size of the scatters, low concentration or poor refractive index contrast between the scatters and the solvent. For scattering particles diffusing following a Brownian motion, it is possible to define the time evolution of the first-order autocorrelation function as an exponential decay (**Equation S5.5**):

$$g^{(1)}(\mathbf{q},t) = \exp(-t/\tau) = \exp(-\mathcal{D}\mathbf{q}^2 t) \qquad \textbf{S5.5}$$

with the characteristic decay time τ being directly related to the diffusion coefficient, $\mathcal{D}$. Assuming the intrinsic sample polydispersity, it should be considered that both the characteristic decay time and the diffusion coefficient are average magnitudes. For spherical Brownian scatters diffusing in a Newtonian medium, it is possible to correlate the diffusion coefficient with an apparent hydrodynamic radius of the scatters, R_h^{app}, using the Stokes-Einstein relationship (**Equation S5.6**):

$$\mathcal{D} = \frac{k_B T}{6\pi\eta R_h^{app}} \qquad \textbf{S5.6}$$

with k_B being the Boltzmann constant, T the absolute temperature and η the shear viscosity of the solvent, *i.e.*, water.

Small-angle neutron scattering (SANS) data analysis

Considering that the lipid headgroups have a hydration of at least 39% (from bilayer analysis), thus a little contrast with respect to the bulk SLD, we took into account only the SLD of the tails to create an appropriate model. Moreover, to calculate the solvent SLD, we took into account the percentage of glycerol, thus obtaining $5.6 \cdot 10^{-6}$ Å^{-2} and $2.1 \cdot 10^{-6}$ Å^{-2} for the 100% D_2O + 11.5% *v/v* glycerol and 42% D_2O + 7% *v/v* glycerol, respectively. The model employed in SasView Version 5.0.4[35] is composed by two populations: bilamellar vesicles and nanodisks. The former,

which comes from the implemented model "multilayer_vescicle"[36], is characterised by the following form factor:

$$P(Q) = \text{scale}\frac{\varphi}{V(R_N)}F^2(Q) + \text{background} \quad \textbf{S5.7}$$

where

$$F(Q) = (SLD_{shell} - SLD_{solv}) \cdot \sum_{i=1}^{N}\left[3V(r_i)\frac{\sin(Qr_i) - Qr_i\cos(Qr_i)}{(Qr_i)^3} - 3V(R_i)\frac{\sin(QR_i) - QR_i\cos(QR_i)}{(QR_i)^3}\right] \quad \textbf{S5.8}$$

For $r_i=r_c+(i-1)\cdot(t_s+t_w)$ and $R_i=r_i+t_s$. φ is the volume fraction of particles, V(r) is the volume of a sphere of radius r, r_c is the radius of the core, t_s is the thickness of the shell, t_w is the thickness of the solvent layer between the shells, SLD_{shell} is the scattering length density of a shell (here, $-0.2\cdot10^{-6}$ Å^{-2}), and SLD_{solv} is the scattering length density of the solvent (bulk). The nanodisk model comes from the implemented model "cylinders"[30,37,38] and has the following form factor:

$$P(Q,\alpha) = \frac{\text{scale}}{V}F^2(Q,\alpha)\sin\alpha + \text{background} \quad \textbf{S5.9}$$

where

$$F(Q,\alpha) = 2(\Delta SLD)V\frac{\sin(\frac{1}{2}QL\cos\alpha)}{\frac{1}{2}QL\cos\alpha}\frac{J_1(QR\sin\alpha)}{QR\sin\alpha}, \quad \textbf{S5.10}$$

α is the angle between the axis of the cylinder and vector Q, $V=\pi R^2L$ is the volume of the cylinder, L is the length of the cylinder, R is the radius of the cylinder, and ΔSLD (contrast) is the SLD difference between the scattering particles and the solvent. J_1 is the first order Bessel function.

Table S5.3 Fitting parameters of SANS analysis in the two contracts.

		100% D_2O	42% D_2O
Bilamellar vesicles	scale	0.000671	0.000650
	R_c (Å)	186	166
	t_s (Å)	33	33
	t_w (Å)	45	44
Nanodisks	scale	0.000185	0.000215
	L (Å)	180	165
	R (Å)	38	39

Figures

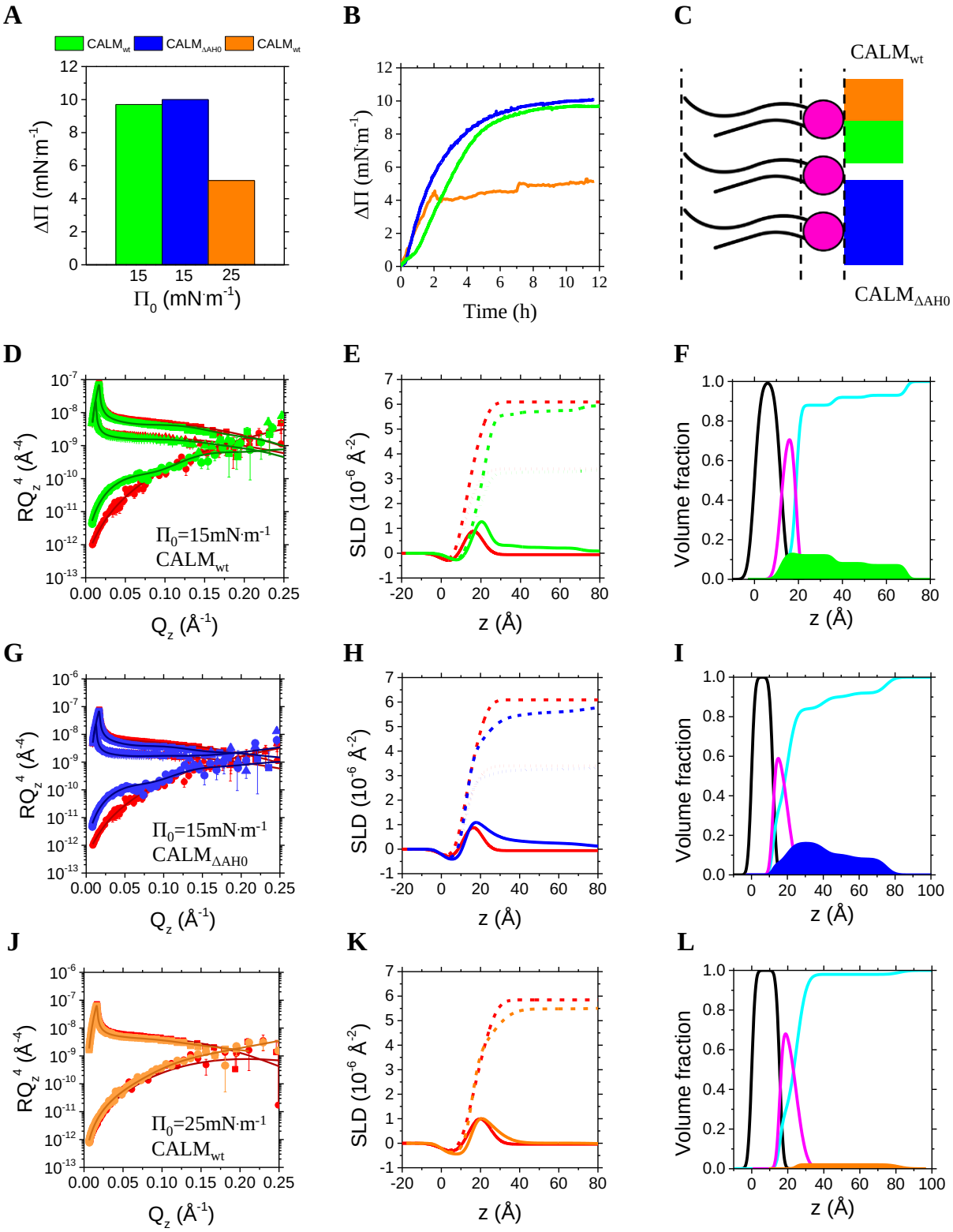

Figure S5.1 Experiments with lipid monolayers.

Panel **A** shows the increase in surface pressure upon CALM injection in the bulk phase, and panel **B** reports the binding kinetics. Data related to $CALM_{wt}$ injected under a Π_0=15 $mN \cdot m^{-1}$ and 25 $mN \cdot m^{-1}$ monolayers are depicted in green and orange respectively. Data related to $CALM_{\Delta AH0}$ are depicted in blue. **C** Sketch indicating a lipid monolayer with protein bound underneath. Tails are depicted in black and headgroups in magenta.

Experimental (symbols) and simulated (lines) NR profiles of lipid monolayers (Π_0=15 $mN \cdot m^{-1}$) in the absence (red) and presence of **D** $CALM_{wt}$ (green) and **G** $CALM_{\Delta AH0}$ (blue). Data at three isotopic contrasts have been measured: D_2O (squares), 60% D_2O (triangles) and ACMW (circles). Experimental (symbols) and simulated (lines) neutron reflectivity profiles of lipid monolayers (Π_0=25 $mN \cdot m^{-1}$) in the absence (red) and presence of **J** $CALM_{wt}$ (orange). Data at two isotopic contrasts have been measured: D_2O (squares) and ACMW (circles). Figures are displayed on an RQ_z^4 scale to show the quality of the fits at high Q_z values. SLD profiles corresponding to fits are plotted in **E**, **H** and **K**. Continuous, short dotted, short dashed lines indicate the SLD profiles in ACMW, 60% D_2O and D_2O isotopic contrast, respectively. Red lines in **E** and **H** refer to purely monolayer profiles (Π_0=15 $mN \cdot m^{-1}$), green and blue lines refer to monolayer+$CALM_{wt}$ and monolayer+$CALM_{\Delta AH0}$ SLD profiles, respectively. Red lines in **K** refer to purely monolayer profiles (Π_0=25 $mN \cdot m^{-1}$), orange lines refer to monolayer+$CALM_{wt}$ SLD profiles. Volume fraction profiles derived from the fit highlight the distribution of tails (black), heads (magenta), water (cyan) and **F** $CALM_{wt}$ underneath a Π_0=15 $mN \cdot m^{-1}$ monolayer (green) and **L** a Π_0=25 $mN \cdot m^{-1}$ monolayer (orange), **I** $CALM_{\Delta AH0}$ underneath a Π_0=15 $mN \cdot m^{-1}$ monolayer (blue).

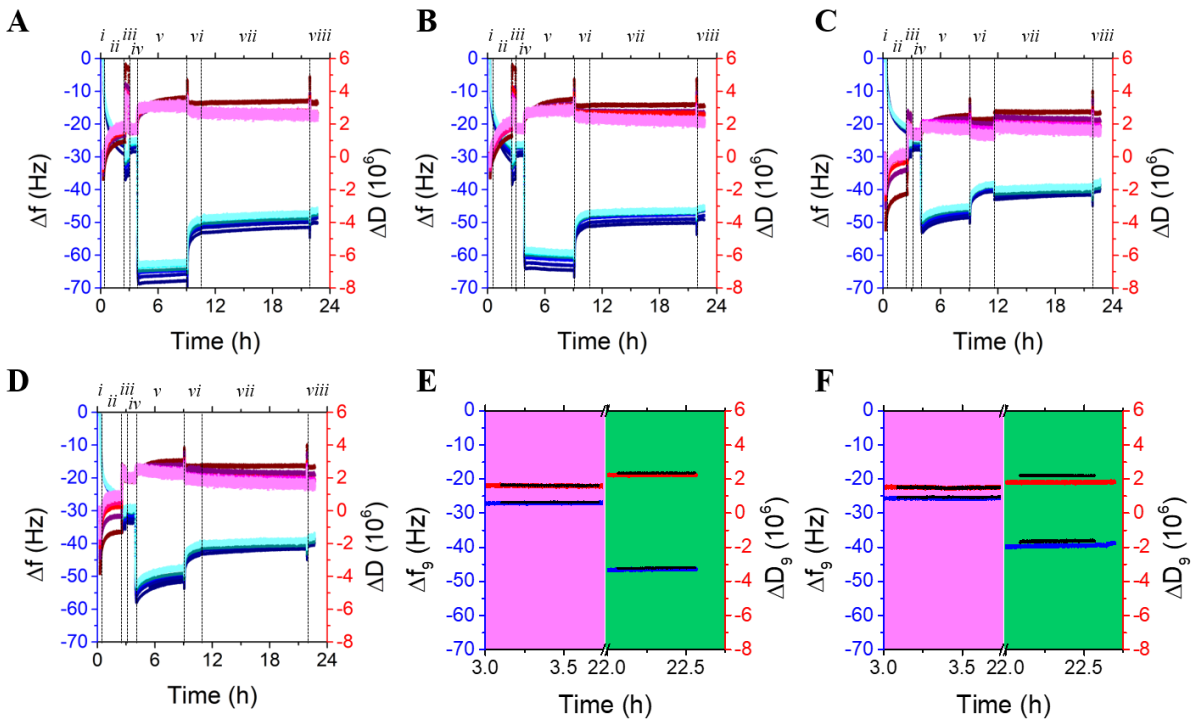

Figure S5.2 QCM-D profiles of bilayers with successive injection of $CALM_{wt}$ in **A, B** HEPES-NaCl (no Mg^{2+}) and **C, D** HKM buffer solutions. Each experiment was repeated in two flow cells. Overtones from 3rd to 13th are shown, for both frequency (navy, royal, blue, dark cyan, cyan and light cyan for overtones from 3rd to 13th, respectively) and dissipation energy (wine, purple, red, pink, magenta and light magenta for overtones from 3rd to 13th, respectively) shifts. Each index indicate a step: *i* - the baseline; *ii* - injection of liposomes and static incubation; *iii* - washing step with NaCl 500 mM; *iv* - washing step with appropriate buffer solution; *v* - protein injection and incubation; *vi* - washing step with appropriate buffer solution; *vii* - protein-bilayer incubation overnight; *viii* - last washing step with appropriate buffer solution. Fit of the data with the viscoelastic model for bilayer (pink region) and bilayer+$CALM_{wt}$ (green region), in **E** HEPES-NaCl and **F** HKM buffer solutions. The fit was performed using overtones from 5rd to

13^{th}, but for simplicity, only overtone 9^{th} is shown. The fitting for the protein layer shown here have been performed using 1.0 $kg \cdot m^{-3}$ as density value. Frequency and dissipation energy shifts are depicted in blue and red respectively, and the related fits are depicted in black.

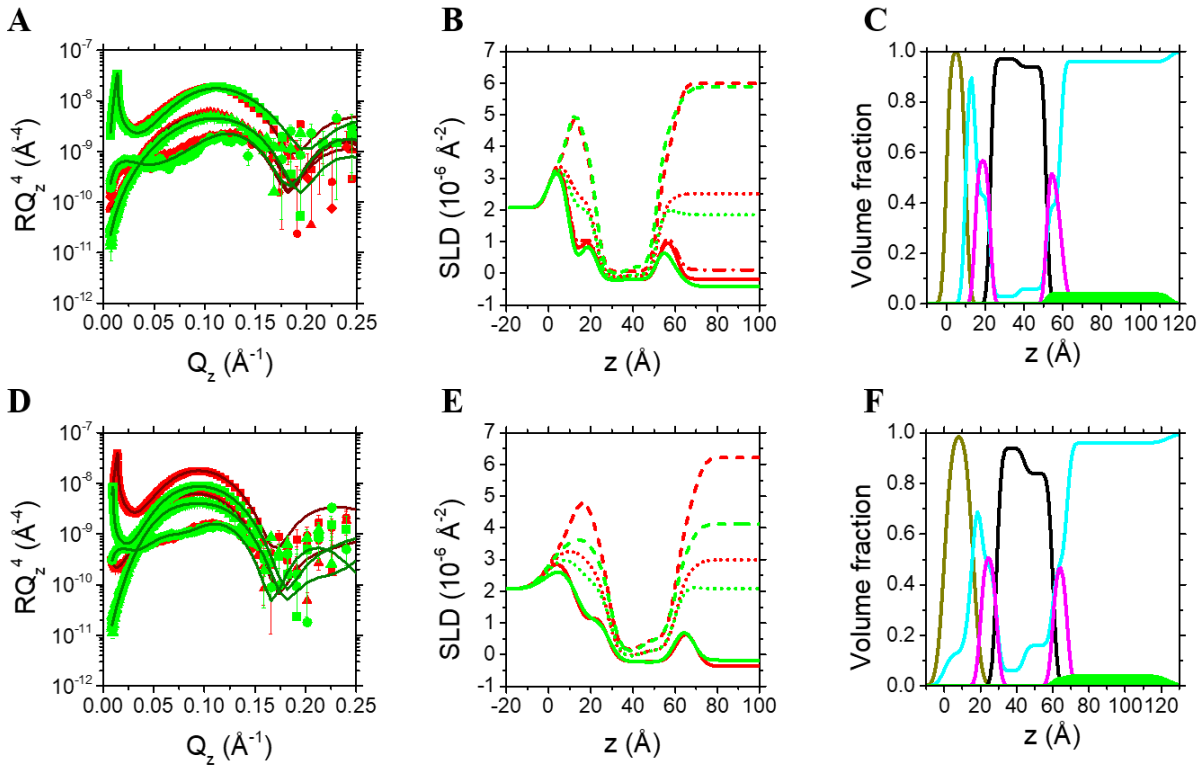

Figure S5.3 NR experiments with supported lipid bilayers. Experimental (symbols) and simulated (lines) neutron reflectivity profiles of solid-supported bilayers in the absence (red) and presence (green) of **A** h-$CALM_{wt}$ and **D** d-$CALM_{wt}$. Data at three isotopic contrasts have been measured for hydrogenous lipid bilayers: D_2O (red squares), H_2O (red circles) and SiMW (red triangles). An additional contrast was measured for the bilayer prior to the injection of h-$CALM_{wt}$, *i.e.*, ACMW, shown as red diamonds. Data at three isotopic contrasts have been measured for bilayers+$CALM_{wt}$: D_2O for h-$CALM_{wt}$ and 62% D_2O for d-$CALM_{wt}$ (green squares), H_2O (green circles) and SiMW (red triangles). Figures are displayed on an RQ_z^4 scale to show the quality of the fits at high Q_z values. Scattering length density profiles corresponding to fits are plotted in **B** and **E**. Red continuous, short dotted, short dashed lines indicate the bilayer SLD profile in H_2O, SiMW and D_2O isotopic contrast, respectively, and the dotted-dashed line indicated the bilayer SLD in ACMW. Green continuous, short dotted, short dashed lines indicate the bilayer+$CALM_{wt}$ SLD profile in H_2O, SiMW and D_2O (60% D_2O for d-$CALM_{wt}$) isotopic contrast, respectively. Volume fraction profiles derived from the fits highlight the distribution of silicon oxide (dark yellow), tails (black), heads (magenta), water (cyan) and **C** h-$CALM_{wt}$ (green), **F** d-$CALM_{wt}$ (green).

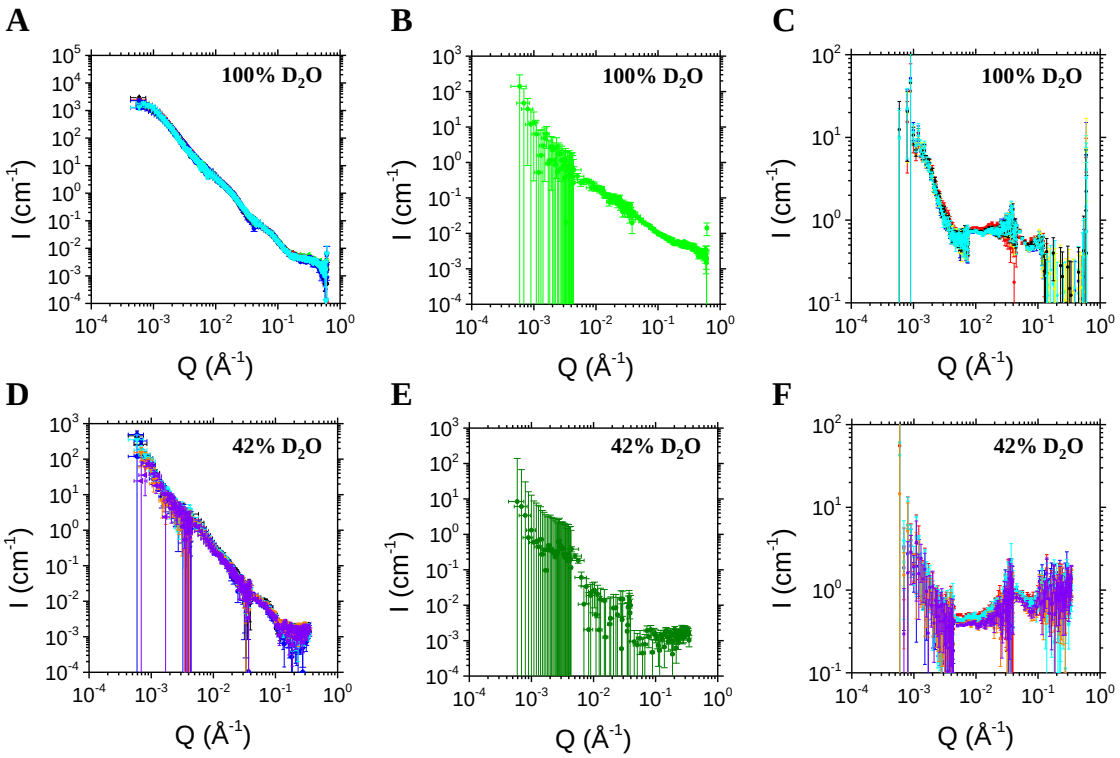

Figure S5.4 SANS profiles of lipids+CALM$_{wt}$ samples in **A** 100% D_2O (with 11.5% glycerol, *v/v*) and **D** 42% D_2O (with 7.7% glycerol, *v/v*). The different curves were recorded with a delay in time (overnight). **B** and **E** show the SANS profiles of CALM$_{wt}$ in the two contrasts. **C** and **F** report the difference profiles: regarding the ones in **C**, the contribution of the protein has been subtracted and the profiles have been normalised with respect to the purely lipid sample (suggesting a loss of ~25% of scattering mass); regarding the profiles in panel **F**, they have been directly normalised by the lipid profile, since the bulk SLD matches the protein ones (suggesting a loss of ~50% of scattering mass). The operation between profiles have been performed with the SAXSutilities2 software[85].

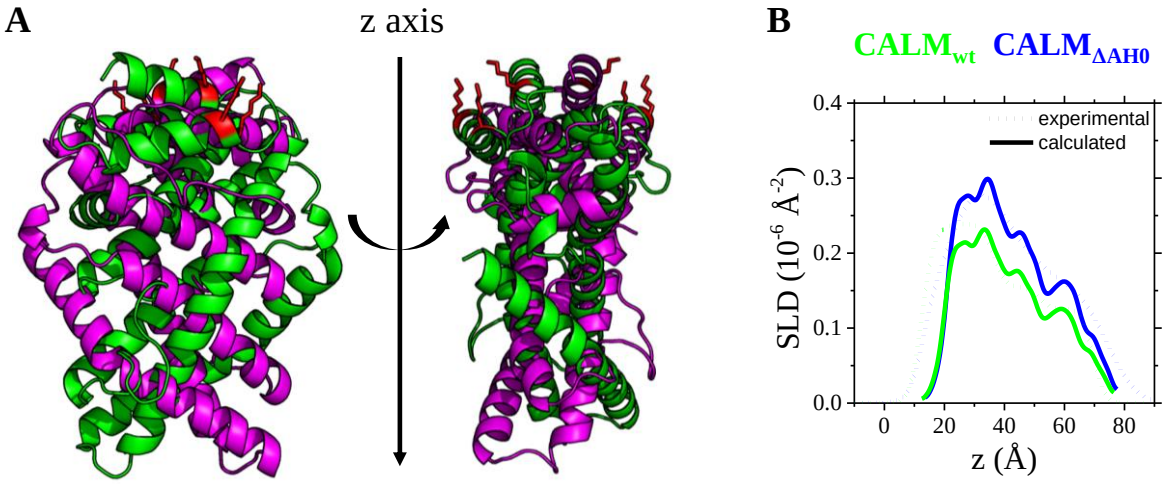

Figure S5.5 A Cartoon representation of the two equivalent orientation of CALM with respect to the z-axis: the orientation α=330°, β=10° is depicted in green, and the one α=150°, β=170° in magenta. The PIP_2 binding site is red. **B** Superimposition of calculated SLD profiles, with only protein contribution, of CALM$_{wt}$ (green) and CALM$_{\Delta AH0}$ (blue); both the experimental profiles (short dotted) and the calculated ones (solid lines), related to the best fits, are shown.

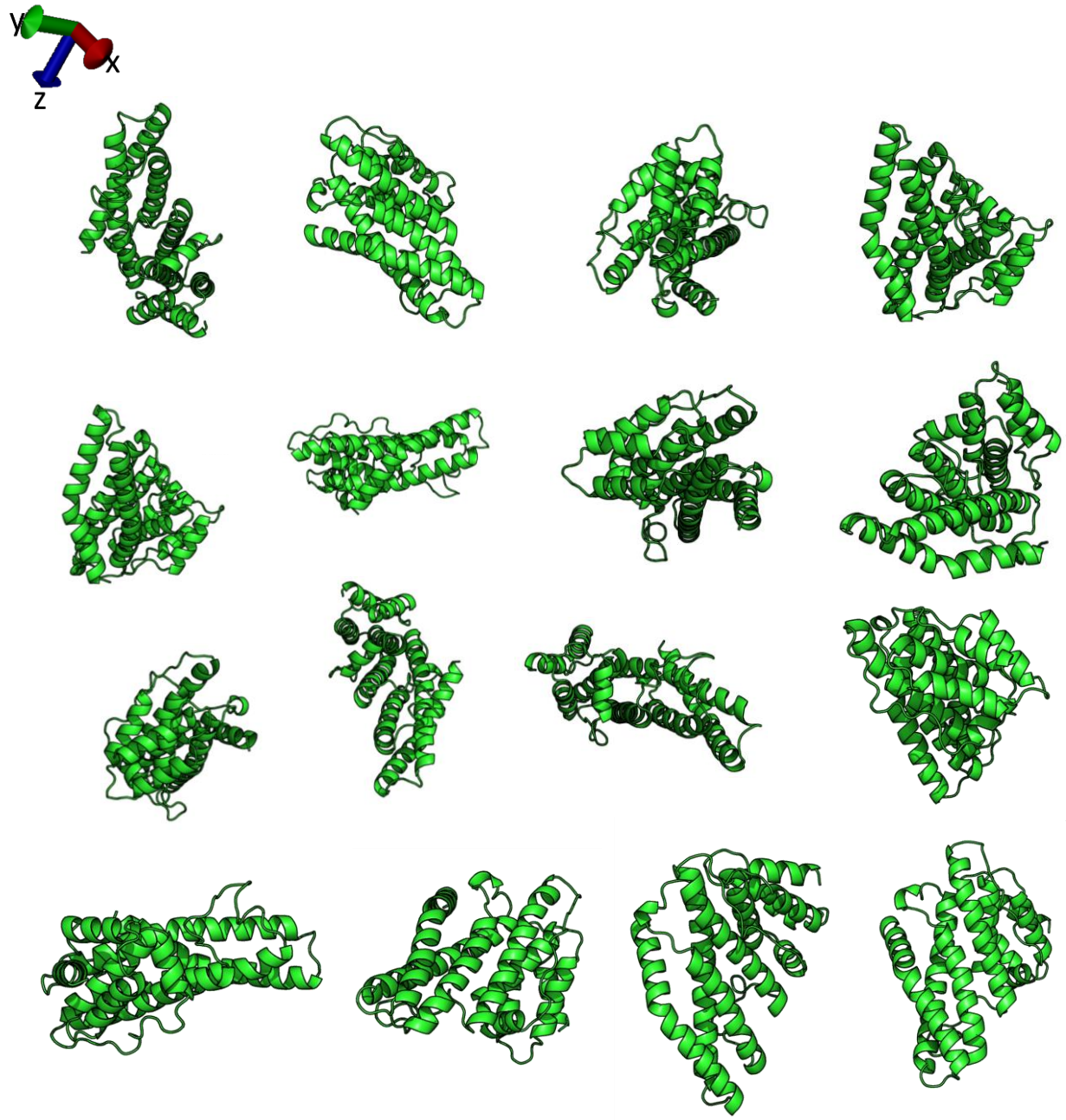

Figure S5.6 Some of the rigid body rotation of CALM (PDB ID: 3ZYK[7]) implemented in the .dcd file.

References

1. Schmid SL, Conner SD. Regulated portals of entry into the cell. *Nature*. 2003;422(March):37-44. www.nature.com/nature.

2. McMahon HT, Boucrot E. Molecular mechanism and physiological functions of clathrin-mediated endocytosis. *Nat Rev Mol Cell Biol 2011 128*. 2011;12(8):517-533. doi:10.1038/nrm3151

3. Owen DJ, Collins BM, Evans PR. ADAPTORS FOR CLATHRIN COATS: Structure and Function. *Annu Rev Cell Dev Biol*. 2004;20(1):153-191. doi:10.1146/annurev.cellbio.20.010403.104543

4. Falkenburger BH, Jensen JB, Dickson EJ, Suh BC, Hille B. Phosphoinositides: Lipid regulators of membrane proteins. *J Physiol*. 2010;588(17):3179-3185. doi:10.1113/jphysiol.2010.192153

5. Traub LM. Sorting it out: AP-2 and alternate clathrin adaptors in endocytic cargo selection. *J Cell Biol*. 2003;163(2):203-208. doi:10.1083/jcb.200309175

6. Kadlecova Z, Spielman SJ, Loerke D, Mohanakrishnan A, Reed DK, Schmid SL. Regulation of clathrin-mediated endocytosis by hierarchical allosteric activation of AP2. *J Cell Biol*. 2017;216(1):167-179. doi:10.1083/jcb.201608071

7. Miller SE, Sahlender DA, Graham SC, et al. The molecular basis for the endocytosis of small R-SNAREs by the clathrin adaptor CALM. *Cell*. 2011;147(5):1118-1131. doi:10.1016/j.cell.2011.10.038

8. David C, McPherson PS, Mundigl O, De Camilli P. A role of amphiphysin in synaptic vesicle endocytosis suggested by its binding to dynamin in nerve terminals. *Proc Natl Acad Sci U S A*. 1996;93(1):331-335. doi:10.1073/pnas.93.1.331

9. Ford MGJ, Mills IG, Peter BJ, et al. Curvature of clathrin-coated pits driven by epsin. *Nature*. 2002;419(6905):361-366. doi:10.1038/nature01020

10. Miller SE, Mathiasen S, Bright NA, et al. CALM Regulates Clathrin-Coated Vesicle Size and Maturation by Directly Sensing and Driving Membrane Curvature. *Dev Cell*.

2015;33(2):163-175. doi:10.1016/j.devcel.2015.03.002

11. Robinson MS, Bonifacino JS. Adaptor-related proteins. *Curr Opin Cell Biol*. 2001;13(4):444-453.

12. Robinson MS. Adaptable adaptors for coated vesicles. *Trends Cell Biol*. 2004;14(4):167-174. doi:10.1016/J.TCB.2004.02.002

13. Blondeau F, Ritter B, Allaire PD, et al. Tandem MS analysis of brain clathrin-coated vesicles reveals their critical involvement in synaptic vesicle recycling. *Proc Natl Acad Sci U S A*. 2004;101(11):3833-3838. doi:10.1073/PNAS.0308186101

14. Borner GHH, Antrobus R, Hirst J, et al. Multivariate proteomic profiling identifies novel accessory proteins of coated vesicles. *J Cell Biol*. 2012;197(1):141-160. doi:10.1083/JCB.201111049/VIDEO-1

15. Koo SJ, Markovic S, Puchkov D, et al. SNARE motif-mediated sorting of synaptobrevin by the endocytic adaptors clathrin assembly lymphoid myeloid leukemia (CALM) and AP180 at synapses. *Proc Natl Acad Sci U S A*. 2011;108(33):13540-13545. doi:10.1073/pnas.1107067108

16. Ford MGJ, Pearse BMF, Higgins MK, et al. Simultaneous binding of PtdIns (4,5) P2 and clathrin by AP180 in the nucleation of clathrin lattices on membranes. *Science*. 2001;291(5506):1051-1055. doi:10.1126/science.291.5506.1051

17. Tebar F, Bohlander SK, Sorkin A. Clathrin assembly lymphoid myeloid leukemia (CALM) protein: Localization in endocytic-coated pits, interactions with clathrin, and the impact of overexpression on clathrin-mediated traffic. *Mol Biol Cell*. 1999;10(8):2687-2702. doi:10.1091/MBC.10.8.2687/ASSET/IMAGES/LARGE/MK0890936010.JPEG

18. Traub LM. Regarding the Amazing Choreography of Clathrin Coats. *PLOS Biol*. 2011;9(3):e1001037. doi:10.1371/JOURNAL.PBIO.1001037

19. Baumgart T, Capraro BR, Zhu C, Das SL. Thermodynamics and Mechanics of Membrane Curvature Generation and Sensing by Proteins and Lipids. *http://dx.doi.org/101146/annurev.physchem012809103450*. 2011;62:483-506. doi:10.1146/ANNUREV.PHYSCHEM.012809.103450

20. Voinova M V, Rodahl M, Jonson M, Kasemo B. Viscoelastic Acoustic Response of Layered Polymer Films at Fluid-Solid Interfaces: Continuum Mechanics Approach. *Phys Scr*. 1999;59(5):391-396. doi:10.1238/physica.regular.059a00391

21. Richter RP, Bérat R, Brisson AR. Formation of solid-supported lipid bilayers: An integrated view. *Langmuir*. 2006;22(8):3497-3505. doi:10.1021/la052687c

22. Nielsen SB, Otzen DE. Quartz Crystal Microbalances as Tools for Probing Protein–Membrane Interactions. *Methods Mol Biol*. 2013;974:1-21. doi:10.1007/978-1-62703-275-9_1

23. Campbell RA, Wacklin HP, Sutton I, Cubitt R, Fragneto G. FIGARO: The new horizontal neutron reflectometer at the ILL. *Eur Phys J Plus*. 2011;126(11):1-22. doi:10.1140/epjp/i2011-11107-8

24. Saerbeck T, Cubitt R, Wildes A, Manzin G, Andersen KH, Gutfreund P. Recent upgrades of the neutron reflectometer D17 at ILL. *urn:issn:1600-5767*. 2018;51(2):249-256. doi:10.1107/S160057671800239X

25. Cubitt R, Fragneto G. D17: the new reflectometer at the ILL. 2002;331:329-331.

26. Gutfreund P, Saerbeck T, Gonzalez MA, et al. Towards generalized data reduction on a chopperbased time-of-flight neutron reflectometer. *J Appl Crystallogr*. 2018. doi:10.1107/S160057671800448X

27. Gerelli Y. Aurore: New software for neutron reflectivity data analysis. *J Appl Crystallogr*. 2016;49:330-339. doi:10.1107/S1600576716000108

28. Nelson A. Co-refinement of multiple-contrast neutron/X-ray reflectivity data using MOTOFIT. *J Appl Crystallogr*. 2006;39(2):273-276. doi:10.1107/S0021889806005073

29. Lindner P, Schweins R. The D11 Small-Angle Scattering Instrument: A New Benchmark for SANS. *https://doi.org/101080/10448631003697985*. 2010;21(2):15-18. doi:10.1080/10448631003697985

30. Pedersen JS. Analysis of small-angle scattering data from colloids and polymer solutions: modeling and least-squares fitting. *Adv Colloid Interface Sci*. 1997;70(1-3):171-210.

doi:10.1016/S0001-8686(97)00312-6

31. Lindner P, Zemb T. *Neutron, X-Rays and Light. Scattering Methods Applied to Soft Condensed Matter - 1st Edition*. (Elsevier: Amsterdam, ed.). Boston; 2002. https://www.elsevier.com/books/neutron-x-rays-and-light-scattering-methods-applied-to-soft-condensed-matter/zemb/978-0-444-51122-5. Accessed May 6, 2022.

32. Guinier A, Walker CB, York N, Wiley J. Small-angle scattering of X-rays. 1955.

33. Breßler I, Kohlbrecher J, Thünemann AF. SASfit: A tool for small-angle scattering data analysis using a library of analytical expressions. *J Appl Crystallogr*. 2015;48(5):1587-1598. doi:10.1107/S1600576715016544/VG5026SUP2.ZIP

34. Kohlbrecher J, Studer A. Transformation cycle between the spherically symmetric correlation function, projected correlation function and differential cross section as implemented in SASfit. *urn:issn:1600-5767*. 2017;50(5):1395-1403. doi:10.1107/S1600576717011979

35. Doucet M, et al. SasView Version 5.0.4. doi:http://doi.org/10.5281/zenodo.4467703

36. Cabane B. Small-Angle Scattering Methods. In: *Surfactant Solutions: New Methods of Investigation*. R. ZANA; 1987.

37. Fournet G. Scattering functions for geometrical forms. *Bull Soc Fr Miner Cristal*. 1951;74:39-113. https://ci.nii.ac.jp/naid/20001479522/. Accessed May 24, 2022.

38. Onsager L. The effects of shape on the interaction of colloidal particles. *Sci Ann New York Acad 1949*. 1949.

39. McLaughlin S, Murray D. Plasma membrane phosphoinositide organization by protein electrostatic. *Nature*. 2005;438. doi:10.1038/nature04398.

40. Graber ZT, Jiang Z, Gericke A, Kooijman EE. Phosphatidylinositol-4,5-bisphosphate ionization and domain formation in the presence of lipids with hydrogen bond donor capabilities. *Chem Phys Lipids*. 2012;165(6):696-704. doi:10.1016/j.chemphyslip.2012.07.003

41. Lupyan D, Mezei M, Logothetis DE, Osman R. A molecular dynamics investigation of

lipid bilayer perturbation by PIP2. *Biophys J*. 2010;98(2):240-247. doi:10.1016/j.bpj.2009.09.063

42. McLaughlin S, Wang J, Gambhir A, Murray D. PIP2 and proteins: Interactions, organization, and information flow. *Annu Rev Biophys Biomol Struct*. 2002;31:151-175. doi:10.1146/annurev.biophys.31.082901.134259

43. Ghosh SK, Castorph S, Konovalov O, Jahn R, Holt M, Salditt T. In vitro study of interaction of synaptic vesicles with lipid membranes. *New J Phys*. 2010;12. doi:10.1088/1367-2630/12/10/105004

44. Levental I, Christian DA, Wang YH, Madara JJ, Discher DE, Janmey PA. Calcium-dependent lateral organization in phosphatidylinositol 4,5-bisphosphate (PIP2)- and cholesterol-containing monolayers. *Biochemistry*. 2009;48(34):8241-8248. doi:10.1021/bi9007879

45. Wang YH, Collins A, Guo L, et al. Divalent cation-induced cluster formation by polyphosphoinositides in model membranes. *J Am Chem Soc*. 2012;134(7):3387-3395. doi:10.1021/ja208640t

46. Bilkova E, Pleskot R, Rissanen S, et al. Calcium Directly Regulates Phosphatidylinositol 4,5-Bisphosphate Headgroup Conformation and Recognition. *J Am Chem Soc*. 2017;139(11):4019-4024. doi:10.1021/jacs.6b11760

47. Ellenbroek WG, Wang YH, Christian DA, Discher DE, Janmey PA, Liu AJ. Divalent cation-dependent formation of electrostatic PIP2 clusters in lipid monolayers. *Biophys J*. 2011;101(9):2178-2184. doi:10.1016/j.bpj.2011.09.039

48. Dietrich U, Krüger P, Gutberlet T, Käs JA. Interaction of the MARCKS peptide with PIP2 in phospholipid monolayers. *Biochim Biophys Acta - Biomembr*. 2009;1788(7):1474-1481. doi:10.1016/j.bbamem.2009.04.001

49. Gamper N, Shapiro MS. Target-specific PIP(2) signalling: how might it work? *J Physiol*. 2007;582(Pt 3):967-975. doi:10.1113/JPHYSIOL.2007.132787

50. Raghava S, Giorda KM, Romano FB, Heuck AP, Hebert DN. The SV40 late protein VP4 is a viroporin that forms pores to disrupt membranes for viral release. *PLoS Pathog*.

2011;7(6). doi:10.1371/journal.ppat.1002116

51. Lodish H, Berk A, Zipursky LS. “Biomembranes: Structural Organization and Basic Functions.” In: *Molecular Cell Biology*. 4th ed. New York: Scientific American Books.; 2000.

52. G. M. Cooper. *“Structure of the Plasma Membrane”. The Cell: A Molecular Approach.* 2nd ed.; 2000.

53. Carrascosa-Tejedor J, Santamaria A, Pereira D, Maestro A. Structure of DPPC Monolayers at the Air/Buffer Interface: A Neutron Reflectometry and Ellipsometry Study. *Coatings 2020, Vol 10, Page 507*. 2020;10(6):507. doi:10.3390/COATINGS10060507

54. Campbell RA, Saaka Y, Shao Y, et al. Structure of surfactant and phospholipid monolayers at the air/water interface modeled from neutron reflectivity data. *J Colloid Interface Sci*. 2018;531:98-108. doi:10.1016/j.jcis.2018.07.022

55. Nagle JF, Scott HL. Lateral compressibility of lipid mono- and bilayers. Theory of membrane permeability. *BBA - Biomembr*. 1978;513(2):236-243. doi:10.1016/0005-2736(78)90176-1

56. Adams EM, Casper CB, Allen HC. Effect of cation enrichment on dipalmitoylphosphatidylcholine (DPPC) monolayers at the air-water interface. *J Colloid Interface Sci*. 2016;478:353-364. doi:10.1016/j.jcis.2016.06.016

57. Clifton LA, Campbell RA, Sebastiani F, et al. Design and use of model membranes to study biomolecular interactions using complementary surface-sensitive techniques. *Adv Colloid Interface Sci*. 2020;277. doi:10.1016/j.cis.2020.102118

58. Lind TK, Cárdenas M. Understanding the formation of supported lipid bilayers via vesicle fusion—A case that exemplifies the need for the complementary method approach (Review). *Biointerphases*. 2016;11(2):020801. doi:10.1116/1.4944830

59. Lind TK, Wacklin H, Schiller J, et al. Formation and Characterization of Supported Lipid Bilayers Composed of Hydrogenated and Deuterated Escherichia coli Lipids. *PLoS One*. 2015;10(12):e0144671. doi:10.1371/JOURNAL.PONE.0144671

60. Åkesson A, Lind T, Ehrlich N, Stamou D, Wacklin H, Cárdenas M. Composition and structure of mixed phospholipid supported bilayers formed by POPC and DPPC. *Soft Matter*. 2012;8(20):5658-5665. doi:10.1039/c2sm00013j

61. Cho NJ, Frank CW, Kasemo B, Höök F. Quartz crystal microbalance with dissipation monitoring of supported lipid bilayers on various substrates. *Nat Protoc*. 2010;5(6):1096-1106. doi:10.1038/nprot.2010.65

62. Luchini A, Nzulumike ANO, Lind TK, et al. Towards biomimics of cell membranes: Structural effect of phosphatidylinositol triphosphate (PIP 3) on a lipid bilayer. *Colloids Surfaces B Biointerfaces*. 2019;173(March 2018):202-209. doi:10.1016/j.colsurfb.2018.09.031

63. Dixon MC. Quartz crystal microbalance with dissipation monitoring: Enabling real-time characterization of biological materials and their interactions. *J Biomol Tech*. 2008;19(3):151-158.

64. Voinova M V., Jonson M, Kasemo B. "Missing mass" effect in biosensor's QCM applications. *Biosens Bioelectron*. 2002;17(10):835-841. doi:10.1016/S0956-5663(02)00050-7

65. Voinova M V., Jonson M, Kasemo B. Dynamics of viscous amphiphilic films supported by elastic solid substrates. *J Phys Condens Matter*. 1997;9(37):7799-7808. doi:10.1088/0953-8984/9/37/011

66. Macháň R, Hof M. Lipid diffusion in planar membranes investigated by fluorescence correlation spectroscopy. *Biochim Biophys Acta - Biomembr*. 2010;1798(7):1377-1391. doi:10.1016/J.BBAMEM.2010.02.014

67. Wu HL, Tong Y, Peng Q, Li N, Ye S. Phase transition behaviors of the supported DPPC bilayer investigated by sum frequency generation (SFG) vibrational spectroscopy and atomic force microscopy (AFM). *Phys Chem Chem Phys*. 2016;18(3):1411-1421. doi:10.1039/C5CP04960A

68. Alessandrini A, Facci P. Phase transitions in supported lipid bilayers studied by AFM. *Soft Matter*. 2014;10(37):7145-7164. doi:10.1039/C4SM01104J

69. Monzel C, Sengupta K. Measuring shape fluctuations in biological membranes. *J Phys D Appl Phys*. 2016;49(24). doi:10.1088/0022-3727/49/24/243002

70. Curtis JE, Zhang H, Nanda H. SLDMOL: A tool for the structural characterization of thermally disordered membrane proteins. *Comput Phys Commun*. 2014;185(11):3010-3015. doi:10.1016/J.CPC.2014.07.006

71. Nanda H, Datta SAK, Heinrich F, et al. Electrostatic interactions and binding orientation of HIV-1 matrix studied by neutron reflectivity. *Biophys J*. 2010;99(8):2516-2524. doi:10.1016/j.bpj.2010.07.062

72. Curtis JE, Raghunandan S, Nanda H, Krueger S. SASSIE: A program to study intrinsically disordered biological molecules and macromolecular ensembles using experimental scattering restraints. *Comput Phys Commun*. 2012;183(2):382-389. doi:10.1016/J.CPC.2011.09.010

73. Humphrey W, Dalke A, Schulten K. VMD: Visual molecular dynamics. *J Mol Graph*. 1996;14(1):33-38. doi:10.1016/0263-7855(96)00018-5

74. Boucrot E, Pick A, Çamdere G, et al. Membrane fission is promoted by insertion of amphipathic helices and is restricted by crescent BAR domains. *Cell*. 2012;149(1):124-136. doi:10.1016/j.cell.2012.01.047

75. Antonny B. Mechanisms of Membrane Curvature Sensing. *http://dx.doi.org/101146/annurev-biochem-052809-155121*. 2011;80:101-123. doi:10.1146/ANNUREV-BIOCHEM-052809-155121

76. Kozlov MM, Campelo F, Liska N, Chernomordik L V., Marrink SJ, McMahon HT. Mechanisms shaping cell membranes. *Curr Opin Cell Biol*. 2014;29(1):53-60. doi:10.1016/J.CEB.2014.03.006

77. Nagle JF, Tristram-Nagle S. Structure of lipid bilayers. *Biochim Biophys Acta - Rev Biomembr*. 2000. doi:10.1016/S0304-4157(00)00016-2

78. Armen RS, Uitto OD, Feller SE. Phospholipid component volumes: Determination and application to bilayer structure calculations. *Biophys J*. 1998;75(2):734-744. doi:10.1016/S0006-3495(98)77563-0

79. Ferry JD. *Viscoelastic Properties of Polymers*. 3rd ed. (Wiley J, ed.). New York; 1980.

80. Philippoff W. Relaxations in Polymer Solutions, Liquids, and Gels. *Phys Acoust*. 1965;2(PB):1-90. doi:10.1016/B978-0-12-395662-0.50011-4

81. Sauerbrey G. The use of quarts oscillators for weighing thin layers and for microweighing. *Z Phys*. 1959;155(206). https://cir.nii.ac.jp/crid/1571417124278253824. Accessed May 25, 2022.

82. Rodahl M, Kasemo B. On the measurement of thin liquid overlayers with the quartz-crystal microbalance. *Sensors Actuators A Phys*. 1996;54(1-3):448-456. doi:10.1016/S0924-4247(97)80002-7

83. Liu G, Zhang G. *QCM-D Studies on Polymer Behavior at Interfaces*.; 2013. doi:10.1007/978-3-642-39790-5

84. Pecora R. *Dynamic Light Scattering - Applications of Photon Correlation Spectroscopy* . (Plenum Press NY and L, ed.).; 1985. doi:10.1002/BBPC.19870910455

85. Michael S. SAXSutilities2: a graphical user interface for processing and analysis of Small-Angle X-ray Scattering data. September 2021. doi:10.5281/ZENODO.5825707

Chapter 6

Investigating the interaction of PIP_2-containing model membranes with CME adaptor and modulator proteins: AP2, FCHo2 and Eps15[a]

1. Introduction

Clathrin-mediated endocytosis (CME) is the main endocytic pathway exploited by cells to internalize membrane protein or, sometimes, viruses[1,2]. CME is a complicated biological pathway that requires the cross-interaction between proteins as well as the anchoring of proteins to the inner leaflet of the plasma membrane, which occurs thanks to the interaction of protein with negatively charged lipids as phosphatidylserines (PS) and phosphatidylinositol (PI), together with their phosphorylated versions (PIP). In particular, phosphatidylinositol 4,5-bisphosphate (PIP_2) is the most abundant PIP, even though it is present only by 1-2% in mol in the inner leaflet of the plasma membrane[3–6]. The proteins involved in the CME pathway can be divided into two different families: (1) adaptor proteins, such as AP2, and (2) modulator proteins, such as FCHo2 and Eps15. The firsts are able to specifically recognize the cargoes to internalize[7,8] as well as bind the membrane[9–13]and recruit clathrin[14]. On the other hand, modulator proteins are essential to stabilize adaptor protein-cargo complexes, localized at the membrane, and they are thought to initiate the CME[15,16] by binding the inner leaflet of the cell membrane[17] and recruit adaptor proteins, affecting their conformation[18–20].

1.1. The adaptor protein AP2

The heterotetrameric Adaptor Protein complexes AP1, AP2, AP3 and AP4[14], are essential for the recruitment of clathrin. Among them, the most studied one is AP2 (**Figure 1.8**). As the other APs, it is composed by four different subunits (α, β, μ, and σ) with different functions. AP2 is characterized by a core made up of the trunk domains of the subunits[12], and flexible appendages, coming from subunits α and β that can bind clathrin[14,21,22] (see cartoon bottom-right panel in **Figure 1.8**). This protein is provided with multiple PIP_2 binding sites, localized at the N-terminus of the α subunit[9–11], and on the surface of the μ subunit[12,13]. Besides, the σ subunit contains the dileucine binding box[7,8], which can bind to the so called CD4 sorting signal peptide. Interestingly,

[a] The data presented here are part of manuscripts in preparation.

the PIP_2 and cargo binding sites are on mutually perpendicular faces, meaning that the cargo binding site is occulted by the β subunit. In fact, after mediation by modulator proteins (such as FCHo2) that recognize AP2 and promote its binding toward PIP_2 phosphate groups, the protein undergoes a conformational change (close to open conformation) that leads to cargo binding[20]. Specifically, PIP_2 competes with the modulator protein, and once AP2 interacts with the lipids, the modulator protein is released, leading to the AP2 conformational change that frees the cargo binding site[20]. Although the structure of the AP2 core was determined in complex with inositol(1,2,3,4,5,6) hexakisophosphate (PDB ID: 1GW5[12]), which mimics PIP_2 headgroup, showing the molecular detail of the binding, and the influence of AP2 on PIP_2-containing membrane was investigated with EM tomography[23] and fluorescence microscopy[20], detailed information is still missing. Recently, the interaction of AP2 with lipid monolayer was investigating, exploiting a plethora of interfacial techniques, and in particular neutron reflectometry (NR) unravelled the three-dimensional orientation of the protein underneath PIP_2-containing lipid monolayer, also in presence of CD4-mimicking short peptide, which was anchored to the monolayer[24]. Here we used a similar model membrane in the form of solid supported bilayer, containing both PIP_2 and CD4 peptide to evaluate AP2 structure upon binding. Firstly, we characterized such complex model membrane, assessing the presence of the peptide, embedded in the headgroup layer, and then we investigating AP2 binding with NR.

1.2. The modulator proteins: FCHo2 and Eps15

FCHo2, *i.e.*, N-terminal Fes-CIP4 homology domain (hence FCH) only protein 2[16,25–29], is a well-known curvature inducing protein, whose surface bears positive charges that can interact with the negative charges of the inner leaflet of the plasma membrane. FCHo2, alongside with other curvature sensing and inducing proteins, can directly sculpt the lipid bilayer, usually by lipid binding via electrostatic interaction or by insertion in the membrane[30]. This protein belongs to the Amphiphysin family, inducing curvature due to the presence of a Bin-Amphiphysin-Rvs167 (BAR) domain. In fact, when a dimeric state is formed, BAR domains, which are characterized by a defined intrinsic curvature, expose a patch of positive charges that can interact with PIP_2 as well as PS negatively charged headgroups. Thus, upon binding to the inner leaflet of the cell membrane, the BAR can either induce or stabilize membrane curvature[30,31]. Other than the BAR (F-BAR) domain, FCHo2 contains intrinsically disordered segments of ~200 amino acid residues, referred

to as flexible linkers, that associates with AP2[18,19,32], and a C-terminal µ-homology domain (µHD) that binds to the pioneer protein Eps15 (epidermal growth factor pathway substrate 15)[15,32–34] (see cartoon in **Figure 6.1**), which in return can bind AP2 appendages[35–37].

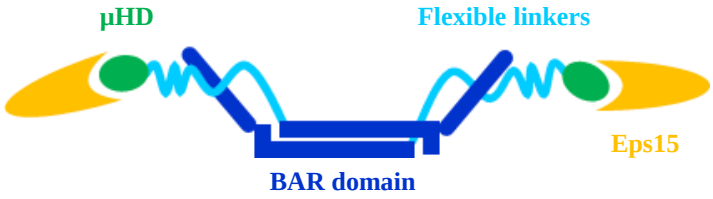

Figure 6.1 Cartoon model representing the FCHo2 domains, including Eps15.

Thus, the cross-interactions between FCHo2, Eps15 and AP2 allow the stabilization of modulator and adaptor protein complexes localized at the plasma membrane, and induce the initiation of the CME pathway. FCHo2 play a key role in local AP2 recruiting and restructuring, as it is among the earliest proteins to mark a nascent CCP[15,16] and affect AP2 conformation directly[18–20]. Although the atomic structure of the F-BAR domain and the µHD domain in complex with Eps15 have been solved (PDB ID: 2V0O[30] and 5JP2[35], respectively, shown in **Figure 1.9**), and biochemical tools together with microscopy have been employed[20,35] to investigate their binding with AP2 appendages, the resultant structure of FCHo2 and FCHo2-Eps15 complex upon membrane binding has yet to be investigated. As an example, questions remain unsolved regarding the position of both flexible linkers and µHD after lipid binding and before Eps15 recruitment. To this end, here we exploited NR with the full-length FCHo2 as well as a truncated version (tFCHo2), lacking the µHD, to get information about the position of the different FCHo2 domains with respect to the lipid membrane.

2. Material and methods

2.1. Protein expression and purification

All the protein constructs (see **Table 6.1**) used in this work were kindly provided from Dr. David J. Owen of the Cambridge Institute for Medical Research (University of Cambridge). Regarding, the expression and purification protocols of the AP2 subunits are described in Ref[12].

Table 6.1 sequences of protein and peptides exploited in this work. * indicates a phosphorylated serine.

AP2	MPAVSKGEGMRGLAVFISDIRNCKSKEAEIKRINKELANIRSKFKGDKALDGYSKKKY VCKLLFIFLLGHDIDFGHMEAVNLLSSNRYTEKQIGYLFISVLVNSNSELIRLINNAIKN DLASRNPTFMGLALHCIANVGSREMAEAFAGEIPKILVAGDTMDSVKQSAALCLLRL YRTSPDLVPMGDWTSRVVHLLNDQHLGVVTAATSLITTLAQKNPEEFKTSVSLAVSR LSRIVTSASTDLQDYTYYFVPAPWLSVKLLRLLQCYPPPEDPAVRGRLTECLETILNKA QEPPKSKKVQHSNAKNAVLFEAISLIIHHDSEPNLLVRACNQLGQFLQHRETNLRYLA LESMCTLASSEFSHEAVKTHIETVINALKTERDVSVRQRAVDLLYAMCDRSNAQQIV AEMLSYLETADYSIREEIVLKVAILAEKYAVDYTWYVDTILNLIRIAGDYVSEEVWYR VIQIVINRDDVQGYAAKTVFEALQAPACHENLVKVGGYILGEFGNLIAGDPRSSPLIQF NLLHSKFHLCSVPTRALLLSTYIKFVNLFPEVKATIQDVLRSDSQLKNADVELQQRAV EYLRLSTVASTDILATVLEEMPPFPERESSILAKLKKKKGMTDSKYFTTNKKGEIFELK AELNNEKKEKRKEAVKKVIAAMTVGKDVSSLFPDVVNCMQTDNLELKKLVYLYLM NYAKSQPDMAIMAVNSFVKDCEDPNPLIRALAVRTMGCIRVDKITEYLCEPLRKCLK DEDPYVRKTAAVCVAKLHDINAQMVEDQGFLDSLRDLIADSNPMVVANAVAALSEI SESHPNSNLLDLNPQNINKLLTALNECTEWGQIFILDCLSNYNPKDDREAQSICERVTP RLSHANSAVVLSAVKVLMKFLELLPKDSDYYNMLLKKLAPPLVTLLSGEPEVQYVAL RNINLIVQKRPEILKQEIKVFFVKYNDPIYVKLEKLDIMIRLASQANIAQVLAELKEYA TEVDVDFVRKAVRAIGRCAIKVEQSAERCVSTLLDLIQTKVNYVVQEAIVVIRDIFRK YPNKYESIIATLCENLDSLDEPDARAAMIWIVGEYAERIDNADELLESFLEGFHDESTQ VQLTLLTAIVKLFLKKPSETQELVQQVLSLATQDSDNPDLRDRGYIYWRLLSTDPVTA KEVVLSEKPLISEETDLIEPTLLDELICHIGSLASVYHKPPNAFVEGSHGIHRKMIGGLFI YNHKGEVLISRVYRDDIGRNAVDAFRVNVIHARQQVRSPVTNIARTSFFHVKRSNIWL AAVTKQNVNAAMVFEFLYKMCDVMAAYFGKISEENIKNNFVLIYELLDEILDFGYPQ NSETGALKTFITQQGIKSQHQTKEEQSQITSQVTGQIGWRREGIKYRRNELFLDVLESV NLLMSPQGQVLSAHVSGRVVMKSYLSGMPECKFGMNDKIVIEKQGKGTADETSKSG KQSIAIDDCTFHQCVRLSKFDSERSISFIPPDGEFELMRYRTTKDIILPFRVIPLVREVGR TKLEVKVVIKSNFKPSLLAQKIEVRIPTPLNTSGVQVICMKGKAKYKASENAIVWKIK RMAGMKESQISAEIELLPTNDKKKWARPPISMNFEVPFAPSGLKVRYLKVFEPKLNYS DHDVIKWVRYIGRSGIYETRCMIRFILIQNRAGKTRLAKWYMQFDDDEKQKLIEEVH AVVTVRDAKHTNFVEFRNFKIIYRRYAGLYFCICVDVNDNNLAYLEAIHNFVEVLNE YFHNVCELDLVFNFYKVYTVVDEMFLAGEIRETSQTKVLKQLLMLQSLE
CD4	CHRRRQAERM[S*]QIKRLLSEK
tFCHo2	GPLGSMAYFVENFWGEKNSGFDVLYHNMKHGQISTKELADFVRERATIEEAYSRSM TKLAKSASNYSQLGTFAPVWDVFKTSTEKLANCHLDLVRKLQELIKEVQKYGEEQV KSHKKTKEEVAGTLEAVQTIQSITQALQKSKENYNAKCVEQERLKKEGATQREIEKA AVKSKKATDTYKLYVEKYALAKADFEQKMTETAQKFQDIEETHLIHIKEIIGSLSNAI KEIHLQIGQVHEEFINNMANTTVESLIQKFAESKGTGKERPGLIEFEECDTASAVEGIKP RKRKTFALPGIIKKEKDAESVECPDADSLNIPDVDEEGYSIKPETNQNDTKENHFYSSS DSDSEDEEPKKYRIEIKPMHPNNSHHTMASLDELKVSIGNITLSPAISRHSPVQMNRNL SNEELTKSKPSAPPNEKGTSDLLAWDPLFGPSLDSSSSSSLTSSSSARPTTPLSVGTIVPP PRPASRPKLTSGKLSGINEIPRPFSPPVTSNTSPPPAAPLARAESSSSISSSASLSAANTPT VGVSR

FCHo2	GPLGSMAYFVENFWGEKNSGFDVLYHNMKHGQISTKELADFVRERATIEEAYSRSM TKLAKSASNYSQLGTFAPVWDVFKTSTEKLANCHLDLVRKLQELIKEVQKYGEEQV KSHKKTKEEVAGTLEAVQTIQSITQALQKSKENYNAKCVEQERLKKEGATQREIEKA AVKSKKATDTYKLYVEKYALAKADFEQKMTETAQKFQDIEETHLIHIKEIIGSLSNAI KEIHLQIGQVHEEFINNMANTTVESLIQKFAESKGTGKERPGLIEFEECDTASAVEGIKP RKRKTFALPGIIKKEKDAESVECPDADSLNIPDVDEEGYSIKPETNQNDTKENHFYSSS DSDSEDEEPKKYRIEIKPMHPNNSHHTMASLDELKVSIGNITLSPAISRHSPVQMNRNL SNEELTKSKPSAPPNEKGTSDLLAWDPLFGPSLDSSSSSSLTSSSSARPTTPLSVGTIVPP PRPASRPKLTSGKLSGINEIPRPFSPPVTSNTSPPPAAPLARAESSSSISSSASLSAANTPT VGVSRGPSPVSLGNQDTLPVAVALTESVNAYFKGADPTKCIVKITGDMTMSFPSGIIK VFTSNPTPAVLCFRVKNISRLEQILPNAQLVFSDPSQCDSNTKDFWMNMQAVTVYLK KLSEQNPAASYYNVDVLKYQVSSNGIQSTPLNLATYWKCSASTTDLRVDYKYNPEA MVAPSVLSNIQVVVPVDGGVTNMQSLPPAIWNAEQMKAFWKLSSISEKSENGGSGSL RAKFDLSEGPSKPTTLAVQFLSEGSTLSGVDFELVGTGYRLSLIKKRFATGRYLADCG HHHHHHHHHH
Eps15	MAAAAQLSLTQLSSGNPVYEKYYRQVDTGNTGRVLASDAAAFLKKSGLPDLILGKI WDLADTDGKGILNKQEFFVALRLVACAQNGLEVSLSSLNLAVPPPRFHDTSSPLLISG TSAAELPWAVKPEDKAKYDAIFDSLSPVNGFLSGDKVKPVLLNSKLPVDILGRVWEL SDIDHDGMLDRDEFAVAMFLVYCALEKEPVPMSLPPALVPPSKRKTWVVSPAEKAK YDEIFLKTDKDMDGFVSGLEVREIFLKTGLPSTLLAHIWSLCDTKDCGKLSKDQFALA FHLISQKLIKGIDPPHVLTPEMIPPSDRASLQKNIIGSSPVADFSAIKELDTLNNEIVDLQ REKNNVEQDLKEKEDTIKQRTSEVQDLQDEVQRENTNLQKLQAQKQQVQELLDELD EQKAQLEEQLKEVRKKCAEEAQLISSLKAELTSQESQISTYEEELAKAREELSRLQQET AELEESVESGKAQLEPLQQHLQDSQQEISSMQMKLMEMKDLENHNSQLNWCSSPHSI LVNGATDYCSLSTSSSETANLNEHVEGQSNLESEPIHQESPARSSPELLPSGVTDENEV TTAVTEKVCSELDNNRHSKEEDPFNVDSSSLTGPVADTNLDFFQSDPFVGSDPFKDDP FGKIDPFGGDPFKGSDPFASDCFFRQSTDPFATSSTDPFSAANNSSITSVETLKHNDPFA PGGTVVAASDSATDPFASVFGNESFGGGFADFSTLSKVNNEDPFRSATSSSVSNVVIT KNVFEETSVKSEDEPPALPPKIGTPTRPCPLPPGKRSINKLDSPDPFKLNDPFQPFPGND SPKEKDPEIFCDPFTSATTTTNKEADPSNFANFSAYPSEEDMIEWAKRESEREEEQRLA RLNQQEQEDLELAIALSKSEISEAKHHHHHH

2.2. Materials

1,2-dipalmitoyl-sn-glycero-3-phosphocholine (DPPC), 1,2-dipalmitoyl-sn-glycero-3-phosphoethanolamine (DPPE) 1,2-dioleoyl-sn-glycero-3-phosphocholine (DOPC), 1,2-dioleoyl-sn-glycero-3- phosphoethanolamine (DOPE) , 1-palmitoyl-2-oleoyl-sn-glycero -3-phosphoserine (POPS) and brain L-α-phosphatidylinositol-4,5-bisphosphate (ammonium salt) PI(4,5)P_2 (PIP_2) were purchased as powder from Avanti Polar Lipids (purity >99%, Alabaster, AL, USA). CD4 peptide was covalently linked to the synthetic lipid 16:0 MPB PE, 1,2-Dipalmitoyl-sn-Glycero-3-Phosphoethanolamine-N-[4-(p-maleimidophenyl) butyramide], kindly provided by Dr. David J. Owen. CD4 was synthesized with a cysteine moiety in the amino-terminal, suscebtible of a conjugation reaction with 16:0 MPB PE, which was achieved through a Thiol-Maleimide Michael addition reaction[8,23,38–40]. The final solutions of the lipopeptide were collected after extraction, dried under nitrogen, resuspended in chloroform:methanol (2:1) and stored at -20 ºC. Solutions of 3 mg·mL^{-1} of DPPC, DPPE, DOPC, DOPE and POPS and a solution of 1 mg·mL^{-1} PIP_2 were

prepared in chloroform stabilized with ethanol (purity 99.8%; Sigma-Aldrich, St. Louis, MO, USA). These solutions were used as stock solutions in order to prepare mixtures with the desired compositions, *i.e.*, DPPC:DPPE:POPS (65:15:20 molar ratio) and DPPC:DPPE:PIP_2 (70:20:10 molar ratio) for monolayer studies with FCHo2, and DOPC:DOPE:PIP_2:CD4 (66.5:20:10:3.5 molar ratio) for bilayer experiments with AP2. Ultra-pure water was generated by passing deionized water through a Milli-Q unit (total organic content = 4 ppb; resistivity = 18 mΩ·cm, Milli-Q, Merck KGaA, Darmstadt, Germany). D_2O (99.9% of isotopical purity) was purchased from Sigma-Aldrich (St. Louis, MO, USA) and used as received. Monolayer experiments were performed in HKM buffer (25 mM HEPES pH 7.2, 125 mM potassium acetate, 5 mM magnesium acetate, 1 mM DTT) and bilayer ones in HEPES-NaCl buffer (5 mM HEPES pH 7.0, 150 mM sodium chloride). HEPES (in solution, 1 M in H_2O, and powder, purity 99.5%), potassium acetate (purity≥99.0%), magnesium acetate (purity≥99.0%), DTT (purity≥99.0%), sodium chloride (purity≥99.0%), magnesium chloride (purity≥98.0%) were purchased from Sigma Aldrich.

2.3. Surface pressure - area isotherm of Langmuir monolayers

A solution of lipids in chloroform with a composition DPPC:DPPE:POPS 65:15:20 molar ratio was prepared at 0.1 $mg \cdot mL^{-1}$ concentration. A Langmuir trough (Kibron, Helsinki, Finland) with a maximum area of 166.4 cm^2 equipped with two dependent symmetric sliding barriers was used to measure the surface pressure (Π) - area isotherm of lipid monolayers. The variation of surface pressure was recorded using a Wilhelmy plate made of filter paper (Whatman CHR1 chromatography paper). The subphase used was made of HKM buffer (120 mL) and the temperature was maintained at 21.0 ± 0.5 °C.

2.4. Neutron reflectometry with lipid mono- and bilayers

NR experiments with monolayer and bilayer model membranes were performed on the time-of-flight reflectometer FIGARO[41] at the ILL. Two different angles of incidence were employed: 0.62° and 3.8° for Langmuir monolayers, and 0.8° and 3.2° for solid supported lipid bilayers. The wavelength resolution used was 7% $d\lambda/\lambda$, with a momentum transfer, $Q_z=(4\pi/\lambda)\sin\theta$, range from 0.01 to 0.25 A^{-1}. Different buffered isotopic solvent contrasts were employed, characterized by different scattering length density (SLD): 100% D_2O *v/v* (SLD=$6.36 \cdot 10^{-6}$ $Å^{-2}$), 80% D_2O *v/v* (SLD=$4.98 \cdot 10^{-6}$ $Å^{-2}$), 38% D_2O *v/v* (called silicon contrast matched water, SiMW, since it has the same SLD of the silicon support, *i.e.*, SLD=$2.07 \cdot 10^{-6}$ $Å^{-2}$), 8.1% D_2O *v/v* (called air

contrast matched water, ACMW, since it has the same SLD of the air, *i.e.*, 0), and 100% H_2O *v/v* (SLD=-0.56·10^{-6} $Å^{-2}$). Lipid monolayers were prepared in Langmuir troughs made at ILL, filled with 42 mL of HKM buffer solution, and after their characterization, protein was injected in the bulk phase to a final concentration of 50 nM for FCHo2 (and its truncated version), and 30 nM for Eps15. Moreover, as previously reported in the case of liquid condensed phase DPPC (as it is for the pressures here reported), a contraction of the palmitoyl tails volume of 15% occurs, which changes the SLD of the tails[42]. For NR experiments on bilayers, solid/liquid flow cells available at the ILL with polished silicon crystals (111) with a surface area of 5×8 cm^2 were used. The silicon crystals were carefully cleaned with organic solvents (chloroform, acetone, and ethanol) and polished for 2 minutes with a Plasma cleaner PDC-002 (230V) (Harrick Plasma, New York, US). Substrate surface was characterized in two different isotopic solvent contrasts, (100% H_2O *v/v* and 100% D_2O *v/v*), before bilayer deposition. Bilayers were formed through vesicle fusion, aided by osmotic shock. After bilayer characterization, AP2 was injected in the flow cell and after appropriate kinetics, the unbounded and physisorbed protein molecules were washed away by a buffer solution washing step, and the bilayer+protein system was characterized. HEPES 5mM, NaCl 150mM (pH=7) buffer solution was used for NR bilayer experiments. The liposome solution also contained 3mM $MgCl_2$ to promote vesicle fusion on the solid support. Three isotopic contrasts were used for DPPC:DPPE:POPS monolayer with tFCHo2 and FCHo2 (see **Figure 6.5**); two isotopic contrasts were used for DPPC:DPPE:POPS monolayer with FCHo2+Eps15 (see **Figure 6.5**) and DPPC:DPPE:PIP_2 monolayer with FCHo2 (see **Figure 6.7**); four isotopic contrasts were used for DOPC:DOPE:PIP_2:CD4 bilayer with AP2 (see **Figure 6.2**). The NR data were reduced and normalized using COSMOS[43]. Subsequent data analysis was performed using AuroreNR[44] and Motofit[45] software, by minimizing the difference between the experimental data points and the calculated reflectivity profiles, which was obtained employing a multi-layer slab model. The latter is made of layers characterized by an in-plane averaged SLD, whose value depend of the volume fraction (*f*) of each component, leading to $SLD_{model} = f_{solvent} \cdot SLD_{solvent} + f_{lipid} \cdot SLD_{lipid} + f_{protein} \cdot SLD_{protein}$[b]; where $f_{solvent} + f_{lipid} + f_{protein} = 1$. Moreover, data analysis was performed using constrains between layer parameters, *i.e.*, taking into account that lipid headgroups and tails must

[b] The SLD of the proteins has been determined using the Biomolecular Scattering Length Density Calculator tool available on the STFC-ISIS online platform (http://psldc.isis.rl.ac.uk/Psldc/).

have the same area per molecule (APM). To this purpose, the fraction of water in the headgroups-layer (f_{wh}) was calculated following **Equation 6.1**:

$$f_{wh} = 1 - \frac{t_t \cdot V_h}{t_h \cdot V_t}, \qquad \textbf{6.1}$$

where t_t and t_h are the thicknesses of tails- and headgroups-layer, respectively, and V_t and V_h are the molecular volumes of tails and headgroups, respectively. **Table 6.1** show the protein sequences, used for SLD determination. All the fixed parameters are tabulated in **Table 6.2**. The roughness (*r*) of the interfaces was also fitted.

Table 6.2 Fixed parameters used for data analysis. Calculated form data found in literature[46,47]. Inner and outer leaflets refer to the bilayer leaflet closer and farer from the support, respectively.

Fixed Parameters	DPPC:DPPE:POPS (65:15:20) monolayer	DPPC:DPPE:PIP_2 (70:20:10) monolayer	DOPC:DOPE:PIP_2:CD4 (65:20:10:5) Inner leaflet	DOPC:DOPE:PIP_2:CD4 (68:20:10:2) Outer leaflet
V_h ($Å^3$)	293.6	320.9	393	502
SLD_h (10^{-6} $Å^{-2}$)	2.23	2.17	2.07	1.99
V_t ($Å^3$)	747.8	732.3	984	979
SLD_t (10^{-6} $Å^{-2}$)	-0.38	-0.42	-0.20	-0.21

3. Results

3.1. The interaction of the adaptor protein AP2 with DOPC:DOPE:PIP_2:CD4 complex bilayer model

The binding of AP2 with the model system that can mimic the inner leaflet of the plasma membrane has been investigated. In particular, a lipid bilayer containing 10% in mol of PIP_2 and also 3.5% in mol of CD4 peptide was exploited, which mimics the intracellular domains of transmembrane cargo proteins recognized by AP2. A CD4 peptide linked to 16:0 MPB PE molecule has been synthesized (see **Methods**), and included in the lipid mixture for bilayer deposition. To the best of our knowledge, this is the first time that a bilayer containing a peptide moiety (to mimic a protein soluble domain) has been deposited onto a silicon crystal surface for NR experiments. This novel *in vitro* lipid system has been characterized with NR, thus assessing the presence of the peptide in the headgroup layer. The model used to fit the data (**Figure 6.2 A**) consisted in 5 layers, each with a constant in-plane averaged SLD: (1) silicon oxide, (2) water, (3)

headgroups+CD4 closer to the support, (4), (5) tails, and (6) headgroups+CD4, exposed to the bulk phase. Layer (1) was characterized prior to the bilayer formation, recording reflectivity profile of the bare silica support interface at two isotopic contrasts (100% H_2O *v/v* and 100% D_2O *v/v*). To characterize the out-of-plane structure of the bilayer, four different isotopic contrasts were employed (by mixing D_2O and H_2O): 100% D_2O *v/v*, 38% D_2O *v/v* (SiMW), 8.1% D_2O *v/v* (ACMW), and 100% H_2O *v/v*. This approach allowed us to determine the molar fraction of CD4 in each headgroup layer. Indeed, we experienced an asymmetry in the bilayer, leading to a 5% in mol% of the peptide in the inner headgroup layer, closer to the support, and 2% in the outer layer, thus a total 7% in the two leaflet. It is worth mentioning that the overall molar percentage of 3.5%, which was used to prepare the sample, is preserved. Moreover, it has to be taken into account that CD4 bears a total positive charge, thus its interaction with the negatively charge support is favourable. **Figure 6.2 D** also shows the contribution of each moiety of lipid molecules to the bilayer, in term of volume fractions. The contribution of CD4 is also reported, shown as plain light magenta area. After the characterization of the lipid bilayer composition as well as out-of-plane structure, AP2 has been injected and its interaction with the model membrane investigated. In particular, NR shed light on the interaction of AP2, demonstrating an insertion of the protein in the outer headgroups layer (layer (6)). This is compatible with the interaction of AP2 with both the CD4 peptide and the phosphate groups of PIP_2 inositol ring, considered embedded in such layer. Besides, an extra layer ((7), as shown in **Figure 6.2 B**) has been taken into account to model the remaining protein structure present outside the bilayer. The total thickness of AP2 obtained here (69±2 Å) is compatible with the crystal structure of the protein in the open conformation[12], as well as with previous NR experiments that showed the orientation of AP2 with lipid monolayer containing PIP_2 and CD4, which reported a total thickness of ~80 Å[24]. **Table 6.3** reports all the fitting parameters, including molar and volume fractions of CD4, and protein volume fraction.

Table 6.3 Fitting parameters. *the values in brackets refer to the volume fraction.

DOPC:DOPE:PIP_2:CD4 bilayer	t (Å)	f_w (%)	CD4 mol% (*v/v*)*	APM (Å^2)	t (Å)	f_w (%)	AP2 % (*v/v*)	APM (Å^2)
(2) Water-layer	5±1	100			7±1	100	0	
(3) Headgroups-layer	10±1	17±1	5 (0.4)*	59±9	10±1	17±1	0	59±7
(4) Tails-layer	17±1	1.8±0.2		59±10	17±1	3.3±0.5	0	60±4
(5) Tails-layer	13	11.3±0.4		87±10	13±1	16±1	0	92±8
(6) Headgroups-layer	8±1	44±1	2 (0.2)*	88±13	8±1	29±1	20±1	90±13
(7) AP2-layer					61±2	96.2±0.2	3.8±0.2	

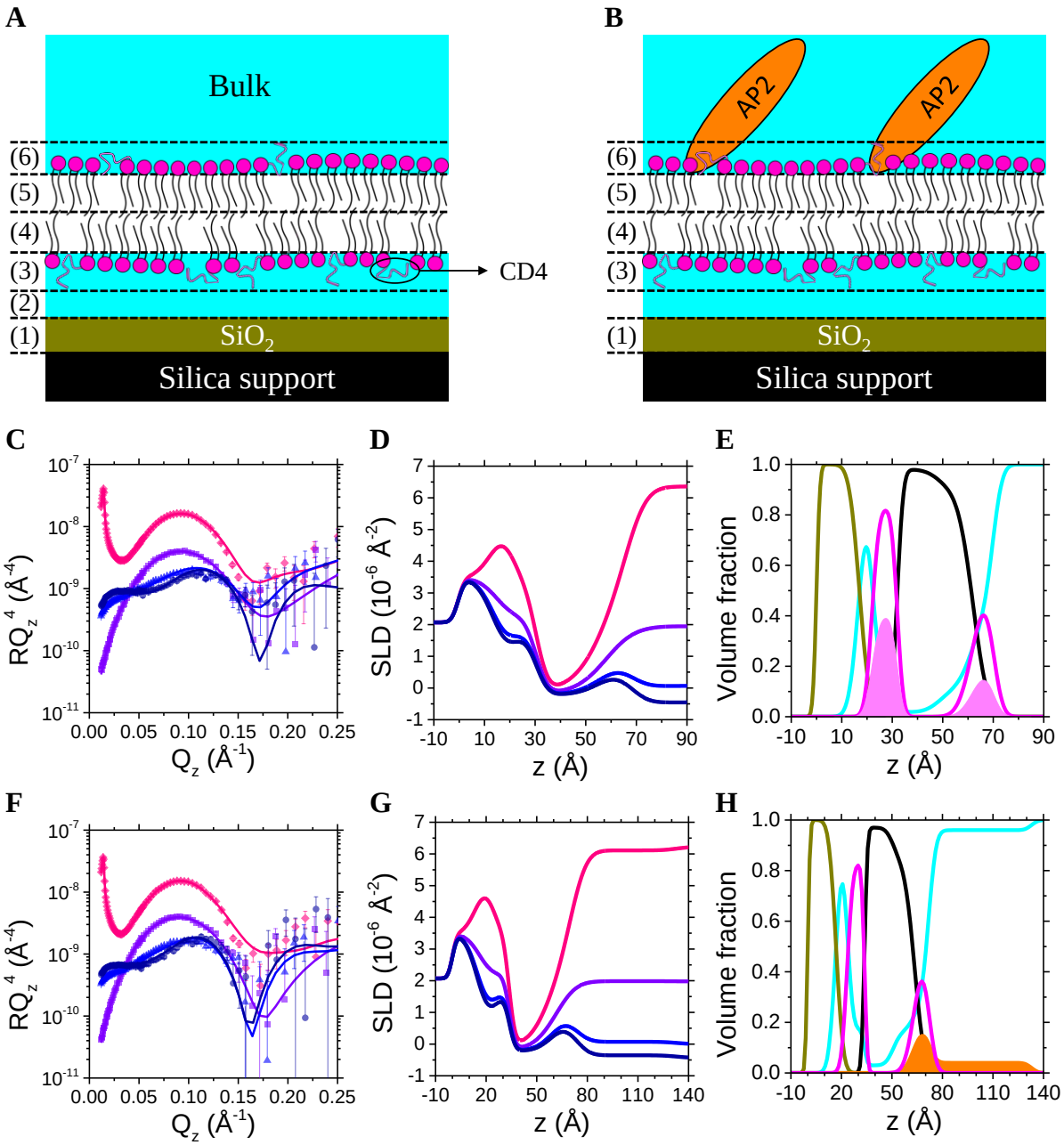

Figure 6.2 Sketches showing the models used to interpret the reflectivity data **A** before and **B** after AP2 addition. Experimental (symbols) and simulated (lines) neutron reflectivity profiles of lipid bilayer **C** before and **F** after AP2 addition. Data at four isotopic contrasts have been measured: 100% D_2O (pink diamonds), SiMW (violet squares), ACMW (blue triangles) and 100% H_2O (dark blue circles). Figures are displayed on an RQ_z^4 scale to show the quality of the fits at high Q_z values. SLD profiles corresponding to fits are plotted in **D** and **G**. Pink, violet, blue and dark blue continuous lines indicate the SLD profiles in 100%D_2O, SiMW, ACMW and 100% H_2O isotopic contrast, respectively. **E**, **H** Volume fraction profiles derived from the fit highlighting the distribution of tails (black), headgroups with CD4 (magenta), water (cyan). Panel **E** also shows the contribution of CD4 (light magenta area), while panel **H** shows the contribution of AP2 (orange area).

3.2. The interaction of modulator proteins with negatively charged lipid monolayers

Lipid monolayer compositions of DPPC:DPPE:PIP_2 and DPPC:DPPE:POPS, in molar ratio 70:20:10 and 65:15:20, respectively, were employed to deposit stable Langmuir monolayers at the air/water interface. The compositions were chosen to replicate the inner leaflet of the plasma membrane, whose phospholipid content is enriched in phosphatidylcholine (PC) and phosphatidylethanolamine (PE)[48–50], but also containing negative charges (PS and PIP_2). Moreover, such compositions had already been used for biochemical studies with proteins from the CME pathway[17,51]. In particular, it was shown that the percentage of PS in liposomes required for maximal FCHo2 binding was approximately 20%[17]. Thus, in our work we exploited both DPPC:DPPE:PIP_2 70:20:10 and DPPC:DPPE:POPS 65:15:20 to explore full-length protein binding. Importantly, the use of saturated palmitoyl chains (DPPC and DPPE) avoided the problem of oxidation of phospholipid tails, which may occur at the air/water interface when multiple unsaturations are present, as for example with di-oleoyl phospholipids. Firstly, the surface pressure (Π) - area (A) per molecule compression isotherms of the DPPC:DPPE:POPS monolayers were recorded in HKM buffer solution at 21°C, and are plotted in **Figure 6.3 A** (the one of DPPC:DPPE:PIP_2 monolayer is shown in **Figure 5.1**). For sake of comparison, the isotherm of a purely DPPC[52] monolayer, measured in the same condition of temperature and buffer solution, is superimposed. Since the DPPC:DPPE:PIP_2 compression isotherm has been extensively discussed in **Chapter 5**, here we focused on the DPPC:DPPE:POPS monolayer. **Figure 6.3 B** shows the corresponding compressional elastic moduli (C_s^{-1}), calculated according to $C_s^{-1} = -A \cdot \left(\frac{\partial \Pi}{\partial A}\right)$.

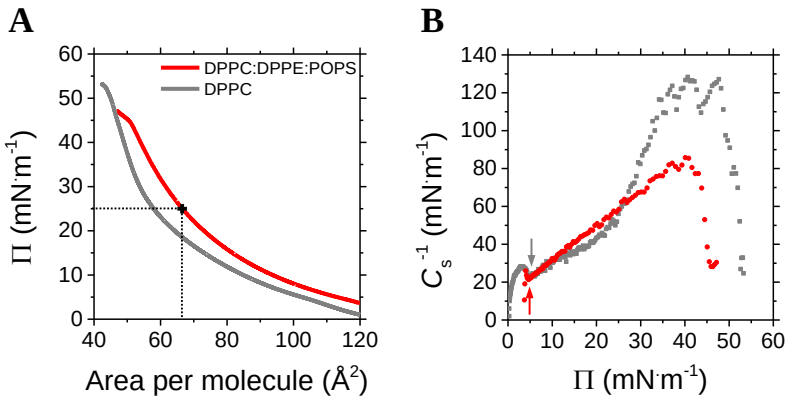

Figure 6.3 A Isotherms of mixed DPPC:DPPE:POPS (red line) and purely DPPC (grey line) monolayers. The surface pressure used for binding studies (*i.e.*, Π=25 mN·m^{-1}) is indicated with a cross. **B** compressibility modulus of mixed DPPC:DPPE:POPS (blue circles) and purely DPPC (grey squares) monolayers. Arrows indicate the minima corresponding to the LC-LE transition.

A simple qualitative analysis of the compression isotherm provide information about the monolayer phase behaviour, by helping distinguish between liquid expanded (LE, fluid-like) phase, characterized by a lack of in-plane spatial and orientational organization of the lipid molecules, and liquid condensed (LC, gel-like) phase, with tightly packed lipids. The isotherms shown in **Figure 6.3 A**, display a LE phase at low values of surface pressure (Π<3-5 $mN \cdot m^{-1}$), followed by an increase in lateral packing upon further compression and the emergence of an LE-LC phase coexistence. However, the identification of the LE-LC transition was not straightforward from the visualization of the Π-A isotherms, but produced a minimum in the C_s^{-1} profile at $\Pi \approx 5$ $mN \cdot m^{-1}$, similar to the one of pure DPPC[42,52]. Further compression yielded a LC phase. Finally, the emergence of a pseudo-plateau in the isotherm at $\Pi \approx 40$ $mN \cdot m^{-1}$ was observed, which may be associated with the collapse of the lipid monolayer. Anyway, two main differences characterized the mixed monolayer with respect to the pure DPPC one: a shift of the isotherm towards larger values of APM, and a reduction in the rigidity from $\Pi \approx 30$ $mN \cdot m^{-1}$. Both these features can be ascribed to the presence of POPS, which contains an oleoyl acyl chain, characterized by a double bond. Thus, the presence of such unsaturation would increase the orientational disorder of the film and decrease its rigidity. This results in the right-shift of the isotherm that was already experienced in the case of DPPC:POPC (75:25 molar ratio)[53]. Finally, as reported in **Chapters 3** and **5**, smaller values of C_s^{-1} at larger areas per molecule compared to DPPC isotherm in pure water[42] are observed, in part due to the presence of Mg^{2+} in the bulk phase, which decrease the lipid packing density[52,54,55].

A surface pressure of Π=25 $mN \cdot m^{-1}$, corresponding to an APM of ~67 $Å^2$ was chosen to perform binding experiments with FCHo2 and Eps15. In order to determine the position of flexible linkers and μHD of the protein, two different constructs were employed: full-length FCHo2 (simply called FCHo2) and a truncated version lacking the μHD (called tFCHo2). The increase in surface pressure ($\Delta\Pi$) of DPPC:DPPE:POPS lipid monolayer after protein injection in the bulk phase was recorded (**Figure 6.4**), alongside with NR experiments (**Figure 6.5**). The $\Delta\Pi$ experienced after FCHo2 and tFCHo2 binding is comparable, suggesting that the absence/presence of μHD does not drastically influence the binding to the monolayer (**Figure 6.4 B**). Indeed, the protein-lipid binding is mainly driven by the BAR domain.

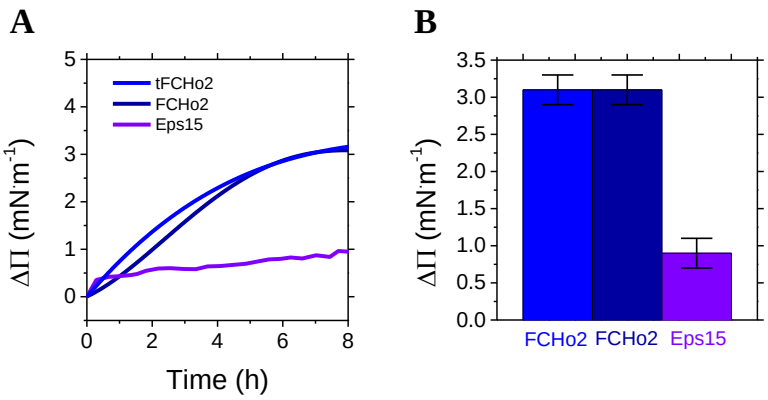

Figure 6.4 A Increase in surface pressure after protein injection in the bulk phase, plotted versus time, for tFCHo2 (blue line), FCHo2 (dark blue line), and Eps15 (injected after FCHo2 binding, violet line). **B** shows the final increment in surface pressure.

NR data of the monolayer with bound tFCHo2 were analysed (**Figure 6.5 A**). A model composed of tails-layer, headgroups-layer and three extra layers accounting for the protein was employed (see **Table 6.4**). No insertion of the protein in the membrane was observed. Moreover, the total thinness obtained (~50 Å) is in agreement with the overall dimensions of the BAR domain, calculated from the crystal structure (PDB ID: 2V0O[30]), *i.e.* ~40 Å. Later on, the same model, in term of number and thickness of layers, was employed with the full-length protein, before and after Eps15 addition. Thus, the protein volume fraction was used as fitting parameter in order to evaluate the percentage of the protein in each layer. Although the increase in the monolayer surface pressure after full-length protein injection is comparable with the one produced by tFCHo2 (**Figure 6.4 B**), there are differences in the volume fraction of the protein (**Figure 6.5 C, F, I**, superimposed in **J**, and **Table 6.4**). NR data showed an increase in protein volume fraction between truncated and full-length protein, which suggests that the μHD is likely closer to the membrane. In fact, the latter has an overall positive charge, thus could interact, even transiently, with negatively charged POPS headgroups. Moreover, considering the large difference in protein volume fractions from layer (3) to layers (4) and (5) (**Table 6.4**), we could infer that they are closer to the membrane. However, other experiments are necessary to confirm this. Finally, the addiction of Eps15 underneath DPPC:DPPE:POPS monolayer with bound FCHo2, did not produce a great increase in surface pressure (**Figure 6.4 B**). However, a considerable increase in the volume fraction is observed, especially in layers (4) (**Table 6.4**), thus suggesting a proximity of Eps15 to the membrane.

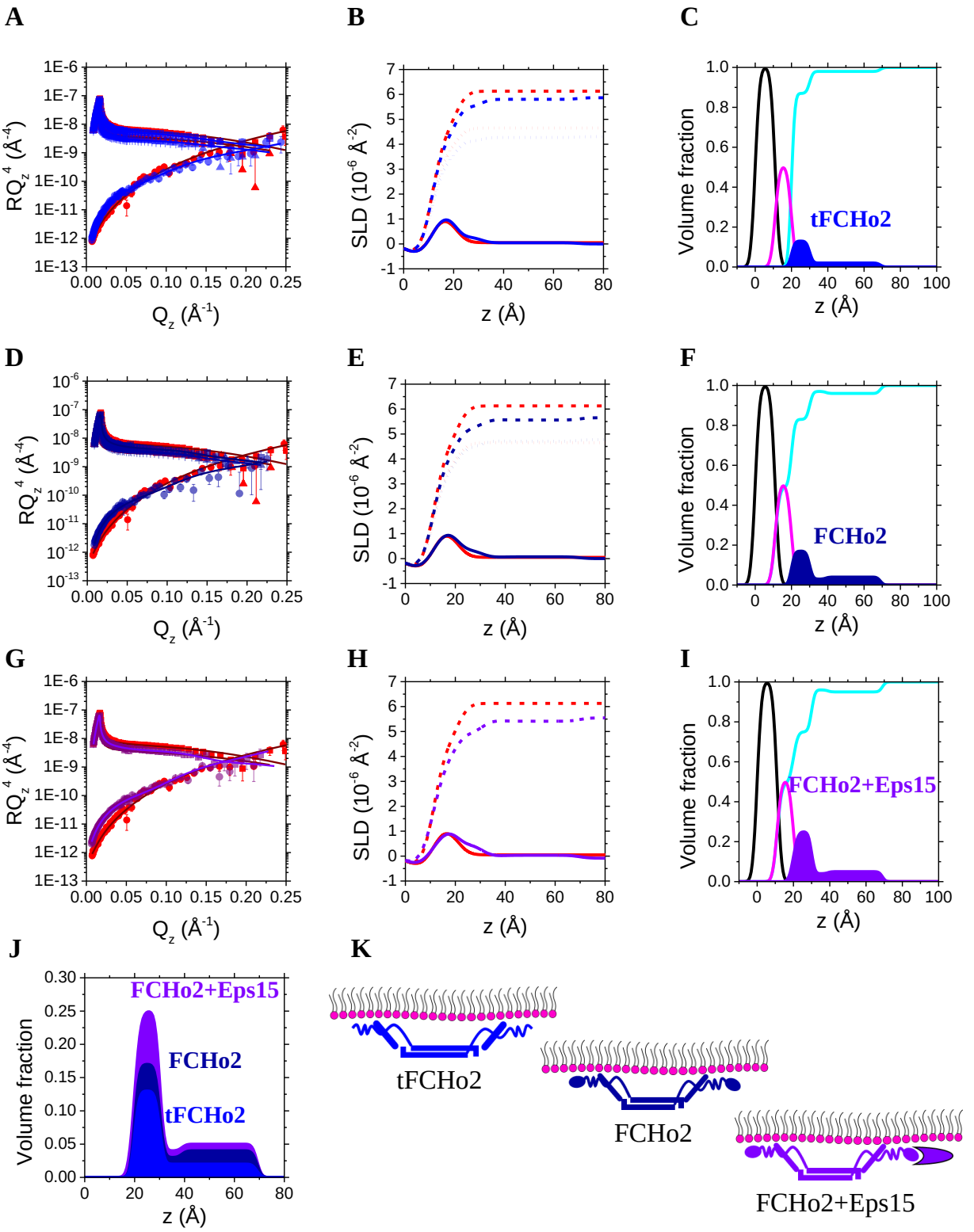

Figure 6.5 Experimental (symbols) and simulated (lines) neutron reflectivity profiles of DPPC:DPPE:POPS lipid monolayers (Π_0=25 mN·m^{-1}) in the absence (red) and presence of **A** tFCHo2 (blue), **D** FCHo2 (dark blue) and **G** FCHo2+Eps15 (violet). Data at three isotopic contrasts have been measured: D_2O (squares), 80% D_2O *v/v* (triangles)

and ACMW (circles). In the case of **G**, only two isotopic contrasts (D_2O and ACMW) have been measured. Figures are displayed on an RQ_z^4 scale to show the quality of the fits at high Q_z values. SLD profiles corresponding to fits are plotted in **B**, **E** and **H**. Continuous, short dotted, short dashed lines indicate the SLD profiles in ACMW, 80% D_2O *v/v* and D_2O isotopic contrast, respectively. Red lines in refer to purely monolayer profiles (Π_0=25 $mN \cdot m^{-1}$), while blue, dark blue and violet (**B**, **E** and **H**, respectively) lines refer to monolayer+tFCHo2, monolayer+FCHo2 and monolayer+FCHo2+Eps15, respectively. Volume fraction profiles derived from the fit highlight the distribution of tails (black), heads (magenta), water (cyan) and **C** tFCHo2 (plain blue area), **F** FCHo2 (plain dark blue area) and **I** FCHo2+Eps15 (plain violet area). **J** reports the superimposition of the proteins volume fractions, while **K** show a schematic model (cartoon) representing the binding and the position of the different domains.

Anyway, calculating the total coverage (*F*) of FCHo2 and Eps15, following $F = \frac{\sum_i t_i f_i}{\sum_i t_i} \cdot 100$, where t is the thickness, *f* is the protein volume fraction and *i* refers to layers (3), (4) and (5), results in *F*=6% and *F*=9% in the case of FCHo2 and FCHo2+Eps15, respectively. Taking into account that the molecular volume of a FCHo2 dimer is ~$220 \cdot 10^3$ $Å^3$ and the one of an Eps15 molecule is ~$120 \cdot 10^3$ $Å^3$ [c], the extra protein coverage of 3% would suggest that only one molecule of Eps15 in bound to the FCHo2 dimer (see model in **Figure 6.5 K**). This is not surprisingly taking into account that, although two molecule of Eps15 should bind an FCHo2 dimer (*i.e.*, each µHD binds an Eps15 molecule), the concentration of Eps15 used in this work is almost half of the FCHo2 concentration (see **Methods**). Finally, taking into account the important role of the flexible linkers and Eps15 in AP2 binding[18,19,32,35–37], their proximity to the membrane surface would help stabilizing the multicomponent complex formed by FCHo2-Eps15-AP2 at the level of the inner leaflet of the plasma membrane, required for CME initialization.

Subsequently, in order to verify eventual differences in FCHo2 binding to POPS- and PIP_2-containing membranes, the binding of the full-length protein was investigated, by injecting it underneath a DPPC:DPPE:PIP_2 monolayer with Π_0=25 $mN \cdot m^{-1}$. The same surface pressure of DPPC:DPPE:POPS monolayer was chosen in order to allow the deposition of monolayers with the same value of compressibility modulus (*i.e.*, $C_s^{-1} \approx 60$ $mN \cdot m^{-1}$, see **Figure 6.3** and **Figure 5.1**). Although the ΔΠ experienced after protein injection is comparable to the one previously obtained with POPS containing (**Figure 6.6 B**), the kinetics of binding is slower (**Figure 6.6 A**).

[c] Calculated using the Biomolecular Scattering Length Density Calculator tool available on the STFC-ISIS online platform (http://psldc.isis.rl.ac.uk/Psldc/).

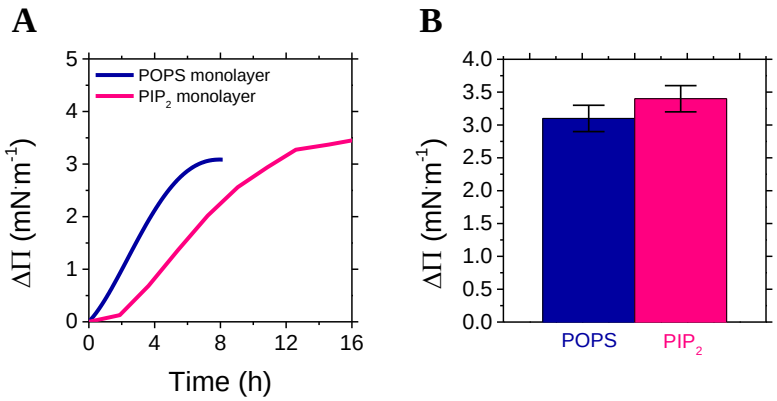

Figure 6.6 A Increase in surface pressure after FCHo2 injection in the bulk phase underneath a DPPC:DPPE:POPS (dark blue line) and DPPC:DPPE:PIP_2 (pink line) monolayers, plotted versus time. **B** shows the final increment in surface pressure.

However, negligible differences in the volume fraction are visible (**Figure 6.7** and **Table 6.4**), alongside with an increment in the related errors, due to the use of only two isotopic contrasts.

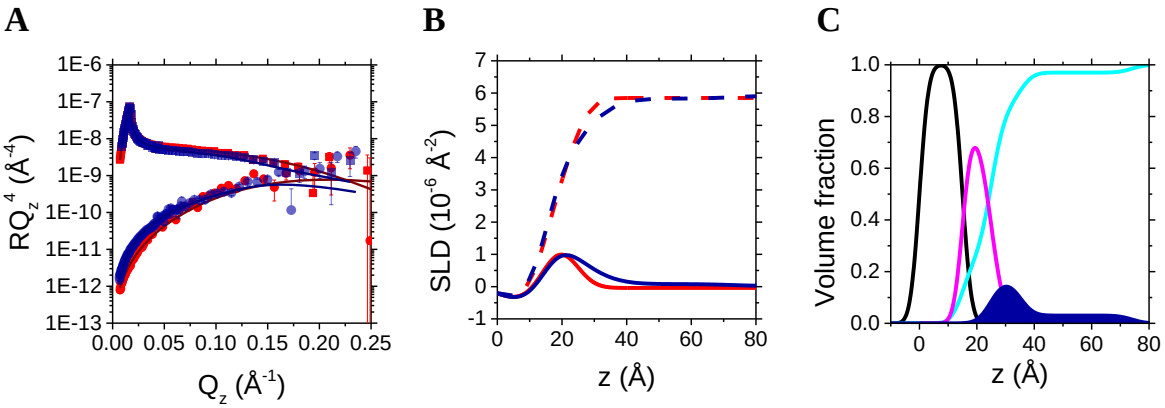

Figure 6.7 A Experimental (symbols) and simulated (lines) neutron reflectivity profiles of DPPC:DPPE:PIP_2 monolayer before (red) and after (dark blue) FCHo2 addition. Data at two isotopic contrasts have been measured: D_2O (squares) and ACMW (circles). Figures are displayed on an RQ_z^4 scale to show the quality of the fits at high Q_z values. **B** SLD profiles corresponding to fits, before (red) and after (dark blue) FCHo2 addition. Dashed and continuous lines indicate the SLD profiles in D_2O and ACMW, respectively. **C** Volume fraction profiles derived from the fit highlighting the distribution of tails (black), headgroups (magenta), water (cyan) and FCHo2 (dark blue).

Table 6.4 Fitting parameters.

DPPC:DPPE:POPS		t (Å)	f_w (%)	APM (Å^2)	t (Å)	f_w (%)	tFCHo2 % (*v/v*)	APM (Å^2)
(1) Tails-layer		11±1	0	66±6	11±1	0	0	66±6
(2) Headgroups-layer		9±1	49±1	61±8	9±1	49±1	0	61±8
(3)	Protein layers				10±1	87±1	13±1	
(4)					9±1	98±2	2±2	
(5)					30±1	98±1	2±1	

DPPC:DPPE:POPS		t (Å)	f_w (%)	FCHo2 % (*v/v*)	APM (Å^2)	t (Å)	f_w (%)	FCHo2+Eps15 % (*v/v*)	APM (Å^2)
(1) Tails-layer		11±1	0	0	66±6	11±1	0	0	66±6
(2) Headgroups-layer		9±1	49±1	0	61±8	9±1	49±1	0	61±8
(3)	Protein layers	10±1	83±1	17±1		10±1	75±1	25±2	
(4)		9±1	97±2	3±2		9±1	96±2	4±2	
(5)		30±1	96±1	4±1		30±1	95±1	5±1	

DPPC:DPPE:PIP$_2$		t (Å)	f_w (%)	APM (Å^2)	t (Å)	f_w (%)	FCHo2 % (*v/v*)	APM (Å^2)
(1) Tails-layer		15±1	0	47±3	0	0	0	47±3
(2) Headgroups-layer		9±1	24±1	46±6	0	24±1	0	46±6
(3)	Protein layers				10±1	83±1	17±3	
(4)					9±1	97±3	3±3	
(5)					30±1	97±1	3±1	

4. Conclusions

Here we reported the study of the interaction of adaptor (AP2) and modulator (FCHo2 and Eps15) proteins from the CME pathway with different model membranes.

The binding of AP2 to model membranes was carried out with supported lipid bilayers, and by depositing complex *in vitro* lipid model systems, enriched in both PIP_2 and CD4, both of which can bind AP2. NR allowed us to obtain information regarding the composition of the deposited bilayer. Hence, we found out that the bilayer was asymmetric, with more CD4 molecules in the headgroups-layer closer to the silicon support (**Figure 6.1**). This effect is probably due to the electrostatic interaction between the negatively charged support and the positively charged peptide. After appropriate characterization of such complex system, AP2 was added to the system and the analysis of the reflectivity data shed light on the insertion of the protein in the membrane.

Indeed, AP2 was able to insert in the headgroups layer (**Figure 6.1**), which is the layer where CD4 and PIP_2 inositol ring (the binding partners of the protein) where considered. Finally, the total thickness obtained for the protein of ~70 Å is compatible with the crystal structure of the protein in the open conformation (bound to PIP_2 inositol and cargo molecules), as well as with previous performed NR experiments that showed the orientation of AP2 with lipid monolayer containing PIP_2 and CD4, and that report a total thickness of ~80 Å.

The experiments performed with FCHo2 allowed us to determine the position of each domain (**Figure 6.5**). Interestingly, we also found out that after Eps15 binding, both the latter and the flexible linkers of FCHo2, which are able to bind AP2, position themselves close to the monolayer. Thus, this proximity to the membrane, would help in stabilizing (*in vivo*) the multicomponent protein complex formed by FCHo2-Eps15-AP2 at the level of the inner leaflet of the plasma membrane, required for CME initialization. Ultimately, the comparison between NR data obtained using monolayers enriched in POPS and PIP_2, did not show any drastic difference in protein binding.

References

1. Schmid SL, Conner SD. Regulated portals of entry into the cell. *Nature*. 2003;422(March):37-44. www.nature.com/nature.

2. McMahon HT, Boucrot E. Molecular mechanism and physiological functions of clathrin-mediated endocytosis. *Nat Rev Mol Cell Biol 2011 128*. 2011;12(8):517-533. doi:10.1038/nrm3151

3. McLaughlin S, Murray D. Plasma membrane phosphoinositide organization by protein electrostatic. *Nature*. 2005;438. doi:10.1038/nature04398.

4. Graber ZT, Jiang Z, Gericke A, Kooijman EE. Phosphatidylinositol-4,5-bisphosphate ionization and domain formation in the presence of lipids with hydrogen bond donor capabilities. *Chem Phys Lipids*. 2012;165(6):696-704. doi:10.1016/j.chemphyslip.2012.07.003

5. Lupyan D, Mezei M, Logothetis DE, Osman R. A molecular dynamics investigation of lipid bilayer perturbation by PIP2. *Biophys J*. 2010;98(2):240-247. doi:10.1016/j.bpj.2009.09.063

6. McLaughlin S, Wang J, Gambhir A, Murray D. PIP2 and proteins: Interactions, organization, and information flow. *Annu Rev Biophys Biomol Struct*. 2002;31:151-175. doi:10.1146/annurev.biophys.31.082901.134259

7. Owen DJ, Evans PR. A structural explanation for the recognition of tyrosine-based endocytotic signals. *Science*. 1998;282(5392):1327-1332. doi:10.1126/science.282.5392.1327

8. Jackson LP, Kelly BT, McCoy AJ, et al. A large-scale conformational change couples membrane recruitment to cargo binding in the AP2 clathrin adaptor complex. *Cell*. 2010;141(7):1220-1229. doi:10.1016/j.cell.2010.05.006

9. Gaidarov I, Keen JH. Phosphoinositide–Ap-2 Interactions Required for Targeting to Plasma Membrane Clathrin-Coated Pits. *J Cell Biol*. 1999;146(4):755-764. doi:10.1083/JCB.146.4.755

10. Padrón D, Wang YJ, Yamamoto M, Yin H, Roth MG. Phosphatidylinositol phosphate 5-kinase Iβ recruits AP-2 to the plasma membrane and regulates rates of constitutive endocytosis. *J Cell Biol*. 2003;162(4):693-701. doi:10.1083/JCB.200302051

11. Page LJ, Robinson MS. Targeting signals and subunit interactions in coated vesicle adaptor complexes. *J Cell Biol*. 1995;131(3):619-630. doi:10.1083/JCB.131.3.619

12. Collins BM, McCoy AJ, Kent HM, Evans PR, Owen DJ. Molecular Architecture and Functional Model of the Endocytic AP2 Complex. *Cell*. 2002;109(4):523-535. doi:10.1016/S0092-8674(02)00735-3

13. Rohde G, Wenzel D, Haucke V. A phosphatidylinositol (4,5)-bisphosphate binding site within μ2-adaptin regulates clathrin-mediated endocytosis. *J Cell Biol*. 2002;158(2):209-214. doi:10.1083/JCB.200203103

14. Owen DJ, Collins BM, Evans PR. ADAPTORS FOR CLATHRIN COATS: Structure and Function. *Annu Rev Cell Dev Biol*. 2004;20(1):153-191. doi:10.1146/annurev.cellbio.20.010403.104543

15. Henne WM, Boucrot E, Meinecke M, et al. FCHo proteins are nucleators of Clathrin-Mediated endocytosis. *Science*. 2010;328(5983):1281-1284. doi:10.1126/science.1188462

16. Taylor MJ, Perrais D, Merrifield CJ. A High Precision Survey of the Molecular Dynamics of Mammalian Clathrin-Mediated Endocytosis. *PLOS Biol*. 2011;9(3):e1000604. doi:10.1371/JOURNAL.PBIO.1000604

17. Uezu A, Umeda K, Tsujita K, Suetsugu S, Takenawa T, Nakanishi H. Characterization of the EFC/F-BAR domain protein, FCHO2. *Genes to Cells*. 2011;16(8):868-878. doi:10.1111/j.1365-2443.2011.01536.x

18. Umasankar PK, Ma L, Thieman JR, et al. A clathrin coat assembly role for the muniscin protein central linker revealed by TALEN-mediated gene editing. *Elife*. 2014;3. doi:10.7554/ELIFE.04137

19. Hollopeter G, Lange JJ, Zhang Y, et al. The membrane-associated proteins FCHo and SGIP are allosteric activators of the AP2 clathrin adaptor complex. *Elife*. 2014;3. doi:10.7554/ELIFE.03648

20. Zaccai NR, Kadlecova Z, Dickson VK, et al. FCHO controls AP2's initiating role in endocytosis through a PtdIns(4,5)P2-dependent switch. *Sci Adv*. 2022;8(17):2018. doi:10.1126/SCIADV.ABN2018

21. Brett TJ, Traub LM, Fremont DH. Accessory Protein Recruitment Motifs in Clathrin-Mediated Endocytosis. *Structure*. 2002;10(6):797-809. doi:10.1016/S0969-2126(02)00784-0

22. DJ O, Y V, BM P, HT M, PR E. The structure and function of the beta 2-adaptin appendage domain. *EMBO J*. 2000;19(16):4216-4227. doi:10.1093/EMBOJ/19.16.4216

23. Kelly BT, Graham SC, Liska N, et al. AP2 controls clathrin polymerization with a membrane-activated switch. *Science*. 2014;345(6195):459-463. doi:10.1126/science.1254836

24. Maestro A, Zaccai NR. Unpublished results.

25. McMahon HT, Gallop JL. Membrane curvature and mechanisms of dynamic cell membrane remodelling. *Nature*. 2005;438(7068):590-596. doi:10.1038/nature04396

26. Frost A, Unger VM, De Camilli P. The BAR Domain Superfamily: Membrane-Molding Macromolecules. *Cell*. 2009;137(2):191-196. doi:10.1016/J.CELL.2009.04.010

27. Itoh T, Takenawa T. Mechanisms of membrane deformation by lipid-binding domains. *Prog Lipid Res*. 2009;48(5):298-305. doi:10.1016/J.PLIPRES.2009.05.002

28. Suetsugu S, Toyooka K, Senju Y. Subcellular membrane curvature mediated by the BAR domain superfamily proteins. *Semin Cell Dev Biol*. 2010;21(4):340-349. doi:10.1016/J.SEMCDB.2009.12.002

29. Aspenström P. A Cdc42 target protein with homology to the non-kinase domain of FER has a potential role in regulating the actin cytoskeleton. *Curr Biol*. 1997;7(7):479-487. doi:10.1016/S0960-9822(06)00219-3

30. Henne WM, Kent HM, Ford MGJ, et al. Structure and Analysis of FCHo2 F-BAR Domain: A Dimerizing and Membrane Recruitment Module that Effects Membrane Curvature. *Structure*. 2007;15(7):839-852. doi:10.1016/j.str.2007.05.002

31. Peter BJ, Kent HM, Mills IG, et al. BAR Domains as Sensors of Membrane Curvature: The Amphiphysin BAR Structure. *Science*. 2004;303(5657):495-499. doi:10.1126/science.1092586

32. Umasankar PK, Sanker S, Thieman JR, et al. Distinct and separable activities of the endocytic clathrin-coat components Fcho1/2 and AP-2 in developmental patterning. *Nat Cell Biol 2012 145*. 2012;14(5):488-501. doi:10.1038/ncb2473

33. Reider A, Barker SL, Mishra SK, et al. Syp1 is a conserved endocytic adaptor that contains domains involved in cargo selection and membrane tubulation. *EMBO J*. 2009;28(20):3103-3116. doi:10.1038/EMBOJ.2009.248

34. Uezu A, Horiuchi A, Kanda K, et al. SGIP1α is an endocytic protein that directly interacts with phospholipids and Eps15. *J Biol Chem*. 2007;282(36):26481-26489. doi:10.1074/JBC.M703815200/ATTACHMENT/74522BA5-599E-4A6D-A3DE-1E0A5DD7AAD8/MMC1.ZIP

35. Ma L, Umasankar PK, Wrobel AG, et al. Transient Fcho1/2·Eps15/R·AP-2 Nanoclusters Prime the AP-2 Clathrin Adaptor for Cargo Binding. *Dev Cell*. 2015;37(5):428-443. doi:10.1016/J.DEVCEL.2016.05.003

36. Benmerah A, Bèguet B, Dautry-Varsat A, Cerf-Bensussan N. The Ear of α-Adaptin Interacts with the COOH-terminal Domain of the Eps15 Protein (∗). *J Biol Chem*. 1996;271(20):12111-12116. doi:10.1074/JBC.271.20.12111

37. Iannolo G, Salcini AE, Gaidarov I, et al. Mapping of the Molecular Determinants Involved in the Interaction between eps15 and AP-21. *Cancer Res*. 1997;57(2):240-245.

38. Höning S, Ricotta D, Krauss M, et al. Phosphatidylinositol-(4,5)-bisphosphate regulates sorting signal recognition by the clathrin-associated adaptor complex AP2. *Mol Cell*. 2005;18(5):519-531. doi:10.1016/j.molcel.2005.04.019

39. Kelly BT, McCoy AJ, Späte K, et al. A structural explanation for the binding of endocytic dileucine motifs by the AP2 complex. *Nature*. 2008;456(7224):976-979. doi:10.1038/nature07422

40. Wrobel AG, Kadlecova Z, Kamenicky J, et al. Temporal Ordering in Endocytic Clathrin-

Coated Vesicle Formation via AP2 Phosphorylation. *Dev Cell*. 2019;50(4):494-508.e11. doi:10.1016/J.DEVCEL.2019.07.017

41. Campbell RA, Wacklin HP, Sutton I, Cubitt R, Fragneto G. FIGARO: The new horizontal neutron reflectometer at the ILL. *Eur Phys J Plus*. 2011;126(11):1-22. doi:10.1140/epjp/i2011-11107-8

42. Campbell RA, Saaka Y, Shao Y, et al. Structure of surfactant and phospholipid monolayers at the air/water interface modeled from neutron reflectivity data. *J Colloid Interface Sci*. 2018;531:98-108. doi:10.1016/j.jcis.2018.07.022

43. Gutfreund P, Saerbeck T, Gonzalez MA, et al. Towards generalized data reduction on a chopperbased time-of-flight neutron reflectometer. *J Appl Crystallogr*. 2018. doi:10.1107/S160057671800448X

44. Gerelli Y. Aurore: New software for neutron reflectivity data analysis. *J Appl Crystallogr*. 2016;49:330-339. doi:10.1107/S1600576716000108

45. Nelson A. Co-refinement of multiple-contrast neutron/X-ray reflectivity data using MOTOFIT. *J Appl Crystallogr*. 2006;39(2):273-276. doi:10.1107/S0021889806005073

46. Nagle JF, Wiener MC. Structure of fully hydrated bilayer dispersions. *BBA - Biomembr*. 1988;942(1):1-10. doi:10.1016/0005-2736(88)90268-4

47. Armen RS, Uitto OD, Feller SE. Phospholipid component volumes: Determination and application to bilayer structure calculations. *Biophys J*. 1998;75(2):734-744. doi:10.1016/S0006-3495(98)77563-0

48. Raghava S, Giorda KM, Romano FB, Heuck AP, Hebert DN. The SV40 late protein VP4 is a viroporin that forms pores to disrupt membranes for viral release. *PLoS Pathog*. 2011;7(6). doi:10.1371/journal.ppat.1002116

49. Lodish H, Berk A, Zipursky LS. "Biomembranes: Structural Organization and Basic Functions." In: *Molecular Cell Biology*. 4th ed. New York: Scientific American Books.; 2000.

50. G. M. Cooper. *"Structure of the Plasma Membrane". The Cell: A Molecular Approach.*

2nd ed.; 2000.

51. Miller SE, Mathiasen S, Bright NA, et al. CALM Regulates Clathrin-Coated Vesicle Size and Maturation by Directly Sensing and Driving Membrane Curvature. *Dev Cell*. 2015;33(2):163-175. doi:10.1016/j.devcel.2015.03.002

52. Carrascosa-Tejedor J, Santamaria A, Pereira D, Maestro A. Structure of DPPC Monolayers at the Air/Buffer Interface: A Neutron Reflectometry and Ellipsometry Study. *Coatings 2020, Vol 10, Page 507*. 2020;10(6):507. doi:10.3390/COATINGS10060507

53. Qiao L, Ge A, Liang Y, Ye S. Oxidative Degradation of the Monolayer of 1-Palmitoyl-2-Oleoyl-sn-Glycero-3-Phosphocholine (POPC) in Low-Level Ozone. *J Phys Chem B*. 2015;119(44):14188-14199. doi:10.1021/acs.jpcb.5b08985

54. Nagle JF, Scott HL. Lateral compressibility of lipid mono- and bilayers. Theory of membrane permeability. *BBA - Biomembr*. 1978;513(2):236-243. doi:10.1016/0005-2736(78)90176-1

55. Adams EM, Casper CB, Allen HC. Effect of cation enrichment on dipalmitoylphosphatidylcholine (DPPC) monolayers at the air-water interface. *J Colloid Interface Sci*. 2016;478:353-364. doi:10.1016/j.jcis.2016.06.016

Chapter 7

Strikingly different roles of SARS-CoV-2 fusion peptides uncovered by neutron scattering[a]

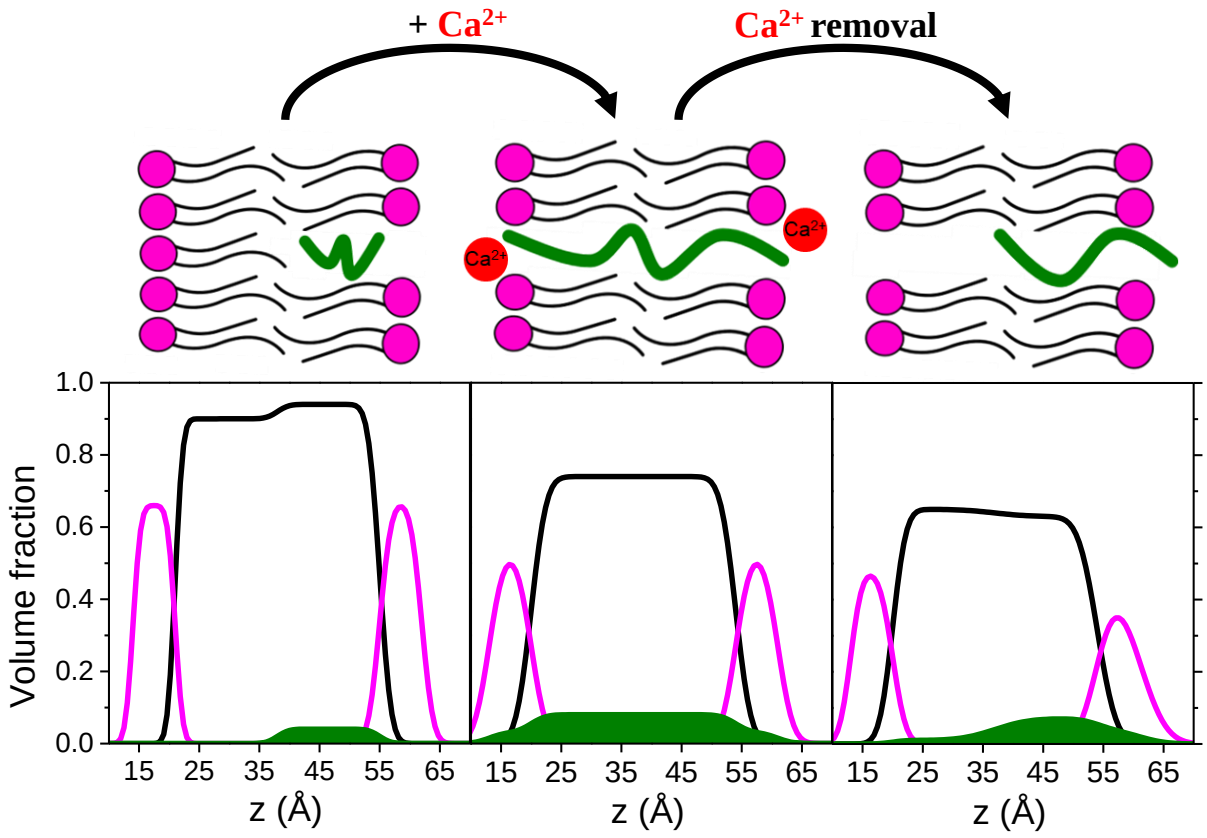

FP1 insertion is Calcium dependent

[a] This chapter reports the student contribution to a work published in the *Journal of American Chemical Society* alongside with other results that are part of a manuscript in preparation (see Publication List at page 279).

Abstract

Coronavirus disease-2019 (COVID-19), a potentially lethal respiratory illness caused by the coronavirus SARS-CoV-2, emerged in the end of 2019 and has since spread aggressively across the globe. A thorough understanding of the molecular mechanisms of cellular infection by coronaviruses is therefore of utmost importance. A critical stage in infection is the fusion between viral and host membranes. Here, we present a detailed investigation of the role of selected SARS-CoV-2 Spike fusion peptides, and the influence of calcium, in this fusion process. Structural information from specular neutron reflectometry revealed strikingly different functions encoded in the Spike fusion domain. Calcium drives the N-terminal of the Spike fusion domain to fully cross the host plasma membrane. Removing calcium however re-orients the peptide back to the lipid leaflet closest to the virus. In conjunction with other regions of the fusion domain which are also positioned to bridge and dehydrate viral and host membranes, the molecular events leading to cell entry by SARS-CoV-2 are proposed.

1. Introduction

β-coronaviruses (CoVs) are single-stranded positive sense RNA viruses[1]. An outbreak of life-threatening respiratory tract infections caused by the SARS-CoV-2 β-coronavirus emerged in late 2019 in China[2,3] and was declared a worldwide pandemic in March 2020. Other β-coronaviruses, including severe acute respiratory syndrome coronavirus 1 (SARS-CoV-1) and Middle Eastern respiratory syndrome coronavirus (MERS-CoV) are also highly contagious pathogens. A thorough understanding of the molecular mechanisms of cellular infection by coronaviruses is therefore of utmost importance.

The main structural components of β-coronaviruses include a lipid envelope, the Spike, Membrane and Envelope proteins, as well as the Nucleoproteins, which form a complex with the viral RNA. The Spike protein has been directly implicated in SARS-CoV-2 infectivity[4–6] and is consequently a target for both vaccine and antiviral drug efforts[7,8]. In a mechanism also present in other RNA viruses, like HIV and the influenza virus[9], this class I viral fusion glycoprotein induces fusion between the viral and host cellular lipid membranes (see **Figure 1.10**), thereby facilitating viral entry. The focus of this chapter is to provide a description of the molecular interactions between SARS-CoV-2 fusion peptides and host membranes. Moreover, cell entry of SARS-CoV-2 can either occur directly through fusion at the plasma membrane[10] (in the presence of calcium),

or after endocytosis, at the endosomal membrane[6] (where free calcium concentrations are greatly reduced[11]). Therefore, this study also focused on the influence of calcium on the fusion of cholesterol-rich membranes, such as the plasma membrane.

The Spike protein (see **Figure 1.11**) N-terminal S1 subunit contains the receptor-binding domain for the angiotensin-converting enzyme 2 (ACE-II). After binding, a proteolysis-triggered conformational change in the C-terminal S2 subunit mediates fusion between the viral and host cell membranes[6,12,13]. S2 continues to be embedded in the viral membrane, but its heptad repeat 1 (HR1) and 2 (HR2) domains associate to form a six-helix bundle fusion core[8]. Proteolysis at the S2' site (at residue 816) subsequently frees the Spike protein fusion domain to associate with the host cell and initiate membrane fusion.

The Spike protein membrane fusion domain is strongly conserved between β-coronaviruses[7]. However, the exact "fusion peptide" has not yet been conclusively identified and is a matter of debate[14–16]. The expected characteristics, *i.e.*, short length, hydrophobicity, with a possible canonical fusion tripeptide (YFG or FXG) along with a central proline residue[17] suggest several putative fusion peptides at or near the newly generated N-terminus of S2': FP1 (SARS-CoV-2 816-837), FP2 (835-856), FP3 (854-874) and FP4 (885-909) (also named internal fusion peptide[15,16]).

In SARS-CoV-1 and MERS-CoV, mutagenesis of the highly conserved S2'-proximal FP1 in the context of full-length Spike protein demonstrated its importance in mediating membrane fusion[18]. SARS-CoV-2 FP1 retains the conserved LLF motif, which was critical for SARS-CoV-1 membrane fusion[19,20]. FP2 is characterized by a pair of highly conserved cysteines, which if reduced in SARS-CoV-1, lead to the abrogation of their membrane-ordering effect. Importantly, SARS-CoV-1 and -2 peptides containing FP1 and FP2 are able to induce membrane ordering in a Ca^{2+}-dependent fashion[14,15,20]. FP3 has an FXG motif at its N-terminus, and near its center, two prolines are surrounded by hydrophobic residues. Adjacent to HR1, FP4 has a central proline and a C-terminal FXG motif. Mutations in equivalent residues in SARS-Cov-1 showed significant reductions in both Spike-mediated pseudovirion entry and cell-cell fusion[21]. Moreover, present within the peptide, the conserved SARS-CoV-1 and -2 GAALQIPFAMQMAYRF sequence can induce hemifusion between small unilamellar vesicles[15].

Different *in vitro* models of increasing complexity were used to characterize the interaction of SARS-CoV-2 peptides with plasma membrane (PM) models. The goal was to recreate important elements of the viral fusion mechanism by simplifying the system down to its core elements. For example, even though solid-supported lipid bilayers are appropriate model membrane systems, a lipid monolayer already provides a simple and versatile model for peptide assembly and insertion into a membrane. By using a Langmuir trough, lateral membrane surface pressure can be controlled by restricting the monolayer lipids to a specific surface area, thereby mimicking the outer plasma membrane leaflet by recreating the pressure experienced within a lipid bilayer. Importantly, synthetic model membranes, as well as biomimetic plasma membrane (PM) with physiological phospholipid and cholesterol composition were studied. No chemical moieties were added to the lipids (or to the peptides), as an important advantage of neutrons in the study of lipid membranes is that the experiments are label-free. Similarly, to avoid problems such as artifactual interactions with the biomimetic PM lipids, the peptides were not modified by introducing additional residues, such as lysine-rich hydrophilic tags.

Through neutron scattering and biophysical experiments, physical and thermodynamic aspects of the membrane fusion mechanism of SARS-CoV-2 were investigated. In particular, specular neutron reflectometry was essential to obtain structural information. The data highlight strikingly different roles for the different regions of the SARS-CoV-2 Spike protein fusion domain. Due to the size and complexity of the Spike protein, our studies focused on individual peptides derived from the protein fusion domain. This simplification provided the opportunity to characterize how specific sections in the unstructured fusion domain interacted with lipids. It also facilitated experimental analysis since much higher molecular concentrations could be achieved.

2. Materials and methods

2.1. Fusion peptides

The fusion peptides were synthesized and purified by GenScript (Amsterdam, The Netherlands). Stock solutions of each peptide in DMSO (dimethyl sulfoxide) were used for all the experiments reported here. The following peptides were investigated (**Figure 1.11**, **Table 7.1** and **Table S7.1**):

Table 7.1 Physicochemical properties of the peptide investigated.

Peptide	Sequence	Number of amino acids	MW (Da)	Net charge
FP1	816-SFIEDLLFNKVTLADAGFIKQY-837	22	2538	-1
FP2	835-KQYGDCLGDIAARDLICAQKFN-856	22	2456	0
FP3	854-KFNGLTVLPPLLTDEMIAQYT-874	21	2351	-1
FP4	885-GWTFGAGAALQIPFAMQMAYRFNGI-909	25	2723	+1

2.2. Lipid samples and buffer solution composition

Biomimetic membranes in the form of monolayers were prepared from phosphatidylcholine (PC), phosphatidylethanolamine (PE) and phosphatidylserine (PS) extracted and purified from perdeuterated and hydrogenous *Pichia pastoris* cell cultures (**Supporting Information**). Hydrogenous cholesterol and egg yolk sphingomyelin were purchased in powder form from Sigma Aldrich. Deuterated cholesterol was obtained from the National Deuteration Facility (NDF) in ANSTO (Australia). For biomimetic PM, the composition in molar ratio was PC 0.2, PE 0.11, PS 0.06, cholesterol 0.5, sphingomyelin 0.13[22] (**Table 7.2**). A simpler biomimetic membrane was also employed, composed by synthetic phospholipids (POPC, and POPS) and cholesterol. 1-palmitoyl-2-oleoyl-sn-glycero-3-phosphocholine (POPC), 1-palmitoyl-2-oleoyl-sn-glycero -3-phosphoserine (POPS) and cholesterol were purchased from Avanti Polar Lipids (Alabaster, AL, USA) and used without further purification. Lipid solutions were prepared in chloroform stabilized with ethanol (purity 99.8%; Sigma-Aldrich, St. Louis, MO, USA).

Table 7.2 Lipid compositions used and experimental techniques. CD: Circular Dichroism; NR: Neutron Reflectometry; BAM: Brewster angle microscopy; Langmuir titration: determination of binding affinity.

Nomenclature	Lipid composition (molar ratio)	*In vitro* lipid model system	Technique
Synthetic model membrane	POPC 0.6, POPS 0.2, cholesterol 0.2	Bilayer (SUV and SLB)	• CD • NR
		Monolayer	• NR – compositional analysis
Plasma membrane (PM)	PC 0.2, PE 0.11, PS 0.06, sphingomyelin 0.13, cholesterol 0.5	Monolayer	• NR – structural analysis • NR – compositional analysis • BAM • Langmuir titration

Ultra-pure water was generated by passing deionized water through a Milli-Q unit (total organic content = 4 ppb; resistivity = 18 mΩ·cm, Milli-Q, Merck KGaA, Darmstadt, Germany). D_2O (99.9% of isotopical purity) was purchased from Sigma-Aldrich and used as received. Experiments were performed in HEPES-NaCl (5 mM HEPES pH 7, 150 mM sodium chloride). A buffer solution of MES-NaCl (10 mM MES pH 5, 150 mM sodium chloride) was also employed. HEPES (in solution, 1 M in H_2O, and powder, purity≥99.5%), MES (powder, purity≥99%), sodium chloride (purity≥99.0%), calcium chloride (anhydrous, granular, ≤7.0 mm, ≥93.0%), ethylenediaminetetraacetic acid (EDTA, purity 99.4-100.6%) were purchased from Sigma Aldrich (Saint Louis, MO, USA).

2.3. Langmuir trough experiments and determination of the binding affinity

A Langmuir trough with a maximum area of 166.4 cm^2 equipped with two symmetric barriers (Kibron, Helsinki, Finland) was used to measure the surface pressure (Π) - area isotherm of lipid monolayers. Π is recorded using a Wilhelmy plate made of filter paper (Whatman CHR1 chromatography paper). Once obtained the compression isotherm of the monolayer, its compressional elastic modulus (C_s^{-1}) was calculated according to the following expression

$$C_s^{-1} = -A \cdot \left(\frac{\partial \Pi}{\partial A}\right) \quad \textbf{7.1}$$

where A is area per molecule. The subphase used was made of HEPES-NaCl buffer pH (120 mL) and the temperature was maintained at 21.0 ± 0.5 °C.

A home-made teflon trough with a total area of 106 cm^2 was used to determine the peptides binding affinity. After careful cleaning, the trough was filled with the buffer (HEPES 5mM, NaCl 150mM), and a 0.2 $mg \cdot mL^{-1}$ lipid solution in chloroform was spread over the subphase using a Hamilton micro-syringe to achieve an initial surface pressure of 22±1 $mN \cdot m^{-1}$, to mimic the outer leaflet of the plasma membrane. The subphase temperature was maintained at 21.5 ± 0.5 °C by making thermostatic water flow through jackets at the bottom of the trough. After the evaporation of the chloroform and the stabilization of the monolayer, peptides were injected underneath the lipid monolayer in the bulk phase. The binding constant of the peptides with the lipid monolayer was calculated by measuring the increase in pressure, $\Delta\Pi = \Pi_\infty - \Pi_0$, observed after the injection of the peptides in the bulk phase, Π_0 = 22±1 $mN \cdot m^{-1}$, until the surface pressure reached a plateau, Π_∞. The differences in the surface pressure ΔΠ, which depend on the amount of peptide injected, were normalized with respect to the maximum value of difference obtained ($\Delta\Pi_{max}$). The obtained

$\Delta\Pi/\Delta\Pi_{max}$ versus peptide concentration profiles were analyzed with a Langmuir adsorption model based on an adsorption equilibrium equation and mass balance between the monolayer and the FPs, assuming that the degree of normalized surface pressure increase is proportional only to the coverage fraction of peptides interacting with the monolayer (φ):

$$\varphi = \frac{\Delta\Pi}{\Delta\Pi_{max}} = \frac{C^n}{C^n + K_D} \quad \textbf{7.2}$$

where C is the bulk concentration of the peptide, n is the Hill coefficient and K_D is a dissociation constant[23].

2.4. Synthetic lipid vesicles for supported lipid bilayer (SLB) studies

Small unilamellar vesicles (SUV) were prepared by dissolving POPC, POPS and cholesterol in chloroform, mixing according to desired membrane composition, *i.e.*, 3:1:1 molar ratio, respectively, as previously described in the Fusion Peptide literature[19,20] (**Table 7.2**), dried under gentle Argon flow and placed in vacuum overnight to ensure evaporation of all solvent. The resulting lipid films were rehydrated at room temperature in buffer at up to 1 $mg \cdot mL^{-1}$ lipid concentration, and vortexed to fully suspend vesicles. Immediately before use for SLB formation, the suspension was tip sonicated for 5 min at pulses of 1 s on/off to produce a visually clear solution of SUVs. SLB formed from vesicle fusion on the surface.

2.5. Circular Dichroism (CD)

Measurements were performed on a Jasco J-810 spectropolarimeter. Spectra with a band width of 2 nm, an acquisition speed of 50 $nm \cdot min^{-1}$ and an integration time of 1 s were collected using 0.1 cm pathlength cuvettes. Peptides at a final concentration of 29 μM in 10 mM phosphate buffer pH = 7, in the presence and absence of 100 nm pore size extruded SUVs (1:100 peptide:lipid mole ratio) were analyzed. Blanks, i.e. the phosphate buffer spectrum, as well as the purely liposome spectrum, were also measured. Raw millidegree data were converted to molar ellipticity. It was not possible to obtain interpretable CD spectra for FP2, as the peptide at 29 μM aggregated in solution.

2.6. Brewster Angle Microscopy (BAM)

In situ visualization of the morphology of Langmuir monolayers at the air/water interface was performed using a BAM Nanofilm EP3 (Accurion, GmgH, Goettigen, Germany). The instrument was equipped with a 50 mW laser emitting p-polarized light at a wavelength 532 nm

directly onto the air/water interface at the Brewster angle (53.1°) and a 10x magnification objective and a polarizer[24]. The reflected light is captured by a CCD camera. The spatial resolution was 2 μm and the field of view 350 x 275 μm^2.

2.7. Neutron reflectometry (NR)

Experiments were performed on the time-of-flight reflectometer FIGARO[25] at the ILL. Two different angles of incidence (0.62° and 3.8°, for Langmuir monolayers and 0.8° and 3.2°, for solid supported lipid bilayers) and a wavelength resolution of 7% $d\lambda/\lambda$, yielding a momentum transfer, $Q_z=(4\pi/\lambda)\sin\theta$, range from 0.007 to 0.25 A^{-1} (the upper limit being limited by sample background) were used to perform the measurements and investigate the structure of the lipid monolayers and bilayers upon peptide interaction. Lipid monolayers were prepared in a Langmuir trough at a surface pressure of $\Pi=22\pm1$ $mN\cdot m^{-1}$. After NR measurements of the lipid monolayer, peptides were injected under the monolayer by a Hamilton syringe to a final bulk concentration of 3 μM. Two different isotopic solvent contrasts (100% D_2O and 8.1% D_2O *v/v* respectively) were used for the characterization. For NR experiments on SLB, solid/liquid flow cells available at the ILL with polished silicon crystals (111) with a surface area of 5×8 cm^2 were used. Substrate surfaces were characterized in 2 different isotopic solvent contrasts, (100% H_2O and 100% D_2O *v/v*), before SLB formation. The membranes were subsequently characterized in at least 3 isotopic solvent contrasts (100% H_2O, 100% D_2O and 38% D_2O *v/v* buffers). The NR data were reduced and normalized using COSMOS[26]. Compositional analysis of FP embedded monolayer were performed exploiting the low-Q_z approach ($0.01<Q_z<0.03$ A^{-1}) using only the smallest angle of incidence (0.62°). This approach directly provides the amount of material present at the interface, by using different lipid isotopic contrasts (*i.e.*, hydrogenous and perdeuterated lipids in the case of PM; hydrogenous phospholipids-deuterated cholesterol, deuterated phospholipids-hydrogenous cholesterol and deuterated phospholipids-deuterated cholesterol for the synthetic mixture). Data analysis was performed using AuroreNR[27] and Motofit[28] software (**Supporting Information**).

3. Results

3.1. A biomimetic plasma membrane.

To better mimic the real picture of the infection, relying on the interaction of the Spike protein with the plasma membrane (PM), a model membrane that could well replicate the latter

was exploited. This PM (**Table 7.2**) biomimetic model membrane has been already introduced in **Chapter 4**, and its out-of-plane structure, as well as its in-plane organization, studied. Here we reported again panels showing the compression isotherm (**Figure 7.1 A**) alongside with the rigidity modulus profile, calculated following **Equation 7.1** (**Figure 7.1 B**), a BAM image at Π=22 $mN \cdot m^{-1}$ (**Figure 7.1 C**) and the volume fraction profile calculated from the NR results (**Figure 7.1 D**).

At a surface pressure of Π≈22 $mN \cdot m^{-1}$, before the rapid increase in rigidity of the monolayer, the in-plane structure of the PM monolayer obtained by BAM shows the coexistence of a densely packed liquid-ordered (L_o) phase (cholesterol-rich, brighter regions) and liquid-disordered (L_d) domains with a high lateral diffusion of lipids (**Figure 7.1 C**). The observed phase separation in lipid-only membranes was previously reported by several laboratories (as reviewed by Marsh[29]). The vertical structure of PM, perpendicular to the plane of the interface, was determined by NR analysis of hydrogenous and deuterated PM lipid monolayers in two different D_2O buffers (**Figure S7.1** and **Table S7.3**). As already reported in **Chapter 4** of this PhD thesis, PM monolayers were effectively modelled as two layers: the 16±1Å long aliphatic lipid tails, which are exposed to air, and the 8±1Å lipid headgroups, in contact with the buffer. The mean area per phospholipid molecule (APM) obtained was ~60 $Å^2$, which is similar to the value determined from the pressure-area isotherm and is also consistent with a compact lipid bilayer[30,31]. From the neutron scattering length density (SLD) distribution (**Figure S7.1**), the volume fraction of the different PM components could be determined (**Figure 7.1 D**). The cholesterol molecules are confined to the aliphatic tails-layer, with no solvent present. A solvent penetration of 63% occurs in the headgroups-layer. **Figure 7.1** report the compression isotherm and rigidity modulus of PM monolayer, alongside with a BAM image corresponding to a pressure of 22 $mN \cdot m^{-1}$ and the volume fraction profile that details the out-of-plane structure of the monolayer.

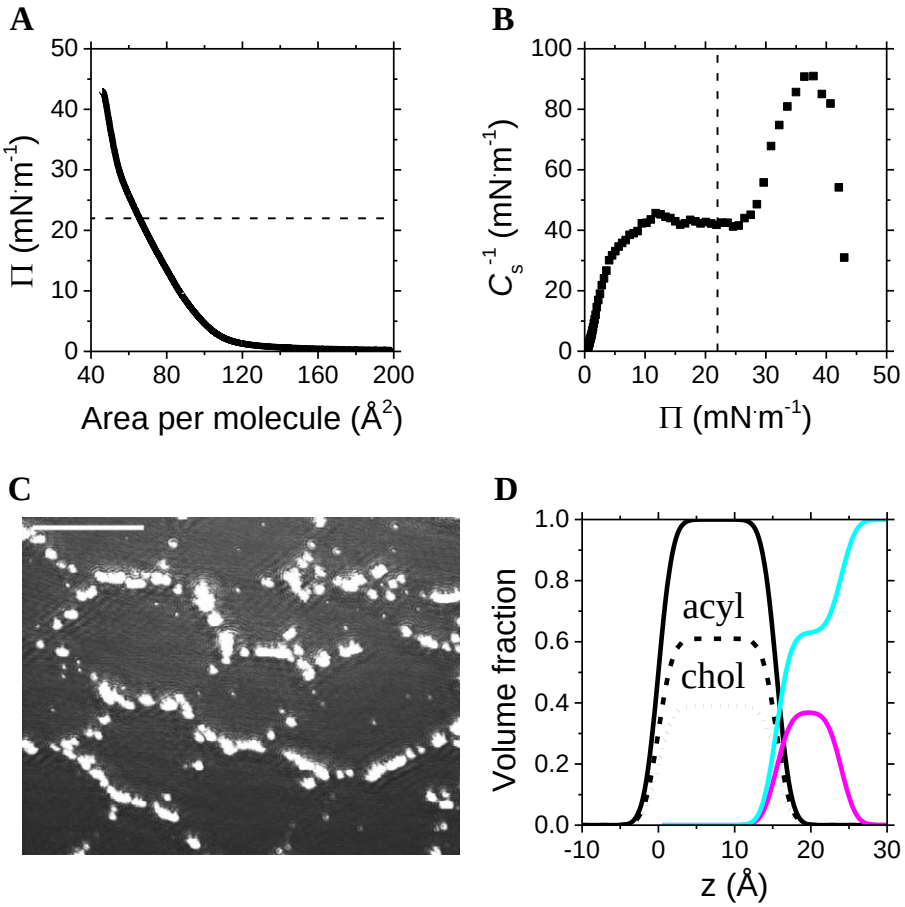

Figure 7.1 A Surface pressure (Π) - area isotherm of hydrogenous PM monolayer and **B** related compressibility modulus. The dashed line indicates the pressure 22 mN·m^{-1}. **C** BAM images of PM monolayer at Π=22 mN·m^{-1}. Bright spots represent cholesterol domains. Scale bar is 100 µm. **D** Volume fraction profile normal to the interface of PM monolayer to highlight the distribution of tails (black) and heads (magenta). The water distribution is shown in cyan.

Solid-supported lipid bilayers subsequently analysed by NR revealed a similar membrane organization, with the cholesterol integrated into the tails-layer. This was also observed in unilamellar vesicles of DOPC-cholesterol membranes[32]. The average area per phospholipid molecule obtained (from 53 to 59Å^2) and the total thickness of 47±2Å agrees with similar systems studied[33]. The coverage was not less than 85% confirming high lipid coverage (**Table S7.5**).

3.2. Interaction of FP1, FP2, FP3 and FP4 with the PM

In the Langmuir trough, the injection of either FP1, FP2, FP3 or FP4 into the bulk buffer underneath the PM monolayer gives rise to an immediate and rapid increase in surface pressure, followed by a slower increase until a plateau is reached typically several hours later (**Figure 7.2 A**). FP3 had the weakest effect, so was not characterized further. The obtained pressure increment (ΔΠ) for FP1, FP2 and FP4, in the presence of 3 µM peptide in the bulk buffer, is plotted in **Figure**

7.2 B. The binding affinity of the different FPs was therefore determined using the Hill-Langmuir model (**Equation 7.2**), by monitoring the resulting change in surface pressure when different amount of FPs were injected underneath the monolayer (**Figure 7.2 C** and **Table 7.3**). Uncharged FP2 had a dissociation constant K_D of 14±8 μM (Hill coefficient, n, of 1.9±0.5). The K_D of FP1 was 0.9±0.1 μM (n=0.61±0.06). An n<1 indicates negative cooperative binding. It may be due to FP1 overall negative charge at physiological pH, which is not counterbalanced on binding the non-negligible amounts of negatively charged PS lipids in the PM outer leaflet[34]. FP4 had the highest affinity to the PM. Its K_D was 80±10 nM, with n=1.6±0.1 (thus>1), indicating a positively cooperative binding, possibly due to FP4 positive charge at acidic and physiological pH being compensated by binding negatively charged PM. **Figure 7.2 C** also shows the fit obtained if the Hill coefficient was set to 1 (dashed curves), which resulted to be a worse model for the experimental data. The resulting binding free energy $\Delta G = RT\ln\left(\frac{K_D}{c}\right)$, where R is the ideal gas constant, T is the temperature and *c* the standard reference concentration (1 M), of FP1, FP2 and FP4 to PM monolayer were 8.2 kcal·mol^{-1}, 6.6 kcal·mol^{-1}, 9.7 kcal·mol^{-1}, respectively (**Table 7.3**).

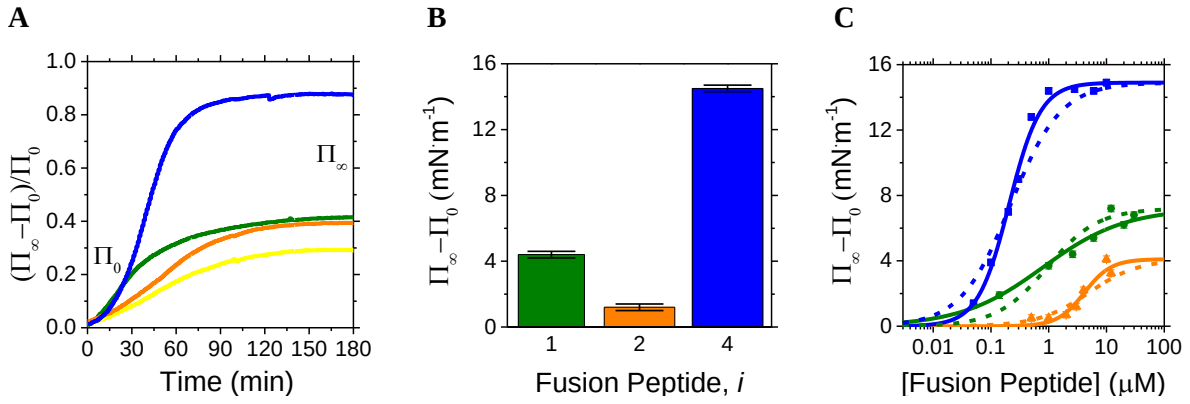

Figure 7.2 A Changes in normalized surface pressure upon FPs interaction with PM monolayers. Data for FP1, FP2, FP3 and FP4 are respectively colored green, orange, yellow and blue. **B** Uppermost surface pressure increment due to the interaction of FP1, FP2, and FP4 with a PM monolayer, at 3μM peptide concentration and Π_0=22± 1 mN.m^{-1}. The increment in the pressure, ΔΠ, is proportional to the amount of peptide partitioning with the monolayer at the air/water interface. **C** Equilibrium analyses and resultant K_Ds for FP1 (green), FP2 (orange) and FP4 (blue) binding to PM. Lines are fits to the data obtained through the Hill-Langmuir equation (**Equation 7.2**). The dashed lines indicate the fits of the experimental data with the Hill coefficient set to 1.

Table 7.3 Values of dissociation constant (K_Ds), Hill coefficient (n) and resulting binding free energy (ΔG).

	FP1	**FP2**	**FP4**
K_D (μM)	0.9 ± 0.1	14 ± 8	0.08 ± 0.01
n	0.6 ± 0.1	1.9 ± 0.5	1.60 ± 0.10
ΔG (kcal·mol^{-1})	8.2	6.6	9.7

The L_o/L_d coexistence in the PM liquid expanded phase, visible in the BAM image, was clearly perturbed by the presence of either FP1 or FP4 (**Figure 7.3 A** and **B**, respectively). The former yields a change in the in-plane morphology where bright spots, potentially representing cholesterol clusters, are now isolated but surrounded by clearly visible domains. In the case of FP4, the resultant bright spots are still interconnected and surrounded by more homogeneous regions. Moreover, in the presence of cholesterol-rich liposomes, the decrease in CD signal between 220nm and 235nm indicates the presence of increased secondary structure for FP1 and FP4 peptides (**Figure 7.3 C**)**.** These observations were previously noted for FP1 with liposomes and for sections of FP1 and FP4 in the lipid mimetic trifluoroethanol[19,35].

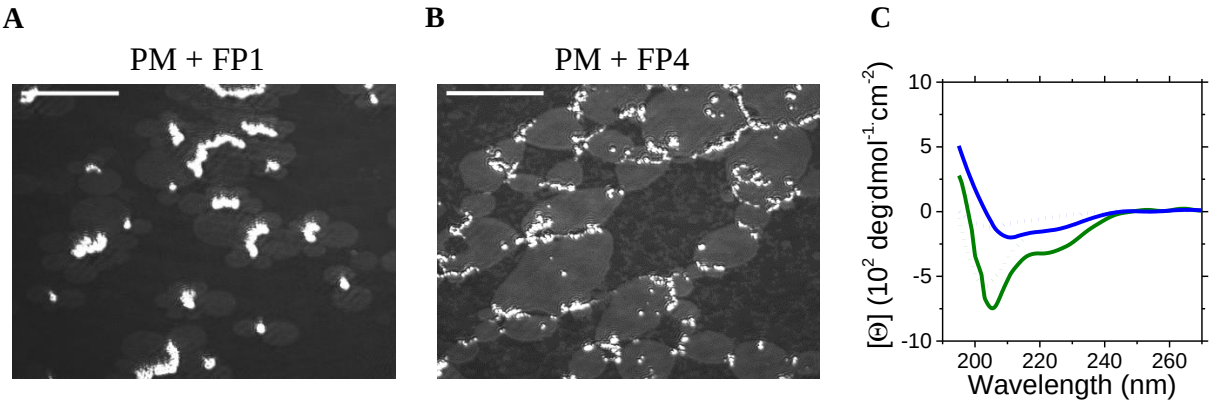

Figure 7.3 BAM images of the PM monolayer after injection of **A** FP1 or **B** FP4. Scale bars are 100 μm. **C** Molar ellipticity profiles of FP1 (green) and FP4 (blue), in the absence (dotted line) and presence of liposomes (continuous line). The decrease in signal in the presence of lipids suggests a related increase in protein secondary structure.

3.3. FP1 buries deep into the PM, while FP2 and FP4 bind lipid headgroups

Due to the weak effect of FP3 on the PM monolayer, NR experiments focused on FP1, FP2 and FP4. **Figure S7.1** shows the reflectivity profiles measured at 4 different isotopic contrasts after the binding of the peptides to the PM monolayer. Data modeling was performed by simultaneously fitting all contrasts to obtain a single set of structural parameters that allow us to determine the volume fraction of peptide partitioning into the lipids (see and **Table S7.5**). Two-layer models,

which included the partition of the FPs into the aliphatic lipid tails and lipid polar headgroups, were adequate to describe the experimental data. Including in the model a third layer for the peptides yielded a worse fit of the data and suggested that the interaction of FP1, FP2 and FP4 with the membrane is not due to a physisorption of the peptides, but rather to their insertion directly into the lipid monolayer.

The bound FP1 is found distributed across the entire PM monolayer, as it is present in both the lipid headgroups (6±1%) and aliphatic tails (7±1%) (**Figure 7.4 A**). In contrast, FP2 and FP4 had a negligible presence in the acyl region (**Figure 7.4 B** and **C**), but interacted more strongly within the lipid headgroups region (17% for FP2 and 25% for FP4), where significant decreases in hydration were observed (**Figure 7.4 D**). Similarly, ESEEM spectroscopy indicated that the SARS-Cov-2 891-906 region within FP4 dehydrates spin-labelled POPC/POPG membranes[36].

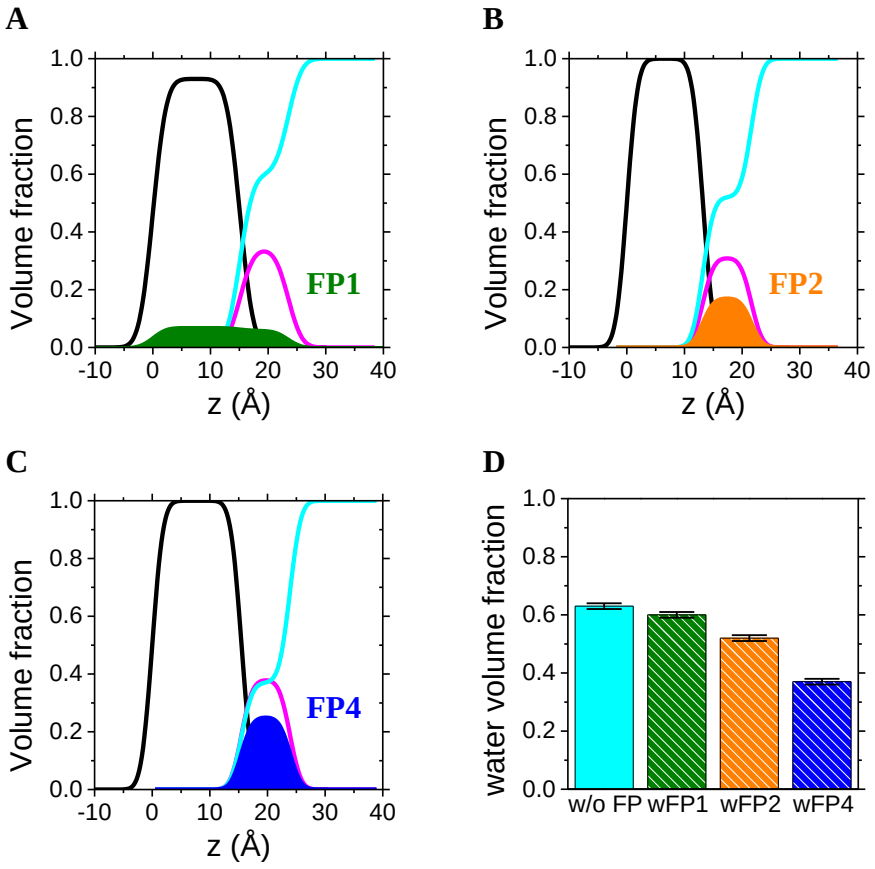

Figure 7.4 Volume fraction profiles normal to the interface of PM monolayers (derived from data plotted in **Figure S7.2**) highlight the distribution of tails (black), heads (magenta), water (cyan) and **A** FP1 (green), **B** FP2 (orange) and **C** FP4 (blue). **D** Bar diagram plot summarizing the volume fraction occupied by the solvent in the lipid headgroups-layer of the PM monolayers without any peptide and with FP1, FP2 and FP4.

Due to the manner in which FP1, FP2 and FP4 partitioned into the lipid monolayer, solid-supported bilayers, composed of synthetic lipids enriched in cholesterol, were also investigated (**Figure S7.3** shows the reflectivity profiles). According to the results obtained here, bilayer integrity is conserved after FP binding (see **Figures S7.3, S7.4** and **S7.5** and **Table S7.5**), although as previously observed in the interaction of the Spike extra cellular domain with lipid bilayers[37], surface coverage was reduced. Again, the best-fit model did not require an additional peptide-rich layer. The changes observed in the tail region of the bilayer after the addition of FP1 (**Figure 7.5 B**) are compatible with the partition of the peptide into the outer leaflet acyl region (4%). FP2 and FP4 (**Figure 7.5 C** and **D**, respectively) are still positioned within the outer headgroups (3% in both cases) although for FP4, its presence is also detected in the outer lipid acyl region (4%). The inner leaflet showed neither FP1, FP2 nor FP4 insertion.

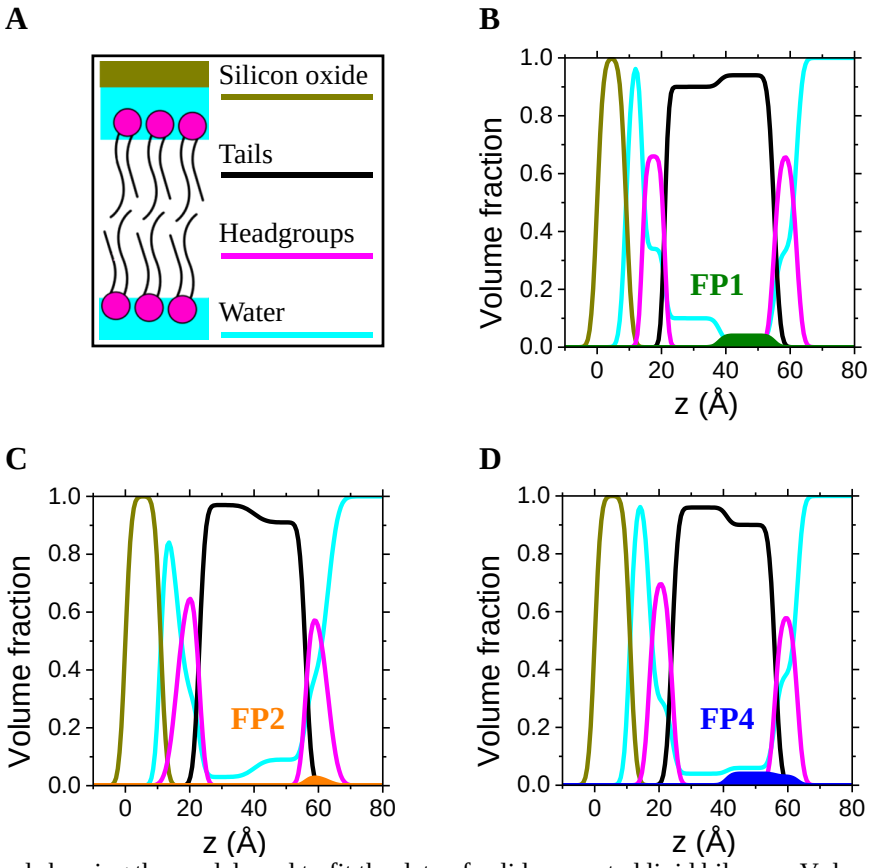

Figure 7.5 A legend showing the model used to fit the data of solid supported lipid bilayers. Volume fraction profiles of solid supported lipid bilayers in the absence of Ca^{2+} (derived from data plotted in **Figure S7.3**) highlight the distribution of Si/SO_2 (dark yellow), tails (black), heads (magenta), water (cyan) and **B** FP1 (green), **C** FP2 (orange), **D** FP4 (blue).

3.4. Calcium induces formation of a transmembrane FP1 across cholesterol-enriched lipid bilayers

The presence of calcium increases the membrane ordering effect of SARS-CoV-2 FP1-2[14,20], but also decreases the rate of FP1-induced vesicle fusion and ability to mediate lipid mixing[16]. To this end, we studied the binding of FP1 and of FP2 in presence of Ca^{2+} (**Figure 7.6**) and we found that, although FP2 still bound within the lipid headgroups region, the partition of FP1 into the membrane bilayer drastically changed. In 2 mM Ca^{2+} containing buffer solution, bound FP1 peptide was no longer limited to the outer leaflet but distributed across the whole lipid bilayer with 7% and 4% peptide in the outer and inner lipid tails region, respectively, and 12% and 3% in both the outer and inner headgroups-layer (**Figure 7.6 B**). At a higher Ca^{2+} concentration (10 mM), an increase in the solvent fraction in both leaflets, from 34 to 43% solvent in the headgroups region but also from 8% to 18% in the tail regions was also observed (**Figure 7.6 C**), and FP1 was distributed in both the tail region (8%) and headgroups regions, inner and outer (3%). Subsequently, adding the chelating agent EDTA (**Figure 7.6 D**) to the buffer solution to remove Ca^{2+} clearly reduced the amount of FP1 partitioned into the bilayer inner leaflet, whilst only slightly affecting the amount of FP1 partitioned in the outer tail region (7%). The FP1 proportion in the outer headgroups region slightly increased from 3 to 4%. These data suggest that FP1 forms a calcium-dependent transmembrane peptide across the bilayer. When calcium is absent or removed by chelation, FP1 would only insert into the bilayer outer leaflet. These NR data also support the hypothesis that FP1 induces lipid reorganization. Upon removal of the calcium, the best fit bilayer model results in a significant increase in solvent percentage in the lipid tail region (from 17% to 30%).

In the case of FP2, in the presence of 2 mM Ca^{2+}, whilst no FP2 is observed in either the tails region or in the inner headgroups-layer, there is a significant increase in peptide bound in the outer headgroups-layer, from 3% to 24% (**Figure 7.6 B**), which is tentatively linked to an increase in affinity to the negatively charged bilayer[34]. The increased peptide coverage to levels observed for FP2 and FP4 in monolayers was also linked to dehydration of the outer leaflet headgroups-layer. However, with lower FP2 and FP4 coverage, a relative increase in solvation in the outer leaflet acyl region, compared to the inner leaflet acyl region, is found instead. These data suggest lower levels of bound FP2 and FP4 render the membrane hydrophobic core accessible, while at higher peptide concentrations, the membrane would become dehydrated. Nonetheless, both cases

would result in a membrane more prone to fusion. **Table S7.5** reports all the volume fractions values.

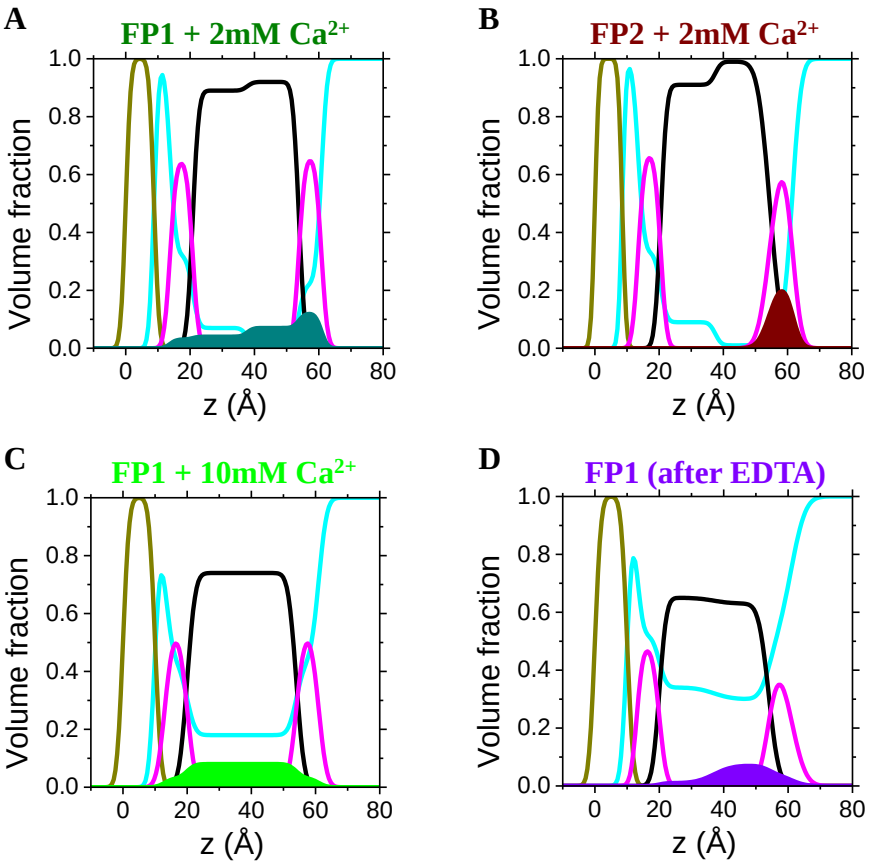

Figure 7.6 Volume fraction profiles of solid supported lipid bilayer (derived from data plotted in **Figure S7.4** and **S7.5**) with **A** FP1 in the presence of 2 mM Ca^{2+} (dark cyan), **B** FP2 in the presence of 2 mM Ca^{2+} (wine), **C** FP1 in the presence of 10 mM Ca^{2+} (light green), **D** FP1 after over-night incubation with EDTA (violet).

3.5. Compositional analysis of FPs-embedded monolayers

In order to investigate the interaction of FP1, FP2 and FP4 with Langmuir monolayer at different values of surface pressure, PM lipid composition in chloroform containing 5% in mol FPs were employed, *i.e.*, a ratio FP:lipid of 1:20. Although this methodology does not represent the real binding between the Spike protein and the cell membrane, it allows depositing FPs-embedded monolayers in which the peptide partitions with the lipids, permitting to evaluate the composition of the film present at the air/water interface at any wanted surface pressure, without waiting for the binding kinetics. To this end, compression isotherms were performed and combined with the NR low-Q_z approach[38], for which hydrogenous and fully deuterated lipids (PM) were used. Thus, the smallest angle of incidence was exploited in the NR measurements (see **Methods**), obtaining a Q_z range from 0.01 to 0.03 $Å^{-1}$ (**Figure S7.6** and **Figure S7.7**). In this range, reflectivity

data are particularly sensitive to the amount of material present at the interface. Thus this method allowed the determination of the surface excess of lipids and peptides, from which we calculated the molar % of each specie (**Table S7.7**). **Figure 7.7** shows the compression isotherms and compressibility moduli of purely PM monolayer and PM+FP monolayers plotted versus the trough area. When the peptides are present in the sample and partition at the air/water interface, the isotherm is clearly shifted towards higher values of area, especially for what it regards FP1 and FP4. Moreover, multiple slope changes are visible in the compression isotherms. Here, there is a change in composition/structure of the monolayer due to the compression. This changes are correlated to local minima in the compression modulus profiles. These features suggest a rearrangement of the material at the interface that could depend on the expulsion of the peptides from the monolayer. In particular, the presence of FP4 increases the value of compressibility modulus of the monolayer, probably due to its drastic dehydration effect. However, in the case of FP2, although there is clearly more material partitioning at the air/water interface, the compression isotherm tends to superpose the one of purely lipids at low areas. Moreover, the compressibility modulus is only slightly changed by the presence of FP2, presenting a minimum at low values of surface pressure (Π=8 mN·m^{-1}), and then shifting the curve towards lower values of compressibility modulus. Finally, employing the NR low-Q_z approach (**Figure S7.6**) allowed us to determine the percentage of lipids and peptide (**Figure 7.7 C**), which is in agreement with the results obtained from full-Q_z measurement and K_Ds calculation: FP4 is the most abundant at any investigated surface pressure; then FP1 is found with a higher molar fraction than FP2, which is the only one whose volume fraction reaches zero at high pressures (Π=30 mN·m^{-1}).

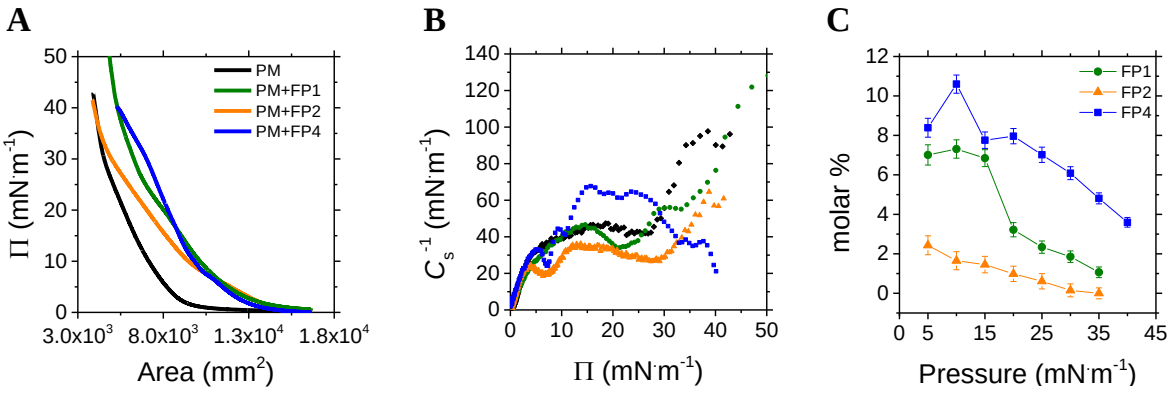

Figure 7.7 A Superimposition of compression isotherms of PM (black line), PM+FP1 (green line), PM+FP2 (orange line) and PM+FP4 (blue line). **B** Respective compressibility modulus profiles of PM (black diamonds), PM+FP1 (green circles), PM+FP2 (orange triangles) and PM+FP4 (blue squares). **C** Molar percentage of FP1 (green circles),

FP2 (orange triangles) and FP4 (blue squares) obtained from low-Q_z measurement (**Table S7.7**), calculated from values reported in **Table S7.6**.

The case of FP2 is particularly interesting. Indeed, it has a net charge of zero (**Table 7.1**), and it is the only one whose concentration in the monolayer tends to zero, when high surface pressures are reached. Moreover, it is interesting to note how its presence reduce the value of the C_s^{-1} of the PM monolayer, despite the retaining of the overall shape by the compressibility modulus curve. This could be explained taking into account a simultaneous effect of softening of the monolayer when the peptide is present, or a possible lipid removal effect. Since the low-Q_z results suggest a very low percentage of FP2 at high pressures, we hypothesized that FP2 is able to remove lipids from the interface, which is in line with the recent finding that the Spike protein remove lipids from solid supported bilayer[37]. However, conversely to the Spike protein, the lipid removal effect of FP2 on solid supported lipid bilayer was not experienced in this work. It is important to underline that the lipid compositions used here is different with respect to the one previously used with the Spike protein, and also the lipid removal activity of the Spike probably derives from a cooperation between different sections of the protein. In this paragraph we exploited the low-Q_z approach to measure eventual variation in the monolayer integrity. To further investigate this, we exploited the POPC:POPS:cholesterol composition, used for bilayer studies, and we evaluated the interaction of FP2 in both acidic (pH=5) and neutral (pH=7) environment. **Figure 7.8 A** shows the compression isotherms of POPC:POPS:cholesterol mixture with and without FP2 at the two different pHs. As already observed in the case of FPs-embedded PM monolayer, the compression tends to force an expulsion of material (possibly FP2) from the interface, thus changing the C_s^{-1} profile of the monolayer by producing local minima at different pressures. Purely lipid monolayer isotherm measured in both pHs show a plateau (semi-plateau at pH=5) at $\Pi \approx 22\text{-}25$ mN·m^{-1}, that corresponds to a minimum in the compressibility modulus profiles. The position of this minimum is influenced by the presence of FP2. In the case of pH=7, the C_s^{-1} minimum is shifted toward higher values of area (**Figure 7.8 B**), before which the rigidity of the monolayer is slightly increased, followed by a reduction at higher values of area. Moreover, a new local minimum at $\Pi \approx 8$ mN·m^{-1} is observed, which is only present at the first compression isotherm (**Figure 7.9**), thus suggesting an expulsion of the peptide from the monolayer at higher compression states. At pH=5, multiple local minima can be observed in the C_s^{-1} curve at $\Pi=10$ mN·m^{-1}, $\Pi=22$ mN·m^{-1} (similar to the one of purely lipid monolayer) and $\Pi=27$ mN·m^{-1}, which are retained even after the first compression isotherm (**Figure 7.9**). Anyway, even in this case the rigidity at high values of area

is reduced by the presence of FP2. To assess whether this phenomenon is ascribable to a softening effect of FP2, or the removal of lipids from the monolayer, the NR low-Q_z approach was employed with this lipid composition at pH=7 (**Figure S7.7**). This allowed us to determine if FP2 prefers to remove phospholipids or cholesterol. The results obtained and plotted in **Figure 7.8 C** show a reduction in the relative amount of cholesterol partitioning at the interface, with respect to the amount of cholesterol present in the purely lipid monolayer (see full symbols with respect to empty ones).

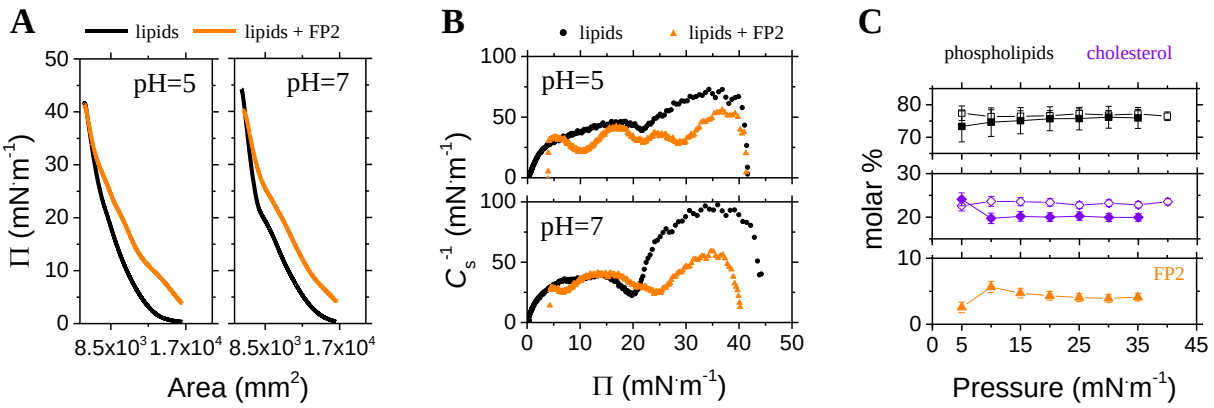

Figure 7.8 A Superimposition of compression isotherms of purely POPC:POPS:cholesterol (black line) and POPC:POPS:cholesterol+5%FP2 (orange line) monolayers at pH=5 and 7. **B** Respective compressibility moduli at the two pHs. **C** molar percentage obtained from the NR low-Q_z approach data analysis. Data related to phospholipids (POPC and POPS), cholesterol and FP2 are shown as black squares, violet diamonds and orange triangles, respectively. Phospholipids and cholesterol data related to the purely lipids monolayer are shown as empty symbols.

It is also interesting to note that performing multiple cycles of compression-expansion (**Figure 7.9**), results in a progressive expulsion of the peptide from the interface, followed by a slight increase in the membrane compressibility modulus.

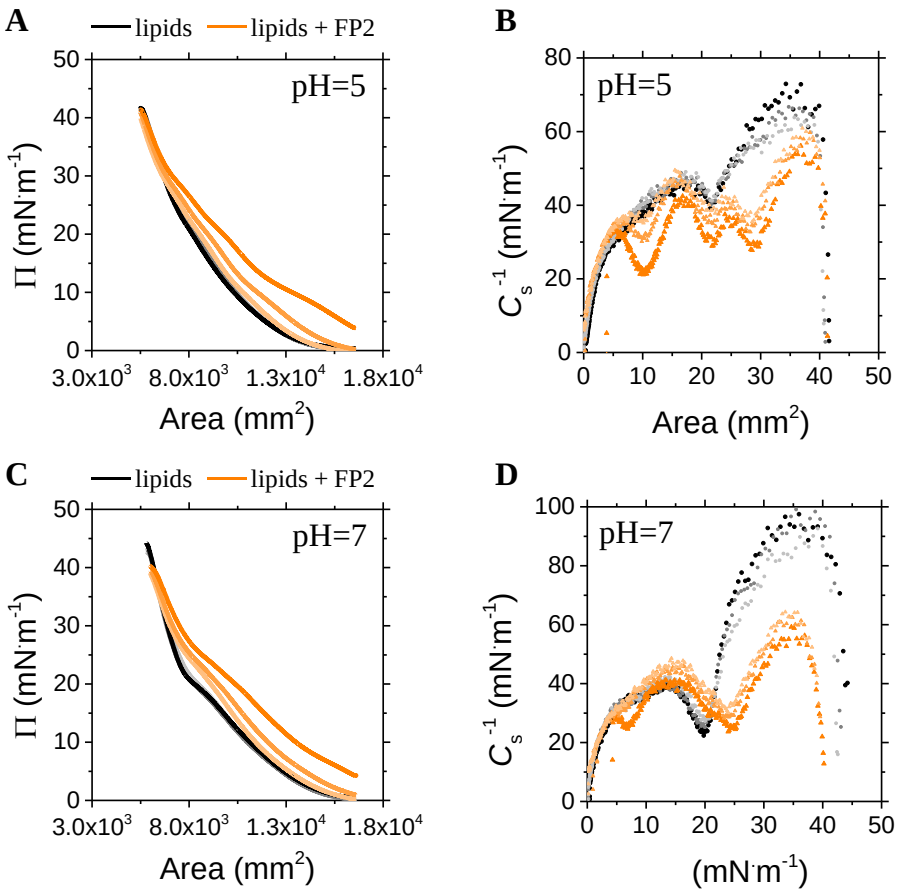

Figure 7.9 Three compression-expansion cycles at the two pHs. Cycles related to purely lipid monolayers and FP2-embedded monolayers are shown as black lines and orange lines at **A** pH=5 and **C** pH=7, respectively. Compressibility modulus curves related to purely lipid monolayers and FP2-embedded monolayers are shown as black circles and orange triangles at **B** pH=5 and **D** pH=7, respectively. The second and third isotherms are shown as gradually lighter color.

Finally, the effect of calcium ions on POPC:POPS:cholesterol + FP2 monolayer was investigated. After the compression isotherms, a solution of calcium chloride was injected in bulk to obtain an overall calcium concentration of 1 mM in the bulk phase. Three compression-expansion cycles were performed (**Figure 7.10**).

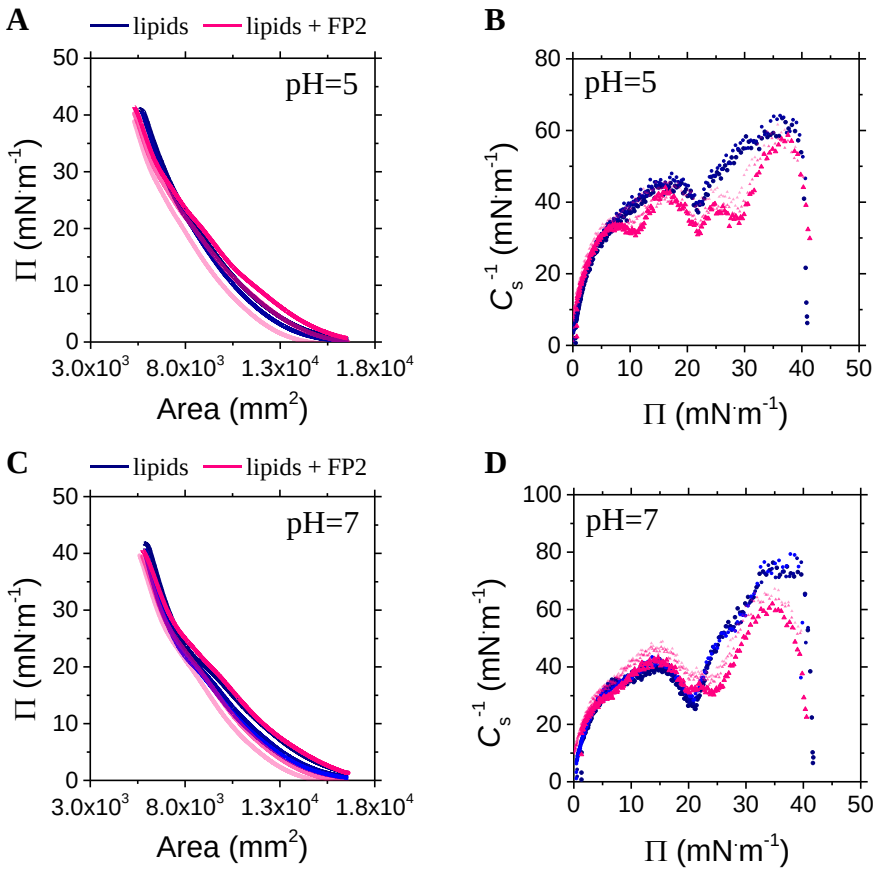

Figure 7.10 Three compression-expansion cycles at the two pHs after Ca^{2+} injection. Cycles related to purely lipid monolayers and FP2-embedded monolayers are shown as blue lines and pink lines at **A** pH=5 and **C** pH=7, respectively. Compressibility modulus curves related to purely lipid monolayers and FP2-embedded monolayers are shown as blue circles and pink triangles at **B** pH=5 and **D** pH=7, respectively. The second and third isotherms are shown as gradually lighter color.

Although full-Q_z measurements with supported lipid bilayers show that calcium increases FP2 binding (at 2 mM Ca^{2+}), the isotherms shown in **Figure 7.10 A** and **C** demonstrate that it does not influence the dynamic behavior of the monolayers. The overall shape of isotherms and the compressibility modulus curves (**Figure 7.10 B** and **D**) are not influenced by the presence of Ca^{2+} ions, being similar to the ones shown in **Figure 7.9**. The only visible effect produced is a slight shift towards higher values of area for the first compression after Ca^{2+} injection (**Figure 7.11**), since divalent cations increase lateral compressibility as well as permeability of the monolayer[39–41]. **Figure 7.11** shows the superimposition, at both pHs, of the first compression isotherm before and after Ca^{2+} injection, and related compressibility modulus profiles.

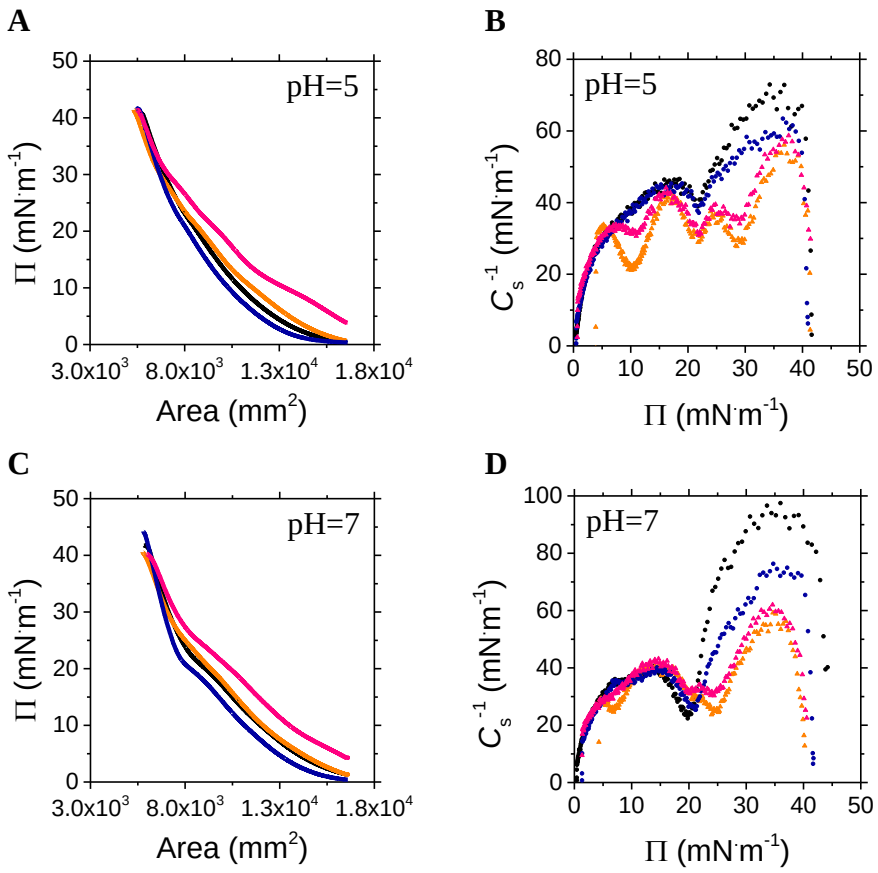

Figure 7.11 Superimposition of first compression isotherms without and with Ca^{2+}. Isotherms related to purely lipid monolayers and FP2-embedded monolayers before Ca^{2+} injection are shown as black lines and orange lines at **A** pH=5 and **C** pH=7, respectively. Isotherms related to purely lipid monolayers and FP2-embedded monolayers after Ca^{2+} injection are shown as blue lines and pink lines at **A** pH=5 and **C** pH=7, respectively. Compressibility modulus curves related to purely lipid monolayers and FP2-embedded monolayers before Ca^{2+} injection are shown as black circles and orange triangles at **B** pH=5 and **D** pH=7, respectively. Compressibility modulus curves related to purely lipid monolayers and FP2-embedded monolayers after Ca^{2+} injection are shown as blue circles and pink triangles at **B** pH=5 and **D** pH=7, respectively.

4. Discussion

SARS-CoV-2 fusion peptides FP1, FP2 and FP4 behave in a striking different manner in the presence of membranes. Fusogenic activity does not necessarily have to occur through membrane disruption but can be simply achieved by the close association of two membranes. By binding with greater affinity to the lipid headgroups, FP4 is better able than FP2 to bridge two bilayers together. In either case, the observed dehydration of the lipid headgroups at high peptide concentration would promote membrane fusion. Dehydration was for example found to be the rate-limiting step in SNARE-assisted membrane fusion[42]. The kinetic barrier to hemifusion is generally estimated to exceed 50 kcal·mol^{-1} [9]. The binding free energy for association of a single FP4 with a lipid bilayer

is ~10 kcal·mol^{-1}, so the pull on a Spike trimer consisting of three FP4 would be ~30 kcal·mol^{-1}. The kinetic barrier can therefore be overcome upon binding two Spike trimers.

The outcomes of this work, and parallel small-angle neutron scattering (SANS), quasi-elastic neutron scattering (QENS) and neutron spin eco (NSE) experiments[43], pointed out that FP1 disrupts the membrane as the peptide penetrates into the hydrophobic acyl region, and increases the dynamics of the lipid tails on a picosecond time and Angstrom length scale. This increase in alkyl chain fluidity, also observed through dynamic measurements with PM lipid monolayers, is consistent with previous observations of lipid disordering that might be associated with a subsequent weakening of lipid membranes (*e.g.*, more prone to rupture), as an effect of lipid-FP interactions. This weakening of lipid membranes has previously been interpreted as a first step towards viral penetration into the host cell[44]. On the nanosecond time scale probed by NSE at low FP1 concentrations in the absence of calcium, an increase in membrane flexibility is more pronounced in the presence of cholesterol-rich PM. A phenomenon also observed by QENS. However, at increased FP1 concentrations, NSE indicates the SUVs membrane rigidity increases, which could be analogous to the increase in local membrane ordering in multi-lamellar vesicles identified by electron spin resonance spectroscopy[14,20]. These effects could possibly be due to the FP1-driven membrane stacking in the absence of calcium, which was observed in the SANS data. A membrane consisting of several bilayers is simply more rigid than a single bilayer.

Free Ca^{2+} concentration varies widely depending on its cellular location. At the plasma membrane, outside the cell, [free Ca^{2+}] ~ 2 mM, while in the early and late endosomes [free Ca^{2+}] drops to ~ 0.3 µM[11]. The affinity of SARS-CoV-2 FP1-2 and the related SARS-CoV-1 FP1 to calcium (~30 µM), determined by ITC[14], would suggest that calcium would not be bound to the fusion peptide in the endosome. As with the calcium-dependence in lipid membrane ordering observed by ESR, our NR data show a clear effect of the cation on SARS-CoV-2 FP1 and FP2 binding to bilayer model membranes. The binding efficiency of the latter increases, but more intriguingly, calcium drastically alters the orientation of bound FP1 in the membrane. The intracellular calcium levels may therefore provide an indication to where the viral and host membranes fuse during SARS-CoV-2 infection.

Depending on cell type, the SARS-CoV-2 virus may enter the host cell through the plasma membrane[10], but can also travel through the endosomal pathway[45] (see **Figure 1.10**). Although the

virus may have associated with the host at the plasma membrane, it is unclear where actual S2'-mediated membrane fusion occur. It may even occur in the late endosome[46]. Our structural data show that at the plasma membrane, in the presence of calcium, the FP1 peptide would penetrate the bilayer and form a transmembrane peptide across the membrane (if folded as a single helix, FP1 length would be comparable to the width of the membrane hydrophobic core). Subsequently as free calcium levels drop in the endosome[11], FP1 would re-position itself to the host lipid leaflet in contact with the viral membrane. Finally, FP2 and, especially, FP4 could function as bridges between the host and the viral membrane, with FP2 helping the insertion of FP1 by removing cholesterol from the membrane.

Two competing models have been put forward to explain protein-driven membrane fusion (reviewed in Lindau and Almers[47]). In the "proximity" model, two membranes are brought together by a fusion peptide, like FP4, and the juxtaposed leaflets of each bilayer merge and their lipids mix. In the "fusion pore" model, initially proposed by Pfenninger[48], membrane hemifusion is initiated by the creation of an aqueous channel, which is tentatively observed for FP1 in the presence of calcium at the PM. Our structural data from NR and SANS[43] show FP1 can associate and consequently possibly puncture through the viral membrane, thereby fusion initiation points occur in both the PM and viral membranes. The initiation points would subsequently expand to allow lipids to travel along the amphipathic fusion peptide and diffuse between the two membranes (**Figure 7.12 A, B**). Importantly, when the influenza haemagglutinin transmembrane domain was replaced by glycolipid anchors, the transfer of fusing membranes occurred at the same rate, even though the viral pore formed solely in the eukaryotic cell membrane[49], so fusion initiation point formation in the viral membrane may not be necessary. By bridging the membranes together, the subsequent role of FP4 and FP1 (after Ca^{2+} removal), would be to bind and dehydrate the two membranes in order to drive the expansion of a hemifusion diaphragm formed between the viral RNA and cellular cytoplasm (**Figure 7.12 C, D, E**). The rest of the S2' domain, due to its extra-membrane bulk, would tentatively be excluded from the interface and be expelled from the contact area formed between the viral and host membranes (**Figure 7.12 F**). It is also possible that initiation points created by FP1 may form on both the viral and the plasma membrane (**Figure 7.12 G**). Any resultant pore linking the two membranes would similarly expand since the Spike protein would be excluded by the two membranes coming together (**Figure 7.12 H**).

In conclusion, this multi-method approach applied to a well parametrized model of the viral protein-host membrane interaction, reveals that different segments of the SARS-CoV-2 Spike protein assume different functions in the initiation of viral infection. Our data are of interest not only in the context of the current Covid-19 pandemic, but also provide a powerful interdisciplinary framework for future investigations of eukaryotic and viral fusion mechanisms.

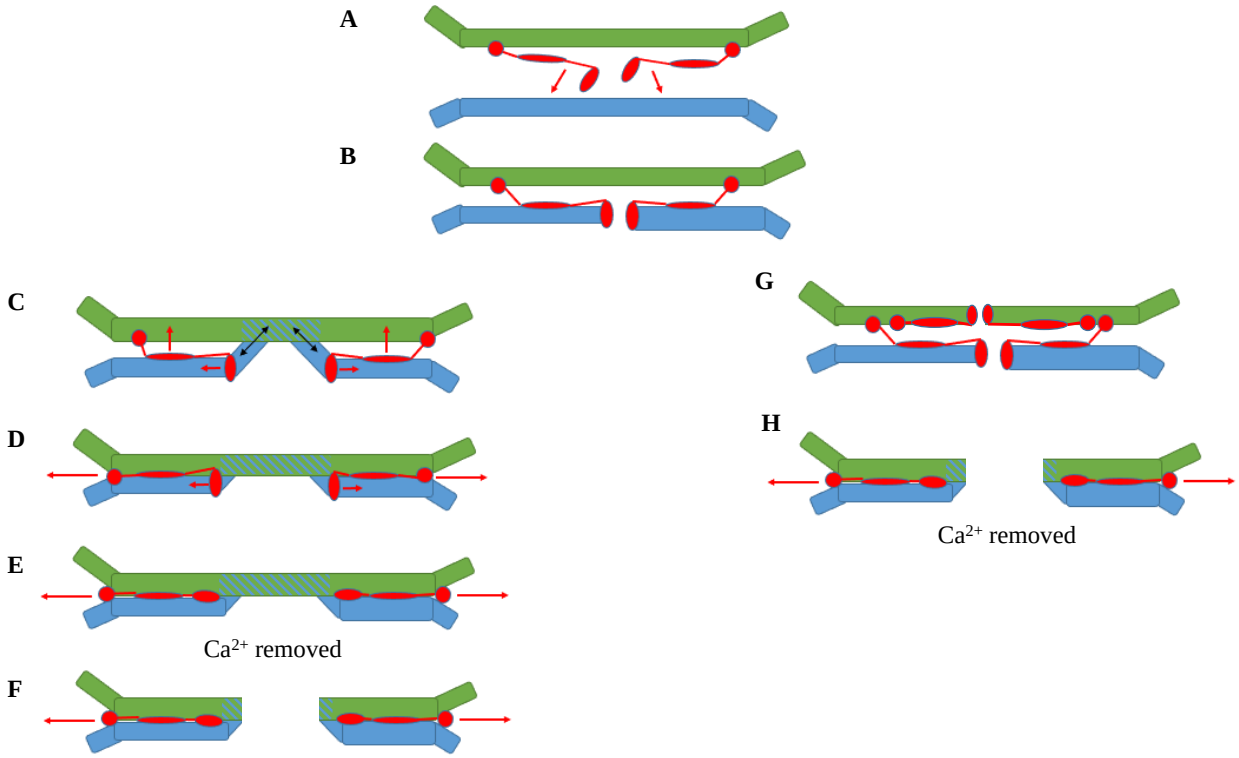

Figure 7.12 Proposed fusion mechanism between SARS-CoV-2 and eukaryotic host membrane. The viral membrane bilayer is colored green, the eukaryotic host membrane in blue, and the S2' protein is in red. The direction of the protein is drawn with red arrows, while the direction of the lipids is drawn with black arrows. FP1and FP4 are represented as ovals, and the structured S2' protein as a circle (attached to the viral membrane). **A** FP1 forms a fusion initiation point on binding the host membrane. **B** The initiation point enlarges provoking lipids mixing between the viral and host membrane, leading to the growth of a hemifusion diaphragm. **C** FP4 bridges the two membranes together thereby facilitating the fusion of the two membranes into a single bilayer. Moreover, the two membranes coming together exclude the folded S2' from the growing synapse. **D, E, F** A hemifusion diaphragm is formed and in the endosome, lower free calcium concentrations lead to FP1 orienting itself like FP4, thereby providing further contact between the two membranes. **G** It is also possible that FP1 initiation points may form on both the viral and the plasma membrane. **H** The two membranes form a pore, and as in **F**, the pore expands as the Spike protein is excluded by the two membranes coming together due to the bridge function encoded in the Spike fusion peptides.

SUPPORTING INFORMATION

Natural lipid extraction and purification for lipid monolayer studies

Biomimetic membranes were prepared from phospholipid mixtures extracted and purified from perdeuterated and hydrogenous *P. pastoris* biomasses. Harvested cells were suspended into 10 mL deionized water and lysed by probe sonication on an ice bath for 3×5 min with 30 s intervals, 20% duty cycle. The resulting cell lysate was poured into boiling ethanol containing 1% butylated hydroxytoluene (BHT) followed by vigorous stirring in order to denature lipases. The total lipid mixtures were then extracted according to the method of Folch et al.[50], followed by evaporation of the organic phase under a N_2 stream and their final reconstitution in $CHCl_3$.

Purification of the various classes of phospholipid mixtures containing molecular species of mixed acyl chain lengths was achieved through sequential purifications, first by passing the lipid extracts through an amino-bonded solid-phase extraction column followed by purification through a diol-modified silica stationary phase column coupled to a High-performance Liquid Chromatography-Evaporative light scattering detector (HPLC-ELSD) (Agilent 1260, United Kingdom) system. The mobile phase employed was a gradient between solvent A ($CHCl_3$/CH_3OH/NH_4OH, 80:20.5:0.5, v/v) and solvent B ($CHCl_3$/CH_3OH/H_2O/NH_4OH, 60:35:5.5:0.5, v/v)[51]. TLC analysis was carried out on a High-Performance Thin-Layer Chromatography (HPTLC) system (CAMAG, Muttenz, Switzerland) to assess the identity and purity of each of the purified classes. Fatty acid compositions of such purified mixtures were measured by Gas Chromatography-Flame Ionization Detection (GC-FID).

Neutron reflectometry (NR)

NR measurements were performed on FIGARO, a time-of-flight reflectometer, at the Institut Laue-Langevin (Grenoble, France). A reflectivity (R) profile, defined as the ratio of neutrons scattered from the interface over the incident intensity of the neutron beam, is measured in specular conditions (*i.e.*, the incident angle of the neutron beam is equal to the reflected angle, denoted as θ) as a function of the momentum transfer vector Q_z normal to the interface (defined as $Q_z = (4\pi \sin\theta)/\lambda$, where λ is the wavelength of the neutron beam). The measured reflectivity can be linked to an in-plane averaged scattering length density (SLD) profile perpendicular to the interface. Two angles of incidence θ (0.62° and 3.8°, for Langmuir monolayers and 0.8° and 3.2°, for solid supported lipid bilayers) and a wavelength resolution of 7% $d\lambda/\lambda$ were used yielding a momentum

transfer range of $0.007 \leq Q_z \leq 0.25$ Å^{-1} (full-Q_z approach, exploited for static measurement) and a residual background reflectivity of R~10^{-7}. The raw time-of-flight experimental data at these two angles of incidence were calibrated with respect to the incident wavelength distribution and the efficiency of the detector yielding the resulting $R(Q_z)$ profile using COSMOS[26].

Measurements were performed in 5 mM HEPES, 150 mM NaCl buffer (pH 7) in different isotopic contrasts, such as H_2O (SLD = $-0.56 \cdot 10^{-6}$ Å^{-2}), D_2O (SLD = $6.36 \cdot 10^{-6}$ Å^{-2}), 8.1% *v/v* D_2O (denominated air-contrast matched water, ACMW, which has an SLD of zero), and 38% *v/v* D_2O (in order to match the silicon SLD, *i.e.*, SLD = $2.07 \cdot 10^{-6}$ Å^{-2}).

In the case of solid-supported bilayers, solid/liquid flow cells with polished silicon crystals (111) with a surface area of 5×8 cm^2 were used. Substrate surfaces were characterized in 2 different isotopic solvent contrasts, (100% H_2O and 100% D_2O), before SLB formation. Lipid bilayers were deposited on silicon crystals by vesicle fusion. The presence of bilayers was confirmed by simultaneously fitting NR profiles measured in 3 isotopic contrasts. Where possible, the bilayer structure was constrained to be symmetric, so that the inner and outer leaflets would be equivalent. The headgroup molecular volumes and thicknesses were fixed to values obtained from X-ray diffraction measurements[30,52], while the acyl tail region, had a molar averaged SLD value. The resulting model consists of four layers describing the inner and outer headgroups, the lipid tail region and a layer of water between the SiO_2 layer and the inner lipid leaflet. The acyl tail region had a low water content for all the bilayers, confirming a lipid coverage of at least 85%. A 3 to 6 Å thick water layer is also present between the bilayer and the silicon crystal.

Data modelling was performed by minimizing the difference between the experimental data points and the calculated reflectivity profile. The latter was obtained by a model consisting of multi-layers of constant SLD using the Parratt's recursive method, with an error function connecting adjacent layers. Data analysis was performed using constrains between layer parameters (thickness, roughness and degree of hydration) and simultaneous co-refinement of all data sets obtained with a global minimization of a least-squares function χ^2 was done to reduce the ambiguity in the modelling by using both AuroreNR[27] and Motofit[28] packages. Following[53], the area-per-molecule of lipidic components was fixed to be the same in each layer, $\mathrm{APM} = {}^{\mathrm{b}_i}/_{\mathrm{SLD}_i \mathrm{t}_i f_i}$ where b is the total scattering length, t is the thickness and *f* is the volume fraction (with *i*=aliphatic tails or headgroups). In presence of the peptides, in each layer (*i.e.*, tails and heads for mimicking

membrane leaflet) the SLD and the volume fraction *f* follows: $SLD_{model} = f_{solvent} \cdot SLD_{solvent} + f_{lipid} \cdot SLD_{lipid} + f_{peptide} \cdot SLD_{peptide}$; where $f_{solvent} + f_{lipid} + f_{peptide} = 1$. All the fixed parameters are tabulated in **Tables S7.2** and **S7.3**, for mono- and bilayer, respectively**.** The fitting parameters are shown in **Tables S7.4 and S7.5**.

In the case of low-Q_z approach[38] (exploited for the compositional analysis), only the data in the 0.01 $Å^{-1}$<Q_z<0.03 $Å^{-1}$ range were used. A one-layer model was exploited to fit the data and to determine the surface excess (*i.e.*, number of lipid molecule per unit area, Γ) at each examined surface pressure. Γ is directly proportional to the SLD and the film thickness, according to $\Gamma = \frac{SLD \cdot t}{\sum b \cdot N_A}$, which leads to $SLD \cdot t = N_A \cdot \sum_i \Gamma_i b_i$, where N_A is the Avogadro number and *i* represents each component present at the interface (*i.e.*, lipid and peptide).

Tables

Table S7.1 Extended physicochemical properties of the peptide investigated.

Peptide	Sequence	Number of amino acids	MW (Da)	pI	Net charge	Volume ($Å^3$)	SLD (10^{-6} $Å^{-2}$)
FP1	816-SFIEDLLFNKVTLADAGFIKQY-837	22	2538	4.56	-1	3188.4	1.852
FP2	835-KQYGDCLGDIAARDLICAQKFN-856	22	2456	6.02	0	2958.5	1.99
FP3	854-KFNGLTVLPPLLTDEMIAQYT-874	21	2351	4.37	-1	2991.7	1.725
FP4	885-GWTFGAGAALQIPFAMQMAYRFNGI-909	25	2723	8.75	+1	3362.8	1.99

Table S7.2. SLD, scattering length and molecular volume values used in NR experiments performed on Langmuir lipid monolayers[30,52].

Fixed Parameters	Plasma Membrane monolayer	
	hydrogenous	deuterated
V_h (Å^3)	304.6	304.6
Σb_h (10^{-5} Å)	60.95	166.91
SLD_h (10^{-6} Å^{-2})	2.00	5.48
V_t (Å^3)	764.1	803.2
Σb_t (10^{-5} Å)	-1.40	425.62
SLD_t (10^{-6} Å^{-2})	-0.02	5.30
f_t (%)	1	1

Table S7.3. SLD, scattering length and molecular volume values used in the NR experiments performed on solid-supported lipid bilayers[30,52].

Fixed Parameters	POPC:POPS:cholesterol bilayer
V_h (Å^3)	261
Σb_h (10^{-5} Å)	47.24
SLD_h (10^{-6} Å^{-2})	1.81
V_t (Å^3)	864
Σb_t (10^{-5} Å)	-16.43
SLD_t (10^{-6} Å^{-2})	-0.19

Table S7.4. Summary of the results obtained from the NR fittings on Langmuir lipid monolayers. APM stands from lipid area per molecule. The APMs showed here refer to the model in which in the headgroups-layer half of the V_h is considered, and in the tails-layer, one acyl chain ($V_t/2$) and half cholesterol ($V_{cholesterol}/2$) are considered, to take into account for 50% of cholesterol.

	PM			PM + FP1			
	t (Å)	f_w (%)	APM (Å^2)	t (Å)	f_w (%)	FP1% (*v/v*)	APM (Å^2)
Tails-layer	16±1		98±6	15±1		7	108±7
Headgroups-layer	8	63±1	98±3	8	60±1	6	108±3

	PM + FP2				PM + FP4			
	t (Å)	f_w (%)	FP2% (*v/v*)	APM (Å^2)	t (Å)	f_w (%)	FP4% (*v/v*)	APM (Å^2)
Tails-layer	13±1		0	116±9	16±1		0	98±6
Headgroups-layer	8	52±1	17	117±4	8	37±1	25	97±3

Table S7.5. Summary of the results obtained from the NR fittings on solid-supported bilayers. APM stands from lipid area per molecule.

	POPC:POPS:chol			POPC:POPS:chol + **FP1**			
	t (Å)	f_w (%)	APM (Å^2)	t (Å)	f_w (%)	FP1% (*v/v*)	APM (Å^2)
Water-layer	5±1	100		4±1	100	0	
Headgroups-layer	7	29±1	53±2	7	34±1	0	56±2
Tails-layer	33±1	2±0.2	53±7	17±1	10±0.4	0	56±6
Tails-layer				17±1	2±0.3	4	55±11
Headgroups-layer	7	29±1	53±2	7	33±2	0	56±3

	POPC:POPS:chol			POPC:POPS:chol + **FP1 + 2 mM Ca^{2+}**			
	t (Å)	f_w (%)	APM ($Å^2$)	t (Å)	f_w (%)	FP1% (*v/v*)	APM ($Å^2$)
Water-layer	4±1	100		5±1	100	0	
Headgroups-layer	7	34±2	56±3	7	32±1	3	57±2
Tails-layer	17±1	11±0.4	56±5	17±1	7±0.3	4	56±6
Tails-layer	16±1	3±0.3	57±9	16±1	1±0.3	7	57±21
Headgroups-layer	7	35±2	57±3	7	22±1	12	56±3

	POPC:POPS:chol			POPC:POPS:chol + **FP1** + **10 mM Ca^{2+}**				POPC:POPS:chol + **FP1** + **EDTA**			
	t (Å)	f_w (%)	APM ($Å^2$)	t (Å)	f_w (%)	FP1% (*v/v*)	APM ($Å^2$)	t (Å)	f_w (%)	FP1% (*v/v*)	APM ($Å^2$)
Water-layer	3±1	100		3±1	100	0		3±1	100	0	
Headgroups-layer	7	34±3	56±5	7	43±1	3	69±2	7	52±1	0	78±2
Tails-layer	33±1	8±0.4	57±5	34±1	18±0.2	8	69±3	17±1	34±0.3	1	78±5
Tails-layer								17±1	30±0.2	7	81±5
Headgroups-layer	7	34±3	56±5	7	43±1	3	69±2	7	50±1	4	80±2

	POPC:POPS:chol			POPC:POPS:chol + **FP2**			
	t (Å)	f_w (%)	APM ($Å^2$)	t (Å)	f_w (%)	FP2% (*v/v*)	APM ($Å^2$)
Water-layer	5±1	100		5±1	100	0	
Headgroups-layer	7	30±1	53±2	7	30±1	0	53±2
Tails-layer	33±1	3±0.2	54±5	17±1	3±0.2	0	54±7
Tails-layer				16±1	9±0.2	0	60±5
Headgroups-layer	7	30±1	53±2	7	35±1	3	60±2

	POPC:POPS:chol			POPC:POPS:chol + **FP2 + 2 mM Ca^{2+}**			
	t (Å)	f_w (%)	APM (Å^2)	t (Å)	f_w (%)	FP2% (*v*/*v*)	APM (Å^2)
Water-layer	5±1	100		5±1	100	0	
Headgroups-layer	7	37±2	59±3	7	33±2	0	56±3
Tails-layer	17±1	15±0.3	59±5	17±1	9±0.4	0	56±6
Tails-layer	16±1	1±0.3	53±19	17±1	1±0.4	0	53±24
Headgroups-layer	7	30±2	53±4	7	6±2	24	53±18

	POPC:POPS:chol			POPC:POPS:chol + **FP4**			
	t (Å)	f_w (*v*/*v*%)	APM (Å^2)	t (Å)	f_w (*v*/*v*%)	FP4% (*v*/*v*)	APM (Å^2)
Water-layer	6±1	100		6±1	100	0	
Headgroups-layer	7	31±1	54±2	7	29±2	0	53±4
Tails-layer	33±1	1±0.2	54±12	17±1	4±0.3	0	53±7
Tails-layer				15±1	6±0.3	4	63±7
Headgroups-layer	7	31±1	54±2	7	38±2	3	63±3

Table S7.6. SLD and scattering length values used in NR low-Q_z experiments performed with lipid monolayers. PL stands for phospholipids.

Fixed Parameters	PM monolayer	**Fixed Parameters**	POPC:POPS:chol monolayer
$b_{h\text{-}PM}$ (10^{-5} Å)	29.33	$b_{h\text{-}PL}$ (10^{-5} Å)	39.5
$b_{d\text{-}PM}$ (10^{-5} Å)	528.46	$b_{d\text{-}PL}$ (10^{-5} Å)	362.20
$SLD_{h\text{-}PM}$ (10^{-6} Å^{-2})	0.5	$b_{h\text{-}chol}$ (10^{-5} Å)	13.2
$SLD_{d\text{-}PM}$ (10^{-6} Å^{-2})	5	$b_{d\text{-}chol}$ (10^{-5} Å)	412.6
b_{FP1} (10^{-5} Å)	590.5	$SLD_{h\text{-}PL\|d\text{-}chol}$ (10^{-6} Å^{-2})	1
b_{FP2} (10^{-5} Å)	582.1	$SLD_{d\text{-}PL\|h\text{-}chol}$ (10^{-6} Å^{-2})	2
b_{FP4} (10^{-5} Å)	669.0	$SLD_{d\text{-}PL\|d\text{-}chol}$ (10^{-6} Å^{-2})	4

Table S7.7 Surface excess (Γ) and molar ratio obtained from the low-Q_z approach.

	PM + 5% FP1			
Π (mN·m^{-1})	Γ (µmol·m^2)		Molar %	
	PM	*FP1*	*PM*	*FP1*
5	1.74±0.01	0.13±0.01	93.0±1.4	7.0±0.5
10	1.89±0.01	0.15±0.01	92.7±1.2	7.3±0.5
15	2.04±0.01	0.15±0.01	93.2±1.2	6.8±0.4
20	2.45±0.01	0.08±0.01	96.8±1.1	3.2±0.4
25	2.79±0.01	0.07±0.01	97.7±0.9	2.3±0.3
30	3.00±0.01	0.06±0.01	98.1±0.9	1.9±0.3
35	3.23±0.01	0.03±0.01	98.9±0.8	1.1±0.3

Π (mN·m^{-1})	**PM + 5% FP2**			
	Γ (µmol·m^2)		Molar %	
	PM	*FP1*	*PM*	*FP1*
5	2.03±0.01	0.05±0.01	97.6±1.3	2.4±0.4
10	2.33±0.01	0.04±0.01	98.3±1.1	1.7±0.4
15	2.54±0.01	0.04±0.01	98.5±1.0	1.5±0.3
20	2.77±0.01	0.03±0.01	99.0±1.0	1.0±0.3
25	3.02±0.01	0.02±0.01	99.4±0.9	0.6±0.3
30	3.32±0.01	0.01±0.01	99.9±0.8	0.1±0.3
35	3.47±0.01	0.00±0.01	100±0.8	0±0.2

Π (mN·m^{-1})	**PM + 5% FP4**			
	Γ (µmol·m^2)		Molar %	
	PM	*FP1*	*PM*	*FP1*
5	1.64±0.01	0.15±0.01	91.6±1.3	8.4±0.5
10	1.68±0.01	0.20±0.01	89.4±1.2	10.6±0.5
15	1.86±0.01	0.16±0.01	92.2±1.2	7.8±0.4
20	1.98±0.01	0.17±0.01	92.0±1.1	8.0±0.4
25	2.13±0.01	0.16±0.01	93.0±1.1	7.0±0.4
30	2.32±0.01	0.15±0.01	93.9±1.0	6.1±0.3
35	2.68±0.01	0.14±0.01	95.2±0.9	4.8±0.3
40	3.04±0.01	0.11±0.01	96.4±0.8	3.6±0.2

Π (mN·m^{-1})	**POPC:POPS:cholesterol**			
	Γ (µmol·m^2)		Γ (µmol·m^2)	
	PL	*PL*	*PL*	*PL*
5	1.61±0.02	1.61±0.02	1.61±0.02	1.61±0.02
10	1.68±0.02	1.68±0.02	1.68±0.02	1.68±0.02
15	1.85±0.02	1.85±0.02	1.85±0.02	1.85±0.02
20	2.00±0.02	2.00±0.02	2.00±0.02	2.00±0.02
25	2.14±0.02	2.14±0.02	2.14±0.02	2.14±0.02
30	2.22±0.02	2.22±0.02	2.22±0.02	2.22±0.02
35	2.30±0.02	2.30±0.02	2.30±0.02	2.30±0.02
40	2.34±0.02	2.34±0.02	2.34±0.02	2.34±0.02

Π (mN·m^{-1})	POPC:POPS:cholesterol + 5% FP2					
	Γ (μmol·m^2)			Molar %		
	PL	*cholesterol*	*FP2*	*PL*	*cholesterol*	*FP2*
5	1.43±0.04	0.47±0.01	0.05±0.01	73.3±4.8	24.1±1.5	2.6±0.8
10	1.59±0.04	0.42±0.01	0.12±0.01	74.6±4.4	19.7±1.2	5.6±0.8
15	1.75±0.04	0.47±0.01	0.11±0.01	75.1±4.0	20.2±1.1	4.7±0.7
20	1.93±0.04	0.51±0.01	0.11±0.01	75.7±3.7	20.0±1.0	4.3±0.6
25	2.06±0.04	0.55±0.01	0.11±0.01	75.7±3.5	20.2±1.0	4.0±0.6
30	2.14±0.04	0.56±0.01	0.11±0.01	76.2±3.4	19.9±0.9	3.9±0.6
35	2.21±0.04	0.58±0.01	0.12±0.01	75.9±3.2	19.9±0.9	4.1±0.6

Figures

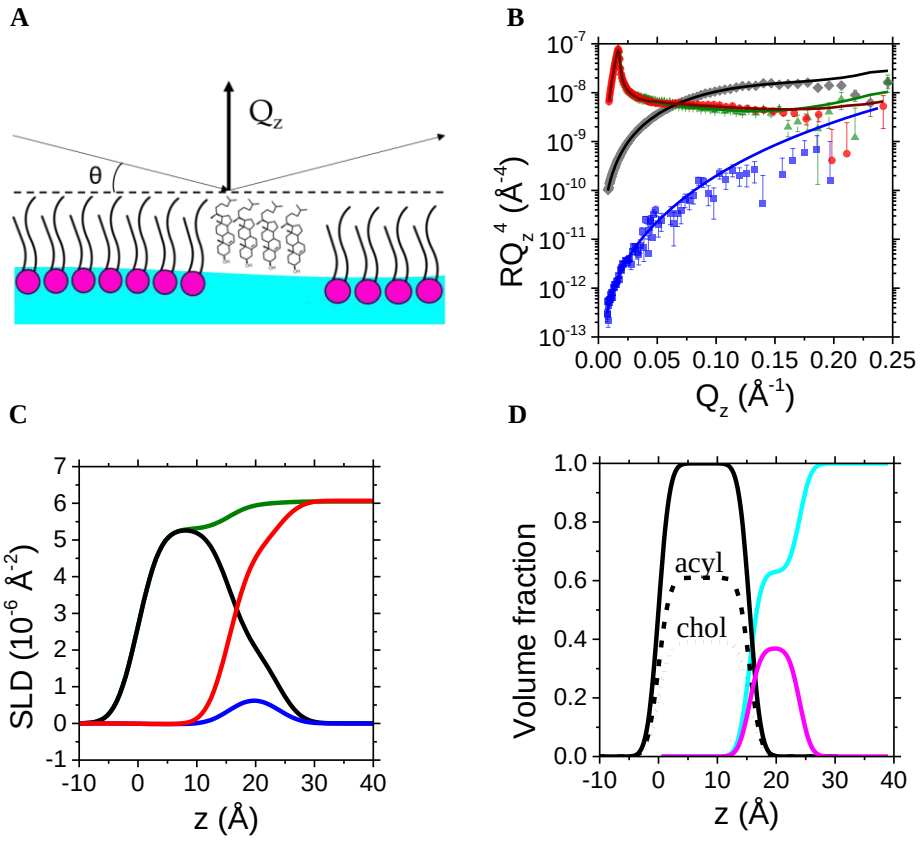

Figure S7.1 A Sketch representing a PM monolayer. Incoming and reflected neutron beams are shown. **B** NR data of fully deuterated PM lipids in D_2O (green triangles) and ACMW (black diamonds) together with hydrogenous PM lipids in D_2O (red circles) and ACMW (blue squares). The fitting curves of deuterated PM lipids in D_2O (green) and

ACMW (black), hydrogenous PM lipids in D_2O (red) and ACMW (blue) are shown. The different panels are displayed on an RQ_z^4 scale to show the agreement between the experimental and theoretical data at higher Q_z values. **C** Scattering length density, SLD, profiles corresponding to fits plotted in **B**. **D** Neutron volume fraction profiles normal to the interface of monolayers to highlight the distribution of tails (black) and heads (magenta). The water distribution is shown in cyan.

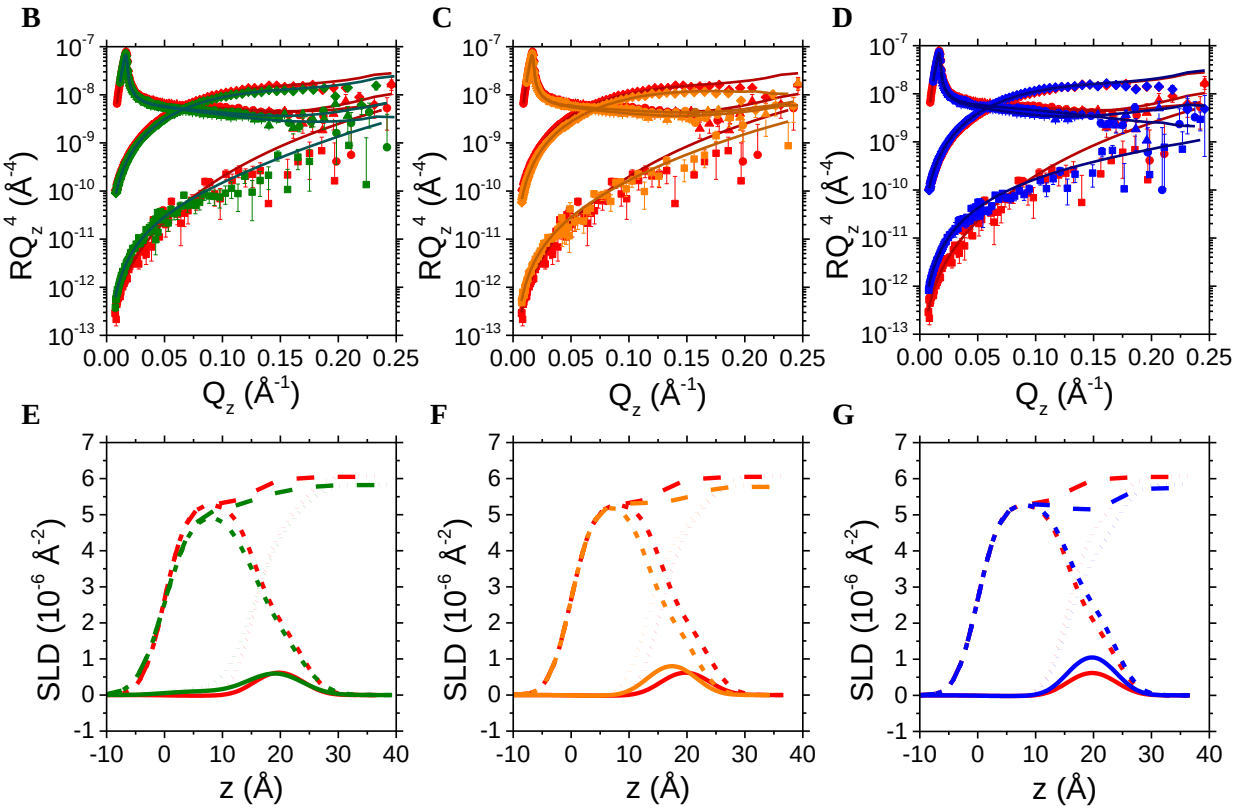

Figure S7.2. Interaction of FPs with PM monolayers. **A-C** Experimental (symbols) and simulated (lines) neutron reflectivity profiles of PM monolayers, at the surface pressure value of 22 $mN \cdot m^{-1}$, in the absence (red) and presence of **B** FP1, **C** FP2 and **D** FP4 (green, orange and blue, respectively). Data at two isotopic contrasts (D_2O and ACMW (8% D_2O)) have been measured for hydrogenous (circle and squares, respectively) and deuterated (triangles and diamonds, respectively) lipid monolayers. Solid lines in **A**, **B** and **C** are simulated curves calculated according to a 2-layers model and the parameter listed in **Table S7.2**. Figures are displayed on a RQ_z^4 scale to show the quality of the fits at high Q_z values. Scattering length density profiles corresponding to fits of the isotopic contrasts are plotted in **D**, **E** and **F**. Continuous, dot-dot, short and long dashed lines indicate the monolayer SLD profile in ACMW and D_2O isotopic contrasts with hydrogenous lipids, and in ACMW and D_2O isotopic contrast with deuterated lipids, respectively.

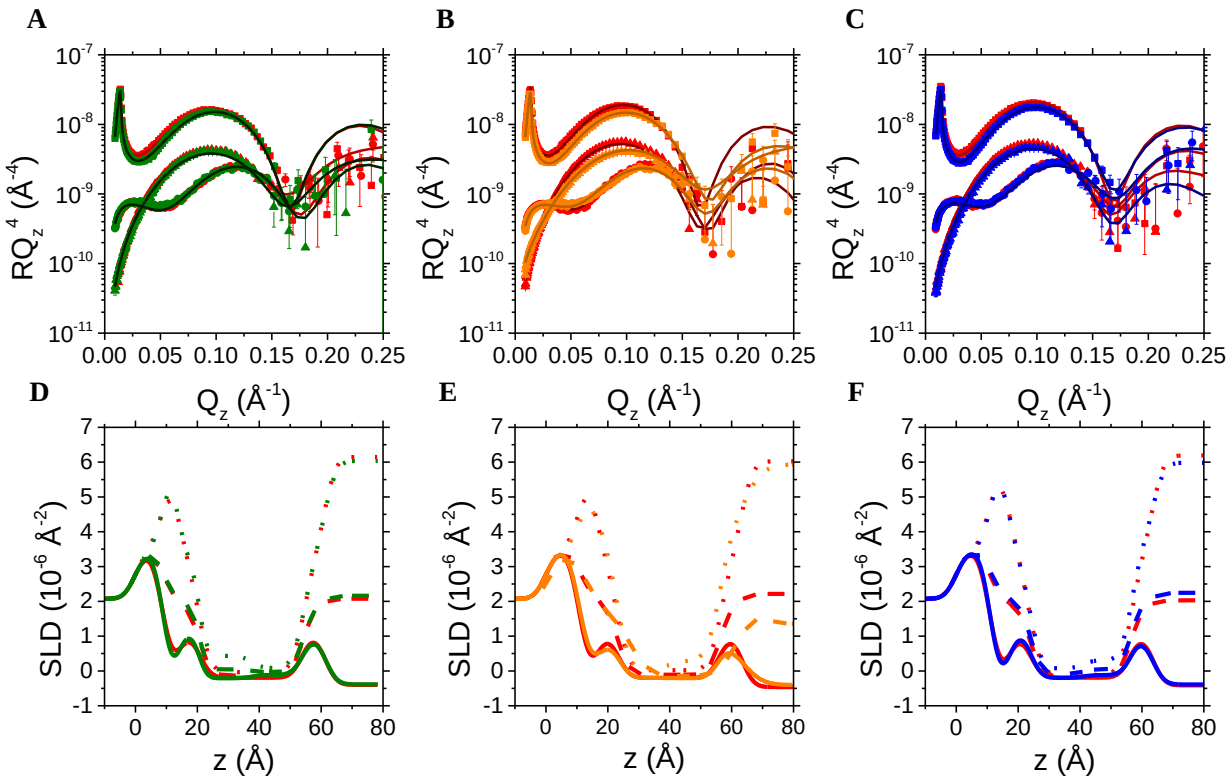

Figure S7.3. NR data of bilayers in the absence and presence of different FP. The fitting curves in D_2O, H_2O, and 38% D_2O (SiMW)-buffers are shown. Experimental (symbols) and simulated (lines) neutron reflectivity profiles of solid-supported bilayers in the absence (red) and presence of **A** FP1, **B** FP2 and **C** FP4 (green, orange and blue respectively). Data at three isotopic contrasts (D_2O, H_2O and SiMW (38% D_2O)) have been measured for hydrogenous lipid bilayers. Solid lines in **A**, **B** and **C** are simulated curves calculated according to the parameters listed in **Table S7.3**. Figures are displayed on an RQ_z^4 scale to show the quality of the fits at high Q_z values. Scattering length density profiles corresponding to fits of each isotopic contrast are plotted in **D**, **E** and **F**, respectively. Continuous, long, short dashed lines indicate the bilayer SLD profile in H_2O, SiMW and D_2O isotopic contrast, respectively.

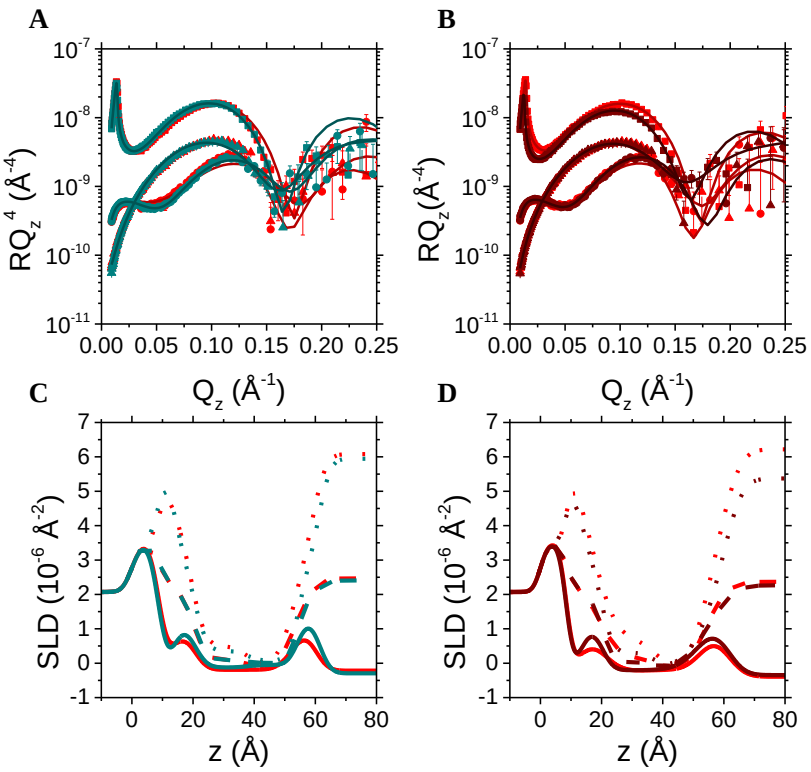

Figure S7.4. NR data and resultant scattering length density profiles of bilayers upon interaction with FP1 and FP2 in the presence of 2 mM Ca^{2+}. The fitting curves in H_2O, D_2O and SiMW (38% D_2O) are shown. Experimental (symbols) and simulated (lines) neutron reflectivity and scattering length density profiles of solid-supported bilayers in the absence (red) and presence of **A, C** FP1 in 2mM Ca^{2+} (dark cyan), **B, D** FP2 in 2mM Ca^{2+} (maroon), Simulated curves were calculated according to a 5-layers model and the parameters are listed in **Table S7.3**. NR profiles are displayed on an RQ_z^4 scale to show the quality of the fits at high Q_z values. Continuous, long and short dashed lines indicate the bilayer SLD profile in H_2O, SiMW (38% D_2O) and D_2O isotopic contrast, respectively.

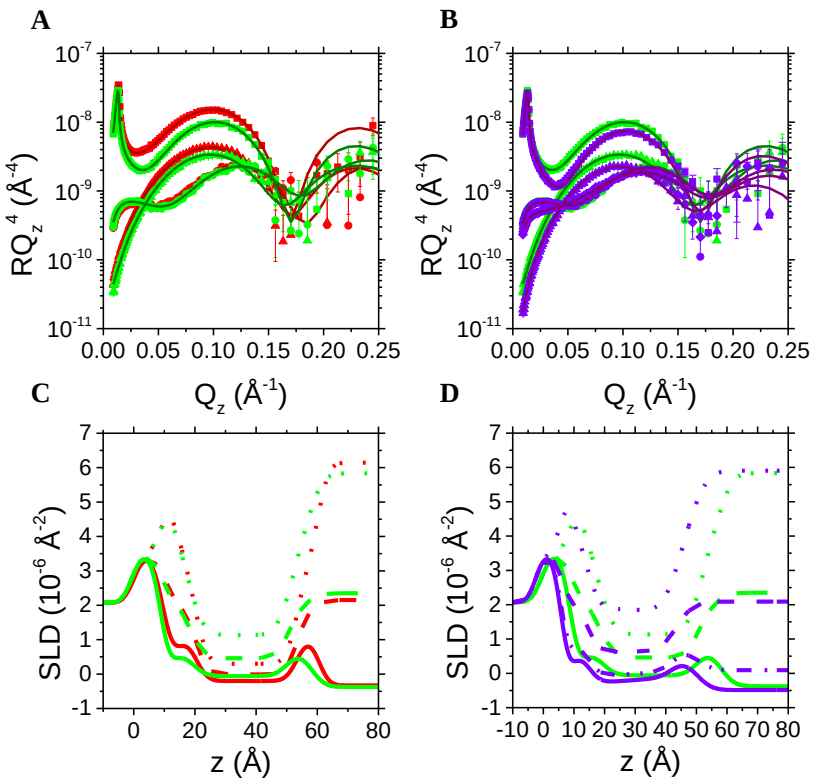

Figure S7.5. Neutron reflectivity data and resultant scattering length density profiles of bilayers upon interaction with FP1 in the presence of 10 mM Ca^{2+}, and successively addiction of EDTA for calcium removal. **A, C** FP1 in 10mM Ca^{2+} (light green) and **B**, **D** FP1 after over-night incubation with EDTA (purple). To better characterize the system after EDTA incubation, another isotopic contrast was measured (ACMW, 8% D_2O). Simulated curves were calculated according to a 5-layers model and the parameters are listed in **Table S7.3**. Neutron reflectivity profiles are displayed on an RQ_z^4 scale to show the quality of the fits at high Q_z values. Continuous, long and short dashed lines indicate the bilayer SLD profile in H_2O, SiMW (38% D_2O) and D_2O isotopic contrast, respectively. The dot-and-dash purple line represents the SLD profile in ACMW isotopic contrast.

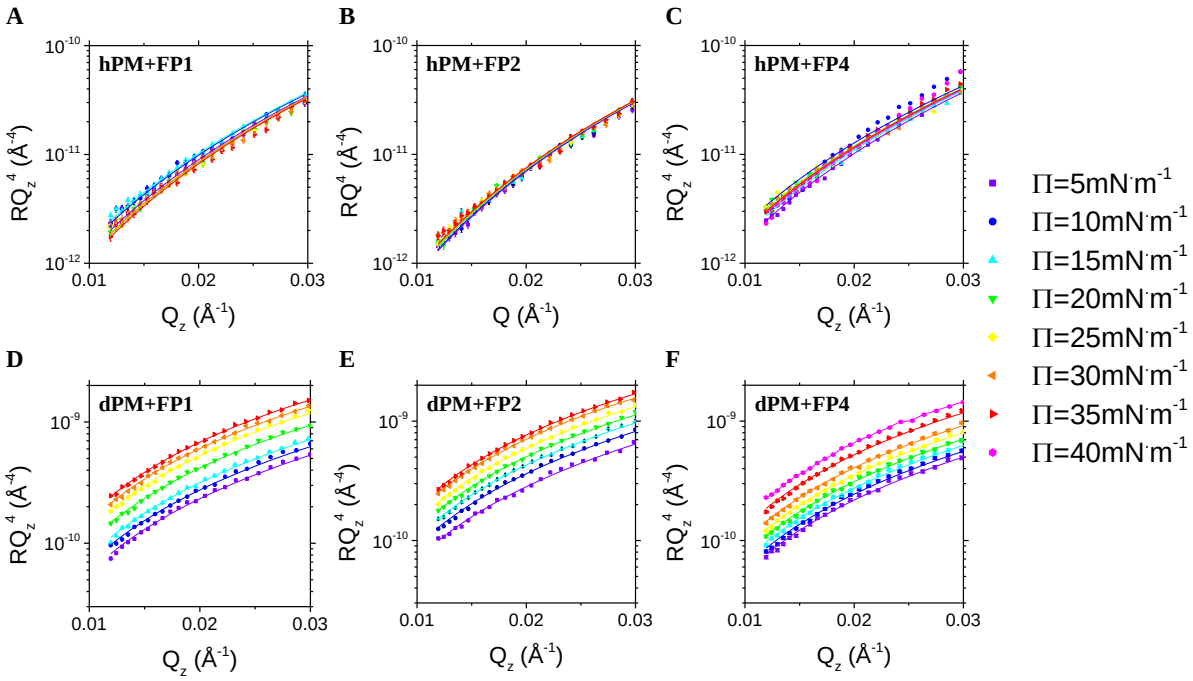

Figure S7.6 NR data acquired with the low-Q_z approach, and related simulated curves of PM+FP samples. All the data, for hPM and dPM monolayer were recorded in ACMW (8% D_2O). The legend is shown on the right.

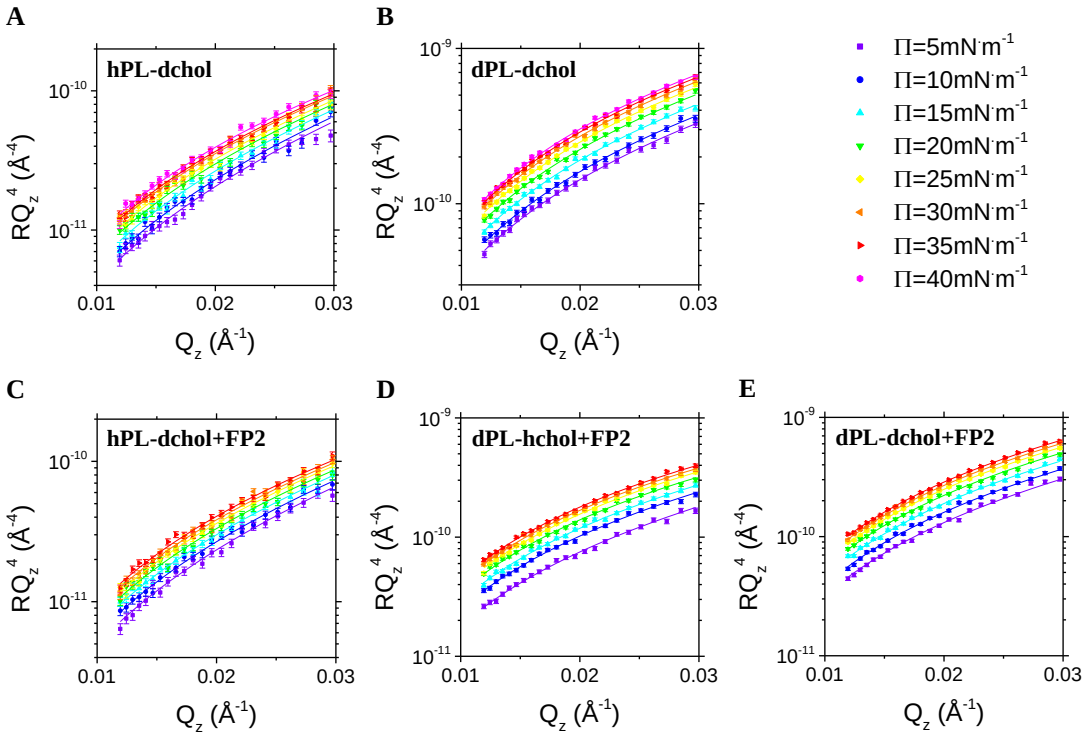

Figure S7.7 NR data acquired with the low-Q_z approach, and related simulated curves of POPC:POPS:cholesterol monolayer with and without FP2. All the data were recorded in ACMW (8% D_2O). The legend is shown on the right.

References

1. Fung TS, Liu DX. Human Coronavirus : Host-Pathogen Interaction. 2019:529-560.

2. Oberfeld B, Achanta A, Carpenter K, et al. SnapShot: COVID-19. *Cell*. 2020;181(4):954-954.e1. doi:10.1016/J.CELL.2020.04.013

3. Wu D, Wu T, Liu Q, Yang Z. The SARS-CoV-2 outbreak: What we know. *Int J Infect Dis*. 2020;94:44-48. doi:10.1016/J.IJID.2020.03.004

4. Li Q, Wu J, Nie J, et al. The Impact of Mutations in SARS-CoV-2 Spike on Viral Infectivity and Antigenicity. *Cell*. 2020;182(5):1284-1294.e9. doi:10.1016/J.CELL.2020.07.012

5. Daly JL, Simonetti B, Klein K, et al. Neuropilin-1 is a host factor for SARS-CoV-2 infection. *Science*. 2020;370(6518):861-865. doi:10.1126/science.abd3072

6. Hoffmann M, Kleine-Weber H, Schroeder S, et al. SARS-CoV-2 Cell Entry Depends on ACE2 and TMPRSS2 and Is Blocked by a Clinically Proven Protease Inhibitor. *Cell*. 2020;181(2):271-280.e8. doi:10.1016/j.cell.2020.02.052

7. Tang T, Bidon M, Jaimes JA, Whittaker GR, Daniel S. Coronavirus membrane fusion mechanism offers a potential target for antiviral development. *Antiviral Res*. 2020;178(April):104792. doi:10.1016/j.antiviral.2020.104792

8. Xia S, Liu M, Wang C, et al. Inhibition of SARS-CoV-2 (previously 2019-nCoV) infection by a highly potent pan-coronavirus fusion inhibitor targeting its spike protein that harbors a high capacity to mediate membrane fusion. *Cell Res*. 2020;2(February). doi:10.1038/s41422-020-0305-x

9. Harrison SC. Viral membrane fusion. *Virology*. 2015;479-480:498-507. doi:10.1016/J.VIROL.2015.03.043

10. Peacock TP, Goldhill DH, Zhou J, et al. The furin cleavage site in the SARS-CoV-2 spike protein is required for transmission in ferrets. *Nat Microbiol*. 2021;6(7):899-909. doi:10.1038/s41564-021-00908-w

11. Narayanaswamy N, Chakraborty K, Saminathan A, et al. A pH-correctable, DNA-based

fluorescent reporter for organellar calcium. *Nat Methods 2018 161*. 2018;16(1):95-102. doi:10.1038/s41592-018-0232-7

12. Cai Y, Zhang J, Xiao T, et al. Distinct conformational states of SARS-CoV-2 spike protein. *Science*. 2020;369(6511). doi:10.1126//science.abd4251

13. Benton DJ, Wrobel AG, Xu P, et al. Receptor binding and priming of the spike protein of SARS-CoV-2 for membrane fusion. *Nat 2020 5887837*. 2020;588(7837):327-330. doi:10.1038/s41586-020-2772-0

14. Lai AL, Freed JH. SARS-CoV-2 Fusion Peptide has a Greater Membrane Perturbating Effect than SARS-CoV with Highly Specific Dependence on Ca2+. *J Mol Biol*. 2021;433(10):166946. doi:10.1016/j.jmb.2021.166946

15. Pattnaik GP, Bhattacharjya S, Chakraborty H. Enhanced Cholesterol-Dependent Hemifusion by Internal Fusion Peptide 1 of SARS Coronavirus-2 Compared to Its N-Terminal Counterpart. *Biochemistry*. 2021;60(8):559-562. doi:10.1021/ACS.BIOCHEM.1C00046/SUPPL_FILE/BI1C00046_SI_001

16. Basso LGM, Zeraik AE, Felizatti AP, Costa-Filho AJ. Membranotropic and biological activities of the membrane fusion peptides from SARS-CoV spike glycoprotein: The importance of the complete internal fusion peptide domain. *Biochim Biophys Acta - Biomembr*. 2021;1863(11):183697. doi:10.1016/J.BBAMEM.2021.183697

17. Sainz B, Rausch JM, Gallaher WR, Garry RF, Wimley WC. Identification and Characterization of the Putative Fusion Peptide of the Severe Acute Respiratory Syndrome-Associated Coronavirus Spike Protein. *J Virol*. 2005;79(11):7195-7206. doi:10.1128/jvi.79.11.7195-7206.2005

18. Alsaadi EAJ, Neuman BW, Jones IM. A Fusion Peptide in the Spike Protein of MERS Coronavirus. *Viruses 2019, Vol 11, Page 825*. 2019;11(9):825. doi:10.3390/V11090825

19. Madu IG, Roth SL, Belouzard S, Whittaker GR. Characterization of a Highly Conserved Domain within the Severe Acute Respiratory Syndrome Coronavirus Spike Protein S2 Domain with Characteristics of a Viral Fusion Peptide. *J Virol*. 2009;83(15):7411-7421. doi:10.1128/JVI.00079-09/ASSET/12442DDA-BF1F-4D5E-A4F5-

621411B033D3/ASSETS/GRAPHIC/ZJV0150921240010.JPEG

20. Lai AL, Millet JK, Daniel S, Freed JH, Whittaker GR. The SARS-CoV Fusion Peptide Forms an Extended Bipartite Fusion Platform that Perturbs Membrane Order in a Calcium-Dependent Manner. *J Mol Biol*. 2017;429(24):3875-3892. doi:10.1016/j.jmb.2017.10.017

21. Ou MY, Xiao Q, Ju XC, et al. The CTNNBIP1-CLSTN1 fusion transcript regulates human neocortical development. *Cell Rep*. 2021;35(13):109290. doi:10.1016/J.CELREP.2021.109290

22. Raghava S, Giorda KM, Romano FB, Heuck AP, Hebert DN. The SV40 late protein VP4 is a viroporin that forms pores to disrupt membranes for viral release. *PLoS Pathog*. 2011;7(6). doi:10.1371/journal.ppat.1002116

23. Gesztelyi R, Zsuga J, Kemeny-Beke A, Varga B, Juhasz B, Tosaki A. The Hill equation and the origin of quantitative pharmacology. *Arch Hist Exact Sci*. 2012. doi:10.1007/s00407-012-0098-5

24. Hénon S, Meunier J. Microscope at the Brewster angle: Direct observation of first-order phase transitions in monolayers. *Rev Sci Instrum*. 1991;62(4):936-939. doi:10.1063/1.1142032

25. Campbell RA, Wacklin HP, Sutton I, Cubitt R, Fragneto G. FIGARO: The new horizontal neutron reflectometer at the ILL. *Eur Phys J Plus*. 2011;126(11):1-22. doi:10.1140/epjp/i2011-11107-8

26. Gutfreund P, Saerbeck T, Gonzalez MA, et al. Towards generalized data reduction on a chopperbased time-of-flight neutron reflectometer. *J Appl Crystallogr*. 2018. doi:10.1107/S160057671800448X

27. Gerelli Y. Aurore: New software for neutron reflectivity data analysis. *J Appl Crystallogr*. 2016;49:330-339. doi:10.1107/S1600576716000108

28. Nelson A. Co-refinement of multiple-contrast neutron/X-ray reflectivity data using MOTOFIT. *J Appl Crystallogr*. 2006;39(2):273-276. doi:10.1107/S0021889806005073

29. Marsh D. Cholesterol-induced fluid membrane domains: A compendium of lipid-raft ternary phase diagrams. *Biochim Biophys Acta - Biomembr*. 2009;1788(10):2114-2123. doi:10.1016/J.BBAMEM.2009.08.004

30. Nagle JF, Tristram-Nagle S. Structure of lipid bilayers. *Biochim Biophys Acta - Rev Biomembr*. 2000. doi:10.1016/S0304-4157(00)00016-2

31. Takamori S, Holt M, Stenius K, et al. Molecular Anatomy of a Trafficking Organelle. *Cell*. 2006;127(4):831-846. doi:10.1016/J.CELL.2006.10.030

32. Chakraborty S, Doktorova M, Molugu TR, et al. How cholesterol stiffens unsaturated lipid membranes. *Proc Natl Acad Sci U S A*. 2020;117(36):21896-21905. doi:10.1073/pnas.2004807117

33. De Ghellinck A, Schaller H, Laux V, et al. Production and Analysis of Perdeuterated Lipids from Pichia pastoris Cells. *PLoS One*. 2014;9(4):e92999. doi:10.1371/JOURNAL.PONE.0092999

34. Fujimoto T, Parmryd I. Interleaflet coupling, pinning, and leaflet asymmetry-major players in plasma membrane nanodomain formation. *Front Cell Dev Biol*. 2017;4(JAN):155. doi:10.3389/FCELL.2016.00155/BIBTEX

35. Liao Y, Zhang SM, Neo TL, Tam JP. Tryptophan-dependent membrane interaction and heteromerization with the internal fusion peptide by the membrane proximal external region of SARS-CoV spike protein. *Biochemistry*. 2015;54(9):1819-1830. doi:10.1021/BI501352U/ASSET/IMAGES/MEDIUM/BI-2014-01352U_0009.GIF

36. Basso LGM, Vicente EF, Crusca E, Cilli EM, Costa-Filho AJ. SARS-CoV fusion peptides induce membrane surface ordering and curvature. *Sci Reports 2016 61*. 2016;6(1):1-19. doi:10.1038/srep37131

37. Luchini A, Micciulla S, Corucci G, et al. Lipid bilayer degradation induced by SARS-CoV-2 spike protein as revealed by neutron reflectometry. *Sci Rep*. 2021;11(1). doi:10.1038/s41598-021-93996-x

38. Campbell RA, Tummino A, Noskov BA, Varga I. Polyelectrolyte/surfactant films spread from neutral aggregates. *Soft Matter*. 2016;12(24):5304-5312. doi:10.1039/c6sm00637j

39. Nagle JF, Scott HL. Lateral compressibility of lipid mono- and bilayers. Theory of membrane permeability. *BBA - Biomembr*. 1978;513(2):236-243. doi:10.1016/0005-2736(78)90176-1

40. Adams EM, Casper CB, Allen HC. Effect of cation enrichment on dipalmitoylphosphatidylcholine (DPPC) monolayers at the air-water interface. *J Colloid Interface Sci*. 2016;478:353-364. doi:10.1016/j.jcis.2016.06.016

41. Carrascosa-Tejedor J, Santamaria A, Pereira D, Maestro A. Structure of DPPC Monolayers at the Air/Buffer Interface: A Neutron Reflectometry and Ellipsometry Study. *Coatings 2020, Vol 10, Page 507*. 2020;10(6):507. doi:10.3390/COATINGS10060507

42. Oelkers M, Witt H, Halder P, Jahn R, Janshoff A. SNARE-mediated membrane fusion trajectories derived from force-clamp experiments. *Proc Natl Acad Sci U S A*. 2016;113(46):13051-13056. doi:10.1073/PNAS.1615885113

43. Santamaria A, Batchu KC, Matsarskaia O, et al. Strikingly Different Roles of SARS-CoV-2 Fusion Peptides Uncovered by Neutron Scattering. *J Am Chem Soc*. 2022. doi:10.1021/jacs.1c09856

44. Heller WT. A small-angle neutron scattering study of the physical mechanism that drives the action of a viral fusion peptide. *Chem Phys Lipids*. 2021;234:105022. doi:10.1016/J.CHEMPHYSLIP.2020.105022

45. Zhou T, Tsybovsky Y, Gorman J, et al. Cryo-EM Structures of SARS-CoV-2 Spike without and with ACE2 Reveal a pH-Dependent Switch to Mediate Endosomal Positioning of Receptor-Binding Domains. *Cell Host Microbe*. 2020;28(6):867-879.e5. doi:10.1016/J.CHOM.2020.11.004

46. Zang R, Case JB, Yutuc E, et al. Cholesterol 25-hydroxylase suppresses SARS-CoV-2 replication by blocking membrane fusion. *Proc Natl Acad Sci U S A*. 2020;117(50):32105-32113. doi:10.1073/PNAS.2012197117

47. Lindau M, Almers W. Structure and function of fusion pores in exocytosis and ectoplasmic membrane fusion. *Curr Opin Cell Biol*. 1995;7(4):509-517. doi:10.1016/0955-0674(95)80007-7

48. Pfenninger K, Akert K, Moor H, Sandri C. The fine structure of freeze-fractured presynaptic membranes. *J Neurocytol 1972 12*. 1972;1(2):129-149. doi:10.1007/BF01099180

49. Kemble GW, Danieli T, White JM. Lipid-anchored influenza hemagglutinin promotes hemifusion, not complete fusion. *Cell*. 1994;76(2):383-391. doi:10.1016/0092-8674(94)90344-1

50. Folch J, Lees M, Sloane stanley GH. A simple method for the isolation and purification of total lipides from animal tissues. *J Biol Chem*. 1957;226(1):497-509. doi:10.1016/s0021-9258(18)64849-5

51. Boselli E, Pacetti D, Lucci P, Frega NG. Characterization of phospholipid molecular species in the edible parts of bony fish and shellfish. *J Agric Food Chem*. 2012;60(12):3234-3245. doi:10.1021/jf205159a

52. Armen RS, Uitto OD, Feller SE. Phospholipid component volumes: Determination and application to bilayer structure calculations. *Biophys J*. 1998;75(2):734-744. doi:10.1016/S0006-3495(98)77563-0

53. Campbell RA, Saaka Y, Shao Y, et al. Structure of surfactant and phospholipid monolayers at the air/water interface modeled from neutron reflectivity data. *J Colloid Interface Sci*. 2018;531:98-108. doi:10.1016/j.jcis.2018.07.022

Chapter 8

Overall Discussion

This PhD thesis aimed at characterizing the out-of-plane structure as well as in-plane organization of different model membranes, exploiting both synthetic and natural lipids. The first refers to the direction orthogonal to the plane of the membrane, while the second concerns the membrane plane. Here, many examples are reported concerning how NR, alongside with SANS and other bench techniques (such as Langmuir trough, ellipsometry, BAM, QCM-D and CD) can provide a detailed characterization of *in vitro* lipid model systems that mimic biologically relevant biomembranes. Besides, the interaction of these lipid model membranes, in the form of monolayers, solid supported bilayers and liposomes, with selected proteins has been investigated, providing information regarding the function and the structure of lipid-interacting proteins, upon binding. In particular, **Chapter 3** and **4** are focused on the characterization of model membranes, while in **Chapters 5** to **7** the interaction of proteins with model membranes has been addressed. The aim of this chapter is to report an overall discussion concerning all the results obtained in this PhD thesis, dividing them into two sections: (**1**) characterization of *in vitro* lipid model systems containing PIP_2, replicating the inner leaflet of the plasma membrane, and their interaction with adaptor and modulator proteins from the clathrin-mediated endocytosis (CME) pathway; (**2**) design of model membranes composed of natural lipids, mimicking the outer leaflet of the plasma membrane, and their interaction with peptides derived from SARS-CoV-2 Spike protein.

1. Characterization of *in vitro* lipid model systems containing PIP_2 and their interaction with adaptor and modulator proteins from the CME pathway

Phosphatidylinositol 4,5-bisphosphate (PIP_2) fulfils important roles in several biological pathways, by forming docking sites on the inner leaflet of membranes, whose task is the recruitment of specific proteins from the cytosol via electrostatic interaction. These negative charges are present in the PIP_2 headgroup that contains an inositol ring phosphorylated in positions 4 and 5. Although PIP_2 has been show to form clusters in model membranes in presence of divalent cations, the domain formation has never been correlated to the out-of-plane structure of the membrane itself. To this end, a simple *in vitro* lipid model system based on mixed DPPC:PIP_2 Langmuir monolayers has been designed, and its structural features investigated with NR and

BAM (**Chapter 3**). NR experiments allowed determining the out-of-plane structure of the monolayer, in particular identifying the orientation of the inositol ring, in terms of its tilt angle with respect to the membrane plane. The latter has been estimated at different surface pressures (*i.e.*, different values of area per molecule, thus lipids packing) and agrees with previous molecular dynamics simulation studies. An empirical equation has been proposed to determine the trajectory of the PIP_2 headgroup tilt angle with the level of monolayer compression. It is worth mentioning that, up to now, the tilt angle of the inositol ring of PIPs lipids has been only calculated via molecular dynamics simulations, or inferred with experimental approaches without providing a final value. Moreover, BAM was employed to visualize the in-plane organization of the lipid film, hence obtaining a relationship between PIP_2 cluster formation and the increase in monolayer surface pressure. Thus, this multi-technique approach has provided a correlation between the orientation of PIP_2 inositol ring (out-of-plane structure) and the in-plane organization of the DPPC:PIP_2 monolayer. The results show that PIP_2 cluster formation depends not only on the presence of divalent cations, but also on the surface pressure, which influences the out-of-plane structure of the lipids: when the inositol-biphosphate ring moves away from the membrane (smaller tilt angle), the formation of clusters is favoured, and larger PIP_2 islands can form. These outcomes may help to get a better understanding of both PIP_2 role in membrane curvature and PIP_2-protein interaction, which has also been investigated here. In fact, the interaction with several proteins from the CME pathways and PIP_2-containing model membranes has been addressed in **Chapters 5** and **6**.

Chapter 5 presented a detailed investigation on the binding of the endocytic adaptor protein CALM to model membranes rich in PIP_2, in the form of monolayer, solid supported bilayer and liposomes. CALM (clathrin assembly lymphoid myeloid leukemia protein) is one of the most abundant clathrin adaptors in endocytic CCVs. It possesses a compacted, stacked-helical domain, called AP180 N-terminal homology (ANTH) domain, with unstructured C-terminal tails containing a clathrin binding site. The PIP_2 binding site is located in the ANTH domain, and corresponds to Lysines 28, 38 and 40. Moreover, CALM is characterized by a membrane-inserting amphipathic helix at the N-terminus (amphipathic helix 0, AH0), whose orientation is thought to change upon membrane binding. CALM senses and induces membrane curvature, being also able to drive pearlized liposomes tubulation, thanks to the insertion of AH0 in the membrane. Although the insertion of the helix in the membrane was hypothesized, it has been never experimentally

proved, alongside with the protein three-dimensional orientation upon lipid binding. Thus, **Chapter 5** aimed firstly at unravelling the orientation of the protein with respect to the membrane, and then at determining the position of the AH0. The obtained orientation makes biological sense since the PIP_2 binding site points towards the membrane, and is partially inserted in it, thus allowing the interaction with the phosphate groups of the inositol ring. NR shed light on the coverage of the protein on lipid membranes (12%), which is similar to the coverage previously obtained in liposome tubulation assays (~16%). Moreover, detailed structural features of the CALM-membrane binding have been unravelled, showing that the AH0 is inserted in the headgroups-layer. Finally, the relationship between the orientation of PIP_2 inositol ring and protein binding was studied, demonstrating that CALM interaction with the phosphate groups is stronger when the ring tends to position itself toward a configuration parallel to the membrane. Other than planar membranes, liposomes were employed as *in vitro* lipid model systems, using DLS and SANS. Anyway, the complex picture emerging after protein-lipids interaction, confirmed by the absence of a true Gaussian-like profile in the intensity distribution of DLS profiles, suggested a polydisperse system. SANS data did not supply with more detailed structural information about the effect of CALM on the bilayer, a part from suggesting an increase in the average size of the scattering particles. Therefore, the protein definitively affect the overall size of the vesicles.

Chapter 6 provided results on the binding of PIP_2-containing membranes with the adaptor protein AP2 and the modulator proteins FCHo2 and Eps15. AP2 is a heterotetrameric protein complex composed of four different subunits (α, β, μ, and σ) with different functions. It contains multiple PIP_2 binding sites on the different subunits, as well as a dileucine binding box, which can bind to the dileucine sorting signal peptide. In this thesis, the NR characterization of a complex model membrane, rich in PIP_2 and also in CD4 peptide, which contains the dileucine sorting signal, was reported. The peptide was linked to a 16:0 MPB PE (1,2-Dipalmitoyl-sn-Glycero-3-Phosphoethanolamine-N-[4-(p-maleimidophenyl) butyramide]) molecule that anchors it to the hydrophobic core of the membrane. However, by determining the out-of-plane structure of the membrane, the peptide was found to be embedded in the headgroups-layer. The characterization of the membrane was followed by protein injection and its binding was assessed via NR. Indeed, AP2 was shown to be bound to PIP_2-CD4-containing membrane, with part of the protein inserted in the headgroups-layer where both CD4 and PIP_2 phosphate groups are, and part laying outside the bilayer region. The total thickness of AP2 obtained here (~70 Å) is compatible with the crystal

structure of the protein (~80 Å), as well as with previously performed experiments that showed the orientation of AP2 with lipid monolayer containing PIP_2 and CD4. Finally, the same chapter also focused on the investigation of the resultant structure of the modulator proteins FCHo2 (Fes-CIP4 homology domain (hence FCH) only protein 2) and Eps15 (epidermal growth factor pathway substrate 15) upon binding with POPS- and PIP_2-containing membranes. FCHo2 is a curvature inducing protein, whose BAR domain (F-BAR) bears positive charges that can interact with the negative charges of the plasma membrane inner leaflet, directly sculpting the lipid bilayer. FCHo2 also contains an intrinsically disordered segment of ~200 amino acid residues (flexible linker), which associates with AP2, and a C-terminal µ-homology domain (HD) that binds to the Eps15 protein (epidermal growth factor pathway substrate 15), which in return can bind AP2 appendages. Thus, the cross-interactions between FCHo2, Eps15 and AP2 allow the stabilization of modulator and adaptor proteins complexes localized at the plasma membrane, and induce the initiation of the CME pathway. Indeed, FCHo2 play a key role in local AP2 recruiting and restructuring, as they are among the earliest proteins to mark a nascent CCP and affect AP2 conformation directly. Although the atomic structure of the F-BAR and µHD (of the homolog protein FCHo1) domains in complex with Eps15 have been solved (PDB ID: 2V0O and 5JP2, respectively), and biochemical tools together with microscopy have been employed to investigate their binding with AP2 appendages, the resultant structure of FCHo2 and FCHo2-Eps15 complex upon membrane binding has yet to be investigated. **Chapter 6** of this PhD thesis also aimed at determining FCHo2 domains position, by using a truncated construct of the protein, lacking the µHD, and the NR results obtained were compared with the ones regarding the full-length protein. Thus, such results led to a hypothesis concerning the domains position, in which both flexible linkers and the µHD are closer to the membrane. Finally, the NR data recorded after the addition of Eps15 underneath the monolayer with bound FCHo2, suggested a proximity of Eps15 to the membrane, although Eps15 does not interact with the membrane on its own. Taking into account that the FCHo2 flexible linkers, as well as Eps15, bind AP2, their proximity to the lipids would help stabilizing the multicomponent complex formed by AP2-FCHo2-Eps15 at the level of the inner leaflet of the plasma membrane, required for CME initialization.

2. Design of model membranes composed of natural lipids and their interaction with peptides from SARS-CoV-2 Spike protein

As explained in **Chapter 4**, natural lipids extracted from yeast cells were appropriately mixed to replicate the plasma membrane (PM) composition, and to deposit stable PM lipid monolayers. The design of such model membrane rose questions regarding the effect of cholesterol on the structure and organization of lipid molecules. To answer these questions, surface pressure-area isotherms, combined with BAM and NR, were used to characterize the in-plane morphology and out-of-plane structure of Langmuir monolayers composed of natural lipids with different cholesterol content. In particular, three different models were deposited: a simple membrane, uniquely composed of natural PC, PE and PS phospholipids (no cholesterol), the endoplasmic-reticulum-Golgi intermediate compartment (ERGIC) membrane (8% cholesterol in mol) and the PM (50% cholesterol in mol). The experiments shed light on the correlation between lipid composition and membrane properties. In particular, the presence of cholesterol lead to a decrease in film thickness as well as an increase in rigidity. Moreover, BAM images showed the presence of densely packed liquid-ordered phase (cholesterol-rich) domains in the PM model, which were absent in the pure phospholipid monolayer. Finally, it is worth mentioning that this is the first time that natural phospholipids extracted from yeast cells were employed to replicate biologically relevant biomembranes, in the form of stable Langmuir monolayers.

This preliminary characterization of the PM model membrane was necessary to study the *in vitro* interaction of cell membranes with viral proteins. In particular, the binding of four peptides derived from the SARS-CoV-2 Spike fusion domain (called fusion peptides, FPs) with the PM membrane was investigated in **Chapter 7**. The aim of this work was to unravel the detailed mechanism behind the fusion process that occurs between the PM and the viral membrane, which is the key step of the infection. The results obtained using NR, Langmuir trough, BAM and CD (alongside with parallel SANS and neutron spectroscopy) shed light on the differences in the FPs binding to PM. In particular, NR demonstrated that FP4, by binding with greater affinity to the lipid headgroups, is better able than the other FPs to bridge two bilayers together. Anyway, the dehydration of the lipid headgroups observed with both FP2 and FP4 would promote membrane fusion. Indeed, dehydration was found to be the rate-limiting step in SNARE-assisted membrane fusion. Moreover, Langmuir trough experiments allowed the determination of the binding free energy to PM monolayer of FP1, FP2 and FP4, which resulted to be ~8, ~7 and ~10 $kcal \cdot mol^{-1}$,

respectively. Thus, the binding free energy for association of three FP4 from a single Spike trimer, would be ~30 kcal·mol^{-1}.The kinetic barrier to hemifusion, which is generally estimated to exceed 50 kcal·mol^{-1}, can therefore be overcome upon binding two Spike trimers. Another interesting result concerns the interaction of FP1 with the model membranes. Indeed, it is the only FP that inserts in the acyl chains of PM lipid monolayers. Intriguingly, FP1 binding to lipid bilayers is calcium-dependent, as such divalent cations drastically alter the orientation of bound FP1. Since cell compartments have different calcium concentration, the correlation between calcium levels and FP1 binding may therefore provide an indication to where the viral and host membranes fuse during SARS-CoV-2 infection. Depending on cell type, the SARS-CoV-2 virus may, more likely, enter the host cell through fusion with the plasma membrane, but can also travel through the endosomal pathway (after endocytosis), with the fusion occurring in the late endosome. The structural data presented show that at the plasma membrane, in the presence of calcium, the FP1 peptide would penetrate the bilayer and form a transmembrane peptide across the membrane (if folded as a single helix, FP1 length would be comparable to the width of the membrane hydrophobic core). Moreover, FP2 and, especially, FP4 could function as bridges between the host and the viral membrane, with FP2 helping the insertion of FP1 by removing cholesterol from the membrane. In conclusion, this multi-technique approach applied to a well parametrized model of the viral protein-host membrane interaction, reveals that different segments of the SARS-CoV-2 Spike protein assume different functions in the initiation of viral infection.

Chapter 9

Conclusions and Perspectives

This PhD thesis investigated the structure as well as lipid organization of selected model membranes (**Chapters 3** and **4**), which were then used for studies of lipid-binding proteins (**Chapters 5** to **7**). Here the main conclusions and perspectives are summarized for (**1**) *in vitro* lipid model systems containing PIP_2, replicating the inner leaflet of the plasma membrane, and their interaction with adaptor and modulator proteins from the clathrin-mediated endocytosis (CME) pathway; and (**2**) model membranes composed of natural lipids, mimicking the outer leaflet of the plasma membrane, and their interaction with peptides from SARS-CoV-2 Spike protein.

1. Characterization of *in vitro* lipid model systems containing PIP_2 and their interaction with adaptor and modulator proteins from the CME pathway

Model membranes containing PIP_2 can be used to mimic the inner leaflet of the mammalian plasma membrane. **Chapter 3** reports the determination of the out-of-plane structure of such membranes in the form of lipid monolayers, thus obtaining the PIP_2 inositol ring tilt angle by exploiting NR, alongside with the visualization of the lipid in-plane organization (*i.e.*, lateral packing), by using BAM. PIP_2 domains were observed, and their formation was correlated with the monolayer surface pressure and out-of-plane structure. In **Chapters 5** and **6**, PIP_2-containing membranes, in the form of monolayers, bilayers and liposomes, were used to investigate the binding of proteins from the CME pathway. In particular, a detailed structural investigation of the adaptor protein CALM, by the means of NR, Langmuir through experiments, QCM-D, DLS and SANS, demonstrated the lipid-binding properties of the protein as well as its three-dimensional orientation upon membrane binding. Moreover, by using different mutants of the protein, NR results directly showed the insertion of CALM amphipathic helix 0 in the membrane, which was only hypothesized so far. Following the same approach, the interaction of the adaptor protein AP2 and the modulator proteins FCHo2 and Eps15 with bilayers and monolayers, respectively, was investigated. In particular, a complex lipid bilayer that bears an AP2 binding peptide moiety has been deposited on a solid support to investigate the interaction with the adaptor protein. NR demonstrated the presence of such peptide and also the insertion of AP2 in the membrane. Finally, Langmuir monolayers containing negatively charged lipids (phosphoserines or PIP_2) were

employed to investigate the binding of FCHo2 and Eps15. NR showed the presence of the proteins and allowed determining the position of the different domains.

As outlooks, atomic force microscopy (AFM) experiments could be performed, with PIP_2-containing lipid monolayers, deposited on solid supports trough Langmuir Blodgett/Schaefer, before and after protein addiction (CALM, AP2 and FCHo2), to visualize the PIP_2 in-plane clusters and also individuate the protein molecules that bind the membrane. Besides, the interaction of AP2 with solid supported bilayers has been already investigated with QCM-D in ILL laboratories; thus the data here presented will be reorganised to be included in a more expanded publication. Finally, ellipsometry will be used to study the interaction of FCHo2 and Eps15 to negatively charged monolayer, alongside with a refined NR data analysis, by using the crystallographic structure of two of the three domains of FCHo2.

2. Design of model membranes composed of natural lipids and their interaction with peptides from SARS-CoV-2 Spike protein

The second section of this PhD thesis was focused on understanding the mechanism of SARS-CoV-2 infection. In the first instance, it was crucial to identify and characterize an *in vitro* lipid model system that could replicate the plasma membrane. In **Chapter 3** the characterization of different model membranes has been reported: Langmuir monolayers, composed by natural lipids extracted form yeast cells and different amount of cholesterol, which mimic biologically relevant membranes, were studied. Such monolayers were characterized by surface pressure-area isotherm, NR and BAM, in order to obtain information of both out-of-plane structure and in-plane lipid organization, and correlate these with the cholesterol amount. Subsequently, the plasma membrane model investigated was employed in **Chapter 7** to study the interaction of fusion peptides derived from the Spike fusion domain of SARS-CoV-2. The experiments reported (surface pressure-area isotherm, lipid monolayer-peptide binding assays, BAM, CD and NR) shed light on the role of each peptide in the interaction with the host cell, thus providing molecular details on the fusion mechanism between viral membrane and host membrane, which is the key step of the infection. Moreover, experiments with solid supported lipid bilayers were used to investigate the influence that calcium ions have on the binding.

As perspectives, NR experiments with a longer fusion peptide will be performed (beamtime awarded at ISIS, number RB2210247), to investigate their interaction with solid supported bilayers

made of synthetic and natural lipids, also exploring the influence of calcium concentration. Moreover, electrophysiology experiments will be performed at ILL to demonstrate the pore formation that FP1 induce when calcium concentration is increased.

Publication list

Chapter 3 is based on: "Unravelling the orientation of the inositol-biphosphate ring and its dependence on PI(4,5)P_2 cluster formation in model membranes", A. Santamaria, J. Carrascosa-Tejedor, E. Guzmán, N. R. Zaccai, A. Maestro, which has been submitted to the *Journal of colloids and interface science.*

Chapter 4 is based on: "Investigation on the relationship between lipid composition and structure in model membranes composed of extracted natural phospholipids", A. Santamaria, K. C. Batchu, G. Fragneto, V. Laux, M. Haertlein, T. A. Darwish, R. A. Russell, N. R. Zaccai, E. Guzmán, A. Maestro, which has been submitted to *Journal of colloids and interface science.*

Chapter 5 is based on: ""Untangling structural molecular details of the endocytic adaptor protein CALM upon binding with PIP_2-containing model membranes", which will be submitted to *Nature Communications*.

The data presented in **Chapter 6** are part of manuscripts in preparation.

Chapter 7 is based on: "Strikingly different roles of SARS-CoV-2 fusion peptides uncovered by neutron scattering", A. Santamaria, K. C. Batchu, O. Matsarskaia, S. F. Prévost, D. Russo, F. Natali, T. Seydel, I. Hoffmann, V. Laux, M. Haertlein, T. A. Darwish, R. A. Russell, G. Corucci, G. Fragneto, A. Maestro, N. R. Zaccai, which has been published on the *Journal of American Chemical Society*, Volume 144, Issue 7, Year 2022 (doi:10.1021/jacs.1c09856). This chapter also contains data that are part of a manuscript in preparation (paragraph 3.5).

Other published journal articles not included in this manuscript

J. Carrascosa-Tejedor, A. Santamaria, D. Pereira, A. Maestro. "Structure of DPPC Monolayers at the Air/Buffer Interface: A Neutron Reflectometry and Ellipsometry Study". *Coatings 2020,* Vol 10, Page 507. 2020;10(6):507. doi:10.3390/COATINGS10060507.

A. Luchini, S. Micciulla, G. Corucci, K. C. Batchu, A. Santamaria, V. Laux, T. Darwish, R. A Russel, M. Thepaut, I. Bally, F. Fieschi, G. Fragneto. "Lipid bilayer degradation induced by SARS-CoV-2 spike protein as revealed by neutron reflectometry". *Sci Rep*. 2021;11(1). doi:10.1038/s41598-021-93996-x.